

REPORT DOCUMENTATION PAGE

Form Approved OMB NO. 0704-0188

The public reporting burden for this collection of information is estimated to average 1 hour per response, including the time for reviewing instructions, searching existing data sources, gathering and maintaining the data needed, and completing and reviewing the collection of information. Send comments regarding this burden estimate or any other aspect of this collection of information, including suggestions for reducing this burden, to Washington Headquarters Services, Directorate for Information Operations and Reports, 1215 Jefferson Davis Highway, Suite 1204, Arlington VA 22202-4302. Respondents should be aware that notwithstanding any other provision of law, no person shall be subject to any penalty for failing to comply with a collection of information if it does not display a currently valid OMB control number.
PLEASE DO NOT RETURN YOUR FORM TO THE ABOVE ADDRESS.

1. REPORT DATE (DD-MM-YYYY) 28-12-2015	2. REPORT TYPE Final Report	3. DATES COVERED (From - To) 15-Aug-2012 - 14-Aug-2015		
4. TITLE AND SUBTITLE Final Report: Multi-Scale Analysis of Deformation and Failure in Polycrystalline Titanium Alloys Under High Strain Rates		5a. CONTRACT NUMBER W911NF-12-1-0376		
		5b. GRANT NUMBER		
		5c. PROGRAM ELEMENT NUMBER 611102		
6. AUTHORS Somnath Ghosh		5d. PROJECT NUMBER		
		5e. TASK NUMBER		
		5f. WORK UNIT NUMBER		
7. PERFORMING ORGANIZATION NAMES AND ADDRESSES Johns Hopkins University Physics & Astronomy 3400 North Charles Street Baltimore, MD 21218 -2685		8. PERFORMING ORGANIZATION REPORT NUMBER		
9. SPONSORING/MONITORING AGENCY NAME(S) AND ADDRESS (ES) U.S. Army Research Office P.O. Box 12211 Research Triangle Park, NC 27709-2211		10. SPONSOR/MONITOR'S ACRONYM(S) ARO		
		11. SPONSOR/MONITOR'S REPORT NUMBER(S) 60053-EG.1		
12. DISTRIBUTION AVAILABILITY STATEMENT Approved for Public Release; Distribution Unlimited				
13. SUPPLEMENTARY NOTES The views, opinions and/or findings contained in this report are those of the author(s) and should not be construed as an official Department of the Army position, policy or decision, unless so designated by other documentation.				
14. ABSTRACT The research has developed a powerful crystal plasticity based computational modeling tool for predicting mechanical response and localization, eventually leading to failure in polycrystalline titanium alloys, e.g. Ti-6Al-4V and Ti-7Al under extreme loading conditions. Ti alloys possess complex heterogeneous microstructures due to non-uniform grain size distribution and strong anisotropy arising from dislocation glide on different slip systems. The computational model aims at enhancing the predictive capabilities, accounting for the effects of morphological and anisotropic features of 3D microstructures and loading characteristics on the deformation and failure.				
15. SUBJECT TERMS Crystal Plasticity FEM, High Strain Rate, Stabilized Tet4 Element, Adiabatic Heating, Localization				
16. SECURITY CLASSIFICATION OF: a. REPORT UU		17. LIMITATION OF ABSTRACT UU	15. NUMBER OF PAGES	19a. NAME OF RESPONSIBLE PERSON Somnath Ghosh
b. ABSTRACT UU		c. THIS PAGE UU		19b. TELEPHONE NUMBER 410-516-8690

Report Title

Final Report: Multi-Scale Analysis of Deformation and Failure in Polycrystalline Titanium Alloys Under High Strain Rates

ABSTRACT

The research has developed a powerful crystal plasticity based computational modeling tool for predicting mechanical response and localization, eventually leading to failure in polycrystalline titanium alloys, e.g. Ti-6Al-4V and Ti-7Al under extreme loading conditions. Ti alloys possess complex heterogeneous microstructures due to non-uniform grain size distribution and strong anisotropy arising from dislocation glide on different slip systems. The computational model aims at enhancing the predictive capabilities, accounting for the effects of morphological and crystallographic features of 3D microstructures and loading characteristics on the deformation and failure mechanisms. Collaboration has been pursued with ARL researchers on material data and experiments. Various modules pursued are:
Microstructural Characterization and Image-Based Virtual Model Generation: We have developed robust 3D models virtual polycrystalline microstructures of Ti-7Al that represent both morphological and crystallographic statistics observed in OIM scans.
Physics-Based Micromechanical Modeling: This work has developed a unified dislocation density-based crystal plasticity model for hcp metals by combining the thermally-activated and drag-dominated stages of dislocation slip. The model is suitable for modeling deformation under a wide range of strain rates. The effects of temperature are considered. The proposed constitutive model is incorporated into a stabilized locking-free large deformation finite element (FE) framework.

Enter List of papers submitted or published that acknowledge ARO support from the start of the project to the date of this printing. List the papers, including journal references, in the following categories:

(a) Papers published in peer-reviewed journals (N/A for none)

Received Paper

TOTAL:

Number of Papers published in peer-reviewed journals:

(b) Papers published in non-peer-reviewed journals (N/A for none)

Received Paper

TOTAL:

Number of Papers published in non peer-reviewed journals:

(c) Presentations

Plenary/Keynote Lectures

1. S. Ghosh, (semi-Plenary) "Computational Mechanics in Advancing the Integrated Computational Materials Science & Engineering (ICMSE) Initiative for Metals and Alloys", 13th US National Congress of Computational Mechanics, San Diego CA, July 27-30, 2015.
2. S. Ghosh, "Integrated Computational Materials Science & Engineering (ICMSE) Initiative in Predicting Deformation and Fatigue in Polycrystalline Metals and Alloys", 5th International Congress on Computational Mechanics and Simulation: ICCMS 2014, CSIR-SERC Chennai, India, December 10-13, 2014.
3. S. Ghosh, "Spatial and Temporal Multi-Scale Modeling of Lightweight Metallic Materials: Addressing the ICMSE Initiative", 2nd Light-Weighting Summit Advances in Materials for Automotive Mass Reduction, Detroit, MI, March 3-5, 2015..

Invited Lectures at Conferences

1. S. Ghosh, A. Shahba and A. Pilchak, "Modeling Fatigue Crack Nucleation in Polycrystalline Ti Alloys Using Crystal Plasticity FE Models", TMS 2015 144th Annual Meeting & Exhibition, Orlando, FL, March 15-19, 2015.
2. A. Shahba, C. Tao, A. Pilchak and S. Ghosh, "Crystal Plasticity Modeling of Single-phase Titanium Alloys", 17th U.S. National Congress on Theoretical & Applied Mechanics, East Lansing, MI, June 18-20, 2014.

Number of Presentations: 5.00

Non Peer-Reviewed Conference Proceeding publications (other than abstracts):

Received Paper

TOTAL:

Number of Non Peer-Reviewed Conference Proceeding publications (other than abstracts):

Peer-Reviewed Conference Proceeding publications (other than abstracts):

Received Paper

TOTAL:

Number of Peer-Reviewed Conference Proceeding publications (other than abstracts):

(d) Manuscripts

Received Paper

TOTAL:

Number of Manuscripts:

Books

Received Book

TOTAL:

Received Book Chapter

TOTAL:

Patents Submitted

Patents Awarded

Awards

2014 Fellow, Engineering Mechanics Institute (EMI), American Society of Civil Engineers

2013 Distinguished Alumnus Award, Indian Institute of Technology (IIT), Kharagpur

2013 Nathan M. Newmark Medal, American Society of Civil Engineers (ASCE)

2012 Lecturer of CISM short course on Multiscale Modelling of Complex Materials, Udine Italy

2016 Chair, IUTAM Symposium SYFSO12 on Integrated Computational Structure-Material Modeling of Deformation and Failure under Extreme Conditions

2014-2016 President, US Association for Computational Mechanics (USACM), (Vice-President 2012-2014, Secretary/Treasurer 2010-2012)

2013-present Founder/Director, JHU Center for Integrated Structure-Materials Modeling & Simulation (CISMMS)

2012-present Director and Principal Investigator, Air Force-JHU Center of Excellence on Integrated Materials Modeling (CEIMM)

2011-2014 Chair, Computational Mechanics Committee, Engineering Mechanics Institute, ASCE (Vice-Chair: 2010-2011, 2014-2015)

2012 Chair, Organizing Committee, 22nd International Workshop on Computational Mechanics of Materials (IWCMM-XXII)

Graduate Students

NAME	PERCENT SUPPORTED	Discipline
Chengcheng Tao	1.00	
Ahmad Shahba	1.00	
Xiaohui Tu	1.00	
FTE Equivalent:	3.00	
Total Number:	3	

Names of Post Doctorates

NAME	PERCENT SUPPORTED
FTE Equivalent:	
Total Number:	

Names of Faculty Supported

NAME	PERCENT SUPPORTED	National Academy Member
Somnath Ghosh	0.08	
FTE Equivalent:	0.08	
Total Number:	1	

Names of Under Graduate students supported

NAME	PERCENT SUPPORTED
FTE Equivalent:	
Total Number:	

Student Metrics

This section only applies to graduating undergraduates supported by this agreement in this reporting period

The number of undergraduates funded by this agreement who graduated during this period: 0.00

The number of undergraduates funded by this agreement who graduated during this period with a degree in science, mathematics, engineering, or technology fields:..... 0.00

The number of undergraduates funded by your agreement who graduated during this period and will continue to pursue a graduate or Ph.D. degree in science, mathematics, engineering, or technology fields:..... 0.00

Number of graduating undergraduates who achieved a 3.5 GPA to 4.0 (4.0 max scale):..... 0.00

Number of graduating undergraduates funded by a DoD funded Center of Excellence grant for Education, Research and Engineering:..... 0.00

The number of undergraduates funded by your agreement who graduated during this period and intend to work for the Department of Defense 0.00

The number of undergraduates funded by your agreement who graduated during this period and will receive scholarships or fellowships for further studies in science, mathematics, engineering or technology fields: 0.00

Names of Personnel receiving masters degrees

NAME

Chengcheng Tao

Total Number:

1

Names of personnel receiving PHDs

NAME

Total Number:

Names of other research staff

NAME

PERCENT_SUPPORTED

FTE Equivalent:

Total Number:

Sub Contractors (DD882)

Inventions (DD882)

Scientific Progress

See Attachments

Technology Transfer

The research team has made significant progress in the modeling in collaboration with Dr. Brian Schuster, Dr. Emily Huskins and their group at ARL. In this collaboration, we are provided with important experimental observations and deformation characteristics which are being used for model development, calibration and validation. We have one joint paper submitted and another one in progress. As an additional component, Dr. Schuster and our team are collaborating with Dr. Adam Pilchak of AFRL for material microstructure characterization of Ti alloys. The PI has also been in discussion with Dr. Rich Becker on the computational models being developed. Some of these codes will possibly be transitioned to the ARL platforms upon completion. Furthermore, we are working with industrial partners like Pratt & Whitney for transitioning some of the technology to their platforms,

**Multi-Scale Crystal Plasticity FEM Modeling of Deformation and
Localized Failure in Polycrystalline Titanium Alloys at High
Strain-Rates**

Sponsor: Army Research Office, Solid Mechanics

Grant No. W911NF-12-1-0376

Period of Performance: 2012-2015

Program Manager: Dr. Asher Rubinstein

By

Somnath Ghosh, Professor

**Departments of Civil Engineering, Mechanical Engineering, and Materials Science & Engineering
Johns Hopkins University, Baltimore, MD 21218**

December 28, 2015

Acknowledgement

The author would like thank the Army Research Office, Solid Mechanics Program, for supporting this work through grant No. W911NF-12-1-0376. He would like to express his gratitude to Dr. Ralph Anthenien and Dr. Asher Rubinstein for their support. Extensive computer support by the JHU Homewood High-Performance Cluster and Maryland Advanced Research Computing Center MARCC is also gratefully acknowledged.

Contents

1	Relevant Information	1
1.1	Personnel Supported	1
1.2	Completed M.S. Thesis	1
1.3	Refereed Journal Publications Acknowledging ARO Grant	1
1.4	Plenary/Keynote Lectures	2
1.5	Invited Lectures at Conferences	2
1.6	Collaborations with Army Research Laboratory and Technology Transfer	2
2	Introduction	3
2.1	Relevance to the Army	3
2.2	Approach	3
2.3	Accomplishments	4
3	Dislocation density-based multi-rate crystal plasticity finite element model for <i>hcp</i> metals	6
3.1	Introduction	6
3.2	Materials, reconstruction of statistically-equivalent microstructure and mesh convergence study	8
3.2.1	Material description	8
3.2.2	Reconstruction of virtual microstructures	8
3.2.3	Mesh convergence study	9
3.3	Mechanical testing of polycrystalline samples	9
3.4	Crystal plasticity constitutive model	11
3.4.1	The constitutive model	12
3.4.2	The Flow rule	13
3.4.3	Evolution of dislocation densities	18
3.4.4	Adiabatic heating	20
3.4.5	Time integration algorithm for crystal plasticity constitutive model	20
3.5	Stabilization of linear tetrahedral elements for CPFE modeling	21
3.6	Numerical results	23
3.6.1	Calibration and validation of constitutive models with experiments	23
3.6.2	Rate dependence of flow stress	29
3.6.3	Temperature-dependence of flow stress	32
3.6.4	Adiabatic heating	33
3.7	Concluding remarks	37

Abstract

The research has developed a powerful crystal plasticity based computational modeling tool for predicting mechanical response and localization, eventually leading to failure in polycrystalline titanium alloys, e.g. Ti-6Al-4V and Ti-7Al under extreme loading conditions. Utilization of Ti alloys in different army applications requires the model to be applicable to a wide range of strain rates and temperatures. Ti alloys possess complex heterogeneous microstructures due to non-uniform grain size distribution and strong anisotropy arising from dislocation glide on different slip systems. The computational model aims at enhancing the predictive capabilities, accounting for the effects of morphological and crystallographic features of 3D microstructures and loading characteristics on the deformation and failure mechanisms.

The project had launched an integrated computational-experimental research program in collaboration with Army Research Laboratory for developing micromechanical crystal plasticity finite element (CPFE) models of Ti alloys that can predict deformation mechanisms leading to failure. Collaboration has been pursued with Dr. Brian Schuster and his team at ARL on material data and experiments. Various modules pursued are:

1. *Microstructural Characterization and Image-Based Virtual Model Generation:* High fidelity 3D representation of polycrystalline microstructures from metallographic observations to the finite element model is essential for reliable prediction of deformation and damage. In collaboration with Dr. Schusters team at ARL, we have developed robust 3D models virtual polycrystalline microstructures of Ti-7Al that represent both morphological and crystallographic statistics observed in OIM scans.
2. *Physics-Based Micromechanical Modeling:* Dislocation motion in metals is governed by the thermally-activated and drag-dominated processes under low and high rates of deformation, respectively. This work develops a unified dislocation density-based crystal plasticity (CP) constitutive model for *hcp* metals by combining the thermally-activated and drag-dominated stages of dislocation slip. The model is suitable for modeling deformation under a wide range of strain rates. The effects of temperature on both elasticity and plasticity are considered and carefully calibrated using experimental results. The proposed constitutive model is incorporated into a stabilized locking-free large deformation finite element (FE) framework. Competency of the methodology is demonstrated for two types of Ti-7Al alloy polycrystals. For simulations, the CPFE model uses the image-based virtual polycrystalline microstructures generated from 2D surface data. Room temperature compression tests at quasi-static (10^{-3} s^{-1}) and dynamic strain rates (1000 - 4000 s^{-1}) are used to calibrate and validate the constitutive model. Rate-dependency of the flow stress is investigated at both single and polycrystalline levels. An elastic overshoot followed by a stress relaxation is observed at very high strain rates in single crystals. In the polycrystalline level, the model is observed to effectively capture the increase in the rate sensitivity at high strain rates. Under adiabatic conditions, the decrease in the hardening rate due to the promotion of slip-driven plasticity is observed to be significant. The effect of degradation of elastic constants on the macroscopic behavior seems to become noticeable only at the later stages of deformation. A careful study on adiabatic heating revealed that unexpectedly the grains undergoing severe plastic deformation do not necessarily endure higher temperatures. In other words, temperature increase in severely plastically deformed grains could be lower than the temperature increase in grains which have undergone a small amount plastic strain.

Chapter 1

Relevant Information

1.1 Personnel Supported

1. Somnath Ghosh, PI
2. Chengcheng Tao, Completed M.S., Graduate Research Associate, 100%
Now at University of Florida.
3. Ahmad Shaba, Ph.D. Student, Graduate Research Associate, 100%
Expected to graduate in 2016
4. Xiaohui Tu, Ph.D. Student, Graduate Research Associate, 100%
Expected to graduate in 2017

1.2 Completed M.S. Thesis

1. C. Tao, M. S. Thesis. 2014, Thesis Title: Crystal Plasticity Based Finite Element Modeling in Polycrystalline Ti-7Al Alloys

1.3 Refereed Journal Publications Acknowledging ARO Grant

1. D. Ozturk, A. Shahba and S. Ghosh, "Crystal plasticity FE study of the effect of thermo-mechanical loading on fatigue crack nucleation in Titanium alloys", *Fatigue & Fracture of Engineering Materials and Structures*, (accepted for publication), 2015.
2. J. Cheng, A. Shahba and S. Ghosh, "Stabilized tetrahedral elements for crystal plasticity finite element analysis overcoming volume locking", *Computational Mechanics*, (accepted for publication), 2015.
3. A. Shahba, X. Tu, E. L. Huskins, B. E. Schuster and S. Ghosh, "Dislocation density crystal plasticity model for Ti Alloys at a range of strain-rates", *International Journal of Plasticity*, (submitted for publication), 2015..
4. A. Shahba, S. Ghosh, A. Pilchak, "An experimentally-validated crystal plasticity finite element modeling of polycrystalline Ti alloys" (to be submitted for publication).

1.4 Plenary/Keynote Lectures

1. S. Ghosh, (semi-Plenary) Computational Mechanics in Advancing the Integrated Computational Materials Science & Engineering (ICMSE) Initiative for Metals and Alloys, 13th US National Congress of Computational Mechanics, San Diego CA, July 27-30, 2015.
2. S. Ghosh, Integrated Computational Materials Science & Engineering (ICMSE) Initiative in Predicting Deformation and Fatigue in Polycrystalline Metals and Alloys, 5th International Congress on Computational Mechanics and Simulation: ICCMS 2014, CSIR-SERC Chennai, India, December 10-13, 2014.
3. S. Ghosh, Spatial and Temporal Multi-Scale Modeling of Lightweight Metallic Materials: Addressing the ICMSE Initiative, 2nd Light -Weighting Summit Advances in Materials for Automotive Mass Reduction, Detroit, MI, March 3-5, 2015..

1.5 Invited Lectures at Conferences

1. S. Ghosh, A. Shahba and A. Pilchak, Modeling Fatigue Crack Nucleation in Polycrystalline Ti Alloys Using Crystal Plasticity FE Models, TMS 2015 144th Annual Meeting & Exhibition, Orlando, FL, March 15-19, 2015.
2. A. Shahba, C. Tao, A. Pilchak and S. Ghosh, Crystal Plasticity Modeling of Single-phase Titanium Alloys, 17th U.S. National Congress on Theoretical & Applied Mechanics, East Lansing, MI, June 18-20, 2014.

1.6 Collaborations with Army Research Laboratory and Technology Transfer

The research team has made significant progress in the modeling in collaboration with Dr. Brian Schuster, Dr. Emily Huskins and their group at ARL. In this collaboration, we are provided with important experimental observations and deformation characteristics which are being used for model development, calibration and validation. We have one joint paper submitted and another one in progress. As an additional component, Dr. Schuster and our team are collaborating with Dr. Adam Pilchak of AFRL for material microstructure characterization of Ti alloys. The PI has also been in discussion with Dr. Rich Becker on the computational models being developed. Some of these codes will possibly be transitioned to the ARL platforms upon completion.

Chapter 2

Introduction

The research in this project has developed a powerful crystal plasticity based computational modeling tool for predicting mechanical response and localization, eventually leading to failure in polycrystalline titanium alloys, e.g. Ti-6Al-4V and Ti-7Al under extreme loading conditions. Utilization of Ti alloys in different army applications requires the model to be applicable to a wide range of strain rates and temperatures. Given the fact that Ti alloys possess a very complicated heterogeneous microstructure due to non-uniform grain size distribution and strong anisotropy arising from dislocation glide on different slip systems, the model aims at enhancing the predictive capabilities, accounting for the effects of morphological and crystallographic features of 3D microstructures and loading characteristics on the deformation and failure mechanisms.

2.1 Relevance to the Army

Due to increasing anti-armor threats, more armor protection has been added to ground combat vehicles, resulting in increasing their weight which consequently affects their transportability and maneuverability. There is an increasing interest in using materials with lighter weight and yet higher strength for armor applications. Titanium alloys are very good candidates for armor applications due to their high strength to weight ratio and good corrosion resistance which lowers the maintenance costs. Application of low-cost titanium alloys brings about a lot of benefits for army applications in terms of performance and life of components and economics. As an example, replacing forged aluminum with titanium in commanders hatch of M2 Bradley fighting vehicle has resulted in 35% of weight saving with increased ballistic protection.

2.2 Approach

The research project had launched an integrated computational-experimental research program in collaboration with Army Research Laboratory for developing micromechanical crystal plasticity finite element (CPFE) models of Ti alloys that can predict deformation mechanisms leading to failure. Collaboration has been pursued with Dr. Brian Schuster and his team at ARL on material data and experiments. Various modules pursued are:

1. *Microstructural Characterization and Image-Based Virtual Model Generation:* High fidelity 3D representation of polycrystalline microstructures from metallographic observations to the finite element model is essential for reliable prediction of deformation and damage. In collaboration with Dr. Schusters team at ARL, we have developed robust 3D models virtual polycrystalline microstructures of Ti-7Al that represent both morphological and crystallographic statistics observed in OIM scans.
2. *Physics-Based Micromechanical Modeling:* This task has developed image-based crystal plasticity finite element models (CPFEM), incorporating experimentally measured morphological and crystallographic details and deformation/failure mechanisms. Three subtasks have been successfully executed in this category.

- i. Crystal plasticity finite element predictions are highly dependent on the local material state. Conventionally used tetrahedral element suffers from volumetric locking as the (near-) incompressible limit approaches, resulting in spurious high hydrostatic stresses and underestimation of displacements. A stabilized tetrahedral element has been developed in this task to provide robust analysis capabilities for large and localized formation in CPFEM.
- ii. A novel dislocation density based flow rule has been developed in this work for dislocation glide for Ti alloys at a range of strain rates. The model is based on experimental observations on dislocation kinetics. Unlike other flow rules in the literature, application of this flow rule is not confined to a certain range of strain rates. It is applicable to a wide range of strain rates, making it possible to use the same modeling framework for simulating deformation and failure in low and high strain rates.
- iii. Adiabatic heating is essential for modeling high rates of deformation due to conversion of plastic work into heat. To address the effects of thermal expansion due to temperature increase in the course of plastic deformation, a thermally-deformed configuration is considered besides the well-known reference, intermediate plastically deformed and current configurations.

2.3 Accomplishments

We have developed a novel image-based crystal plasticity finite element (CPFE) model for high strain rate deformation behavior of Ti alloys, e.g. Ti-7Al. The experimentally validated models are expected to predict finite deformation behavior both at micro and macro-scales in comparison with experiments at a range of strain rates and temperatures. Eventually the models should be able to predict deformation induced localization and microcracking in microstructures of polycrystalline metals. Important mechanisms that are incorporated in the crystal plasticity model include: dislocation glide mechanisms, size dependence in polycrystalline models through geometrically necessary dislocations (GNDs), and formation of adiabatic shear banding. The following tasks have been achieved in this project.

1. Microstructural Characterization and Image-Based Virtual Model Generation

3D microstructures are generated using electron back-scattered diffraction (EBSD) data of sections of the material microstructure. The work employs a method of estimating 3D statistics from extrapolation of 2D surface measurements and data on polycrystalline specimens. A code DREAM.3D is used for this reconstruction. The reconstruction algorithm is based on stereology, a method of creating statistically equivalent 3D morphologies from 2D measurements. 2D EBSD maps are studied and the relevant statistical distributions such as grain size, orientation and etc. are extracted and fed into DREAM3D to generate different microstructures based on the same set of distributions.

2. Stabilized 3D Tetrahedral Elements for Locking-free Crystal Plasticity Modeling

Linear tetrahedral elements are favorable for the discretization process due to their inherent simplicity in formulations, tortuosity and complex geometry of grains in the microstructure and the necessity of conformity of the mesh to the geometry. However, these elements suffer from volumetric locking as the material deformation approaches (near-) incompressibility leading to underestimation of displacement field and overestimation of pressure field accompanied with checker-board oscillation of pressure in the computational domain. As plasticity is inherently volume-conserving, utilizing tetrahedral elements for crystal plasticity FE simulations is accompanied with errors due to locking. In order to relieve volumetric locking, the F-bar-patch method is developed for crystal plasticity simulations, where the deformation gradient for stress calculation is modified such that incompressibility is satisfied in a weak sense rather than a point-wise strong sense. Elements in the mesh are assigned to different non-overlapping patches.

3. Novel Dislocation Density based CPFEM for Modeling at a Range of Strain-Rates

The crystal plasticity model is developed to overcome the limitations of phenomenological formulations by incorporating underlying physics of mechanisms. It adopts a dislocation density-based formulation where the effect of strain rate is addressed through the evolution of dislocation densities and velocity of dislocations. In this model, density of mobile dislocations is responsible for plastic deformation, and strain hardening is primarily

due to the entanglement of mobile dislocations with barriers. To have a unified flow rule for a wide range of strain rates and temperatures, it is necessary to adopt a proper flow rule which is explicitly temperature-dependent and reflects the rate sensitivity of dislocation glide correctly. The commonly used flow rules in the literature are either not explicitly temperature dependent or they are applicable to a certain range of strain rates. Experimental observations show that screw dislocations are responsible for plastic flow in Ti alloys. Screw dislocations glide on slip plane through a double-kink mechanism which is a thermally activated process. Once a kink is formed, it will broaden sideways under drag-dominated regime. At time t , kink has broadened completely and the whole dislocation line is brought to the next Peierls valley. At lower strain rates, the waiting time is larger than running time, i.e. the dislocation motion is thermally-activated. However in higher rates of deformation, the running time gets larger than the waiting time and renders the dislocation motion drag-dominated. At lower levels of stress the new velocity profile matches the velocity due to only thermal activation, whereas at higher stresses it matches the one due to only drag forces and it does a smooth transition from thermally-activated to drag-dominated regime in between. A unified constitutive relation is developed in this work to reflect this effect.

4. Incorporating Adiabatic Heating at Different Strain-Rates in CPFEM

Under high rate of deformation, the plastic work is converted into heat. The time scale for thermal conduction is larger in comparison with the time scale for dynamic deformation; therefore, it is a fair assumption that heating is adiabatic. The rate of plastic work is calculated in the crystal plasticity model and localized temperature evolution is predicted. It is observed that adiabatic heating softens the response by promoting plasticity through thermal activation. To address the thermal expansion due to temperature increase, the deformation kinematics is modified to include a thermally-deformed configuration.

Chapter 3

Dislocation density-based multi-rate crystal plasticity finite element model for *hcp* metals

3.1 Introduction

Titanium alloys are widely used in manufacturing components for automotive and aerospace industries due to their high strength to weight ratio, high fracture toughness and good corrosion resistance at elevated temperatures. Extensive use of these alloys in critical industrial and military applications, such as compressor blades of jet engines and armor of ground combat vehicles [58], has motivated researchers to understand, measure and tailor the mechanical properties of these alloys over a wide range of strain rates and temperatures. Of special interest has been the mechanical response of these alloys under high rates of deformation [20, 70, 46, 45, 47] and failure under cyclic/dwell fatigue [10, 75, 68]. Over the years, these experimental observations have provided modelers with enlightening insight to develop new constitutive models and methodologies to explain many of the observations from a computational mechanics point of view and hopefully help designers design components with a better understanding of the failure modes and expected lifetime of the components.

One of the most powerful methods developed in the past two decades for modeling material behavior is crystal plasticity finite element method (CPFEM). Its advantages inhere within its capability to describe the mechanical anisotropy and material heterogeneity via micro-mechanism-based constitutive laws, which could be informed from multiple length-scales ranging from sub-grain level to the polycrystalline level [44]. The accuracy of CPFE models and their capability in prediction of material response in polycrystalline level are dependent on majorly three factors, including creation of a virtual realistic polycrystalline aggregate model, utilization of a robust element formulation for finite element calculations and description of material response with a proper constitutive law.

Accuracy of CPFE models have significantly improved over the past few years due to the advances in image-based modeling and reconstructing statistically equivalent polycrystalline aggregates using the collected 2D or 3D data [34, 35, 36]. This is a crucial step toward understanding the macroscopic behavior of the material in terms of its morphological and crystallographic properties. Development of meshing codes and software products [74] which can discretize the complex polycrystalline microstructures into simple finite elements has been also instrumental in paving the way towards realistic CPFE simulations.

In order to carry out a finite element analysis, it is required that the elements conform to the geometry of the computational domain. This requirement has an implication for CPFE analysis of polycrystalline aggregates. Linear constant strain tetrahedral elements are used to discretize the polycrystalline aggregates due to the complex morphology of grains and the magnificent capability of these elements to conform to tortuous geometries. However, these elements suffer from severe volumetric locking when simulating the deformation of (nearly-) incompressible materials. Various methods have been proposed to relieve volumetric locking in tetrahedral elements, for instance node-based

uniform strain formulation [27, 69], **F**-bar-patch method [25] and mixed enhanced formulation [54]. Since plasticity is inherently isochoric, volumetric locking of tetrahedral elements is highly relevant to the CPFE simulation; however, its detrimental effect on the solution has been generally overlooked by the materials modeling community. The adverse effects of volumetric locking on predicting the response of microstructures in 2D [83] and 3D [19] have been shown recently. In this work, the model proposed in Cheng et al [19] is used to relieve volumetric locking in CPFE simulations.

Describing the material response with a proper constitutive law plays a key role in the success of the CPFE models to represent the behavior of the material. The most critical part of a CP constitutive law is the flow rule which interrelates the the local material state (e.g. dislocation density) and local stress state with the kinematics (e.g. slip rates). Suitability of a constitutive law for a certain application inheres in how rigorously the flow rule can capture the governing deformation mechanism(s). Selection of the proper type of flow rule is largely problem-dependent since flow rules are developed on the premise of certain assumptions and pose some limitations with respect to their use. The most commonly used expressions for the flow rule are the phenomenological power-law model [67], Arrhenius-type activation energy-based model [48] and linear model [48].

- The **power-law model** is a simple and yet effective flow rule for modeling materials deforming under low strain rates. This flow rule could be also used for modeling moderately high strain deformations, provided that the effects of temperature increase on the plastic flow are taken into account.
- Arrhenius-type **activation energy-based model** [43, 28] is applicable as long as the dislocation glide is governed by the thermally-activated processes, e.g. deformations under low up to moderately high strain rates ($10^4 \sim 10^5 \text{ s}^{-1}$). Since this flow rule has explicit dependence on the temperature, it can be effectively used for simulating phenomena which are highly temperature-dependent such as dwell fatigue in Ti alloys [84, 65].
- The **linear flow rule** is suitable for modeling metals deforming under strain rates exceeding 10^5 s^{-1} where the dislocation motion is administered by the drag-dominated processes.

Deriving a rate-dependent physics-based flow rule whose application is not limited to a certain range of strain rates is desired. Using such a flow rule is encouraged in simulation of polycrystalline aggregates where the local stress and strain rates might be lower or higher than the applied macroscopic stress or strain rate. For instance, in Ti alloys under applied creep load σ_{app} , stress redistribution happens locally in the microstructure due to the grain-level load shedding from the *soft* grains to the adjacent *hard* grains [39]. This is known as *load-shedding* mechanism which induces stresses higher than σ_{app} in the *hard* grains while the stress in the adjacent *soft* grain could be lower than σ_{app} . Similarly, a polycrystalline microstructure which is macroscopically deforming under a very high strain rate (in the range of applicability of linear flow rule) could locally undergo a lower rate of deformation (in the range of applicability of activation energy-based flow rule). A new unified flow rule is sought which could be used for both low and high rates of deformation. This unified flow rule should automatically adjusts its functional form based on the local deformation rate , local stress state and internal state variables. Such a flow rule can be obtained based on some physical considerations via combining the thermally-activated and drag-dominated stages of dislocation motion.

Valuable works have been done towards deriving a unified flow rule by formulating new formulations for average velocity of dislocations. Frost and Ashby [32] were the first to propose a dislocation velocity formulation based on combining the thermal activation and drag mechanisms. Dislocation inertial models were later developed to model plasticity in superconductors [49, 42]. Hiratani and Nadgorny [40] developed a unified model to study dislocation motion in 2D through an array of obstacles in a prototype *fcc* metal. A similar unified model was implemented in a discrete dislocation dynamics code to model dislocation behavior in *fcc* metals under creep conditions [41]. Unified flow rules were developed in the context of macroscale J2 plasticity for modeling deformation behavior of *bcc* vanadium and tantalum [11, 12]. Recently, Austin and McDowell [9] developed a unified flow rule to model viscoplastic deformation of *fcc* aluminum alloys under shock loading using a dislocation density-based crystal plasticity framework. Most of the works on the development of a unified flow rule have been in the realm of analytical models or modeling motion of discrete dislocations in a 2D array of obstacles. There are very few works that have investigated the capability of these unified flow rules in modeling deformation of polycrystalline aggregates within the framework of CPFE analysis. In this work, we build upon the existing formulations in the literature and extend the idea of unified flow rules to the CPFE simulation of *hcp* metals, Ti alloys in particular.

In this work, the mechanical response of an α Ti alloy with two different microstructures (due to different methods of material processing) is investigated under low and high rates of deformation. Section 3.2 discusses the materials and explains the procedure of reconstructing statistically equivalent microstructures from collected 2D data. This section concludes with a FE mesh convergence study. Section 3.3 provides the details of the quasi-static and dynamic tests. Section 3.4 discusses the constitutive model in details. Stabilization of the linear tetrahedral elements will be briefly explained in Section 3.5. Section 3.6 discusses the procedure of calibration and validation of the constitutive models. Numerical results are provided which highlight the rate-dependency of flow stress and importance of temperature in the context of isothermal and adiabatic simulations.

3.2 Materials, reconstruction of statistically-equivalent microstructure and mesh convergence study

To predict mechanical response of crystalline metals, it is important to represent relevant morphological and crystallographic features of the microstructure, such as grain size distribution, orientation distribution and misorientation distribution, in the 3D reconstructed virtual microstructures. There are different methods to generate 3D virtual microstructures based on experimental measurements. Electron back-scattered diffraction (EBSD) data collected from focused ion beam (FIB)-based serial sectioning of polycrystalline samples could be utilized to obtain 3D statistics and generate realistic microstructures [13, 33]. Alternatively if data for serial sectioning of the microstructure is not available, it is possible to reconstruct virtual microstructures based on the 3D statistical distributions estimated from the 2D measurements.

In this section, the material used in this study is briefly introduced and reconstruction of 3D virtual microstructures from 2D measurements is then explained in details. A mesh convergence study is then conducted for the CPFE simulations of statistically-equivalent microstructures.

3.2.1 Material description

The material studied is Ti-7.02Al-0.11O-0.015Fe (wt%) alloy with a predominant *hcp* microstructure [14]. The composition of this alloy is very close to the α phase of many commercially important titanium alloys [68]. Mechanical testing is done on two variants of this alloy in this study, referred to as the AR (as-rolled) and RA (rolled-annealed) samples. The AR sample corresponds to the one which has been only rolled whereas the RA sample corresponds to a sample manufactured by first rolling and subsequently annealing it to improve its ductility and increase the grain size, followed by a cooling process. Scanning electron microscopy (SEM) based electron back-scattered diffraction (EBSD) is done under supervision of Dr. Adam Pilchak in the Air Force Research Laboratory (AFRL) to quantify the texture of large-area EBSD scans. The surface EBSD scans for the AR and RA samples are respectively $5425 \times 2190 \mu\text{m}^2$ and $5175 \times 2135 \mu\text{m}^2$, collected at $5 \mu\text{m}$ step size. Figure 3.1 shows a part of surface EBSD scans collected for both samples after being processed to remove *noise* from the data. Average diameter for equivalent projected circle in 2D is calculated to be $34.12 \mu\text{m}$ and $83.4 \mu\text{m}$ for the AR and RA samples, respectively.

3.2.2 Reconstruction of virtual microstructures

2D surface EBSD images for both samples are characterized and crystallographic distributions, viz. orientation and misorientation distributions, and morphological distribution, i.e. distribution of equivalent projected circle diameters (*ECD*), are obtained. 2D crystallographic distributions could be directly used for generating 3D crystallographic statistics; however, it is necessary to employ stereology [72] to estimate 3D morphological distributions from 2D measurements. Using the principles of stereology, the average equivalent sphere diameter (*ESD*) could be expressed in terms of \overline{ECD} as

$$\overline{ESD} = \frac{4}{\pi} \overline{ECD} \quad (3.1)$$

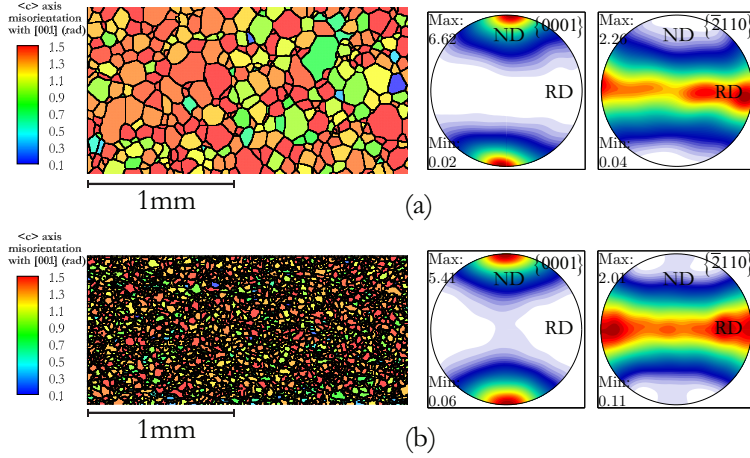


Figure 3.1: processed EBSD scans and pole figures for the (a) RA and (b) AR samples

It has been observed that a log-normal distribution function can adequately represent the grain size distribution in Ti alloys [79]. Method of maximum-likelihood is used to estimate the average and standard deviation parameters for the grain size distribution function. Eventually both morphological and crystallographic distributions are fed into DREAM.3D software [36] to create 3D statistically-equivalent virtual microstructures using the methods described in [34, 35].

Following the aforementioned steps, several statistically-equivalent microstructures, with different numbers of grains, are reconstructed for each sample. Figure 3.2 shows the convergence of orientation, misorientation, and grain size distributions as the number of grains increases in the RA microstructure. Comparing the statistical distributions of virtual microstructures with the ones from 2D EBSD data, it is observed that the distributions for the 529-grain RA microstructure generally show a good agreement; hence, it will be used for the CPFE simulations. Following the same strategy, a convergence study on the distributions is conducted for the AR sample and a 515-grain microstructure is deemed suitable and used for the CPFE simulations. The reconstructed AR and RA microstructures are depicted in Figure 3.3.

3.2.3 Mesh convergence study

It is necessary to conduct a mesh convergence study with respect to both macroscopic and microscopic quantities in CPFE simulations. Simmetrix® software [74] is used to discretize the computational domain into linear constant strain tetrahedral (TET4) elements. Deformation of the microstructure under constant rate of deformation $\dot{\epsilon} = 1.1 \times 10^3 \text{ s}^{-1}$ along [100] is modeled using CPFE simulation. Figure 3.4 shows the results for two mesh densities with 536090 and 754916 elements in terms of macroscopic volumetric-averaged stress-strain response and von Mises stress along an X-directed line passing through the centroid of the RA microstructure. It is inferred from the mesh convergence study that the 536090-element mesh provides sufficient resolution for the CPFE simulations. Similar mesh convergence study is conducted for the AR microstructure where a 517023-element mesh is observed to provide satisfactory convergent results.

3.3 Mechanical testing of polycrystalline samples

The mechanical response of the material was evaluated through room temperature compression tests at quasi-static (10^{-3} s^{-1}) and dynamic strain rates ($1000 - 4000 \text{ s}^{-1}$). Tests were conducted along the three orthogonal directions (normal, rolled, and transverse) for both the as-rolled and rolled-annealed materials. To minimize the frictional effects in all tests, the ends of the specimens were polished and lubricated.

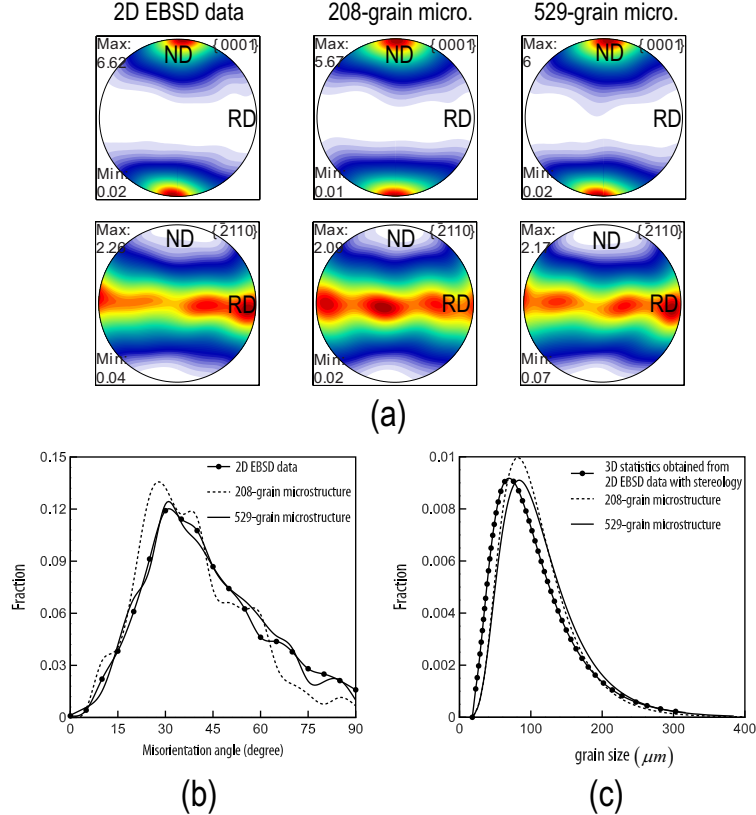


Figure 3.2: Convergence of different distributions with increasing number of grains for the RA microstructure, (a) orientation distribution, (b) misorientation distribution and (c) grain size distribution

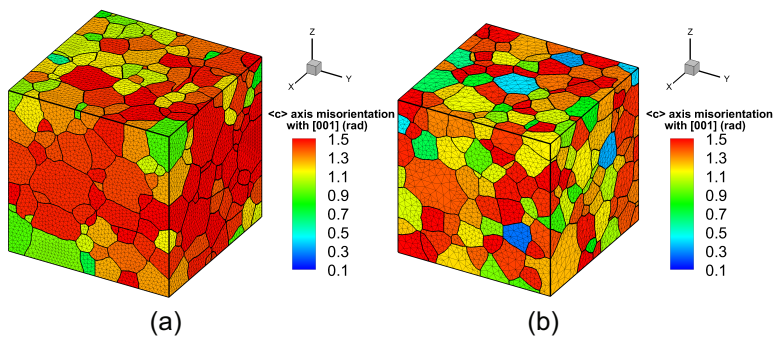


Figure 3.3: Statistically-equivalent microstructures for (a) $960 \times 960 \times 960 \mu\text{m}^3$ RA polycrystalline volume with 529 grains discretized into 536090 linear tetrahedral elements and (b) $300 \times 300 \times 300 \mu\text{m}^3$ AR polycrystalline volume with 515 grains discretized into 517023 linear tetrahedral elements

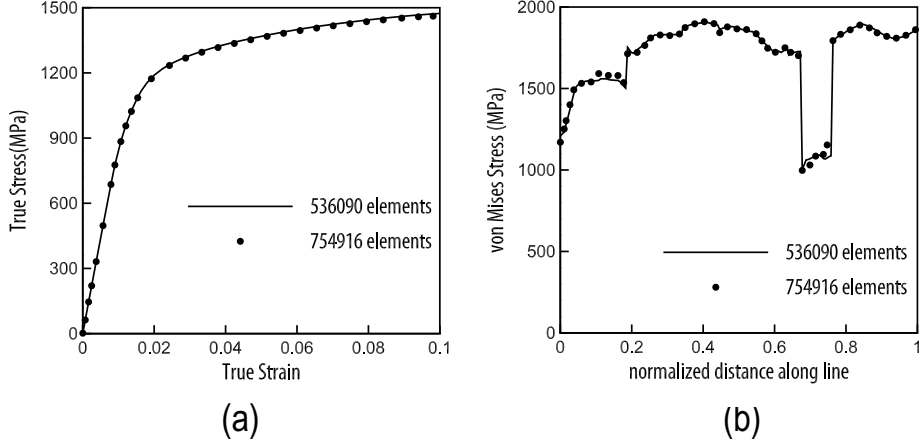


Figure 3.4: mesh convergence study for the RA microstructure with respect to (a) volumetric-averaged loading direction stress-strain response and (b) von Mises stress at 2% strain along an X-directed line passing through the centroid

Quasi-static (QS) tests were conducted on a screw-driven Instron load frame under displacement control conditions. The specimens were rectangular with dimensions $3.5 \times 3.5 \times 7\text{mm}$ (aspect ratio of 2). A compression subpress fixture ensured proper axial alignment during loading. Displacement was measured using a stereoscopic digital image correlation (DIC) system consisting of two 2.3 MP cameras. The choice of a two-camera system was made to eliminate the effect of out of plane motion on the strain measurements. DIC speckle pattern was applied to the surface of the specimen using a fine airbrush. VicSnap and Vic3D were used to acquire the images and perform the correlation (subset 29, step 10). Uniaxial strain was calculated using a digital extensometer. None of the specimens failed during testing. Unloading was initiated either after sufficient data was obtained or the specimen began to deform in a non-uniform manner upon which the data became invalid. The response of the material along rolling and transverse directions was observed to be very similar. Compared to the response along the rolling and transverse directions, over 26% increase is observed in the 0.2% yield strength along the normal direction. Strain hardening is observed for all orientations and is slightly higher along the normal direction. The hardening does not change significantly at dynamic strain rates.

Dynamic strain rate tests were conducted on a compression Kolsky (Split-Hopkinson) bar. The specimens were rectangular with dimensions $3.5 \times 3.5 \times 2.5\text{mm}$ (aspect ratio of 0.7). The Kolsky bar consists of two $3/8\text{in}$ (9.5mm) maraging steel bars, referred to as the input and output bars, with the specimen sandwiched between them. A gas gun accelerates a projectile, which strikes the input bar, creating a compressive stress pulse that travels down the input bar and loads the specimen. The foil strain gages located on the input and output bars record the reflected and transmitted stress pulses, respectively. These data are used to calculate the stress and strain rate history of the specimen once it has reached stress equilibrium. The strain rate history is integrated over time to obtain the strain history, which is correlated with the stress history to form stress-strain curves. A complete description of the Kolsky bar experimental technique is provided by Chen and Song [17].

3.4 Crystal plasticity constitutive model

Microstructure of commercial titanium alloys is composed of either a hexagonal close packed (*hcp*) α or body-centered cubic (*bcc*) β phase or a combination of these two phases. The microstructure phase is highly dependent on the alloying elements and the material processing [22]. We focus on modeling deformation mechanisms in α Ti alloys. Dislocation activity is considered to be the main deformation mechanism for plasticity in these alloys. Dislocation slip was observed to be distributed inhomogeneously into planar arrays due to short range ordering of Ti and Al atoms [59]. Plastic deformation is accommodated by dislocation slip on 30 possible slip systems, categorized into five different

families of slip system as shown in Figure 3.5. The $\langle a \rangle$ - basal and prism slip families have the lowest critical resolved shear stress (CRSS), making them the most active slip families in α Ti alloys. The $\langle c + a \rangle$ - pyramidal slip families have the largest CRSS, 2~3 times the one for the basal or prism slip systems [51].

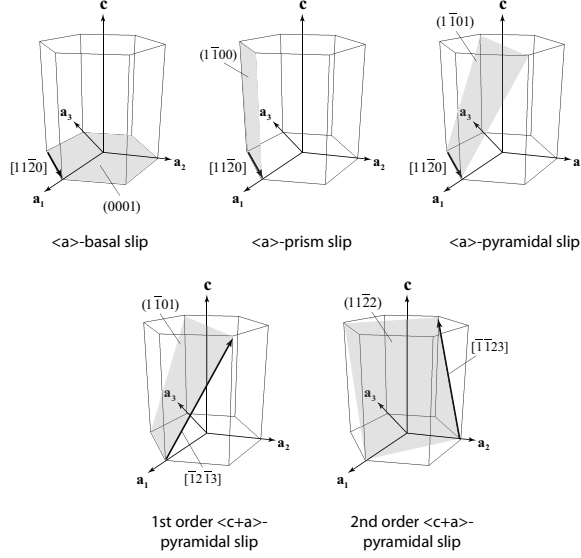


Figure 3.5: Schematic of non-orthogonal base vectors $\{a_1, a_2, a_3, c\}$ and slip system families in *hcp* metals

Twining is another deformation mechanism, contributing to plasticity in *hcp* metals. Deformation twinning is observed in Ti alloys deforming either under high rates or at low temperatures. Deformation twinning has been observed in unalloyed Ti at all temperatures below 500°C [20]. However, alloying Ti with Al inhibits twinning such that titanium alloyed with 6% Al does not twin even at temperatures as low as 100K [66, 82]. Due to the high level of Al content in the alloy of interest, deformation twinning is not considered in the constitutive model.

In this section, the constitutive model is first described and the flow rule is explained in details. Evolution laws for dislocation densities and adiabatic heating are then introduced. This section concludes with the time integration scheme used for updating the CP constitutive law.

3.4.1 The constitutive model

Crystal plasticity FE models describe deformation of polycrystalline aggregates in terms of micro-mechanisms and crystallographic orientations at individual material points. The CP constitutive model presented here is developed for finite deformation of crystalline metals under general non-isothermal conditions. As illustrated in Figure 3.6, the total deformation gradient \mathbf{F} could be multiplicatively decomposed into elastic \mathbf{F}^e , thermal \mathbf{F}^θ and plastic \mathbf{F}^p components as

$$\mathbf{F} = \mathbf{F}^e \mathbf{F}^\theta \mathbf{F}^p \quad (3.2)$$

\mathbf{F}^e accounts for the elastic stretch and rigid body rotations. \mathbf{F}^θ represents the deformation of the crystal lattice due to thermal loading and evolves as [50]

$$\dot{\mathbf{F}}^\theta = \dot{T} \boldsymbol{\alpha} \mathbf{F}^\theta \quad (3.3)$$

where T is the temperature and the overdot represents differentiation with respect to time. $\boldsymbol{\alpha}$ is a diagonal tensor containing thermal expansion coefficients along the principal crystallographic directions expressed with respect to the principal crystallographic coordinate system. *Ab initio* calculations [61, 76] and experimental observations [62] have shown the anisotropic thermal expansion of α titanium over a wide range of temperatures. The thermal expansion

coefficients along $\langle a \rangle$ (in the basal plane) and $\langle c \rangle$ (normal to the basal plane) are respectively taken as $1.8 \times 10^{-5} K^{-1}$ and $1.1 \times 10^{-5} K^{-1}$ [76].

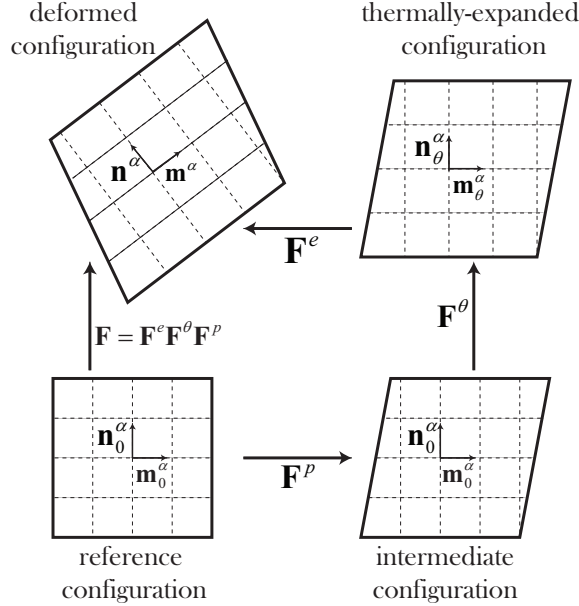


Figure 3.6: Multiplicative decomposition of the total deformation gradient \mathbf{F} into elastic \mathbf{F}^e , thermal \mathbf{F}^θ and plastic \mathbf{F}^p components

\mathbf{F}^p corresponds to the isochoric plastic deformation due to dislocation slip, i.e. $\det \mathbf{F}^p = 1$. The \mathbf{F}^p mapping neither distorts nor rotates the crystal lattice. Using the kinematics of dislocation glide, the plastic velocity gradient tensor \mathbf{L}^p in the intermediate configuration is obtained as [7]

$$\mathbf{L}^p = \dot{\mathbf{F}}^p \mathbf{F}^{p-1} = \sum_{\alpha=1}^{n_{\text{slip}}} \dot{\gamma}^\alpha \mathbf{m}_0^\alpha \otimes \mathbf{n}_0^\alpha \quad (3.4)$$

where $\dot{\gamma}^\alpha$ is the slip rate on slip system α . The summation is done over all slip systems n_{slip} in the crystal, $n_{\text{slip}} = 30$ for the *hcp* crystalline structure. \mathbf{m}_0^α and \mathbf{n}_0^α denote respectively the slip direction and slip plane normal for slip system α in the reference configuration.

The constitutive law is written in the thermally-expanded configuration as

$$\mathbf{S} = \det(\mathbf{F}^e) \mathbf{F}^{e-1} \boldsymbol{\sigma} \mathbf{F}^{e-T} = \mathbb{C} : \mathbf{E}^e \quad (3.5)$$

\mathbb{C} corresponds to the fourth order anisotropic elasticity tensor. \mathbf{S} denotes the second Piola-Kirchhoff stress in the thermally-expanded configuration which is work conjugate to the elastic Green-Lagrange strain $\mathbf{E}^e = \frac{1}{2} (\mathbf{F}^{eT} \mathbf{F}^e - \mathbf{I})$. $\boldsymbol{\sigma}$ is the Cauchy stress. The time integration scheme used for the constitutive updates will be explained later in Section 3.4.5.

3.4.2 The Flow rule

Slip-driven plasticity is interpreted in terms of dislocation glide on specific plane and quantified in terms of slip rates on individual slip systems. In the CP framework, this is achieved by adopting a proper flow rule which expresses the slip rates in terms of the stress state and relevant internal state variables. In the following, first the phenomenological power-law flow rule is briefly introduced. Then the new physics-based flow rule would be derived and explained in

details. Both of these flow rules will be used to model deformation of Ti alloys under various conditions in Section 3.6 where their limitations and capabilities will be highlighted.

Phenomenological power-law flow rule

Phenomenological power-law flow rule, referred to as PL flow rule hereafter, is a simple and yet effective flow rule which has been used for modeling plastic deformation in metals with different crystalline structures. In this section, the PL flow rule developed in [39, 26, 80, 81] for modeling deformation of Ti alloys under low strain rates, creep and dwell fatigue conditions is briefly introduced. The rate-dependent PL flow rule reads as

$$\dot{\gamma}^\alpha = \dot{\gamma}_0^\alpha \left(\frac{|\tau^\alpha| - s_{\text{GND,P}}^\alpha}{s^\alpha} \right)^{\frac{1}{m}} \text{sign}(\tau^\alpha) \quad (3.6)$$

Here m and $\dot{\gamma}_0^\alpha$ are respectively the material rate sensitivity parameter and reference plastic shearing rate. τ^α is the resolved shear stress on slip system α calculated as

$$\tau^\alpha = \det(\mathbf{F}^\theta) \mathbf{C}^e \mathbf{S} : (\mathbf{F}^\theta \mathbf{m}_0^\alpha \otimes \mathbf{n}_0^\alpha \mathbf{F}^{\theta-1}) \quad (3.7)$$

$s_{\text{GND,P}}^\alpha$ denotes the long-range stresses due to the geometrically necessary dislocations (GNDs). $\mathbf{C}^e = \mathbf{F}^{eT} \mathbf{F}^e$ is the right elastic Cauchy-Green deformation tensor. s^α stands for the resistance to dislocation glide on slip system α due to the interaction with other dislocations through self and latent hardening mechanisms. $s_{\text{GND,P}}^\alpha$ and s^α are formulated as

$$s_{\text{GND,P}}^\alpha = c_1 \mu^\alpha b^\alpha \sqrt{\rho_{\text{GND,P}}^\alpha} \quad (3.8a)$$

$$s^\alpha = s_0^\alpha + \int_{t'=0}^{t'=t} \sum_{\beta=1}^{n_{\text{slip}}} h^{\alpha\beta} |\dot{\gamma}^\beta| dt' + \frac{Q^\alpha}{c_2 c_3 b^{\alpha 2}} \sqrt{\rho_{\text{GND,F}}^\alpha} \quad (3.8b)$$

where μ^α and b^α are respectively the shear modulus and magnitude of Burgers vector for slip system α . c_1 is the fitting constant for the long-range impeding stresses arising due to GNDs. c_2 and c_3 are respectively the jump and obstacle width constants [53]. c_1 , c_2 and c_3 are calibrated for *hcp* crystals as 0.1, 0.2 and 1.0, respectively [18]. Q^α is the activation energy to overcome forest GND dislocation population, approximated as $Q^\alpha = 10\mu^\alpha b^\alpha$ for *hcp* crystals [18]. $h^{\alpha\beta}$ is the hardening matrix which accounts for the self and latent hardening of slip systems. $h^{\alpha\beta}$ is calculated as

$$h^{\alpha\beta} = \chi^{\alpha\beta} h_{\text{ref}}^\beta \left| 1 - \frac{s^\beta}{s_{\text{sat}}^\beta} \right|^r \text{sign} \left(1 - \frac{s^\beta}{s_{\text{sat}}^\beta} \right) \quad \text{where} \quad s_{\text{sat}}^\beta = \tilde{s}^\beta \left(\frac{\dot{\gamma}^\beta}{\dot{\gamma}_0^\beta} \right)^n \quad (3.9)$$

r , n and h_{ref}^β are fitting constants. \tilde{s}^β denotes the saturation stress on slip system β . $\chi^{\alpha\beta}$ is the interaction factor, defining the strengthening effect of slip system β on slip system α . $\chi^{\alpha\beta}$ is taken as 1 in this work. s_0^α corresponds to the grain-size dependent initial slip system resistance which follows a Hall-Petch type relationship as [80]

$$s_0^\alpha = s_{0*}^\alpha + \frac{K^\alpha}{\sqrt{D_g}} \quad (3.10)$$

where s_{0*}^α and D_g are the inherent initial slip system resistance and equivalent grain diameter, respectively. $K^\alpha = \sqrt{\frac{(2-\nu)\pi\tau^*Gb^\alpha}{2(1-\nu)}}$ is the Hall-Petch coefficient. Here ν , G and τ^* are respectively the Poisson's ratio, shear modulus of material and barrier strength for the grain boundary taken as $\tau^* = 0.01G$ [80].

$\rho_{\text{GND,P}}^\alpha$ in Eq. 3.8a is the parallel GND density, defined as total GND density projected onto the slip plane α . $\rho_{\text{GND,F}}^\alpha$ in Eq. 3.8b corresponds to the forest GND density, defined as total GND density projected along the normal to slip

plane α . The Parallel and forest GND dislocation densities for slip system α could be calculated as

$$\rho_{\text{GND,P}}^{\alpha} = \sum_{\beta=1}^{n_{\text{slip}}} \chi^{\alpha\beta} \left[\left| \rho_{\text{GNDs}}^{\beta} \sin(\mathbf{n}_0^{\alpha}, \mathbf{m}_0^{\beta}) \right| + \left| \rho_{\text{GNDet}}^{\beta} \sin(\mathbf{n}_0^{\alpha}, \mathbf{t}_0^{\beta}) \right| + \left| \rho_{\text{GNDen}}^{\beta} \sin(\mathbf{n}_0^{\alpha}, \mathbf{n}_0^{\beta}) \right| \right] \quad (3.11\text{a})$$

$$\rho_{\text{GND,F}}^{\alpha} = \sum_{\beta=1}^{n_{\text{slip}}} \chi^{\alpha\beta} \left[\left| \rho_{\text{GNDs}}^{\beta} \cos(\mathbf{n}_0^{\alpha}, \mathbf{m}_0^{\beta}) \right| + \left| \rho_{\text{GNDet}}^{\beta} \cos(\mathbf{n}_0^{\alpha}, \mathbf{t}_0^{\beta}) \right| + \left| \rho_{\text{GNDen}}^{\beta} \cos(\mathbf{n}_0^{\alpha}, \mathbf{n}_0^{\beta}) \right| \right] \quad (3.11\text{b})$$

$\rho_{\text{GNDs}}^{\beta}$, $\rho_{\text{GNDen}}^{\beta}$ and $\rho_{\text{GNDet}}^{\beta}$ are the vectorial components of GND density on slip system β with Burgers vector along \mathbf{m}_0^{β} and line tangent vector parallel to \mathbf{m}_0^{β} , \mathbf{n}_0^{β} and $\mathbf{t}_0^{\beta} = \mathbf{m}_0^{\beta} \times \mathbf{n}_0^{\beta}$ [53]. Augmenting the slip resistances in Eqs. 3.8 with GND-related resistances renders the model non-local as calculation of GNDs involves some non-local calculations on \mathbf{F}^p mapping. The procedure for calculation of GNDs will be elaborated in details in Section 3.4.3.

Unified flow rule

Dislocation motion in the glide plane is controlled by both thermal activation and drag mechanisms. The strength of these mechanisms changes with the stress level and rate of deformation such that the thermally-activated processes are the main rate controlling mechanism up to strain rates of $10^4 \sim 10^5 \text{ s}^{-1}$ while the drag processes take over the dislocation glide at strain rates beyond 10^5 s^{-1} . Motivated by this fact, generally flow rules have been developed either in a thermal activation framework or a drag-dominated one. Unifying the two classes of flow rules and formulating one physics-based unified flow rule, whose application is not limited to a specific range of strain rates, is desired. Using such a flow rule is encouraged as it ensures the mechanism of local dislocation-induced plasticity is consistent with the local stresses and strain rates. It becomes important in simulation of polycrystalline aggregates where the local stress and strain rates might be lower or higher than the applied macroscopic stress or strain rate. The unified flow rule is obtained by combining thermal activation and drag-dominated (CTD) processes. This type of flow rule is referred to as a CTD flow rule hereafter.

We use Orowan equation which expresses the slip rate on slip system α in terms of dislocation density ρ^{α} and average dislocation velocity v^{α} as

$$\dot{\gamma}^{\alpha} = \rho^{\alpha} b^{\alpha} v^{\alpha} \text{sign}(\tau^{\alpha}) \quad (3.12)$$

Experimental observations [82, 14] have shown that dislocations of screw character are responsible for plastic deformation in Ti alloys. Screw dislocations move over the Peierls hills in the glide plane through the well-known double-kink mechanism. This mechanism involves thermally-activated nucleation of kink pairs. Considering some simplifying assumptions such as nucleation of one kink pair per dislocation line, dislocation motion by this mechanism could be thought to take place in two stages. In the first stage, the dislocation lies in a Peierls valley and waits for some time, referred to as the *waiting time* t_w^{α} , until a successful local thermal activation takes place and a pair of kinks with a separation distance of l_{kink}^{α} nucleates and moves to the next Peierls valley [37]. Figure 3.7 illustrates nucleation of a pair of kinks. The second stage is a drag-dominated stage where the kinks move apart and bring the whole dislocation line to the next Peierls valley [48]. The time spent in this stage is called the *running time* t_r^{α} . The average dislocation velocity could be formulated as [41]

$$v^{\alpha} = \frac{\lambda^{\alpha}}{t_w^{\alpha} + t_r^{\alpha}} \quad (3.13)$$

where λ^{α} is the spacing between two consecutive Peierls valleys, approximated as b^{α} here.

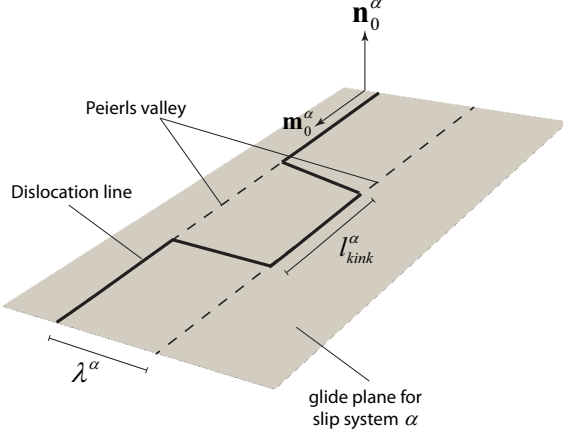


Figure 3.7: Illustration of screw dislocation motion over Peierls hills in the glide plane via a double-kink mechanism

Waiting time corresponds to the thermally-activated nucleation of a kink pair. Hence, an Arrhenius-type relationship can be invoked to formulate t_w^α in terms of temperature as [78]

$$t_w^\alpha = \left[2 \frac{\nu_D b^\alpha}{l_{kink}^\alpha} \frac{l^\alpha}{l_{kink}^\alpha} \exp\left(-\frac{Q_{\text{slip}}^\alpha}{K_B T}\right) \sinh\left(\frac{|\tau^\alpha| - \tau_{\text{ath}}^\alpha}{\tau_{\text{th}}^\alpha}\right) \right]^{-1} \quad (3.14)$$

in which l^α is the average length of a straight dislocation line which is inversely proportional to the square root of the forest dislocation population ρ_F^α ; that is, $l^\alpha = c_l^\alpha / \sqrt{\rho_F^\alpha}$ where c_l^α is a fitting constant [3]. K_B is the Boltzmann constant and ν_D is the Debye frequency ($9.13 \times 10^{13} \text{ s}^{-1}$ for titanium). Q_{slip}^α is the effective activation energy for dislocation slip. The term $\frac{\nu_D b^\alpha}{l_{kink}^\alpha}$ corresponds to the attempt frequency for nucleation of a kink pair and the term $\frac{l^\alpha}{l_{kink}^\alpha}$ is the number of competing sites for the nucleation on the dislocation line. τ_{ath}^α and τ_{th}^α are respectively the athermal and thermal resistances to dislocation motion on slip system α , given by [53]

$$\tau_{\text{ath}}^\alpha = c_{\text{ath}}^\alpha \mu^\alpha b^\alpha \sqrt{\rho_F^\alpha} + s_0^\alpha \quad (3.15a)$$

$$\tau_{\text{th}}^\alpha = \frac{K_B T}{c_{\text{act}}^\alpha l_{kink}^\alpha b^{\alpha 2}} \quad (3.15b)$$

c_{ath} and c_{act} are fitting parameters. The term $c_{\text{act}}^\alpha l_{kink}^\alpha b^{\alpha 2}$ corresponds to the activation volume. As described earlier in Eq. 3.10, s_0^α is the grain size-dependent initial resistance which contributes to the athermal resistance [60]. Similar to Eq. 3.11, the total parallel and forest dislocation populations on slip system α could be calculated as

$$\rho_P^\alpha = \sum_{\beta=1}^{n_{\text{slip}}} \chi^{\alpha\beta} \left[\left| \rho_{\text{GNDs}}^\beta \sin(\mathbf{n}_0^\alpha, \mathbf{m}_0^\beta) \right| + \left| \rho_{\text{GNDet}}^\beta \sin(\mathbf{n}_0^\alpha, \mathbf{t}_0^\beta) \right| + \left| \rho_{\text{GNDen}}^\beta \sin(\mathbf{n}_0^\alpha, \mathbf{n}_0^\beta) \right| + \left| \rho^\beta \sin(\mathbf{n}_0^\alpha, \mathbf{m}_0^\beta) \right| \right] \quad (3.16a)$$

$$\rho_F^\alpha = \sum_{\beta=1}^{n_{\text{slip}}} \chi^{\alpha\beta} \left[\left| \rho_{\text{GNDs}}^\beta \cos(\mathbf{n}_0^\alpha, \mathbf{m}_0^\beta) \right| + \left| \rho_{\text{GNDet}}^\beta \cos(\mathbf{n}_0^\alpha, \mathbf{t}_0^\beta) \right| + \left| \rho_{\text{GNDen}}^\beta \cos(\mathbf{n}_0^\alpha, \mathbf{n}_0^\beta) \right| + \left| \rho^\beta \cos(\mathbf{n}_0^\alpha, \mathbf{m}_0^\beta) \right| \right] \quad (3.16b)$$

In the last term on RHS of Eqs. 3.16a and 3.16b, the angle between \mathbf{n}_0^α and \mathbf{m}_0^β is used to project ρ^β onto the slip system α . \mathbf{m}_0^β is used here since the tangent line is parallel to the Burgers vector for the screw dislocations.

Running time corresponds to the stage where dislocation motion is governed by the retarding drag forces due to the phonon-dislocation interactions. Running time can be written in terms of viscous drag velocity v_d^α as [41, 40]

$$t_r^\alpha = \frac{\lambda^\alpha}{v_d^\alpha} \quad (3.17)$$

Depending on the temperature, several types of phonon-dislocation interaction are possible such as flutter, scattering, radiation mechanisms and etc [48, 40]. These interactions yield a temperature-dependent drag coefficient B_0 of the form [48]

$$B_0 = \frac{c_d K_B T}{v_s b^\alpha} \quad (3.18)$$

Here v_s is the shear wave speed. c_d is the drag constant, taken as 45. Solving the equation of motion for a unit length of dislocation line and recognizing that the effective dislocation line mass density is negligible compared to the drag coefficient B_0 , viscous drag velocity is obtained as [38]

$$v_d^\alpha = \frac{(|\tau^\alpha| - \tau_{ath}^\alpha) b^\alpha}{B_0} \quad (3.19)$$

In order to ensure that the dislocation drag velocity does not exceed the shear wave speed, relativistic effects should be implemented, i.e. the drag coefficient needs to be modified as [9]

$$B = \frac{B_0}{1 - \left(\frac{v_d^\alpha}{v_s}\right)^2} \quad (3.20)$$

This modification basically implies that as the dislocation drag velocity v_d^α approaches the shear wave speed, the drag coefficient B grows very large and consequently very large resolved shear stresses would be required. Replacing B_0 in Eq. 3.19 with B and solving for v_d^α , the modified dislocation drag velocity is obtained as [9]

$$v_d^\alpha = v_s \left[\sqrt{1 + \left(\frac{B_0 v_s}{2(|\tau^\alpha| - \tau_{ath}^\alpha) b^\alpha} \right)^2} - \frac{B_0 v_s}{2(|\tau^\alpha| - \tau_{ath}^\alpha) b^\alpha} \right] \quad (3.21)$$

Substituting Eqs. 3.17 and 3.14 into Eq. 3.13, the expression for the unified average dislocation velocity, informed by both thermally-activated and drag-dominated processes, is obtained as

$$v^\alpha = \frac{v_d^\alpha}{\left[2 \frac{v_p b^\alpha}{l_{kink}^\alpha} \frac{l_a}{l_{kink}^\alpha} \exp\left(-\frac{Q_{slip}^\alpha}{K_B T}\right) \sinh\left(\frac{|\tau^\alpha| - \tau_{ath}^\alpha}{\tau_{th}^\alpha}\right) \right]^{-1} + 1} \quad (3.22)$$

The unified average dislocation velocity profile is plotted in Figure 3.8 and compared with the velocity profile for a purely thermally-activated and purely drag-dominated dislocation motion. In this plot, only the resolved shear stress is varied to obtain a schematic of the average dislocation velocity for a given dislocation density and temperature. It is observed that at low stresses the unified velocity profile is following the average velocity of a purely thermally-activated motion. As stress increases, the rate of successful thermal activations boosts up and t_w^α decreases exponentially, therefore diminishing the rate controlling effect of thermally-activated processes. At higher stress levels, the unified average velocity follows the average velocity of a purely drag-dominated dislocation motion. Note the transition of the unified velocity from a thermally-activated regime to a mixed regime at about an average velocity of 90m/s. This transition point is close to that of the screw dislocations in tantalum [11]. The multi-scale strength model developed by Barton et al. [11] suggested that the average velocity of screw dislocations departs from a thermally-activated regime at roughly 100m/s.

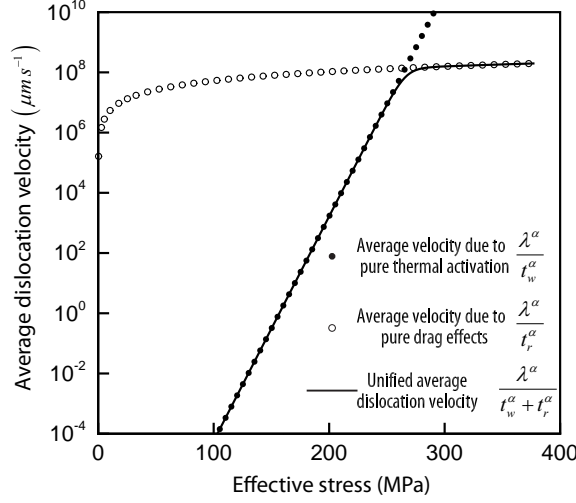


Figure 3.8: Comparison of the unified average dislocation velocity profile with purely thermally-activated and purely drag-dominated average velocities

Having derived the average dislocation velocity, one can evaluate the slip rate on different slip systems using Eq. 3.12, provided that the dislocation density is known. Section 3.4.3 discusses the evolution of dislocation density on different slip systems during the course of plastic deformation.

3.4.3 Evolution of dislocation densities

Dislocation population could be divided into two distinct classes, namely statistically stored dislocations (SSDs) and geometrically necessary dislocations (GNDs). SSDs are characterized by a vanishing net Burgers vector. They evolve during deformation through numerous mechanisms such as multiplication, thermal and athermal annihilation and etc [53]. GNDs, on the other hand, correspond to the storage of polarized dislocation densities and are characterized by a non-zero net Burgers vector [6]. GNDs account for the crystal lattice curvatures which become prominent in single crystal bending and near the polycrystalline grain boundaries.

The overall slip resistance is assumed to be due to both the SSDs and GNDs. The SSD density, unlike the GND density, is not an internal state variable for the PL flow rule. Therefore, as shown in Eqs. 3.8, the effect of GND densities on the slip system resistances is explicitly taken into account, whereas the contribution of SSDs to the evolution of slip system resistances are considered in a phenomenological form via Eq. 3.9. In contrast with the PL flow rule, the CTD flow rule considers both the SSD and GND densities as internal state variables. This enables us to explicitly formulate and explain the slip system hardening in terms of both SSD and GND densities, as shown in Eqs. 3.15. In the following, the evolution of SSDs (applicable only to the CTD flow rule) and GNDs (applicable to both PL and CTD flow rules) are explained in details.

Evolution of statistically stored dislocations

A dislocation density-based CP framework gives the modelers the opportunity to track material hardening more tangibly in terms of the interaction and entanglement of dislocations on different slip systems. Dislocation population is controlled by a competition between dislocation multiplication and annihilation mechanisms. Multiplication corresponds to the introduction of new dislocations from a pre-existing population of dislocations. The multiplication rate is proportional to the square root of dislocation density [29] and could be written as

$$\dot{\rho}_{mult}^\alpha = c_{multi}^\alpha \sqrt{\rho^\alpha} |\dot{\gamma}^\alpha| \quad (3.23)$$

where c_{multi}^α is a fitting constant. Two dislocations of opposite sign can annihilate each other athermally if they come within a critical distance. The rate of athermal annihilation could be formulated as [3]

$$\dot{\rho}_{ann}^\alpha = c_{annih}^\alpha \rho^\alpha |\dot{\gamma}^\alpha| \quad (3.24)$$

c_{annih}^α is a fitting constant. The rate of dislocation evolution could then be written as

$$\dot{\rho}^\alpha = \dot{\rho}_{multi}^\alpha - \dot{\rho}_{ann}^\alpha \quad (3.25)$$

This equation is basically a simplified Kocks-Mecking type relationship [55]. Note that multiplication and athermal annihilation are only two of the many possible mechanisms that could contribute to the evolution of dislocation population. Considering other dislocation evolution mechanisms is absolutely possible; however, it is at the expense of adding to the complexity of the model and introducing more fitting constants.

Calculation of geometrically necessary dislocations

Presence of GNDs in the microstructure are attributed to the incompatibility in the plastic strain field. Due to plastic anisotropy of *hcp* crystal, plastic response is highly dependent on the crystallographic orientation of grains. This strong orientation-dependent plastic response leads to the accumulation of GNDs majorly near the grain boundaries where high gradients in plastic strain take place due to the distinct crystallographic orientation across the grain boundary.

From a continuum mechanics viewpoint, the Nye dislocation tensor Λ which measures the incompatibility in the intermediate configuration could be derived in terms of \mathbf{F}^p mapping as

$$\Lambda = -(\nabla_X \times \mathbf{F}^{p^T})^T \quad (3.26)$$

where ∇_X is the gradient operator with respect to the reference coordinates. The Nye dislocation tensor could be equivalently expressed in terms of GNDs from a dislocation mechanics viewpoint as [24]

$$\Lambda = \sum_{\alpha=1}^{n_{slip}} b^\alpha \left(\rho_{GNDs}^\alpha \mathbf{m}_0^\alpha \otimes \mathbf{m}_0^\alpha + \rho_{GNDet}^\alpha \mathbf{m}_0^\alpha \otimes \mathbf{t}_0^\alpha + \rho_{GNDen}^\alpha \mathbf{m}_0^\alpha \otimes \mathbf{n}_0^\alpha \right) \quad (3.27)$$

There are in general $3 \times n_{slip}$ unknown GND densities; 90 for *hcp* crystals. However, one could observe that there are only 9 independent ρ_{GNDs}^α , 24 independent ρ_{GNDet}^α and 30 independent ρ_{GNDen}^α . Hence, the number of unknown GND densities reduces to 63 for *hcp* crystals. Equating Eqs. 3.26 and 3.27, yields

$$\hat{\Lambda} = \mathbf{A} \rho_{GND} \quad (3.28)$$

in which $\hat{\Lambda}$ is the 9×1 vectorial form of Λ , \mathbf{A} is a 9×36 matrix containing the basis vectors $\mathbf{m}_0^\alpha \otimes \mathbf{m}_0^\alpha$, $\mathbf{m}_0^\alpha \otimes \mathbf{t}_0^\alpha$ and $\mathbf{m}_0^\alpha \otimes \mathbf{n}_0^\alpha$ and ρ_{GND} is the 63×1 column vector of unknown independent GND components. It is clear that Eq. 3.28 is an under-determined system of linear equation and may not have a unique solution. Based on geometric considerations, Arsenlis and Parks [6] set up a functional of the form

$$\mathcal{F}(\rho_{GND}, \lambda) = \rho_{GND}^T \rho_{GND} + \lambda^T (\mathbf{A} \rho_{GND} - \hat{\Lambda}) \quad (3.29)$$

whose minimization yields the GND densities. Here λ is the vector of Lagrange multipliers. Minimizing the functional \mathcal{F} , the GND densities are obtained as

$$\rho_{GND} = \mathbf{A}^T (\mathbf{A} \mathbf{A}^T)^{-1} \hat{\Lambda} \quad (3.30)$$

Incorporating GNDs in the CP framework renders the model size-dependent and non-local since the Nye dislocation tensor is derived in terms of the gradient of \mathbf{F}^p field in Eq. 3.26. In this work, the constitutive updates are performed at the integration points of the elements. Therefore, all the internal state variables and kinematic quantities such as \mathbf{F}^p are known only at the the integration points of the elements. In order to calculate the gradient of \mathbf{F}^p field over an element, one could interpolate \mathbf{F}^p field using the shape functions N_i as $\mathbf{F}^p(\mathbf{X}) = \sum_{i=1}^{n_{node}} N_i(\mathbf{X}) \mathbf{F}_{nodal_i}^p$ where n_{node} is number of nodal points per element and $\mathbf{F}_{nodal_i}^p$ is the value of \mathbf{F}^p at the nodal points. It is clear that the nodal values

of \mathbf{F}^p should be determined from the known values of \mathbf{F}^p at the integration points. The super-convergent patch recovery method (SPR) developed by Zienkiewicz and Zhu [85] is deemed to be an appropriate method for this purpose. A detailed discussion on the derivation of nodal value of \mathbf{F}^p using SPR technique is given in Cheng and Ghosh [18].

3.4.4 Adiabatic heating

Plastic deformation generates heat in the material. The energy dissipated due to the plasticity converts into thermo-plastic heating, thermo-elastic heating and defect energy [21]. At low strain rates, the generated heat conducts out of the microstructure; however, if the deformation process is rapid, there is not enough time to conduct heat away and temperature increases locally in an adiabatic fashion. Even deformations at moderate strain rates could be treated as essentially adiabatic [70]. Temperature increase due to adiabatic heating is very important since it promotes plasticity by boosting up the rate of thermal activation.

The rate of temperature increase due to adiabatic heating could be formulated as

$$\dot{T} = \frac{\beta_t}{\rho \hat{c}} \dot{W}_p \quad (3.31)$$

in which ρ is the material mass density, 4428 kg/m^3 for typical Ti alloys. \hat{c} is the specific heat capacity which changes with temperature as $\hat{c} = 559.77 - 0.1473T + 0.00042949T^2 \text{ JKg}^{-1} \text{ K}^{-1}$ for $278 < T < 1144 \text{ K}$ [1]. $\dot{W}_p = \sigma : \mathbf{d}^p$ is the plastic power per unit deformed volume. \mathbf{d}^p is the symmetric part of the plastic velocity gradient in the current configuration $\mathbf{I}^p = \mathbf{F}^e \mathbf{F}^\theta \mathbf{F}^p \mathbf{F}^{p-1} \mathbf{F}^{\theta-1} \mathbf{F}^{e-1}$. β_t corresponds to the fraction of plastic work which converts into heat. Ignoring the thermo-elastic heating, $1 - \beta_t$ denotes the fraction of plastic work which is stored in the material in the form of defects, referred to as the stored energy of cold work. Most of the plastic work has been observed to convert into heat for metals. In this work, β_t is taken as 1.

3.4.5 Time integration algorithm for crystal plasticity constitutive model

Several time integration algorithms have been proposed in the literature for updating CP constitutive models. An excellent summary of various time integration schemes is provided by Ling et al [52]. In this work, a set of six nonlinear algebraic equations, corresponding to each component of the second Piola-Kirchhoff stress, is derived. Then, a semi-implicit algorithm is used to solve the set of equations. In an increment from t to $t + \Delta t$, the following quantities are known/prescribed:

- known values of kinematic quantities, viz. $\mathbf{F}(t)$, $\mathbf{F}^\theta(t)$, $\mathbf{F}^p(t)$
- known values of internal state variables (ISV), viz. $T(t)$, $\dot{W}_p(t)$, $s^\alpha(t)$ (only for PL flow rule) and $\rho^\alpha(t)$ (only for CTD flow rule)
- prescribed $\mathbf{F}(t + \Delta t)$

For the constitutive updates in the time interval $(t, t + \Delta t]$, the GND densities are calculated using $\mathbf{F}^p(t)$. Furthermore, it is necessary to update temperature and thermal deformation gradient for simulation of high rate deformations. For adiabatic simulations, thermal deformation gradient at $t + \Delta t$ is obtained as $\mathbf{F}^\theta(t + \Delta t) = \exp\left(\alpha \frac{\beta_t \dot{W}_p(t) \Delta t}{\rho \hat{c}}\right) \mathbf{F}^\theta(t)$ and temperature is found explicitly using the information at time t as $T(t + \Delta t) = T(t) + \frac{\beta_t \dot{W}_p(t) \Delta t}{\rho \hat{c}}$.

Integrating Eq. 3.4 with respect to time, \mathbf{F}^p at time $t + \Delta t$ is obtained as

$$\mathbf{F}^p(t + \Delta t) = \left(\mathbf{I} + \sum_{\alpha=1}^{n_{\text{slip}}} \Delta \gamma^\alpha \mathbf{m}_0^\alpha \otimes \mathbf{n}_0^\alpha \right) \mathbf{F}^p(t) \quad (3.32)$$

where $\Delta \gamma^\alpha = \dot{\gamma}^\alpha \Delta t$. Using Eqs. 3.32 and 3.2, the elastic deformation gradient is derived as

$$\mathbf{F}^e(t + \Delta t) = \mathbf{F}(t + \Delta t) \mathbf{F}^{p-1}(t) \left(\mathbf{I} - \sum_{\alpha=1}^{n_{\text{slip}}} \Delta \gamma^\alpha \mathbf{m}_0^\alpha \otimes \mathbf{n}_0^\alpha \right) \mathbf{F}^{\theta-1}(t + \Delta t) \quad (3.33)$$

Substituting $\mathbf{F}^e(t + \Delta t)$ into Eq. 3.5, a set of nonlinear equations in terms of the updated second Piola-Kirchhoff stress is obtained as

$$\mathbf{S}(t + \Delta t) = \mathbf{S}^{tr} - \sum_{\alpha=1}^{n_{slip}} \Delta \gamma^\alpha (\mathbf{S}(t + \Delta t), \text{ISV}) \mathbf{B}^\alpha \quad (3.34)$$

where

$$\tilde{\mathbf{A}} = \mathbf{F}^{p-T}(t) \mathbf{F}^T(t + \Delta t) \mathbf{F}(t + \Delta t) \mathbf{F}^{p-1}(t) \quad (3.35a)$$

$$\mathbf{S}^{tr} = \mathbb{C} : \left[\frac{1}{2} \left(\mathbf{F}^{\theta-T}(t + \Delta t) \tilde{\mathbf{A}} \mathbf{F}^{\theta-1}(t + \Delta t) - \mathbf{I} \right) \right] \quad (3.35b)$$

$$\mathbf{B}^\alpha = \frac{1}{2} \mathbb{C} : \left[\mathbf{F}^{\theta-T}(t + \Delta t) \left(\tilde{\mathbf{A}} \left(\mathbf{m}_0^\alpha \otimes \mathbf{n}_0^\alpha \right) + \left(\mathbf{n}_0^\alpha \otimes \mathbf{m}_0^\alpha \right) \tilde{\mathbf{A}} \right) \mathbf{F}^{\theta-1}(t + \Delta t) \right] \quad (3.35c)$$

Newton-Raphson iterative solver is used to solve the nonlinear equation 3.34 in two stages. In the first stage, Eq. 3.34 is solved for $\mathbf{S}(t + \Delta t)$ while the slip system resistance-related quantities, i.e. $s^\alpha(t + \Delta t)$ for PL flow rule or $\rho^\alpha(t + \Delta t)$ for CTD flow rule, are held fixed. The i -th iteration of the Newton-Raphson algorithm reads as

$$\mathbf{S}^{i+1}(t + \Delta t) = \mathbf{S}^i(t + \Delta t) - \mathbb{J}^{-1} : \mathbf{R}^i \quad (3.36)$$

where the residual \mathbf{R} and Jacobian \mathbb{J} are computed

$$\mathbf{R}^i = \mathbf{S}^i(t + \Delta t) - \mathbf{S}^{tr} + \sum_{\alpha=1}^{n_{slip}} \Delta \gamma^\alpha \mathbf{B}^\alpha \quad (3.37a)$$

$$\mathbb{J} = \frac{\partial \mathbf{R}}{\partial \mathbf{S}^i} = \mathbb{I}_{sym} + \sum_{\alpha=1}^{n_{slip}} \mathbf{B}^\alpha \otimes \frac{\partial \Delta \gamma^\alpha}{\partial \mathbf{S}^i} \quad (3.37b)$$

where \mathbb{I}_{sym} is the symmetric fourth order identity tensor. Once $\mathbf{S}(t + \Delta t)$ is determined, the slip system resistance-related quantities are evolved in the second stage. Next the first stage is repeated again with the evolved resistances and so on. The sequence of computational operation needed for CP constitutive update is given in Table 3.1.

3.5 Stabilization of linear tetrahedral elements for CPFE modeling

Modeling material response and predictions of localized phenomenon such as fatigue crack nucleation [5, 4] and twinning [18] in the framework of CP are highly dependent on the ability of the model (both material constitutive model and numerical method) to accurately calculate the local state of the material, viz. local stress state and kinematic variables. This calls for the development of appropriate constitutive models and robust numerical schemes. In this section, we focus on improving the conventional finite element for the CP modeling of microstructures.

Linear constant strain tetrahedral elements (TET4) are preferred for CPFE simulations due to their inherent simplicity, high efficiency and their excellent capability to conform to the complex geometry of polycrystalline aggregates with tortuous grains. However, these elements have been observed to suffer from volumetric locking for modeling (nearly-) incompressible materials. Volumetric locking of TET4 elements can adversely affect the accuracy of CPFE simulations in both local and global levels due to the presence of isochoric plastic deformation. The locking-induced instability is manifested in the simulation results in the form of over-predicted stress levels, checker-board pattern of pressure field and under-predicted displacement field.

In this paper, the methodology proposed in a recent paper by the authors [19] is used to relieve volumetric locking for efficient and accurate CPFE simulations. In this model, the F-bar-patch method [25] is implemented into the CPFE framework. The basic idea behind F-bar-patch method is to modify deformation gradient for constitutive calculations

Step A	Purpose: determining second Piola-Kirchhoff stress and slip rates
1	<i>Initialization of relevant quantities for Newton-Raphson algorithm:</i> $\mathbf{S}^0(t + \Delta t) = \mathbf{S}(t)$ $s^\alpha(t + \Delta t) = s^\alpha(t)$ (for PL flow rule) $\rho^\alpha(t + \Delta t) = \rho^\alpha(t)$ (for CTD flow rule)
2	<i>for the i-th iteration in the Newton-Raphson algorithm:</i> (a) Calculate the resolved shear stress using Eq. 3.7 (b) Evaluate the slip rate using Eq. 3.6 for PL flow rule or Eq. 3.12 for CTD flow rule (c) Update the second Piola-Kirchhoff stress using Eq. 3.36 (d) Check for convergence: if no, return to step (a); if yes, proceed to step 3
3	<i>calculate the resolved shear stress and slip rate based on the converged second Piola-Kirchhoff stress</i>
Step B	Purpose: updating slip system resistances
4	<i>Compute hardening-related quantities:</i> Calculate the hardening matrix using Eq. 3.9 for PL flow rule Evolve dislocation densities using Eq. 3.25 for CTD flow rule
5	<i>Update slip system resistances:</i> Use Eq. 3.8b for PL flow rule Use Eq. 3.15a for CTD flow rule
6	<i>Check for convergence of slip system resistances: if no, return to step 2; if yes, proceed to step 7</i>
7	<i>Evaluate elastic deformation gradient using Eq. 3.2 and Cauchy stress using Eq. 3.5</i>

Table 3.1: Sequence of computational operations for constitutive update procedure

such that the incompressibility is enforced over a patch of elements, rather than on individual elements. In order to apply **F**-bar-patch method for CPFE simulations, it is required to divide the entire mesh into non-overlapping patches of elements. Consider a set of elements forming a patch \mathcal{P} . The modified deformation gradient for element $K \in \mathcal{P}$ at time t is calculated as

$$\bar{\mathbf{F}}_K = \left[\frac{\Omega'_\mathcal{P}}{\Omega_\mathcal{P}^0 \det \mathbf{F}_K} \right]^{\frac{1}{3}} \mathbf{F}_K \quad (3.38)$$

where $\Omega_\mathcal{P}^{t+\Delta t}$ and $\Omega_\mathcal{P}^0$ are respectively the volume of the patch in the current and undeformed configurations. The modified deformation gradient $\bar{\mathbf{F}}_K$ is then passed on to the material routine for constitutive calculations.

F-bar-patch method could be used for any type of material constitutive law. It does not require addition of new degrees of freedom to the system, and the constitutive updates are performed at the quadrature points of the element. Implementation of **F**-bar-patch method into any standard displacement-based FE code is straightforward.

3.6 Numerical results

In this section, the PL and CTD flow rules are first calibrated and validated using the results of quasi-static and dynamic experiments. The models are then used to investigate the effect of deformation rate on the flow stress. The section concludes with an investigation on the effect of temperature on the material behavior in the context of isothermal and adiabatic conditions.

3.6.1 Calibration and validation of constitutive models with experiments

Calibration and validation of material constitutive models against experiments are critical to meaningful simulation of deformation processes of metals. The material parameters are calibrated using quasi-static and dynamic experiments. For the sake of brevity, the experiments are referred to in an XX-YY-ZZ format. XX corresponds to the type of microstructure, either AR or RA microstructure. YY corresponds to the rate of deformation, either quasi-static (QS) or dynamic (DY). ZZ refers to the loading direction which could be either normal (ND), rolling (RD) or transverse (TD) direction. It is worthy to mention that ND, RD and TD correspond respectively to the global [100], [010] and [001] directions in our simulations. There are in total eight experiments where four of them are used for the calibration of parameters and the other four are used for the validation of the models. Table 3.2 reports the types of experiments used in this study along with their role in either calibration or validation of the models. A high-fidelity calibration is expected since various experiments with different rates and loading directions are employed.

microstructure	strain rate (s^{-1})	loading direction	experiment title	role
RA	1.0×10^{-3}	ND	RA-QS-ND	calibration
	$1.1 \times 10^{+3}$	ND	RA-DY-ND	calibration
	2.0×10^{-3}	RD	RA-QS-RD	calibration
	$2.6 \times 10^{+3}$	RD	RA-DY-RD	calibration
	1.0×10^{-3}	TD	RA-QS-TD	validation
	$2.7 \times 10^{+3}$	TD	RA-DY-TD	validation
AR	$1.1 \times 10^{+3}$	ND	AR-DY-ND	validation
	$2.6 \times 10^{+3}$	RD	AR-DY-RD	validation

Table 3.2: details of experiments used for calibration and validation purposes

The material parameters to be calibrated are generally the anisotropic elastic constants and slip system-dependent crystal plasticity parameters. α titanium with an *hcp* lattice-parameter ratio $c/a = 1.59$ shows a transversely isotropic elastic response. Consider a material coordinate system defined by the orthonormal basis $(\mathbf{e}_1^c, \mathbf{e}_2^c, \mathbf{e}_3^c)$ where 1, 2 and 3

directions correspond respectively to $[\bar{1}2\bar{1}0]$, $[\bar{1}010]$ and $[0001]$ directions of the *hcp* crystal lattice. The anisotropic elasticity tensor in this coordinate system could be expressed in Voigt notation as

$$\left[C_{IJ}^e \right] = \begin{bmatrix} C_{11} & C_{12} & C_{13} & 0 & 0 & 0 \\ & C_{22} & C_{23} & 0 & 0 & 0 \\ & & C_{33} & 0 & 0 & 0 \\ & & & C_{44} & 0 & 0 \\ & & & & C_{55} & 0 \\ & & & & & C_{66} \end{bmatrix}_{sym} \quad (3.39)$$

Due to the transverse isotropic property, there are only 5 independent elastic constants, viz. $C_{11} = C_{22}$, $C_{12} = C_{23}$, $C_{33} = C_{66}$ and $C_{44} = (C_{11} - C_{12})/2$. The elastic constants are measured via resonant ultrasound spectroscopy experiments on Ti-7 single crystal samples at room temperature [73] and tabulated in Table 3.3. Experimental measurements for elastic constants of α Ti show that they decrease almost linearly with increasing the temperature, but with different slopes. The experimental results of Ogi et al. [63] are used to obtain the linear slopes for different elastic constants. Figure 3.9 depicts the variation of different principal elastic constants with temperature. The linear slopes corresponding to the reduction of elastic constants with temperature are given in Table 3.3.

	C_{11}	C_{12}	C_{13}	C_{33}	C_{55}
$[C_{IJ}]$ (GPa)	164.7	82.5	61.8	175.2	48.5
Linear slope (MPa/K)	48	8.9	21	21	21.9

Table 3.3: anisotropic elastic constants obtained from resonant ultrasound spectroscopy measurements at room temperature and linear slopes for reduction of elastic constants with temperature

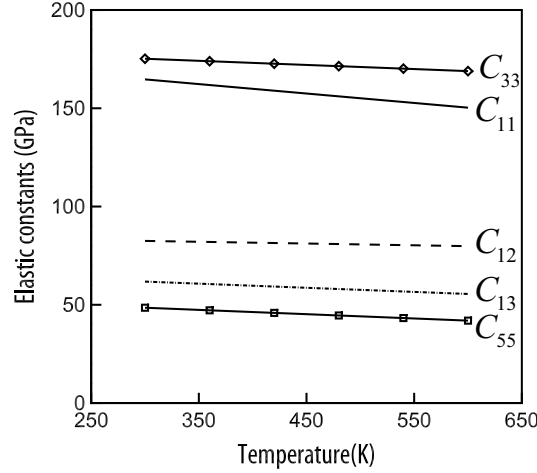


Figure 3.9: Variation of principal elastic constants with temperature

PL model has been previously calibrated for Ti-6Al alloy [39] with a chemical composition relatively close to that of Ti-7Al alloy. Hence, we start with the calibration of the PL model since the bounds of fitting parameters are fairly known. Performing a sensitivity analysis, it is realized that $\dot{\gamma}_0^\alpha$, s_{0*}^α and m are the parameters controlling the onset of plasticity, i.e. yield point, and h_{ref}^α , \tilde{s}^α , r^α and n^α are the ones controlling the hardening rate. It is also observed that m is the main rate-controlling parameter. The general idea is to use quasi-static tests done at room temperature to calibrate parameters controlling the onset of plasticity and hardening-related parameters. Dynamic tests are then

utilized to calibrate the rate-controlling parameter. This process is clearly iterative as the rate-controlling parameter m has an impact on the yield stress, as well.

Using the four calibration tests mentioned earlier in Table 3.2, the PL model is calibrated and stress-strain plots comparing simulation results with experiments are shown in Figure 3.10. The calibrated parameters for the PL model are given in Table 3.4. It is observed that the response to ND loading is stiffer than the RD one. This is due to the rolling process done on the material which aligns the $\langle c \rangle$ -axis of grains along ND; therefore, loading along ND direction will favor activation of $\langle c+a \rangle$ -pyramidal slip systems whose critical resolved shear stress is $2 \sim 3$ times larger than the $\langle a \rangle$ -basal or prismatic slip systems [51].

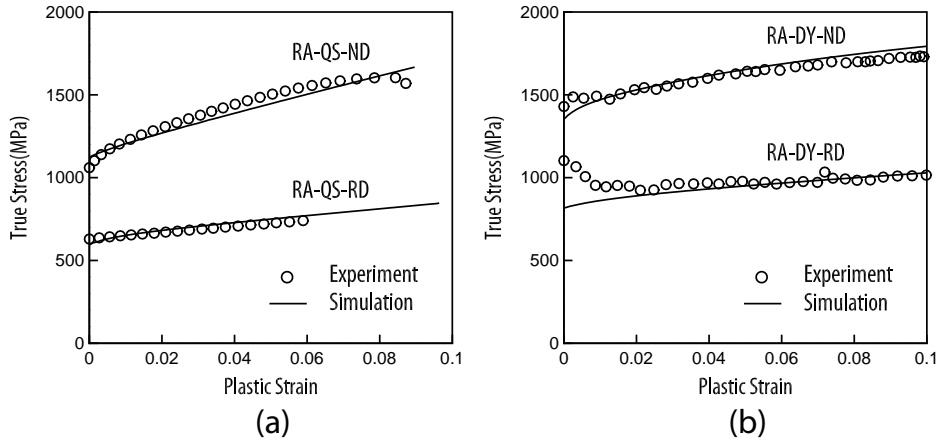


Figure 3.10: Calibration of the PL model using (a) quasi-static and (b) dynamic experiments

parameters	unit	$\langle a \rangle$ - basal	$\langle a \rangle$ - prismatic	$\langle a \rangle$ - pyramidal	$\langle c+a \rangle$ - pyramidal
s_{0*}^{α}	MPa	230	205	500	610
$\dot{\gamma}_0^{\alpha}$	s^{-1}	0.003	0.003	0.003	0.003
h_{ref}^{α}	MPa	250	250	1200	2000
m	-	0.019	0.019	0.019	0.019
r^{α}	-	0.02	0.02	0.02	0.02
n^{α}	-	0.3	0.3	0.3	0.3
\tilde{s}^{α}	MPa	1600	1600	1600	1800

Table 3.4: Calibrated parameters of the PL model for different slip systems

It is necessary to take into account the effect of temperature increase on plasticity in high strain rate simulations due to adiabatic heating. As temperature increases, the rate of successful thermal activation attempts is boosted up and consequently plastic flow is enhanced. In other words, the resistance to plastic flow reduces as temperature rises. This is automatically captured in the CTD model where temperature is explicitly considered. In the PL model, this is phenomenologically accounted for by scaling the slip system resistances with temperature as $s_*^{\alpha} = s_{ref*}^{\alpha} (T/T_{ref})^p$ where s_{ref*}^{α} is the slip system resistance at reference temperature T_{ref} and p is a fitting parameter [21]. In this work, T_{ref} is set to room temperature and s_{ref*}^{α} will consequently correspond to s_{0*}^{α} . The p exponent is set to -1 using the experimental results of Williams et al. [82] on α Ti alloys in which they measured the variation of yield stress and critical resolved shear stresses for different slip systems in a wide range of temperatures. The results reported in [82] are shifted such that yield stress at room temperature matches the one using the calibrated parameters in Table 3.4. Figure 3.11 shows the variation of 0.2% yield stress with temperature for single crystal samples oriented for activation

of $\langle a \rangle$ -basal and $\langle c+a \rangle$ - pyramidal slip systems. For the sake of clarity of the plot, the results for $\langle a \rangle$ - prism slip is not shown since it is very close to the response of $\langle a \rangle$ - basal slip system.

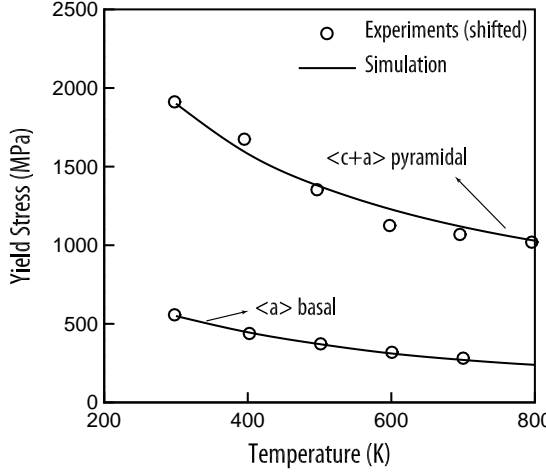


Figure 3.11: Variation of yield stress with temperature for single crystals oriented for activation of different slip systems

In order to validate the PL model and check the fidelity of calibrated parameters, the four validation tests are simulated and compared with experiments in Figure 3.12 where a good agreement is observed. It is worth noting that the model predicts the deformation of AR microstructure very well although the parameters were calibrated using the RA tests. This indicates that the grain size-dependence mechanisms in the model, i.e. GND hardening and Hall-Petch effect, are properly developed since the major difference between the AR and RA microstructures is the average grain size.

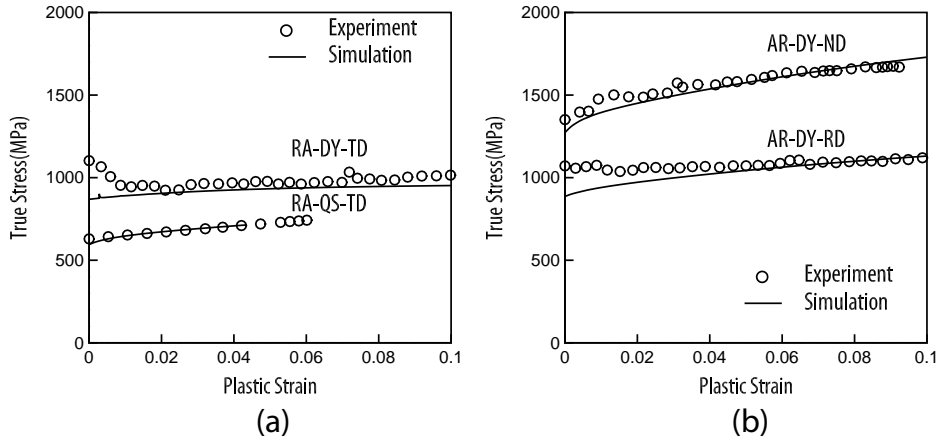


Figure 3.12: Validation of PL model using quasi-static and dynamic experiments on (a) RA and (b) AR microstructures

Similar to the calibration of the PL model, it is possible to calibrate the CTD model following the same steps. However since CPFE simulation of single crystals takes considerably less time compared to that of the polycrystalline microstructures, it is desirable to calibrate parameters using single crystal tests. Unfortunately single crystal experimental tests are not available for this alloy; nevertheless this is possible to reproduce such tests using the validated

PL model. A single crystal model shown in Figure 3.13 is set up where the crystal is oriented differently to favor activation of different slip systems. PL constitutive model is first used to simulate deformation of this model under different strain rates ranging from 10^{-3} to $10^{+3} s^{-1}$. The stress-strain plots are then used to calibrate parameters in the CTD model. The stress-strain plots comparing the two constitutive models are shown in Figure 3.14. Experimental observations [2, 77] suggest that the effective activation energy is generally temperature-dependent. In this study, effective activation energy is expressed in terms of temperature as $Q_{\text{slip}}^{\alpha}(T) = Q_{\text{ref}}^{\alpha} + c_Q^{\alpha} (T/T_{\text{ref}} - 1)^{p_Q^{\alpha}}$ and is being calibrated using Williams et al. [82] data. The complete list of calibrated parameters for the CTD model is given in Table 3.5.

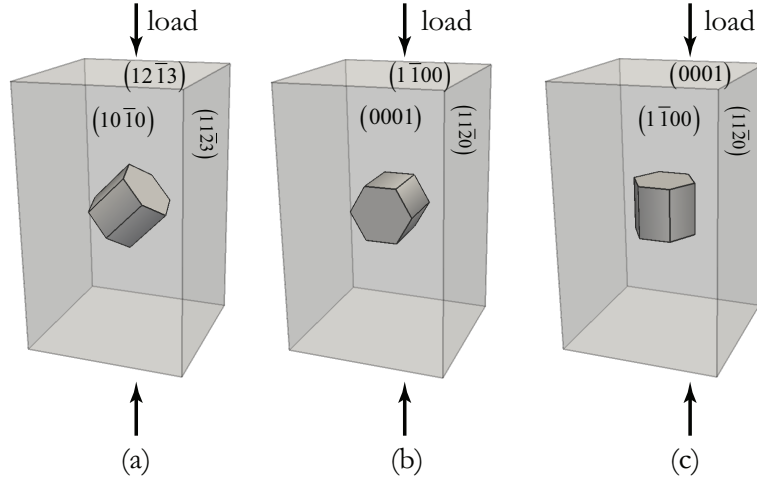


Figure 3.13: Single crystal model oriented for activation of (a) $\langle a \rangle$ - basal, (b) $\langle a \rangle$ - prismatic and (c) $\langle c + a \rangle$ - pyramidal slip systems

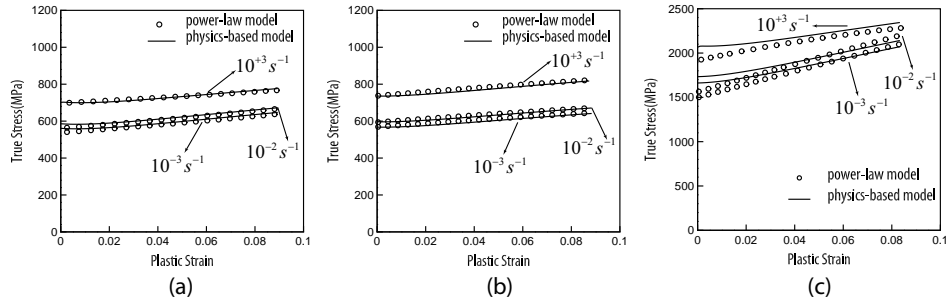


Figure 3.14: Calibration of CTD model using the validated PL model for (a) $\langle a \rangle$ - basal (b) $\langle a \rangle$ - prismatic and (c) $\langle c + a \rangle$ - pyramidal slip systems

CPFE simulations are carried out using the calibrated CTD model and the simulation results are compared with the experiments in Figure 3.15 for validation purposes. A good agreement is observed between the simulation results and experiments for all the eight tests, indicating the competency of the proposed constitutive model for modeling deformation processes under both low and high rates of deformation.

parameters	unit	$\langle a \rangle$ - basal	$\langle a \rangle$ - prismatic	$\langle a \rangle$ - pyramidal	$\langle c + a \rangle$ - pyramidal
Q_{ref}^{α}	J	2.1×10^{-19}	2.2×10^{-19}	3.0×10^{-19}	2.6×10^{-19}
l_{kink}^{α}	b^{α}	20	20	20	20
s_{0*}^{α}	MPa	5.0	5.0	5.0	5.0
c_{ath}^{α}	-	0.8	0.62	0.7	0.5
c_{act}^{α}	-	0.7	0.7	0.1	0.04
c_l^{α}	-	8.0	8.0	8.0	8.0
c_{multi}^{α}	μm^{-1}	150	230	500	500
c_{annih}^{α}	-	10	10	10	10
c_Q^{α}	J	2.3×10^{-20}	3.7×10^{-20}	1.8×10^{-20}	0.9×10^{-20}
p_Q^{α}	-	1.6	1.6	1.6	1.6

Table 3.5: Calibrated parameters of CTD model for different slip systems

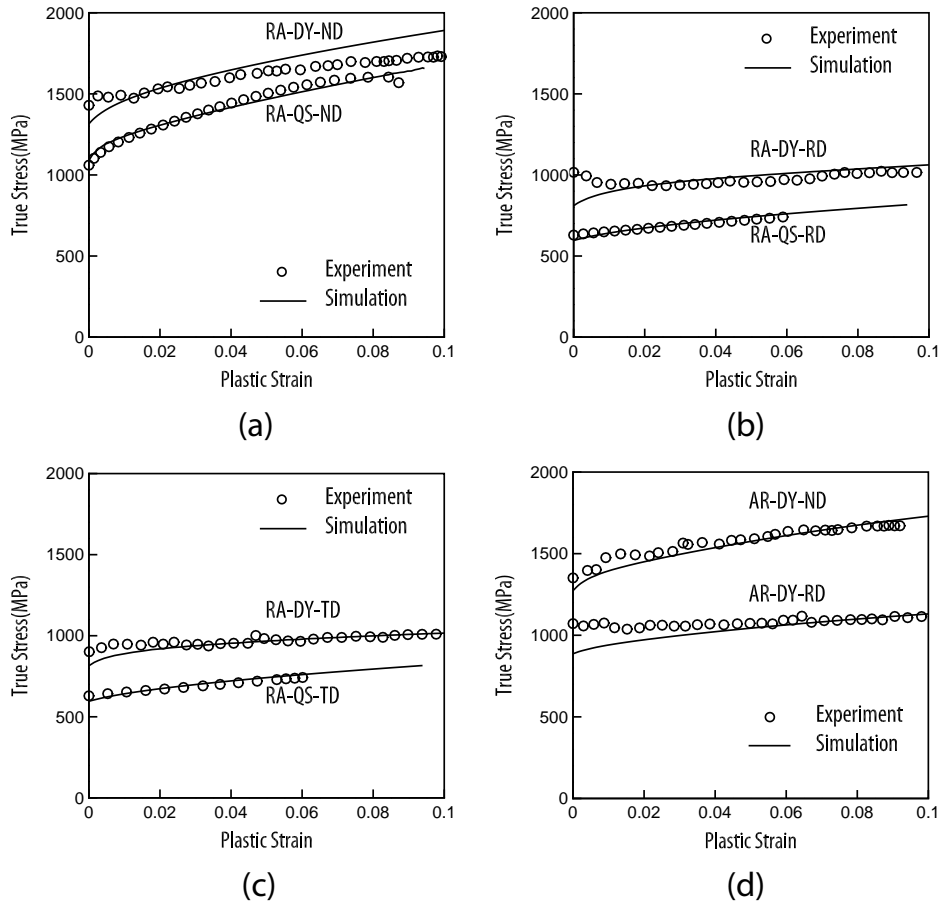


Figure 3.15: Validation of CTD constitutive model using quasi-static and dynamic experiments on (a-c) RA and (d) AR microstructures

3.6.2 Rate dependence of flow stress

CPFE simulation of single crystals under uniaxial deformation is informative and provides insight into deformation processes in complex polycrystalline aggregates. Deformation of single crystal models illustrated earlier in Figure 3.13 is revisited in this section to understand how underlying dislocation glide mechanisms change under a wide range of strain rates. Figure 3.16 shows the dependence of flow stress at 8% true strain predicted by the PL and CTD models for different strain rates ranging from 10^{-4} to 10^7 s^{-1} . It is observed that the two models are generally in good agreement in terms of flow stress before they start to deviate for strain rates higher than 10^5 s^{-1} . The CTD model predicts that the flow stress increases linearly with the logarithm of strain rate up to a critical strain rate, here 10^5 s^{-1} . Beyond this critical strain rate, the flow stress still varies linearly with the logarithm of strain rate, but with a higher slope. Similar observations were made for single crystal model favorable for prism slip which is not shown in Figure 3.16 for the sake of clarity of the plot. This trend is observed to be the case for different orientations. This change in rate sensitivity is not unusual and has been observed to be the case for many metals [31]. The results in Figure 3.16 suggest that the PL model can decently model deformation up to strain rates as high as 10^5 s^{-1} .

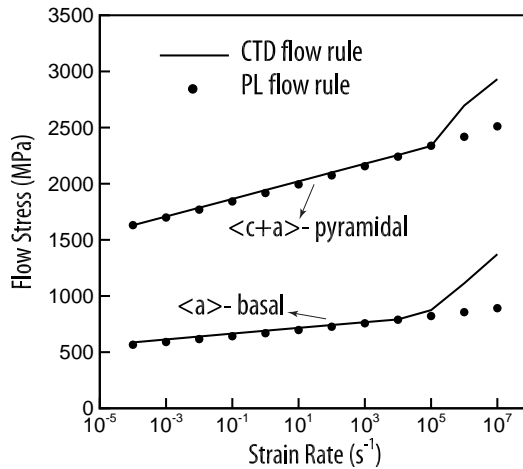


Figure 3.16: rate dependence of flow stress of single crystal model at 8% strain

Studying the response of the single crystal model oriented favorably for $\langle a \rangle$ - basal slip under high rate of deformation reveals some salient features of the CTD model. Figure 3.17 depicts the loading direction stress-strain response for the single crystal model oriented favorably for $\langle a \rangle$ - basal slip at different strain rates. An elastic overshoot occurs in the stress response at strain rates beyond 10^6 s^{-1} , and it becomes more pronounced as the applied strain rate increases. Elastic overshoot has been also reported in the simulations of copper [38] and vanadium [11] under high rates of deformation.

The initial peak in the stress can be explained in terms of dislocation activity on individual slip systems. Schmid factor analysis can provide some insight regarding the activity of slip systems. The Schmid factor analysis given in Table 3.6 indicates that $\bar{[2110]}$ basal slip system has the highest Schmid factor, leading to a prevailing single-slip mode. The Schmid factor is not provided in Table 3.6 for $\langle a \rangle$ - pyramidal and $\langle c+a \rangle$ - pyramidal slip system families due to their inactivity in this particular loading case. In order to measure the importance of the effects of thermally-activated and drag-dominated processes on dislocation glide, a quantity, referred to as *drag proportion*, is introduced and defined as the ratio of the time spent on the drag-dominated stage over the total travel time, i.e. $f_d = t_r / (t_w + t_r)$. f_d is only defined for active slip systems and falls in the range $(0, 1]$, where $f_d \rightarrow 0$ corresponds to predominantly thermally-activated dislocation glide and $f_d = 1$ denotes purely drag-dominated glide. Figure 3.18 shows the evolution of temperature, plastic shearing rate and drag proportion on the basal and prism slip system families at the strain rate of 10^7 s^{-1} . All slip systems in the basal and prism families become active at some point during deformation except

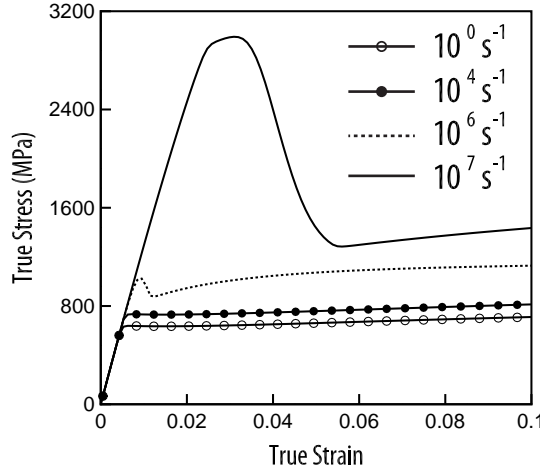


Figure 3.17: the loading direction stress-strain response for the single crystal model oriented favorably for $\langle a \rangle$ - basal slip

for P2; therefore, it is not included in the plots in Figure 3.18. The course of deformation could be generally divided into multiple stages, enumerated in Figure 3.18. Stage 1 corresponds to a purely elastic regime where the resolved shear stress on all slip systems is smaller than the long-range stress, viz. passing stress. In stage 2, dislocation slip starts to occur on B2; however, the initial dislocation density is not sufficient to accommodate the applied strain rate with plastic deformation. Therefore, the material needs to deform elastically until a sufficient amount of dislocations becomes available. This translates into an increase in the stress level and consequently provides enough resolved shear stress to activate the other basal and prism slip systems with lower Schmid factors, as shown in Figure 3.18(b). Figure 3.18(d) shows the transition of dislocation glide from a thermally-activated mechanism into a drag-dominated one in this stage. In stage 3, there is collectively sufficient dislocation content to accommodate the applied strain rate with plastic shearing rate, and therefore the macroscopic stress-strain response deviates clearly from a predominant elastic response. During this stage, dislocation glide remains in the drag-dominated regime, and plastic shearing rate on active slip systems, specifically on B2, increases, causing the self and latent hardening to become more pronounced. Figure 3.18(c) shows the evolution of temperature in this stage due to the significant amount of plastic work. During stage 4, dislocation glide on B2 remains in the drag-dominated regime, and sufficient dislocation density accumulates on B2 to accommodate further plastic deformation. Hence a drop in the stress level is observed in this stage. As the stress decreases, the plastic contribution of slip systems with lower Schmid factor, namely B1, B3, P1 and P3, progressively reduces until these slip systems eventually become inactive at the end of this stage. In Stage 5, B2 is the sole active slip system, and self hardening through the evolution of the parallel dislocation population is the main source of strain hardening observed in Figure 3.18(a). During this step, the thermally-activated processes become more significant, and the mechanism governing dislocation glide transitions from a drag-dominated mode to a mixed mode.

The high stresses induced by the elastic overshoot at very high strain rates could be relieved in real materials by either nucleating new dislocations (in addition to the dislocation multiplication considered) [9] or deformation twinning [30, 20]. Considering the contribution of homogeneous and heterogeneous dislocation nucleation to the evolution of dislocation population could be of benefit in simulation of polycrystals subject to very high strain rate and shock loading [57, 15].

The model presented considers dislocation slip as the major deformation mechanism based on the experimental results in [66, 82] where twinning was not reported for Ti alloys with high Al concentration. Nevertheless, augmenting the model with deformation twinning mechanism could be advantageous for simulating deformation of (un-)alloyed titanium at very low temperatures or high strain rates.

Experiments on polycrystalline Ti samples have shown an increasing rate sensitivity with logarithm of strain rate

slip system family	Miller-Bravais index	label	Schmid factor
basal	(0001) $[1\bar{2}10]$	B1	-0.25
	(0001) $[\bar{2}110]$	B2	0.50
	(0001) $[11\bar{2}0]$	B3	-0.25
prism	$(10\bar{1}0)[\bar{1}2\bar{1}0]$	P1	0.22
	$(01\bar{1}0)[\bar{2}110]$	P2	0.00
	$(\bar{1}100)[\bar{1}120]$	P3	-0.22

Table 3.6: List of Schmid factors for basal and prism slip families for the single crystal model oriented favorably for $\langle a \rangle$ - basal slip

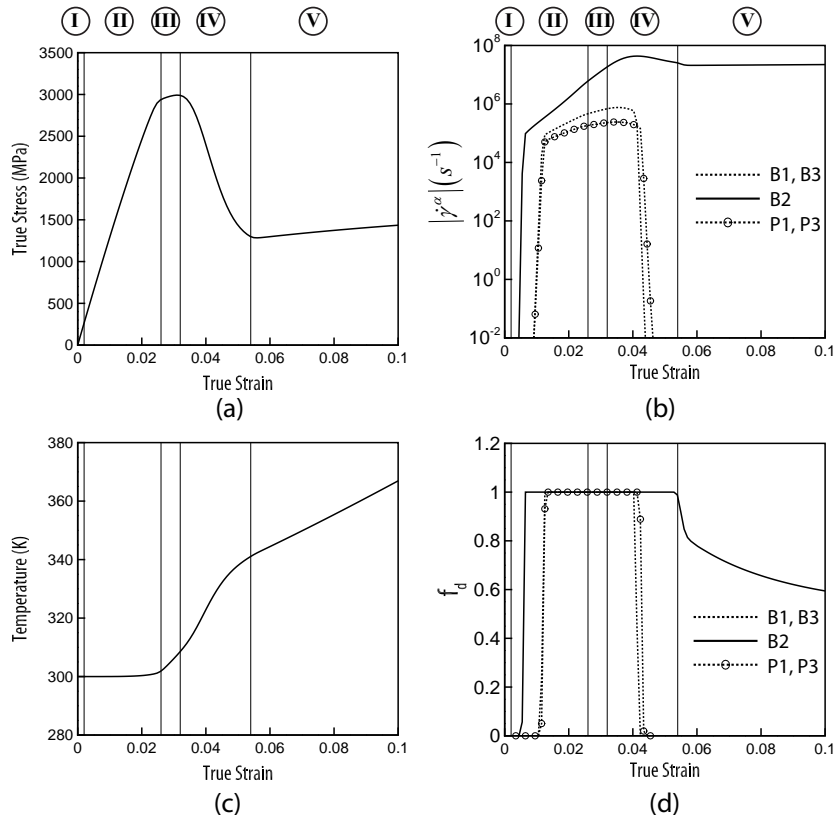


Figure 3.18: CPFE simulation of the single crystal model oriented favorably for $\langle a \rangle$ - basal slip at strain rate of $10^7 s^{-1}$, (a) the loading direction stress-strain response, evolution of (b) plastic shearing rate, (c) temperature and (d) drag proportion. (the Roman numerals denote different stages of deformation)

[20]. Based on the rate sensitivity study conducted on the single crystal models, it is expected that the CTD model could show the change in the rate sensitivity of polycrystalline microstructures, as well. Compression of the RA sample along ND is simulated under different rates of deformation. Flow stress at 6% strain is extracted and compared with the available experimental results on rate sensitivity of some Ti polycrystals in Figure 3.19. It is observed that the PL model exhibits a constant rate sensitivity across different strain rates whereas the CTD model shows a change in the rate sensitivity for strain rates higher than $10^5 s^{-1}$. This is in good agreement with the experimental results of Casem [16] where an enhanced hardening effect is observed beyond strain rates of $10^4 s^{-1}$.

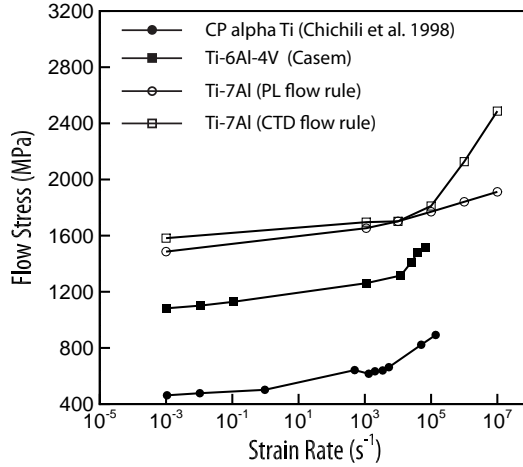


Figure 3.19: rate dependence of flow stress in Ti polycrystals at 6% strain

3.6.3 Temperature-dependence of flow stress

Ti alloys are used in military and aerospace components which experience different thermal environments during service. Changes in temperature influence both the elastic and plastic responses of the material. As temperature increases, the elastic constants reduce which indirectly affect the slip-driven plasticity by reducing the shear modulus-dependent strength of slip systems [8], represented by the athermal stress. Increasing temperature would also directly promote plasticity by boosting up the rate of successful thermal activation attempts. In this section, the effects of temperature on deformation is studied in the context of deformations under isothermal conditions. All subsequent simulations are done using the CTD model.

Compression of the AR microstructure along ND and RD at strain rate of $10^{-3} s^{-1}$ is simulated under isothermal conditions, but at different initial temperatures. The loading direction stress-strain responses are plotted in Figure 3.20(a). As the temperature increases, it is seen that the yield stress decreases significantly while the elastic stiffness reduces negligibly. Figure 3.20(b) shows the variation of the yield stress with temperature within a temperature range of 300K to 700K. It is observed that the yield stress decreases almost linearly with temperature within the specified temperature range, consistent with the experimental results of Khan et al. [46] on another Ti alloy, Ti-6Al-4V. It is worthy to note that the yield stress corresponding to the AR-ND simulations decreases more rapidly with temperature in comparison with the one for the AR-RD simulations. This is owing to the crystallographic orientation of the grains and dissimilar variation of critical resolved shear stress (CRSS) on different slip systems with temperature. The crystallographic orientations of the grains in the AR sample are such that the $\langle a \rangle$ - basal and prism slip systems are the favorable modes of slip when the sample is loaded along RD, whereas $\langle c+a \rangle$ - pyramidal slip is the favorable one for the case of loading along ND. As shown earlier in Figure 3.11, the CRSS for the $\langle c+a \rangle$ - pyramidal slip system reduces at a higher rate with respect to temperature, compared to the one for the $\langle a \rangle$ - basal and prism slip systems. This explains why the yield stress corresponding to the AR-ND simulations decreases more rapidly with temperature

in Figure 3.20(b).

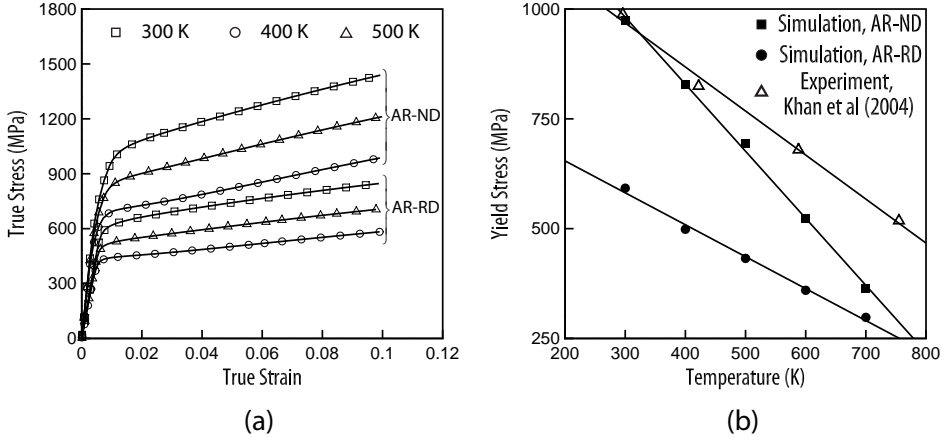


Figure 3.20: CPFE simulation of the AR microstructure at different initial temperatures subject to strain rate of $10^{-3} s^{-1}$, (a) the loading direction stress-strain response, (b) variation of yield stress with temperature

3.6.4 Adiabatic heating

The effects of temperature on the high-rate deformation of metals could be investigated in the context of adiabatic thermal conditions. In order to perceive the effects of adiabatic heating on the elasticity and plasticity, compression of the AR microstructure along ND is simulated at strain rate of $10^4 s^{-1}$. Different cases are considered in the simulations. Case 1 corresponds to a simulation in which adiabatic heating is ignored, i.e. isothermal condition is assumed. Case 2 refers to a simulation where adiabatic heating is taken into account; however, the reduction of elastic constants with temperature is neglected. Case 3 denotes a simulation in which both adiabatic heating and reduction of elastic constants with temperature are considered. The macroscopic stress-strain response for the three different cases are given in Figure 3.21. Comparing the macroscopic stress-strain curves, it is observed that the pre-yield part of the stress-strain response is barely affected by the adiabatic heating since the amount of plastic work is limited and the local temperature slightly increases in this stage of deformation. With the evolution of temperature during the course of deformation, the effect of adiabatic heating becomes more evident at higher strains where a lower strain hardening is obtained for case 3, compared to case 1 where the temperature evolution was suppressed. Moreover, based on the macroscopic response for cases 2 and 3 in Figure 3.21, it is inferred that the effect of reduction of elastic constants with temperature becomes noticeable only at strains beyond 0.15. In other words, considering elastic softening is of secondary importance if the failure processes of the material due to nucleation and evolution of microstructural defects start at early stages of deformation. This is consistent with the results in [64] where the effect of temperature evolution on the failure of Ti alloys were investigated.

Failure of Ti alloys under high rates of deformation is attributed to formation of adiabatic shear bands (ASBs) which could in turn be related to the emergence of hot spots due to adiabatic heating. In order to inspect the temperature evolution at the grain level for case 3, the granular temperature increase, denoted by $\Delta\bar{T}_g$, is calculated for each grain, and its distribution over the entire microstructure at four different stages of deformation is plotted in Figure 3.22(a). The granular temperature increase for an arbitrary grain, say g , is evaluated as $\Delta\bar{T}_g = \sum_{i=1}^{N_e^{(g)}} \Omega_i \Delta\bar{T}_i / \sum_{i=1}^{N_e^{(g)}} \Omega_i$ where $N_e^{(g)}$ is the number of elements in grain g and Ω_i and $\Delta\bar{T}_i$ are respectively the volume and temperature increase in the i -th element in grain g . Evolution of $\Delta\bar{T}_g$ distribution clearly indicates that not only the average temperature in individual grains, but also the standard deviation increases during the course of deformation. Similar trend is observed for the distribution of the granular effective plastic strain, shown in Figure 3.22(b). The increase in the heterogeneity

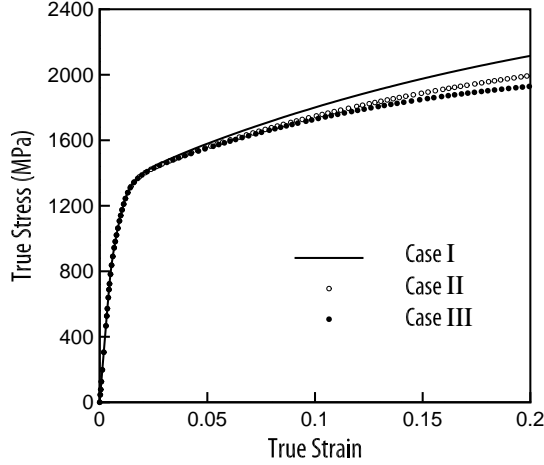


Figure 3.21: the loading direction stress-strain response for compression of the AR microstructure along ND at strain rate of 10^4 s^{-1}

of plastic strain field implies that the micro-plasticity distribution transitions from a nearly uniform state in the early stages of deformation to a non-uniform one in the later stages. The tendency of the deformation towards non-uniform distribution of the plastic strain indicates the development of severely plastically-deformed grains. If the grains happen to be located adjacent to each other, a large region of localized deformation is created, as shown in Figure 3.23. In this region, both plastic deformation and temperature are high. Formation of these regions may facilitate nucleation of the adiabatic shear bands and therefore expedite activation of the failure processes.

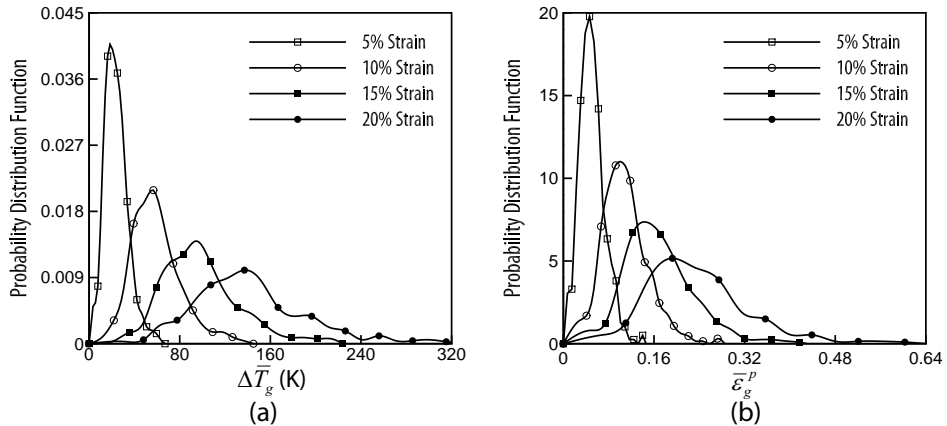


Figure 3.22: CPFE simulation of the AR microstructure along ND at strain rate of 10^4 s^{-1} , evolution of probability distribution function of (a) $\Delta \bar{T}_g$ and (b) $\bar{\epsilon}_g^p$ at different stages of deformation

Since the adiabatic heating is inter-related with the plastic deformation, one might think that the distributions shown in Figure 3.22 are consistent with each other; that is, as plasticity gets localized in certain grains, the temperature also adiabatically increases in those grains and causes the increase in the standard deviation in Figure 3.22(a). However, further inspection of the microstructure revealed some unexpected behavior in the contours of plastic strain

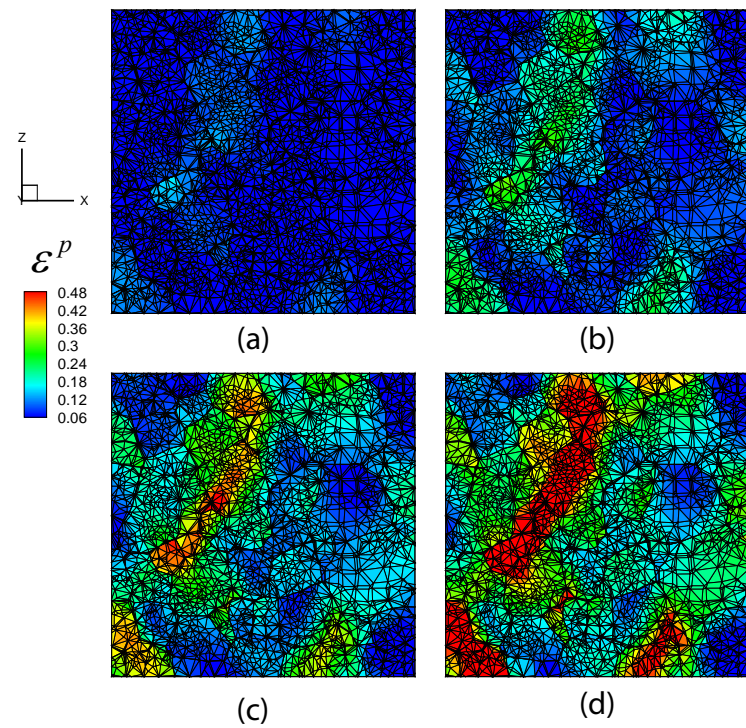


Figure 3.23: Development of a region of plastic localization in the AR microstructure under compression along ND at strain rate of $10^4 s^{-1}$. The contours are drawn in the undeformed configuration.

and temperature. It was observed that the regions with high value of plastic strain does not necessarily correspond to the hot spots in the contour plot of temperature field and vice versa. For example, the contour plot of effective plastic strain in Figure 3.24(a) shows that grain A is highly plastically deformed, however the contour plot of temperature field in Figure 3.24(b) does not suggest an elevated temperature in this grain. On the other hand, grains B, C and D are experiencing an elevated thermal field although they are undergoing moderate plastic deformation. In order to realize the reason behind this unexpected behavior, the formulation of plastic power density is recalled, $\dot{W}_p = \sigma : \mathbf{d}^p$. The rate of plastic work is dependent on the stress level and the rate of plastic deformation in a multiplicative form. Hence, a high value of plastic strain by itself does not constitute a high value of plastic work and consequently adiabatic heating. Temperature may increase more at a material point with high level of stress but low plastic strain, compared to another material point with higher plastic strain and lower stress. In light of this point, the temperature trends in grains A, B, C and D sound more reasonable by considering the contour plot of von Mises stress, as a measure of stress tensor, shown in Figure 3.24(c).

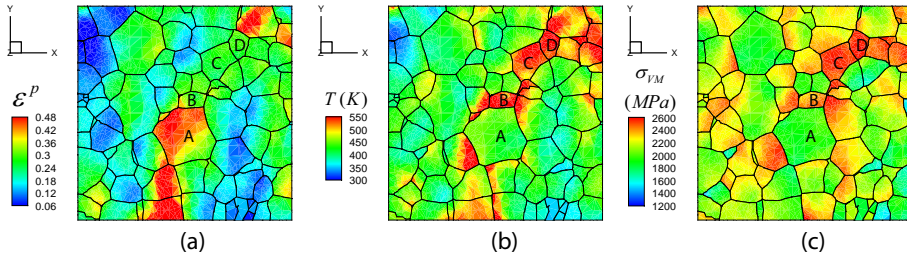


Figure 3.24: CPFE simulation of the AR microstructure along ND at strain rate of $10^4 s^{-1}$, contour plots of (a) effective plastic strain, (b) temperature and (c) von Mises stress at 20% strain

The observation that the grains with severe plastic deformation do not necessarily endure high rates of adiabatic heating is not a coincidence. A bi-crystal model consisting of a *hard* and *soft* grain is generated, as shown in Figure 3.25(a). The orientations of the *soft* and *hard* grains are identical to the ones shown in Figures 3.13(a) and 3.13(c), respectively. Figure 3.25(b) shows the macroscopic loading direction stress-strain response of the bi-crystal model under compression along [001] at strain rate of $10^4 s^{-1}$. Three stages of deformation are selected as indicated in Figure 3.25(b). The evolution of relevant micro-mechanical variables are investigated at these stages along an X-directed line passing through the centroid of the bi-crystal model. At stage 1, the plastic flow has already started in the soft grain whereas the hard grain has barely deformed plastically. Thus, as shown in Figure 3.26(a), the temperature in the soft grain is higher than the one in the hard grain, but slightly. In the next stages of deformation, it is observed that the temperature in the hard grain becomes much higher in comparison with the soft grain. It is instructive to remember that it is the soft grain which undergoes a higher level of plastic strain during the entire deformation. Here again the rate of adiabatic heating is governed by the stress state. The temperature difference between the two grains grows larger in the course of deformation as shown in Figures 3.26(b) and 3.26(c).

This bi-crystal problem is a simple but yet enlightening problem. The importance of the results in Figure 3.26 goes beyond the determination of the *hot* grain and impacts the predictions of models for formation of adiabatic shear bands under high rates of deformation. Given the formation and propagation of ASBs are beyond the scope, we content with a brief introduction to different criteria for formation of ASBs and simply state their implication on nucleation site of ASBs in the bi-crystal problem. Different criteria have been proposed in the literature for estimating the formation of adiabatic shear bands. These criteria are based on selecting a specific thermo-mechanical quantity, such as plastic shear strain [23], temperature [56] and stored energy of cold work [64, 71]. These criteria predict formation of ASBs in the material once the specified thermo-mechanical quantity exceeds a critical value. In light of the results shown in Figure 3.26, these criteria do not predict the same grain as the nucleation site for ASBs in the bi-crystal problem. Using the critical plastic shear strain criterion, ASBs nucleate in the soft grain since it undergoes higher levels of plasticity, whereas both the critical temperature and critical stored energy of cold work criteria suggest

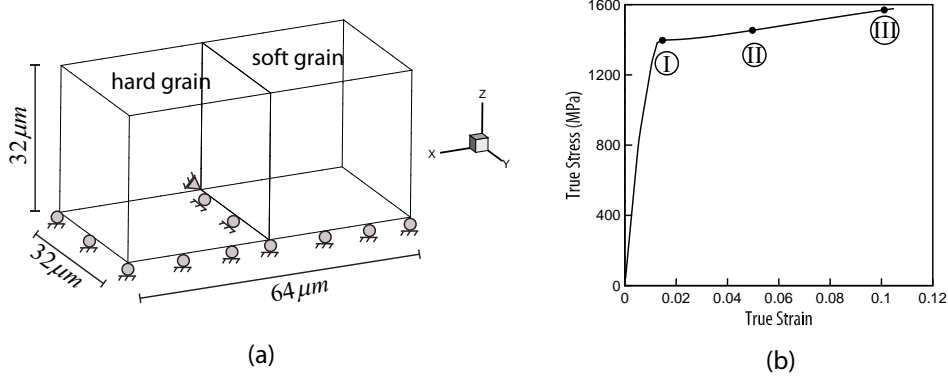


Figure 3.25: (a) bi-crystal model consisting of 5103 linear tetrahedral elements, (b) macroscopic loading direction stress-strain response for compression at strain rate of $10^4 s^{-1}$ along [001]

that the nucleation site for ASBs is the hard grain due to the higher level of plastic work. If the experimental apparatus allows for the experimentation on a bi-crystal sample, the observations in terms of nucleating site for ASBs could provide some insight and be used to test validity of the nucleation models.

3.7 Concluding remarks

A crystal plasticity constitutive model is proposed which could be used for a wide range of strain rates. Flow rule in the proposed constitutive model is the Orowan equation which expresses the slip rate on a given slip system in terms of the dislocation density and average dislocation velocity. Capability of the model in simulating deformations across decades of strain rate inheres in formulating the average dislocation velocity in terms of both the thermally-activated and drag-dominated stages of screw dislocation motion in the glide plane. The proposed constitutive model is explicitly temperature dependent which makes it suitable for modeling high strain rate deformations where temperature increase adiabatically due to the conversion of plastic work into heat. Effects of temperature on elasticity and plasticity are carefully calibrated using the experimental results.

Simulation results demonstrate the competency of the model in predicting material response in quasi-static and dynamic rates. The model can effectively capture the increase in the rate sensitivity of flow stress at higher rates of deformation due to the transition in the rate controlling mechanism of dislocation motion. The model predicts an elastic overshoot in the single crystal level under very high strain rates due to the insufficient dislocation content to accommodate the applied strain rate. Consistent with experiments, isothermal quasi-static simulations show that the 0.2% yield stress decreases almost linearly with temperature in the temperature range of interest. The rate of decrease is observed to be higher along ND since the CRSS for $\langle c+a \rangle$ - drops faster with temperature compared to the one for the $\langle a \rangle$ - type slip systems. Adiabatic simulations show that the effect of temperature on enhancing plasticity is more pronounced than its effect on degradation of the elastic constants. Analysis of high strain rate simulations showed the tendency of the microstructure towards localizing plastic deformation as the material straining progresses. Unexpectedly careful analysis of adiabatic heating revealed that the grains with severe plastic deformation do not necessarily endure high temperatures as a result of conversion of plastic work into heat.

The work presented focused on modeling the deformation under different strain rates. This is the first step towards modeling failure in Ti alloys. The next step of the research is to develop proper physics-based criterion for nucleation of adiabatic shear bands, a precursor to the material failure. The propensity of the material for twinning and its relationship with the local temperature increase need to be investigated as well.

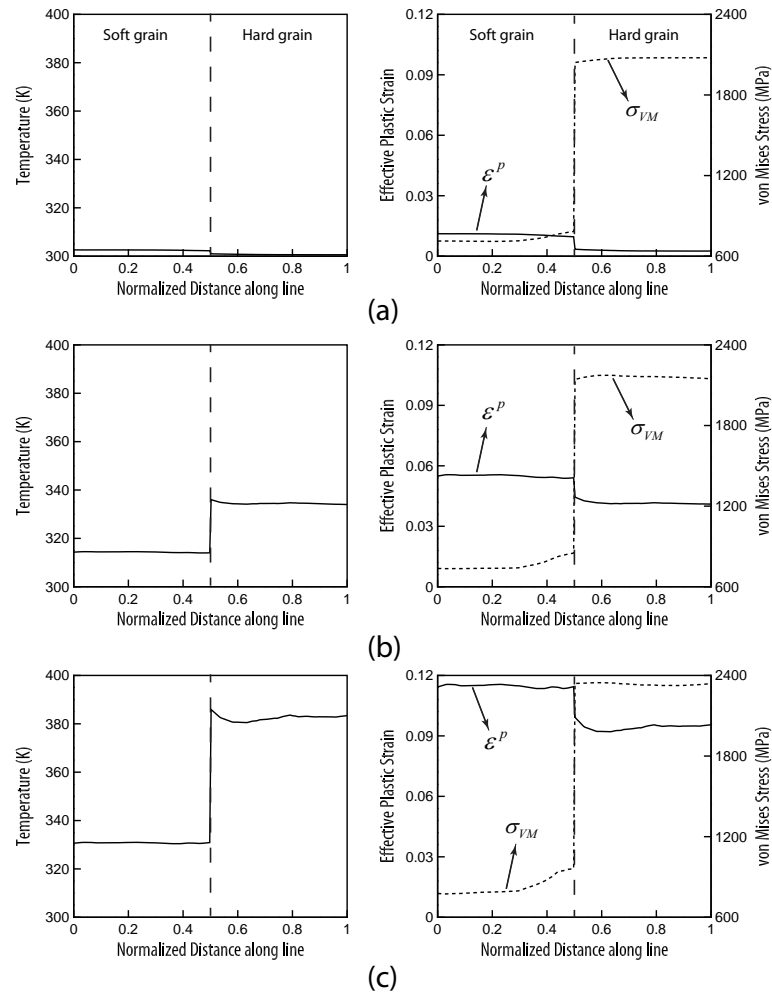


Figure 3.26: Profile of temperature, effective plastic strain and von Mises stress along a line at (a) 1.5% strain (stage 1), (a) 5% strain (stage 2) and (a) 10% strain (stage 3)

Bibliography

- [1] *Metallic Materials and Elements for Aerospace Vehicle Structures*. U.S. Department of Defense, 1998.
- [2] A. Akhtar and E. Teghtsoonian. prismatic slip in α -titanium single crystals. *Metall Mater Trans A*, 6:2201–2208, 1975.
- [3] Alankar Alankar, Philip Eisenlohr, and Dierk Raabe. A dislocation density-based crystal plasticity constitutive model for prismatic slip in α -titanium. *Acta Mater*, 59(18):7003 – 7009, 2011.
- [4] Masoud Anahid and Somnath Ghosh. Homogenized constitutive and fatigue nucleation models from crystal plasticity {FE} simulations of Ti alloys, part 2: Macroscopic probabilistic crack nucleation model. *Int J Plasticity*, 48:111 – 124, 2013.
- [5] Masoud Anahid, Mahendra K. Samal, and Somnath Ghosh. Dwell fatigue crack nucleation model based on crystal plasticity finite element simulations of polycrystalline titanium alloys. *J Mech Physics Solids*, 59(10):2157 – 2176, 2011.
- [6] A. Arsenlis and D. M. Parks. Crystallographic aspects of geometrically-necessary and statistically-stored dislocation density. *Acta Mater*, 47:1597–1611, 1998.
- [7] R.J. Asaro and J.R. Rice. Strain localization in ductile single crystals. *J Mech Physics Solids*, 25(5):309 – 338, 1977.
- [8] M.F. Ashby. The deformation of plastically non-homogeneous materials. *Phil Magazine*, 21(170):399–424, 1970.
- [9] R.A. Austin and D.L. McDowell. A dislocation-based constitutive model for viscoplastic deformation of fcc metals at very high strain rates. *Int J Plasticity*, 27(1):1 – 24, 2011.
- [10] M.R Bache. A review of dwell sensitive fatigue in titanium alloys: the role of microstructure, texture and operating conditions. *Int J Fatigue*, 25(911):1079 – 1087, 2003.
- [11] N.R. Barton, J.V. Bernier, R. Becker, A. Arsenlis, R. Cavallo, J. Marian, M. Rhee, H.S. Park, B.A. Remington, and R.T. Olson. A multiscale strength model for extreme loading conditions. *J Appl Physics*, 109(7), 2011.
- [12] R. Becker, A. Arsenlis, J. Marian, M. Rhee, M. Tang, and L. Yang. Continuum level formulation and implementation of a multi-scale model for vanadium. Technical report, Lawrence Livermore National Laboratory, 2009.
- [13] Y. Bhandari, S. Sarkar, M. Groeber, M.D. Uchic, D.M. Dimiduk, and S. Ghosh. 3D polycrystalline microstructure reconstruction from FIB generated serial sections for FE analysis. *Comput Mater Sci*, 41(2):222 – 235, 2007.
- [14] M. Brandes. *Creep, fatigue, and deformation of alpha and alpha-beta titanium alloys at ambient temperature*. PhD thesis, Materials science and engineering, Ohio State University, USA, 2008.

[15] L. Capolungo, D.E. Spearot, M. Cherkaoui, D.L. McDowell, J. Qu, and K.I. Jacob. Dislocation nucleation from bicrystal interfaces and grain boundary ledges: Relationship to nanocrystalline deformation. *J Mech Phys Solids*, 55(11):2300 – 2327, 2007.

[16] D.T. Casem, Private communication.

[17] W. Chen and B. Song. *Split Hopkinson (Kolsky) Bar: Design, Testing and Applications*. Springer Science+Business Media, LLC, Boston, MA, 2011.

[18] J. Cheng and S. Ghosh. A crystal plasticity (FE) model for deformation with twin nucleation in magnesium alloys. *Int J Plasticity*, 67:148 – 170, 2015.

[19] J. Cheng, A. Shahba, and S. Ghosh. Stabilized tetrahedral elements for crystal plasticity finite element analysis overcoming volumetric locking. *Comput Mech*, page in press, 2016.

[20] D.R. Chichili, K.T. Ramesh, and K.J. Hemker. The high-strain-rate response of alpha-titanium: experiments, deformation mechanisms and modeling. *Acta Mater*, 46(3):1025 – 1043, 1998.

[21] J.D. Clayton. Dynamic plasticity and fracture in high density polycrystals: constitutive modeling and numerical simulation. *J Mech Phys solids*, 53:261301, 2005.

[22] H. Conrad, M. Doner, and B. de Meester. *Titanium science and technology*. Plenum press, 1973.

[23] R.S. Culver. *Thermal instability strain in dynamic plastic deformation*. Metallurgical efects at high strain rates. Plenum press, 1973.

[24] H. Dai. *Geometrically-necessary dislocation density in continuum plasticity theory, FEM implementation and applications*. PhD thesis, Department of Mechanical Engineering, Massachusetts Institute of Technology, USA, 1997.

[25] E. A. de Souza Neto, F. M. Andrade Pires, and D. R. J. Owen. F-bar-based linear triangles and tetrahedra for finite strain analysis of nearly incompressible solids. part I: formulation and benchmarking. *Int J Numer Meth Eng*, 62(3):353–383, 2005.

[26] D. Deka, D. S. Joseph, S. Ghosh, and M. J. Mills. Crystal plasticity modeling of deformation and creep in polycrystalline Ti-6242. *Metall Trans A*, 37A(5):1371–1388, 2006.

[27] C.R. Dohrmann, M. W. Heinstein, J. Jung, S. W. Key, and W. R. Witkowski. Node-based uniform strain elements for three-node triangular and four-node tetrahedral meshes. *Int J Numer Meth Eng*, 47(9):1549–1568, 2000.

[28] F.P.E. Dunne, D. Rugg, and A. Walker. Lengthscale-dependent, elastically anisotropic, physically-based hcp crystal plasticity: Application to cold-dwell fatigue in Ti alloys. *Int J Plasticity*, 23(6):1061 – 1083, 2007.

[29] U. Essmann and H. Mughrabi. Annihilation of dislocations during tensile and cyclic deformation and limits of dislocation densities. *Phil Mag A*, 40(6):731–756, 1979.

[30] P.S. Follansbee and G.T. Gray. An analysis of the low temperature, low and high strain-rate deformation of Ti-6Al-4V. *Metall Trans A*, 20:863 – 874, 1989.

[31] P.S. Follansbee, G. Regazzoni, and U.F. Kocks. *Mechanical Properties at High Rates of Strain, Proceedings of the Third Conference on the Mechanical Properties of Materials at High Rates of Strain Held in Oxford, 9-12 April 1984*. Conference series. Inst. of Physics, 1984.

[32] H. J. Frost and M. F. Ashby. Motion of a dislocation acted on by a viscous drag through an array of discrete obstacles. *J Appl Physics*, 42(13):5273–5279, 1971.

[33] S. Ghosh, Y. Bhandari, and M. Goeber. CAD-based reconstruction of 3D polycrystalline alloy microstructures from FIB generated serial sections. *Computer-Aided Design*, 40(3):293 – 310, 2008.

[34] M. Groeber, S. Ghosh, M.D. Uchic, and D.M. Dimiduk. A framework for automated analysis and simulation of 3D polycrystalline microstructures: Part 1: statistical characterization. *Acta Mater*, 56(6):1257–1273, 2008.

[35] M. Groeber, S. Ghosh, M.D. Uchic, and D.M. Dimiduk. A framework for automated analysis and simulation of 3D polycrystalline microstructures. part 2: Synthetic structure generation. *Acta Mater*, 56(6):1274–1287, 2008.

[36] M.A. Groeber and M.A. Jackson. DREAM.3D: A digital representation environment for the analysis of microstructure in 3D. *Integr Mater Manuf Innov*, 3(5), 2014.

[37] P. Guyot and J.E. Dorn. a critical review of the Peierls mechanism. *Canadian J Physics*, 45(2):983–1016, 1967.

[38] B.L. Hansen, I.J. Beyerlein, C.A. Bronkhorst, E.K. Cerreta, and D. Dennis-Koller. A dislocation-based multi-rate single crystal plasticity model. *Int J Plasticity*, 44:129 – 146, 2013.

[39] V. Hasija, S. Ghosh, M. J. Mills, and D. S. Joseph. Deformation and creep modeling in polycrystalline Ti6Al alloys. *Acta Mater*, 51:4533–4549, 2003.

[40] M. Hiratani and E.M. Nadgorny. Combined model of dislocation motion with thermally activated and drag-dependent stages. *Acta Mater*, 49(20):4337 – 4346, 2001.

[41] M. Hiratani, H.M. Zbib, and M.A. Khaleel. Modeling of thermally activated dislocation glide and plastic flow through local obstacles. *Int J Plasticity*, 19(9):1271 – 1296, 2003.

[42] R. D. Isaac and A. V. Granato. Rate theory of dislocation motion: Thermal activation and inertial effects. *Phys Rev B*, 37:9278–9285, 1988.

[43] Shahriyar Keshavarz and Somnath Ghosh. Multi-scale crystal plasticity finite element model approach to modeling nickel-based superalloys. *Acta Mater*, 61(17):6549 – 6561, 2013.

[44] Shahriyar Keshavarz and Somnath Ghosh. Hierarchical crystal plasticity {FE} model for nickel-based superalloys: Sub-grain microstructures to polycrystalline aggregates. *Int J Solids Struct*, 55:17 – 31, 2015.

[45] Akhtar S. Khan, Rehan Kazmi, and Babak Farrokh. Multiaxial and non-proportional loading responses, anisotropy and modeling of Ti6Al4V titanium alloy over wide ranges of strain rates and temperatures. *Int J Plasticity*, 23(6):931 – 950, 2007.

[46] Akhtar S. Khan, Yeong Sung Suh, and Rehan Kazmi. Quasi-static and dynamic loading responses and constitutive modeling of titanium alloys. *Int J Plasticity*, 20(12):2233 – 2248, 2004.

[47] Akhtar S. Khan and Shaojuan Yu. Deformation induced anisotropic responses of Ti6Al4V alloy. part i: Experiments. *Int J Plasticity*, 38:1 – 13, 2012.

[48] U.F. Kocks, A.S. Argon, and M.F. Ashby. Thermodynamics and kinetics of slip. *Prog Mater Sci*, 19, 1975.

[49] A. I. Landau. The effect of dislocation inertia on the thermally activated low-temperature plasticity of materials. i. theory. *Physica Status Solidi A*, 61(2):555–563, 1980.

[50] Bing-Jean Lee, KennethS. Vecchio, Said Ahzi, and Scott Schoenfeld. Modeling the mechanical behavior of tantalum. *Metal Mater Trans A*, 28(1):113–122, 1997.

[51] H. Li, D.E. Mason, T.R. Bieler, C.J. Boehlert, and M.A. Crimp. Methodology for estimating the critical resolved shear stress ratios of α -phase ti using ebsd-based trace analysis. *Acta Mater*, 61(20):7555 – 7567, 2013.

[52] X. Ling, M. F. Horstemeyer, and G. P. Potirniche. On the numerical implementation of 3d rate-dependent single crystal plasticity formulations. *Int J Numer Meth Eng*, 63(4):548–568, 2005.

[53] A. Ma, F. Roters, and D. Raabe. A dislocation density based constitutive model for crystal plasticity {FEM} including geometrically necessary dislocations. *Acta Mater*, 54(8):2169 – 2179, 2006.

[54] K. MatouÅ and A.M. Maniatty. Finite element formulation for modelling large deformations in elasto-viscoplastic polycrystals. *Int. J. Numer. Meth. Eng.*, 60:2313 – 2333, 2004.

[55] H. Mecking and U.F. Kocks. Kinetics of flow and strain-hardening. *Acta Metal*, 29(11):1865 – 1875, 1981.

[56] Sergey N. Medyanik, Wing Kam Liu, and Shaofan Li. On criteria for dynamic adiabatic shear band propagation. *J Mech Phys Solids*, 55(7):1439 – 1461, 2007.

[57] M.A. Meyers, F. Gregori, B.K. Kad, M.S. Schneider, D.H. Kalantar, B.A. Remington, G. Ravichandran, T. Boehly, and J.S. Wark. Laser-induced shock compression of monocrystalline copper: characterization and analysis. *Acta Mater*, 51(5):1211 – 1228, 2003.

[58] JonathanS. Montgomery, MartinG.H. Wells, Brij Roopchand, and JamesW. Ogilvy. Low-cost titanium armors for combat vehicles. *JOM*, 49(5), 1997.

[59] T. Neeraj and M.J. Mills. Short-range order (sro) and its effect on the primary creep behavior of a Ti6wt. % Al alloy. *Mater Sci Eng A*, 319321:415 – 419, 2001.

[60] S. Nemat-Nasser, W.G. Guo, and J.Y. Cheng. Mechanical properties and deformation mechanisms of a commercially pure titanium. *Acta Mater*, 47(13):3705 – 3720, 1999.

[61] Yaozhuang Nie and Youqing Xie. *Ab initio* thermodynamics of the hcp metals Mg, Ti, and Zr. *Phys Rev B*, 75:174117, May 2007.

[62] V.I. Nizhankovskii, M.I. Katsnelson, G.V. Peschanskikh, and A.V. Trefilov. Anisotropy of the thermal-expansion of titanium due to proximity to an electronic topological transition. *JETP lett*, 59:733–737, 1994.

[63] H. Ogi, S. Kai, H. Ledbetter, R. Tarumi, M. Hirao, and K. Takashima. Titanums high-temperature elastic constants through the hcpbcc phase transformation. *Acta Mater*, 52(7):2075–2080, 2004.

[64] S. Osovski, D. Rittel, and A. Venkert. The respective influence of microstructural and thermal softening on adiabatic shear localization. *Mech Mater*, 56:11 – 22, 2013.

[65] D. Ozturk, A. Shahba, and S. Ghosh. Crystal plasticity FE study of the effect of thermo-mechanical loading on fatigue crack nucleation in titanium alloys. *Fatigue Fract Eng Mater Struct*, page in press, 2016.

[66] N.E. Paton, R.G. Baggerly, and J.C. Williams. Deformation and solid solution strengthening of titanium-aluminum single crystals. Technical report, Rockwell Int. Report, 1976.

[67] D. Peirce, R.J. Asaro, and A. Needleman. An analysis of nonuniform and localized deformation in ductile single crystals. *Acta Metal*, 30(6):1087 – 1119, 1982.

[68] Adam L. Pilchak. Fatigue crack growth rates in alpha titanium: Faceted vs. striation growth. *Scripta Mater*, 68(5):277 – 280, 2013.

[69] M. A. Puso and J. Solberg. A stabilized nodally integrated tetrahedral. *Int. J. Numer. Meth. Eng.*, 67:841 – 867, 2006.

[70] G. Ravichandran, A. J. Rosakis, J. Hodowany, and P. Rosakis. On the conversion of plastic work into heat during high-strain-rate deformation. In *Shock Compression of Condensed Matter*, volume 620 of *American Institute of Physics Conference Series*, pages 557–562, 2002.

[71] D. Rittel, Z. G. Wang, and M. Merzer. Adiabatic shear failure and dynamic stored energy of cold work. *Phys Rev Lett*, 96:075502, 2006.

[72] J.C. Russ and R.T. Dehoff. *Practical streology, 2nd edition*. Plenum press, 1999.

[73] P. Shade, Private communication.

[74] Simulation Modeling Suite. Simmetrix Inc. <http://www.simmetrix.com>, 2015.

[75] V. Sinha, M.J. Mills, and J.C. Williams. Determination of crystallographic orientation of dwell-fatigue fracture facets in Ti-6242 alloy. *J Mater Sci*, 42(19):8334–8341, 2007.

[76] P. Souvatzis, O. Eriksson, and M. I. Katsnelson. Anomalous thermal expansion in α -titanium. *Phys Rev Lett*, 99:015901, Jul 2007.

[77] T. Tanaka and H. Conrad. Deformation kinetics for $10\bar{1}011\bar{2}0$ slip in titanium single crystals below $0.4t_m$. *Acta Metal*, 20(8):1019 – 1029, 1972.

[78] M. Tang, L.P. Kubin, and G.R. Canova. Dislocation mobility and the mechanical response of b.c.c. single crystals: A mesoscopic approach. *Acta Mater*, 46(9):3221 – 3235, 1998.

[79] J. Thomas, M.A. Groeber, and S. Ghosh. Image-based crystal plasticity FE framework for microstructure dependent properties of Ti6Al4V alloys. *Mater Sci Eng A*, 553(15):164–175, 2012.

[80] G. Venkataramani, S. Ghosh, and M. J. Mills. A size dependent crystal plasticity finite element model for creep and load-shedding in polycrystalline Titanium alloys. *Acta Mater*, 55:3971–3986, 2007.

[81] G. Venkataramani, K. Kirane, and S. Ghosh. Microstructural parameters affecting creep induced load shedding in Ti-6242 by a size dependent crystal plasticity FE model. *Int J Plasticity*, 24:428–454, 2008.

[82] J.C. Williams, R.G. Baggerly, and N.E. Paton. Deformation behavior of HCP Ti-Al alloy single crystals. *Metall Mater Trans A*, 33:837850, 2002.

[83] W. Zeng, J.M. Larsen, and G.R. Liu. Smoothing technique based crystal plasticity finite element modeling of crystalline materials. *Int J Plasticity*, 65:250 – 268, 2015.

[84] Zhen Zhang, M. A. Cuddihy, and F. P. E. Dunne. On rate-dependent polycrystal deformation: the temperature sensitivity of cold dwell fatigue. *Proc Royal Soc London A*, 471(2181), 2015.

[85] O.C. Zienkiewicz and J.Z. Zhu. The superconvergent patch recovery (SPR) and adaptive finite element refinement. *Comput Meth Appl Mech Eng*, 101(13):207 – 224, 1992.

Crystal Plasticity FE Study of the Effect of Thermo-Mechanical Loading on Fatigue Crack Nucleation in Titanium Alloys

Deniz Ozturk, Ahmad Shahba, Somnath Ghosh*

Department of Civil Engineering, Johns Hopkins University, Baltimore, MD
21218

* Corresponding author. Tel: +1-410-516-7833, Fax: +1-410-516-7473

Email: sghosh20@jhu.edu

Abstract

In this paper, crystal plasticity simulations are conducted with a stabilized finite deformation finite element model to study the effects of microstructure as well as thermal and mechanical loading conditions on fatigue crack nucleation of Ti alloys. The crystal plasticity model includes a non-local crack nucleation model. Results of simulations are used to understand the effects of dwell loading periods and micro-texture on fatigue nucleation life in polycrystalline microstructures in comparison with experiments. From the thermo-mechanical studies of these alloys, it is found that anisotropic thermal expansion under thermal loading can induce stresses normal to the basal plane which can help opening up micro-cracks. Moreover, in agreement with experimental results, the simulations show diminished load shedding at elevated temperature due to weakening of plastic anisotropy.

Keywords: Crystal plasticity model; Dwell fatigue loading; Crack nucleation; Microtexture; Thermal stress; Load shedding

Nomenclature

A_i	Surface area of grain i
A_{ij}	Common surface area between grains i and j
\mathbf{B} , B	Crack opening displacement vector and magnitude
b^α	Burgers vector
\mathbf{B}_{CF}	Closure failure of Burgers circuit
c	Equilibrium crack length
\mathbf{C} , $[C_{ij}]$	Fourth order and Voigt representation of elasticity tensor
\mathbf{E}^e	Elastic Green-Lagrange strain tensor
\mathbf{F}	Total deformation gradient
\mathbf{F}^e , \mathbf{F}^θ , \mathbf{F}^p	Elastic, thermal and inelastic components of deformation gradient
g^α	Slip system resistance
G^α	Shear modulus
K_c , K_{mix} , K_n , K_t	Critical, mixed, normal and shear intensity factors
m	Material rate sensitivity
MI	$< c >$ – axis misorientation index
\mathbf{m}_0^α	Slip direction
N_{nucl}	Number of cycles to crack nucleation
n_{slip}	Total number of slip systems
\mathbf{n}^b	Normal to crack surface
\mathbf{n}_0^α	Slip plane normal
Q^α	Activation energy
R	Crack nucleation parameter
\mathbf{S}	Second Piola-Kirchhoff stress tensor
\mathbf{a}	Tensor containing thermal expansion coefficients
β	Ratio of shear to normal fracture toughness
$\dot{\gamma}^\alpha$	Plastic slip rate on slip system α
γ_s	Surface energy
θ	Temperature
$\mathbf{\Lambda}$, $\{\Lambda\}$	Tensorial and vectorial representation of Nye dislocation tensor
ν	Poisson's ratio
$\mathbf{\sigma}$	Cauchy stress tensor
ρ_{GF}^α , ρ_{GP}^α	Forest and parallel GND densities
ρ_{GNDen}^β , ρ_{GNDs}^β , ρ_{GNDet}^β	Vectorial components of GND
τ^α	Resolved shear stress on slip system α
τ_{GF}^α , τ_{GP}^α	Short and long range impeding stresses due to GNDs
χ^α	Back-stress
$\chi^{\alpha\beta}$	Slip system interaction matrix

1. Introduction

Titanium alloys with an *hcp* crystalline structure are used in components in automotive and aerospace industries due to their high strength to weight ratio, high fracture toughness and good corrosion resistance at elevated temperatures. Despite these attractive properties, these alloys suffer from time-dependent plastic deformation at temperatures lower than those at which diffusion-mediated processes occur. The accumulation of creep strain has been reported for applied stresses as low as 60% of macroscopic yield stress¹. In addition to their sensitivity to room-temperature creep, Ti alloys are prone to early fatigue failure at cold temperatures. Experiments showed that dwell loading with finite hold times reduces the fatigue life compared to cyclic loading with no hold time². It has also been observed that dwell debit, defined as the ratio of life under regular cyclic loading to that under dwell loading, increases with increasing applied macroscopic stress.

Sensitivity of dwell debit to dwell time and applied stress indicates that underlying time-dependent mechanisms contribute to the cyclic fatigue damage. Experimental evidence²⁻⁵, as well as micro-mechanical modeling efforts⁶⁻⁸, suggests that accumulation of creep strain at the grain level is a major time-dependent contributor to dwell fatigue. Dwell fatigue crack initiation sites are typically sub-surface and characterized by faceted cracks within the α grains, indicating a quasi-brittle crack initiation of the grains. Electron Backscattered Diffraction (EBSD) imaging combined with quantitative tilt fractography method have revealed that facet surfaces lie within 5-10 degrees off the crystallographic basal planes of primary α -grains⁹⁻¹². These fractured α grains at the initiation sites tend to be oriented such that the crystallographic $\langle c \rangle$ -axis lies within 10-25 degrees of the loading direction^{10,13}; in other words, the basal plane is almost perpendicular to the loading direction, and are subjected to a large normal stress component under dwell loading.

On account of the *hcp* crystalline structure, α -Titanium alloys exhibit elastic and plastic anisotropy, with [0001] direction showing high resistance to plastic deformation and also higher elastic stiffness. The aforementioned observations on relative orientation of the basal planes, facets and load direction suggest that the quasi-brittle fracture of the basal planes is driven by the large normal stresses incident on the basal planes of these *hard* grains. In addition, EBSD imaging has shown that these faceted α grains are typically surrounded by grains that are suitably oriented for plastic deformation, with a high Schmid factor for basal and/or prismatic slip⁹. This combination of neighboring *soft* and *hard* grains has been hypothesized to trigger a time-dependent stress redistribution mechanism^{4,12}. This load-shedding phenomenon, arising out of the elastic and plastic anisotropy of *hcp* crystals, is deemed to be a major cause of the premature crack initiation under dwell fatigue.

Grain-scale micromechanical modeling has also provided supporting evidence and insight on the mechanisms of heterogeneous grain-scale time-dependent creep in dwell fatigue. Rate-dependent crystal plasticity finite element (CPFE) models for Ti-6Al and Ti-6242 have been developed by Hasija *et al.*⁶ and Deka *et al.*⁷ to show the effect of time-dependent stress relaxation on the soft grains leading to stress concentration on the hard grain. Time-dependent creep occurs on the soft grain during each dwell cycle, while the response of the neighboring hard grain has more of an elastic character. Due to the compatibility requirement, this local creep is accompanied by stress redistribution, resulting in a time-dependent stress concentration on the hard grain with large normal tensile components on the basal plane. This stress component progressively increases with dwell cycles. An experimentally validated rate- and size-dependent CPFE model for Ti-6242 has been proposed by Venkatramani *et al.*^{14,15}, where the effects of grain and colony size and also

microstructural parameters such as Schmid factor, misorientation, and fraction of the primary α phase on the load shedding behavior were studied under creep and dwell fatigue loading. It has been shown that stress concentration on the hard grain increases with accumulating time-dependent plastic strain. The larger soft grain size and higher fraction of α phase have also been found to have detrimental effects, consistent with experimental observations³. The influence of the grain boundary morphology, and relaxation time-scales have been studied by Dunne *et al.*^{8,16} using a rate-dependent crystal plasticity model, which incorporates geometrically necessary dislocations (GNDs) that provides a physical length scale for plasticity. It was also shown that load-shedding on the hard grain is more pronounced under stress controlled rather than strain-controlled loading, suggesting the necessity for a stress-dependent criterion for dwell crack initiation. In a recent paper, Zhang *et al.*¹⁷ have investigated the effect of temperature on the time scale associated with the load shedding during the dwell cycles. They argued that the rapid stress relaxation at elevated temperatures leads to the loss of load shedding behavior above 200°C. In this paper, it is argued that the reduction of plastic anisotropy of α -Titanium might be the underlying cause of the loss of dwell effect at temperatures above 200°C.

Motivated by the observation that fatigue crack nucleation is considerably influenced by the crystallographic and morphological features of the microstructure, an experimentally-validated microstructure-dependent crack nucleation model has been developed by Anahid *et al.*^{18,19} to predict the microstructural location and cycles to crack nucleation for Ti alloys under dwell loading. The criterion is based on the development of stresses in the hard grain and the accumulation of dislocations in the soft grain near the grain boundary adjacent to the hard grain. Hierarchical models of deformation and crack nucleation have been initiated by Ghosh and Anahid^{20,21}, taking into account the effects of the microstructural features such as grain size, crystallographic orientation, misorientation and micro-texture.

In the present work, the crack nucleation model described in Refs. [18,19] is employed to study three important aspects controlling the dwell fatigue nucleation of Ti alloys. These include:

- (i) investigation of the effect of mechanical loading profile, viz. dwell time on crack nucleation;
- (ii) investigation of microstructure crystallographic features, e.g. grain-to-grain crystallographic misorientation on fatigue life; and
- (iii) investigation of thermal loading on the fatigue life of components.

Two Ti alloys, viz. Ti-7Al (Ti-7) and Ti-6Al-2Sn-4Zr-2Mo (Ti-6242), are modeled in this paper under dwell fatigue loading. The predictive capability of the model is compared with established experimental observations. Parametric studies provide new insights into the role of thermo-mechanical environment on dwell fatigue crack nucleation. In section 2, the crystal plasticity constitutive model along with some considerations for capturing thermal effects in the framework of CP is explained. This section concludes with an introduction to a stabilized locking-free crystal plasticity element formulation. The crack nucleation model is outlined in section 3. The predictive capability of this model is demonstrated in section 4 followed by concluding remarks in section 5.

2. Crystal Plasticity Finite Element (CPFE) Model

The alloy Ti-7 is a near- α alloy with an *hcp* crystalline structure, whereas Ti-6242 has a biphasic microstructure consisting of equiaxed primary α grains of *hcp* structure and transformed- β grains with alternating laths of α (*hcp*) and β (*bcc*) structures. The microstructure of Ti-6242

has been described in an earlier work ⁷. This microstructure consists of 70% primary α grains and 30% transformed β grains. Within the transformed β grains, α and β laths are observed to have volume fractions of 88% and 12% respectively. To predict material response, it is important to represent relevant morphological and crystallographic features of the microstructure, such as grain size distribution, orientation distribution and misorientation distribution, in the 3D reconstructed virtual microstructures. The DREAM.3D software ²², based on methods described in Refs. [23,24] has been used to reconstruct statistically equivalent 3D microstructures for both Ti-7 and Ti-6242 alloys as shown in Fig 1. These microstructures are discretized linear constant strain tetrahedral (TET4) elements using Simmetrix® software²⁵.

Plasticity in Ti alloys is primarily attributed to dislocation slip, where dislocations are inhomogeneously distributed into planar arrays due to short range ordering of Ti and Al atoms ²⁶. Twinning is another deformation mechanism contributing to plasticity in *hcp* metals which is observed at low temperatures and high strain rate loading. Deformation twinning has been observed in unalloyed Ti at all temperatures below 500°C ²⁷. However, alloying Ti with Al inhibits twinning such that titanium alloyed with %6 Al does not twin even at temperatures as low as 100 K ^{28,29}. These data show that twinning is not a major deformation mechanism for the problem of interest and need not be accounted for in the constitutive model. In this section, the experimentally-validated size-dependent rate sensitive crystal plasticity constitutive model developed in Refs. [6,7,14,15,30] is briefly introduced. This is followed by a short discussion on temperature effects.

2.1. Crystal plasticity constitutive model

A crystal plasticity constitutive model for finite strain deformation of Ti alloys under general non-isothermal conditions is presented in this section. This model is non-local due to the incorporation of geometrically necessary dislocations (GNDs) which renders the model size-dependent. As illustrated in Fig 2, the total deformation gradient \mathbf{F} is multiplicatively decomposed of into elastic \mathbf{F}^e , thermal \mathbf{F}^θ and inelastic \mathbf{F}^p components as

$$\mathbf{F} = \mathbf{F}^e \mathbf{F}^\theta \mathbf{F}^p \quad (1)$$

where \mathbf{F}^e accounts for elastic stretching and rigid body rotations. \mathbf{F}^θ denotes the deformation of crystal lattice due to thermal changes and evolves as ³¹,

$$\dot{\mathbf{F}}^\theta = \dot{\theta} \mathbf{a} \mathbf{F}^\theta \quad (2)$$

where θ is the temperature and \mathbf{a} is a diagonal tensor with respect to principal crystallographic coordinate system containing thermal expansion coefficients along the principal crystallographic directions. \mathbf{F}^p represents isochoric plastic deformation ($\det \mathbf{F}^p = 1$) where crystal lattice is neither distorted nor rotated. Using the kinematics of dislocation glide, the rate of evolution of \mathbf{F}^p could be expressed in terms of slip rate $\dot{\gamma}^\alpha$ as ³²:

$$\mathbf{L}^p = \dot{\mathbf{F}}^p \mathbf{F}^{p^{-1}} = \sum_{\alpha=1}^{n_{\text{slip}}} \dot{\gamma}^\alpha \mathbf{m}_0^\alpha \otimes \mathbf{n}_0^\alpha \quad (3)$$

in which \mathbf{L}^p is the plastic velocity gradient in the intermediate configuration, n_{slip} corresponds to number of slip systems and \mathbf{m}_0^α and \mathbf{n}_0^α are respectively slip direction and slip plane normal for slip system α in the reference configuration.

The constitutive equation in terms of second Piola-Kirchhoff stress \mathbf{S} and elastic Green-Lagrange strain tensor $\mathbf{E}^e = \frac{1}{2}(\mathbf{F}^{e^T} \mathbf{F}^e - \mathbf{I})$ in the thermally-expanded configuration is expressed as:

$$\mathbf{S} = \mathbf{C}(\theta) : \mathbf{E}^e \quad (4)$$

\mathbf{C} is the temperature-dependent fourth order anisotropic elasticity tensor.

The plastic slip rate has a power-law dependence on resolved shear stress τ^α , given as

$$\dot{\gamma}^\alpha = \dot{\gamma}^\alpha \left| \frac{\tau^\alpha - \chi^\alpha - \tau_{GP}^\alpha}{g^\alpha + \tau_{GF}^\alpha} \right|^{\frac{1}{m}} \text{sign}(\tau^\alpha - \chi^\alpha - \tau_{GP}^\alpha) \quad (5)$$

Here m and $\dot{\gamma}^\alpha$ are respectively the material rate sensitivity parameter and reference plastic shearing rate. χ^α is the back-stress which accounts for kinematic hardening in cyclic deformation and g^α is the slip system resistance due to evolution of statistically stored dislocations (SSDs) which correspond to homogeneous plastic deformation. Effect of grain size on initial slip system resistance has been considered and incorporated through a Hall-Petch type relationship^{14,15}. Besides SSDs, geometrically necessary dislocations (GNDs), which have a non-zero cumulative Burgers vector are also present due to incompatibility of plastic strain near grain boundaries. GNDs contribute to the slip system resistances by providing short and long range stresses³³, given as:

$$\tau_{GF}^\alpha = \frac{Q^\alpha}{c_2^\alpha b^\alpha} \sqrt{\rho_{GF}^\alpha} \quad , \quad \tau_{GP}^\alpha = c_1^\alpha G^\alpha b^\alpha \sqrt{\rho_{GP}^\alpha} \quad (6)$$

in which c_1^α and c_2^α are material constants, G^α , Q^α and b^α are respectively shear modulus, activation energy and Burgers vector for slip system α . ρ_{GP}^α are ρ_{GF}^α respectively GND components parallel and normal to slip plane α , calculated as:

$$\rho_{GP}^\alpha = \sum_{\beta=1}^{n_{\text{slip}}} \chi^{\alpha\beta} \left[\left| \rho_{GNDs}^\beta \sin(\mathbf{n}_0^\alpha, \mathbf{m}_0^\beta) \right| + \left| \rho_{GNDet}^\beta \sin(\mathbf{n}_0^\alpha, \mathbf{t}_0^\beta) \right| + \left| \rho_{GNDen}^\beta \sin(\mathbf{n}_0^\alpha, \mathbf{n}_0^\beta) \right| \right] \quad (7a)$$

$$\rho_{GF}^\alpha = \sum_{\beta=1}^{n_{\text{slip}}} \chi^{\alpha\beta} \left[\left| \rho_{GNDs}^\beta \cos(\mathbf{n}_0^\alpha, \mathbf{m}_0^\beta) \right| + \left| \rho_{GNDet}^\beta \cos(\mathbf{n}_0^\alpha, \mathbf{t}_0^\beta) \right| + \left| \rho_{GNDen}^\beta \cos(\mathbf{n}_0^\alpha, \mathbf{n}_0^\beta) \right| \right] \quad (7b)$$

where $\mathbf{t}_0^\beta = \mathbf{m}_0^\beta \times \mathbf{n}_0^\alpha$. ρ_{GNDs}^β , ρ_{GNDen}^β and ρ_{GNDet}^β are the vectorial components of GND density with Burgers vector parallel to \mathbf{m}_0^β . ρ_{GNDet}^β and ρ_{GNDen}^β are the edge components of GND density on slip system β with dislocation tangent line parallel to \mathbf{n}_0^α and \mathbf{t}_0^β , respectively. ρ_{GNDs}^β is the screw counterpart with dislocation tangent line parallel to \mathbf{m}_0^β . $\chi^{\alpha\beta}$ is the interaction matrix between slip systems α and β , taken as unity in this study. In order to calculate GND densities on different slip systems, it is necessary to evaluate Nye's dislocation tensor

$$\mathbf{\Lambda} = \sum_{\alpha=1}^{n_{\text{slip}}} b^\alpha \left(\rho_{GNDs}^\alpha \mathbf{m}_0^\alpha \otimes \mathbf{m}_0^\alpha + \rho_{GNDen}^\alpha \mathbf{m}_0^\alpha \otimes \mathbf{n}_0^\alpha + \rho_{GNDet}^\alpha \mathbf{m}_0^\alpha \otimes \mathbf{t}_0^\alpha \right) = \nabla^T \times \mathbf{F}^p \quad (8)$$

There are in general $3 \times n_{\text{slip}}$ unknown GND densities, which corresponds to 90 for *hcp* crystals. Of these, however, there exist only 63 independent densities including 9 ρ_{GNDs}^α s, 24 ρ_{GNDet}^α s and 30 ρ_{GNDen}^α s. Eq. (8) could be rewritten as

$$\{\mathbf{\Lambda}\} = \mathbf{A}\{\rho_{GND}\} \quad (9)$$

where $\{\mathbf{\Lambda}\}$ is 9×1 vectorial representation of the Nye tensor, \mathbf{A} is a 9×63 matrix containing the basis vectors and $\{\rho_{GND}\}$ is a 63×1 vector containing unknown GND densities. Eq. (9) is an underdetermined system of equations. An L2 minimization approach has been proposed by Arsenlis and Parks³⁴ to solve Eq. (9) to obtain dislocation densities as:

$$\{\rho_{GND}\} = (\mathbf{A}^T \mathbf{A})^{-1} \mathbf{A}^T \{\mathbf{\Lambda}\} \quad (10)$$

Considering GNDs renders the constitutive model non-local and size-dependent. The material CP constants for each constituent phase and individual slip systems in this model have been experimentally calibrated and validated by Deka *et al.*⁷ and Venkatramani *et al.*^{14,30} against a large set of experiments including different constant strain-rate tests and creep tests under different load levels.

2.2. Temperature effects

Temperature changes play a critical role in mechanical behavior of Ti alloys by affecting both elastic and plastic properties. In order to capture the effects of temperature changes in the framework of crystal plasticity, it is required to consider variation of both elasticity and plasticity-related constants with temperature. In Ti-6242, α titanium with an *hcp* lattice-parameter ratio $c/a = 1.59$ shows transverse isotropic elastic response, whereas β Ti shows cubic symmetry due to the *bcc* crystalline lattice. The anisotropic elasticity tensor in the Voigt notation may be written as

$$[C_{ij}] = \begin{bmatrix} C_{11} & C_{12} & C_{13} & 0 & 0 & 0 \\ C_{21} & C_{22} & C_{23} & 0 & 0 & 0 \\ & & C_{33} & 0 & 0 & 0 \\ & & & C_{44} & 0 & 0 \\ & & & & C_{55} & 0 \\ & & & & & C_{66} \end{bmatrix} \quad (11)$$

For α Ti, there are only five independent elastic constants, viz. $C_{11} = C_{22}$, $C_{12} = C_{23}$, C_{33} , $C_{55} = C_{66}$ and $C_{44} = (C_{11} - C_{12})/2$. In order to represent anisotropy for β Ti, only three independent elastic constants are required, viz. $C_{11} = C_{22} = C_{33}$, $C_{12} = C_{13} = C_{23}$ and $C_{44} = C_{55} = C_{66}$. Elastic constants for α and β phases have been calibrated at room temperature by Deka *et al.*⁷. Experimental measurements for elastic constants of α Ti show that they decrease almost linearly with increasing the temperature, but with different slopes. The experimental results by Ogi *et al.*³⁵ are used to obtain the linear slopes for different elastic constants. Fig 3 depicts the variation of different principal elastic constants with temperature. The temperature dependence of Young's modulus for polycrystals is also plotted in this figure, which also varies linearly with temperature. The linear slopes corresponding to the reduction of elastic constants with temperature increase are given in Table 1. Due to lack of experimental results on variation of elastic constants for β -Ti in the temperature range of interest, the values of slopes are approximated by averaging the α -Ti slopes separately for the volumetric (C_{11}, C_{22}, C_{33}), normal-dilatational (C_{13}, C_{23}, C_{12}) and shear (C_{44}, C_{55}, C_{66}) elasticity coefficients, yielding respectively 39 MPa/K, 8.9 MPa/K and 21.9 MPa/K for the β phase. The error introduced to the grain-scale variation of the stress fields, due to this uncertainty, is expected to be small, since the overall volume fraction of the β phase within the polycrystal is about 4%. The decrease in the Young's modulus of the simulated polycrystalline Ti-6242 model is 18 GPa over the temperature range of 300 K – 650 K (E_{poly} shown in Figure 3), which is in good agreement with the experimentally measured decrease (~20 GPa over 300K – 650K) for polycrystalline Ti-6242 in the same (bi-modal) microstructural condition³⁶.

Temperature changes also significantly influence the plastic behavior due to thermally-activated glide of dislocations. As temperature increases, the rate of successful thermal activation attempts is boosted up and consequently plastic flow is enhanced. In other words, the resistance to plastic flow reduces as temperature rises. In the crystal plasticity framework, each slip system has a slip resistance assigned to it. The experimental results reported by Williams *et al.*²⁹ for α Ti alloys are used here to derive the initial slip resistances for different *hcp* slip systems as a function temperature. The resistances reported by Williams *et al.*²⁹ are shifted such that at room temperature they match the slip resistances reported in Deka *et al.*⁷. Fig 4 shows the variation of slip resistances with temperature. The initial resistances are expressed in terms of temperature as

$$g^\alpha(\theta) = g_0^\alpha - \hat{g}^\alpha \left(1 - \exp \left(-\frac{\theta - \theta_{\text{ref}}^\alpha}{\hat{\theta}^\alpha} \right) \right) \quad (12)$$

where g_0^α is the initial grain size-dependent slip system resistances calibrated at room temperature in Deka *et al.*⁷ and \hat{g}^α , θ_{ref}^α and $\hat{\theta}^\alpha$ are calibrated constants, given in Table 2. In this form, \hat{g}^α represents the part of the slip resistance that can be overcome with thermal activation. The test data of Williams *et al.*²⁹ for $\langle c+a \rangle$ slip shows a transition to a steep softening response above 400K. To represent this transition, a linear variation is assumed from room temperature up to 400K given by $g^\alpha(\theta) = g_0^\alpha - (\theta - 300) \times 0.95 \text{ MPa}$ and an exponential decrease above 400K given by

$$g^\alpha(\theta) = g^\alpha_{400K} - \hat{g}^\alpha \left(1 - \exp \left(-\frac{\theta - \theta_{ref}^\alpha}{\hat{\theta}^\alpha} \right) \right) \text{ with } \theta_{ref}^\alpha = 400K$$

The difference in slip system resistances decrease as temperature increases. This implies that the material becomes more plastically isotropic with increasing temperature. Due to lack of experimental observation on temperature dependence of β -Ti slip system resistances in the literature, it is assumed that their dependence on temperature is similar to those of *hcp* basal systems.

2.3. Stabilization of constant strain tetrahedral elements for CPFE modeling

Modeling material behavior and predicting localized phenomenon such as fatigue crack nucleation requires accurate calculation of local material state variables like stresses and kinematic variables. This can only be achieved by using an appropriate material constitutive law and a robust computational framework that provided adequate resolution with accuracy. Given the requirement of mesh conformity to the computational domain, the complexity of polycrystalline microstructures often requires discretization of polycrystalline aggregates into tetrahedral elements. Linear constant strain tetrahedral elements (TET4) are preferred for CPFE simulations due to their capability in conforming to the complex geometries in the microstructure and inherent simplicity in the element formulation. However, these elements have been shown to suffer from volumetric locking resulting in spuriously increased stresses as the material approaches the incompressibility limit^{37,38}. This locking induced instability can adversely affect the results of CPFE simulations in the presence of isochoric plastic deformation. The effect of volumetric locking on local stress field in a CPFE simulation of polycrystalline Ti-7 alloy is shown in Fig. 5. The simulation is conducted for a constant strain-rate tensile test with $\dot{\varepsilon} = 9 \times 10^{-5} \text{ s}^{-1}$ along the global z-axis. The instability on the form of spurious elemental hydrostatic stress on the YZ face of the microstructure after 500 s are shown in Fig 5, resulting in a checker-board pattern.

A method of stabilizing TET4 elements and relieving volumetric locking for efficient and accurate CPFE simulations has been proposed in a recent paper by the authors³⁹. In this model, the **F**-bar-patch method⁴⁰ has been incorporated into the CPFE framework. The **F**-bar patch method modifies the deformation gradient for stress tensor calculations, such that incompressibility is enforced over a patch of elements rather than on individual elements. This requires that elements in the mesh be assigned to non-overlapping patches. If P denotes a set of elements forming a patch, the modified deformation gradient for element $K \in P$ at time t is

calculated as $\bar{\mathbf{F}}_K = \left[\frac{\Omega_{patch}^t}{\Omega_{patch}^0 \det \mathbf{F}_K} \right]^{\frac{1}{3}} \mathbf{F}_K$ where \mathbf{F}_K is deformation gradient of element K and Ω_{patch}^t and Ω_{patch}^0 are respectively the current and undeformed volumes of the patch P . The modified deformation gradient $\bar{\mathbf{F}}_K$ is then used to solve constitutive law at the integration point of the element.

3. Microstructural Crack Nucleation Model

Dislocation slip in *hcp* materials is highly orientation-dependent, as the critical resolved shear stress (CRSS) for hard slip mode, $\langle c+a \rangle$ - type slip on pyramidal planes, is approximately 3–6 times higher than the CRSS for easy slip modes, $\langle a \rangle$ - type slip on basal and prism planes⁴¹. During the hold period in dwell loading, grains which are properly oriented for $\langle a \rangle$ - type slip, soft grains undergo significant time-dependent plastic deformation, whereas the contiguous hard grains, which are less favorably oriented for $\langle a \rangle$ - type slip, experience large local stress concentrations near the shared coherent grain boundaries from considerations of compatibility across the grain boundaries^{18,19}. This phenomenon leads to stress re-distribution or load shedding that is considered to be responsible for early crack nucleation for dwell loading. Figs 6a and 6b show a soft grain 1 with a high basal Schmid factor (SF) and a moderate prism SF and a neighboring hard grain 2 with low basal and prism SFs. As grain 1 is favorably oriented for dislocation slip on basal plane, it plastically deforms and causes load shedding on the neighboring grain 2 as shown in Fig 6c. The distribution of norm of Nye tensor, which is a measure for dislocation activity in the microstructure, is depicted in Fig 6d. A higher value is observed in the soft grains close to neighboring hard grain. Thus the fatigue crack nucleation process in this case is dependent on both morphological and crystallographic features of the microstructure such as grain size distribution, grain orientation distribution, misorientation distribution and microtexture.

A microstructure-based crack nucleation model for polycrystalline Ti alloys under dwell fatigue loading has been proposed and experimentally validated by Anahid *et al.*^{18,19}. This model introduces crack nucleation in the hard grain due to plasticity in the adjacent soft grain. It encompasses the following characteristics:

- (i) Wedge micro-crack nucleates in the hard grain due to dislocation pileup in soft grain at the shared grain boundary;
- (ii) Crack opening displacement corresponds to the closure failure along a Burger's circuit surrounding the piled-up dislocations;
- (iii) Traction across the micro-crack tip in hard grain opens up the crack.

The edge dislocation, defined as an extra half plane of atoms wedged between two perfect lattice planes, is equivalent to a micro-crack with an opening displacement of one lattice constant. The opening displacement increases as deformation continues and more dislocations pile up at the grain boundary. In this section, this model is briefly introduced with some improvements.

Consider a soft-hard grain combination as illustrated in Fig 7. The Nye dislocation tensor is used to measure the dislocation pile-up in the soft grain near the grain boundary. At point P, the closure failure of a Burgers circuit due to dislocations piercing an arbitrary plane with normal \mathbf{n} in the soft grain could be calculated as:

$$\mathbf{B}_{CF} = \int \mathbf{\Lambda} \cdot \mathbf{n} dA \quad (13)$$

Since dislocations are distributed throughout the grain, the integration in Eq. (13) is calculated over the entire grain. For a grain discretized into elements, this integration is effectively calculated over the soft grain as:

$$\mathbf{B}_{CF} = \sum_{e=1}^{N_e^{cut}} w_e A_e \mathbf{\Lambda}_e \cdot \mathbf{n} \quad (14)$$

Here N_e^{cut} is the total number of elements in the grain, which are cut by a plane with normal \mathbf{n} containing point P. A_e is the surface area of the element cut by the plane and approximated as $A_e = \pi R_e^2$ in which R_e is the radius of a sphere which has the same volume as the element. $w_e = \exp(-r_e^2/4r_{max}^2)$ is a weighting parameter signifying that the effects of dislocations on the crack opening displacement diminishes as the distance of the element centroid to point P, r_e , increases. r_{max} is distance of the furthest element centroid cut by the plane to point P.

Depending on the type of dislocations piercing the surface, the Burger's circuit closure failure can make any arbitrary angle with respect to the surface. For wedge-like cracks, the closure failure component lying in the surface contributes to crack opening displacement. The crack opening displacement vector is hence calculated as:

$$\mathbf{B} = \mathbf{B}_{CF} - (\mathbf{B}_{CF} \cdot \mathbf{n}) \mathbf{n} \quad (15)$$

The crack opening displacement and crack surface normal are respectively given as:

$$B = \|\mathbf{B}\| \quad , \quad \mathbf{n}^b = \frac{\mathbf{B}}{B} \quad (16)$$

The equilibrium length of crack may be calculated as $c = GB^2/8\pi(1-\nu)\gamma_s$ where ν and γ_s correspond respectively to Poisson's ratio and surface energy⁴². The stress state in the hard grain helps the crack to open up. It is assumed^{18,19} that cracks nucleate when the mixed-mode intensity factor $K_{mix} = \sqrt{K_n^2 + \beta K_t^2}$ is larger than a critical value K_c , i.e.

$$K_{mix} \geq K_c \quad (17)$$

β is the ratio of shear to normal fracture toughness and is set to 0.7071 in this study. Normal and shear intensity factors are respectively calculated as:

$$K_n = \langle T_n \rangle \sqrt{\pi c} \quad , \quad K_t = T_t \sqrt{\pi c} \quad (18)$$

in which $T_n = \mathbf{n}^b \cdot (\boldsymbol{\sigma} \cdot \mathbf{n}^b)$ and T_t are respectively the normal and in-plane components of traction vector on the crack surface. The McCauley bracket is used for normal traction to signify that only tensile normal stress component aids the crack growth. The crack nucleation relation is derived from Eq. (17) as:

$$R \geq R_c \quad \text{where } R = \sqrt{c(\langle T_n \rangle^2 + \beta T_t^2)} \text{ and } R_c = K_c / \sqrt{\pi} \quad (19)$$

This model is non-local in the sense that crack nucleates in the hard grain due to local stress field in the hard grain, and the dislocation pile-up in the adjacent soft grain at the hard-soft boundary.

3.1. Implementation of the crack nucleation model

In order to determine the number of cycles to the first crack nucleation event N_{nucl} , every grain pair is examined in the post-processing stage of FE analysis. The maximum value R in the microstructure is obtained as follows:

- i. Each grain-pair in the microstructure is probed, and the two constituent grains are labeled as hard-soft grain pair based on the effective plastic strain.
- ii. The TET4 elements in the hard grain, which have a triangular face on the shared boundary are determined. The nodes of these elements are the common nodes between the pair. The crack nucleation criterion in Eq. (19) is checked for these common nodes.
- iii. The highest stress intensity factor is calculated for each common node by the following steps.
 - a. Sample the orientation space for \mathbf{n} and determine the elements in the soft grain cut by a plane with normal \mathbf{n} .
 - b. Using Eqs. (14-16), calculate the normal to the crack surface \mathbf{n}^b and crack opening displacement B . Normal and in-plane components of traction are then easily obtained.
 - c. Stress intensity factor is calculated for every sample \mathbf{n} . The highest K_{mix} value corresponds to the critical \mathbf{n} and \mathbf{n}^b .
- iv. As cracks nucleate over a finite area, the calculated nodal stress intensity factors at common nodes in the pair are spatially regularized using a simple Gaussian function introduced for damage by Bažant and Pijaudier-Cabot ⁴³. This will lead to a much better convergence of stress intensity factor on mesh refinement.

Following the above-mentioned steps, the maximum value R_{max} in the entire microstructure is obtained. The cycles/time-to-crack nucleation corresponds to the time when R_{max} exceeds the critical value, R_c . Following steps delineated in the earlier study¹⁹, the critical value is obtained to be $R_c = 731.4 \text{ MPa}\sqrt{\mu\text{m}}$. This determination involves an improved method of calculating non-local closure failure in the Burgers circuit \mathbf{B}_{CF} using the stabilized locking-free elements.

4. Numerical Results

Numerical examples are discussed in this section to study the effects of three aspects on crack nucleation of Ti alloys, viz. (i) dwell time in a dwell loading cycle, (ii) temperature in thermo-mechanical loading microtexture in polycrystalline aggregates and (iii) microtexture in polycrystalline aggregates. The dwell time analysis signifies the effects of loading profile on fatigue life, whereas the study on the effects of microtexture aims at understanding the importance of underlying microstructure on life. For dwell fatigue loading simulations, the tractions are applied along the global z-axis and minimum displacement boundary conditions are applied to

suppress rigid body translation and rotation. Each dwell loading cycle consists of 1 second of loading/unloading and 120 seconds of dwell hold, unless mentioned otherwise. The ratio of minimum to maximum applied traction in each cycle is 0.1.

4.1. Dependence of N_{nucl} on dwell time

To study the effect of dwell time on the number of cycles to crack nucleation, simulations are conducted for the Ti-7 polycrystals under different dwell loading cycles with hold periods of 15, 30, 60 and 120 seconds. Each loading cycle has a maximum applied traction of 572 MPa corresponding to ~95% of the macroscopic yield stress. The number of cycles to crack nucleation is plotted in Fig 8 for different dwell periods. It is observed that N_{nucl} decreases dramatically as dwell time is increased due to the accumulation of time-dependent local strain during dwell periods and thus stronger load shedding mechanism. The simulated dependence of N_{nucl} on dwell time is in good agreement with the experimental data on IMI834 reported by Bache¹², also shown in Fig 8 for comparison. The results are also consistent with other experimental observations on the adverse effect of dwell period on fatigue life of Ti alloys, reported by Bache² and Sinha *et al.*⁴⁴. The ratio of N_{nucl} for 15 seconds of dwell period to the one for 120 second of dwell period is approximately 9. Results in Fig 8 suggest that this ratio would even get larger with further reduction of dwell period, i.e. approaching perfect cyclic loading conditions. This is qualitatively in agreement with experimental results reported by Sinha *et al.*⁴⁴, where dwell debit is reported to be 18 for applied stress of 95.5% yield stress.

4.2. Effect of temperature in thermal loading on crack nucleation

Titanium alloys are often exposed to both thermal and mechanical loading in their applications. In this section, the influence of temperature on load shedding and dwell crack nucleation is investigated to identify the thermo-mechanical conditions that adversely influence fatigue behavior.

4.2.1. Loss of load shedding at elevated temperatures

Experimental observations have indicated the significance of dwell debit at temperatures below 200°C^{2,12,44}. However, it has been reported^{44,45} that dwell debit diminishes at temperatures above 200°C. The loss of dwell sensitivity at elevated temperatures has yet remained elusive. To study the micro-mechanical basis of this dwell sensitivity transition, several isothermal dwell fatigue loading simulations are conducted for the Ti-6242 alloy at temperatures ranging from 300 K (room temperature, 23°C) up to 600 K (327°C) in 100 K increments. As the yield stress drops with higher temperatures, the dwell load for each test temperature is set to 90% of the respective macroscopic yield stress for the sake of coherency in comparisons. The evolution of local stress component σ_{zz} after 1, 250 and 500 dwell load cycles is compared for ambient temperatures of 300 K and 600 K in Fig 9b and c. Local stresses are extracted along the line AB shown in Fig 9a. Defining θ_c as the angle between the crystal $\langle c \rangle$ -axis and the loading direction, grains with $\cos(\theta_c)$ close to 1 correspond to the hard grains with negligible slip activity on basal and/or prismatic systems. Time-dependent concentration of stress in the hard grains, shown in Fig 9,

manifests that the load shedding mechanism is in effect at 300 K, while it clearly diminishes at 600 K.

To quantitatively evaluate the effect of the load shedding phenomenon at different temperatures, a *load shedding factor* is defined as the maximum local stress in a hard grain normalized by the applied external stress during the dwell period. Load shedding factors in the critical hard grain is plotted in Fig 10 for the different temperatures between 300 K and 600 K. At and beyond 600 K, the level of time-dependent load shedding becomes insignificant due to the substantial decrease in plastic strength of the *hcp* crystal along the [0001] direction (hard direction). In essence, plastic anisotropy of the *hcp* titanium, responsible for heterogeneous local creep and load shedding, is significantly reduced at elevated temperatures. This is evident from single crystal experiments conducted on Ti-Al alloys by Williams *et al.*²⁹, as shown in Fig 4. Slip resistances of the $\langle c+a \rangle$ –pyramidal slip systems are marked by a dramatic decrease above 400 K. The ratio of the critical resolved shear stress for the $\langle c+a \rangle$ –slip systems to the one for $\langle a \rangle$ –basal system decreases from ~ 1.8 to ~ 1.2 from room temperature to 600 K. Results in the present simulations suggest that the diminution of load shedding as the time-dependent component of the fatigue damage accumulation might be responsible for the loss of dwell debit observed at elevated temperatures.

4.2.2. Effect of anisotropic thermal expansion on normal basal stresses

Several studies based on ab-initio calculations and experimental observations have reported that *hcp* Ti crystals exhibit anisotropic thermal expansion over a wide range of temperatures^{46,47}. In this work for Ti-6242, the thermal expansion coefficients for α phase along the principal crystallographic coordinate system are taken as $\alpha_{\langle a \rangle} = 1.8 \times 10^{-5} \text{ K}^{-1}$ and $\alpha_{\langle c \rangle} = 1.1 \times 10^{-5} \text{ K}^{-1}$ ⁴⁷. The thermal expansion for β phase is isotropic with a thermal coefficient expansion of $\alpha = 0.9 \times 10^{-5} \text{ K}^{-1}$ ⁴⁸.

For a wide range of loading conditions, experimental observations suggest that both crack nucleation and short crack propagation in Ti alloys predominantly occur along the basal plane^{11,49–51}. Therefore, the stress component normal to the crystallographic basal plane is highly relevant to its fatigue response. Since the thermal expansion along [0001] direction is lower than the in-plane basal expansion, the tensile normal stresses are induced on the basal plane due to thermal loading. This may play an important role for crack nucleation and propagation in Ti alloys.

For an otherwise thermally-isotropic material, which is free of external constraints, no thermo-elastic stresses would develop under a spatially uniform increase of temperature. However, due to the anisotropic thermal expansion of *hcp* titanium, a uniform increase of temperature within the polycrystalline aggregate induces thermal stresses due to the incompatibility of anisotropic thermal strains. To study the potential impact of grain-scale anisotropy-induced thermal stresses due to temperature variations, thermo-elasto-plastic simulations are carried out for both Ti-7 and Ti-6242 alloys under a thermal loading profile. The load profile is made to approximately correspond to flight conditions for an aircraft. The thermal cycle has a spatially-uniform increase

of temperature from 300 K to 750 K over 10 minutes, followed by a 1 hour temperature hold at 750 K and eventually a 10 minute long cool-down to room temperature. The minimum boundary conditions are applied to the polycrystalline model to suppress rigid body motions. Fig 11 shows the tensile normal traction developed on the basal planes after 50 minutes on representative cross-sections. Only tensile tractions are of interest in this paper as they may facilitate mode I crack opening on basal planes. For both Ti-7 and Ti-6242 microstructures, the maximum local values of tensile normal stress on basal planes are observed to be as high as 700 MPa for this temperature increase of 450 K. Resolved shear stresses for basal and prismatic slip are negligibly small, and do not induce considerable micro-plasticity. The stress concentrations typically occurred at the grain boundaries with high misorientation. Grain-averaged normal basal stresses are as high as 350 MPa and they vary with the degree of misorientation of each individual grain with its neighbors. The range and distribution of the magnitudes of tensile normal stresses on the basal planes are very similar for both materials, suggesting that both α - and near- α classes of Ti alloys may be affected by this mechanism, as long as the thermal expansion anisotropy of the α -phase is significant.

A parametric study is conducted to quantify the effects of $\langle c \rangle$ -axis misorientation of neighboring grains, on the basal normal stresses developed due to thermal loading. The two-grain system illustrated in Fig 12a is modeled for a 200 second period, over which the temperature linearly rises from 300 K to 750 K. The $\langle c \rangle$ -axis of the inner grain is rotated with respect to the outer grain to generate a range of misorientations. A $\langle c \rangle$ -axis misorientation index of grain a with its neighboring grains is defined as $MI = 1 - \sum_b \frac{A_{ab}}{A_a} |\mathbf{c}_a \cdot \mathbf{c}_b|$ where \mathbf{c}_a and A_a respectively denote $\langle c \rangle$ -axis and surface area of grain a and A_{ab} is the common surface area between grains a and b . The summation is done over all grains neighboring grain a . It is evident that MI is zero if the $\langle c \rangle$ -axis of the two neighboring grains are aligned parallel to each other. The maximum and grain-averaged normal basal stresses induced in the inner grain as a function MI are plotted in Fig 12b. It is observed that the system will not experience any stress if $\langle c \rangle$ -axes of the two grains are parallel to one another. However as MI increases, higher stresses develop on the basal plane of the inner grain, which can potentially assist crack opening on these planes.

To evaluate the effect of the crystallographic texture on normal basal stresses within a polycrystalline sample, the response for a strong basal texture, typically seen in rolled titanium, is compared to the reference case of the Ti-6242 sample whose texture is based on a forged Ti-6242 specimen⁷. The rolled basal texture is synthetically generated and its pole figure is shown in Fig 13a, in addition to that of the forged Ti-6242. The same polycrystalline grain structure is used for both textures. The grain-averaged normal basal stresses after 50 minutes during thermal hold is plotted in Fig 13b for the two textures. It is seen that grains with high MI experience higher basal stresses. Since the misorientation is less on the rolled texture, anisotropy-induced thermal stresses are smaller. These results suggest that rolled Ti alloys will experience lower thermal stresses in comparison with the forged one in environments prone to temperature changes.

4.3. Influence of microtexture on dwell crack initiation

Many studies have been conducted for understanding the dependence of fatigue life on microstructural properties such as the grain-size, micro- and macro-texture, α -grain volume

fraction, lamellae-size and prior- β grain size in multiphase near α and $\alpha + \beta$ alloys ^{11,52}. This section is aimed at illuminating the effects of microtexture on micro-plasticity, load shedding, dwell crack nucleation and fatigue life. The α grains that nucleate from the same prior β grain during cool-down obtain similar crystallographic orientations and form microtextured regions. The size and extent of these microtextured regions are effectively controlled by the size of the prior β grains and the thermo-mechanical processing above the β -transus temperature. It is documented in the literature that large microtextured regions, favorably oriented for easy basal or prismatic plastic slip, lead to early dwell fatigue failure by acting as a large soft grain. Representing microtextured regions as a single soft grain, it was shown by Venktaramani *et al.* ¹⁴ that the amount of stress concentration due to load shedding increases with the size of the soft region.

To study the effect of microtexture on dwell fatigue response, two polycrystalline models with the same morphology and orientations but different levels of microtexture are studied. The overall texture corresponding to the forged Ti-6242 microstructure, shown in Fig 1b, is adopted as starting data. Using an iterative algorithm the grain orientations are swapped between grain pairs to generate two misorientation distributions with low and high average misorientations. These two limiting cases of misorientation distribution, referred to as MS^{tex} and MS^{mis} , are shown in Fig 14a. MS^{tex} corresponds to a microstructure in which grains with similar orientations are clustered together to form microtextured regions. On the other hand, MS^{mis} corresponds to a microstructure in which grains with disparate orientations tend to neighbor each other, resulting in a microstructure devoid of microtexture. These two microstructures are depicted in Fig 14b.

Dwell fatigue simulations are conducted under 750 MPa corresponding to 90% macroscopic yield stress of the microstructure shown in Fig 1b. Investigation of both microtextured and highly misoriented microstructures reveal significant differences in their micro-plastic responses. Fig 15 shows the distribution of the local stress component σ_{zz} and the local plastic strain after 500 dwell cycles at representative cross-sections in both microstructures, along with the predicted location of the crack nucleation and crack plane in MS^{tex} . The response of MS^{tex} is characterized by: (i) significant plastic strain accumulation within the clusters of similarly oriented grains that are favorably oriented for plastic slip, (ii) confinement of plastic deformation to these microtextured regions and ending abruptly at the boundaries adjacent to hard grain clusters, and (iii) stress concentration due to load shedding occurring predominantly at boundaries of the hard microtextured regions. These features result in a dwell crack nucleation at the boundary of a hard microtextured region, neighboring a soft region as shown in Fig 15a. The highly misoriented microstructure MS^{mis} exhibits milder and less variable response of local plasticity and stress compared to the response of MS^{tex} . The lack of clustered soft grains and grain-scale alternation of plastic anisotropy results in a fiber-like strengthening effect, suppressing plastic strain accumulation in the grains as shown in Fig 16. Consequently, load shedding is less pronounced in this microstructure. Micro-plasticity accumulation are consistent with the experimental observations that microtextured regions facilitate plastic strain accumulation ¹¹. Such a difference in micro-plasticity between these two microstructures is interesting given that both MS^{mis} and MS^{tex} have the same grain morphology and texture.

The evolution of the crack nucleation parameter R for MS^{tex} and MS^{mis} is plotted in Fig 17 along with the pole figures of the forged Ti-6242 texture. The dwell crack nucleation model predicts an earlier crack nucleation for MS^{tex} . The soft grain predicted by the model as the initiation site for dwell fatigue crack is located at the boundary of a microtextured region with high prismatic Schmid factor adjacent to a hard grain, which is lies within a cluster of grains with low basal and prismatic Schmid factors.

A new set of orientations are generated synthetically, as shown in Fig 18a, to verify these results and confirm that the predicted effects of microtexture persist over different over different textures. The grain orientations are then re-assigned using the aforementioned iterative algorithm to obtain the two limiting cases. The same observations are made on the distribution of microplasticity and stress concentrations and the microtextured model was observed to be more critical in terms of crack nucleation as shown in Fig 18b.

5. Summary ad Conclusions

This paper develops a stabilized crystal plasticity finite element model, incorporating a rate sensitive size-dependent crystal plasticity constitutive law, to perform thermo-mechanical simulations for studying crack nucleation in polycrystalline Ti alloys. The simulations are used to comprehend factors that are responsible dwell fatigue crack nucleation in polycrystalline microstructures of these alloys. A crack nucleation model that has been developed by Anahid *et al.*^{18,19} is employed to predict crack nucleation in the polycrystalline microstructures.

Three important aspects regarding dwell fatigue crack nucleation are studied. These are respectively the cyclic load profile, temperature in thermo-mechanical loading, and local microstructural features. For the study on the cyclic loading profile, the effect of hold or dwell time on the number of cycles to crack nucleation is studied. The model predicts that as dwell time reduces and fatigue loading approaches a regular cyclic loading profile, the number of cycles to the first crack nucleation event increases. This is in agreement with experimental observations and signifies the adverse effects of dwell fatigue loading on the life of components. In the second study, the effect of temperature and thermo-mechanical loading on stress redistribution is studied, in light of the anisotropic thermal properties of Ti alloys. It is shown that thermal loading can induce tensile stresses on basal planes even under free expansion conditions due to the anisotropy of thermal expansion coefficients. These thermally-induced stresses are larger for grains with high misorientation with respect to their neighbors. Orientation-sensitive basal normal stresses can facilitate crack nucleation and early crack propagation in Ti alloys, and are important variables in a fatigue analysis. Moreover, the CPFE simulation results are able to reproduce the experimentally observed diminution of dwell effects at elevated temperatures. Within the framework of this model, this phenomenon is explained by the weakening of plastic anisotropy and correspondingly, suppression of time-dependent load shedding mechanism. To highlight the effects of microstructure on the life of Ti alloys under dwell fatigue loading, the influence of microtexture is investigated by simulating two models with high and low levels of microtexture. In agreement with experiments, the simulations predict that the microtextured regions are more critical in dwell fatigue. This is due to higher rate of accumulation of plastic strains and a stronger load shedding mechanism.

Acknowledgement

This work has been supported through a subcontract to JHU (sub-recipient) from the Ohio State University (main recipient) through a subaward No. 60038238 from an AFRL grant No. FA8650-13-2-2347 as a part of the AFRL Collaborative Center of Structural Sciences. The program managers of this grant are Dr. R. Penmetsa and Dr. R. Chona and the PI is Prof. J. McNamara. This support to JHU is gratefully acknowledged. It has also been partially supported by the Army Research Office through grant No. W911NF-12-1-0376 (Program Manager: Dr. A. Rubinstein). Computer use of the Hopkins High Performance Computing facilities is gratefully acknowledged.

References

1. Odegard, B. C. & Thompson, A. W. (1974). Low temperature creep of Ti-6 Al-4 V. *Metall. Trans.*, 5, 1207–1213.
2. Bache, M. (2003). A review of dwell sensitive fatigue in titanium alloys: the role of microstructure, texture and operating conditions. *Int. J. Fatigue*, 25, 1079–1087.
3. Kassner, M. E., Kosaka, Y. & Hall, J. S. (1999). Low-cycle dwell-time fatigue in Ti-6242. *Metall. Mater. Trans. A*, 30, 2383–2389.
4. Evans, W. J. & Bache, M. (1994). Dwell-sensitive fatigue under biaxial loads in the near-alpha titanium alloy IMI685. *Int. J. Fatigue*, 16, 443–452.
5. Sinha, V., Mills, M. J. & Williams, J. C. (2006). Crystallography of fracture facets in a near-alpha titanium alloy. *Metall. Mater. Trans. A*, 37, 2015–2026.
6. Hasija, V., Ghosh, S., Mills, M. J. & Joseph, D. S. (2003). Deformation and creep modeling in polycrystalline Ti-6Al alloys. *Acta Mater.*, 51, 4533–4549.
7. Deka, D., Joseph, D. S., Ghosh, S. & Mills, M. J. (2006). Crystal plasticity modeling of deformation and creep in polycrystalline Ti-6242. *Metall. Mater. Trans. A*, 37, 1371–1388.
8. Dunne, F. P. E., Rugg, D. & Walker, A. (2007). Lengthscale-dependent, elastically anisotropic, physically-based hcp crystal plasticity: Application to cold-dwell fatigue in Ti alloys. *Int. J. Plast.*, 23, 1061–1083.
9. Sinha, V., Spowart, J. E., Mills, M. J. & Williams, J. C. (2006). Observations on the faceted initiation site in the dwell-fatigue tested ti-6242 alloy: Crystallographic orientation and size effects. *Metall. Mater. Trans. A*, 37, 1507–1518.
10. Sinha, V., Mills, M. J. & Williams, J. C. (2007). Determination of crystallographic orientation of dwell-fatigue fracture facets in Ti-6242 alloy. *J. Mater. Sci.*, 42, 8334–8341.
11. Szczepanski, C. J., Jha, S. K., Larsen, J. M. & Jones, J. W. (2008). Microstructural Influences on Very-High-Cycle Fatigue-Crack Initiation in Ti-6246. *Metall. Mater. Trans. A*, 39, 2841–2851.
12. Bache, M. (1997). Dwell sensitive fatigue in a near alpha titanium alloy at ambient

temperature. *Int. J. Fatigue*, 19, 83–88.

- 13. Pilchak, A. L. & Williams, J. C. (2011). Observations of Facet Formation in Near- α Titanium and Comments on the Role of Hydrogen. *Metall. Mater. Trans. A*, 42, 1000–1027.
- 14. Venkatramani, G., Ghosh, S. & Mills, M. (2007). A size-dependent crystal plasticity finite-element model for creep and load shedding in polycrystalline titanium alloys. *Acta Mater.*, 55, 3971–3986.
- 15. Venkataramani, G., Kirane, K. & Ghosh, S. (2008). Microstructural parameters affecting creep induced load shedding in Ti-6242 by a size dependent crystal plasticity FE model. *Int. J. Plast.*, 24, 428–454.
- 16. Dunne, F. P. E., Walker, a. & Rugg, D. (2007). A systematic study of hcp crystal orientation and morphology effects in polycrystal deformation and fatigue. *Proc. R. Soc. A Math. Phys. Eng. Sci.*, 463, 1467–1489.
- 17. Zhang, Z., Cuddihy, M. A. & Dunne, F. P. E. (2015). On rate-dependent polycrystal deformation: the temperature sensitivity of cold dwell fatigue. *Proc. R. Soc. A Math. Phys. Eng. Sci.*, 471, 20150214.
- 18. Anahid, M., Chakraborty, P., Joseph, D. S. & Ghosh, S. (2009). Wavelet decomposed dual-time scale crystal plasticity FE model for analyzing cyclic deformation induced crack nucleation in polycrystals. *Model. Simul. Mater. Eng.*, 17, 064009.
- 19. Anahid, M., Samal, M. K. & Ghosh, S. (2011). Dwell fatigue crack nucleation model based on crystal plasticity finite element simulations of polycrystalline titanium alloys. *J. Mech. Phys. Solids*, 59, 2157–2176.
- 20. Ghosh, S. & Anahid, M. (2013). Homogenized constitutive and fatigue nucleation models from crystal plasticity FE simulations of Ti alloys, Part 1: Macroscopic anisotropic yield function. *Int. J. Plast.*, 47, 182–201.
- 21. Anahid, M. & Ghosh, S. Homogenized constitutive and fatigue nucleation models from crystal plasticity FE simulations of Ti alloys, Part 2: Macroscopic probabilistic crack nucleation model. *Int. J. Plast.* 48, 111–124 (2013).
- 22. Groeber, M. A. & Jackson, M. A. DREAM.3D: A Digital Representation Environment for the Analysis of Microstructure in 3D. *Integr. Mater. Manuf. Innov.* 3, 5 (2014).
- 23. Groeber, M., Ghosh, S., Uchic, M. D. & Dimiduk, D. M. (2008). A framework for automated analysis and simulation of 3D polycrystalline microstructures. Part 1: Statistical characterization. *Acta Mater.*, 56, 1257–1273.
- 24. Groeber, M., Ghosh, S., Uchic, M. D. & Dimiduk, D. M. (2008). A framework for automated analysis and simulation of 3D polycrystalline microstructures. Part 2: Synthetic structure generation. *Acta Mater.*, 56, 1274–1287.
- 25. SIMMETRIX Inc. at <<http://www.simmetrix.com/>>
- 26. Neeraj, T. & Mills, M. (2001). Short-range order (SRO) and its effect on the primary creep behavior of a Ti-6wt.%Al alloy. *Mater. Sci. Eng. A*, 319-321, 415–419.

27. Chichili, D. R., Ramesh, K. T. & Hemker, K. J. (1998). The high-strain-rate response of alpha-titanium: experiments, deformation mechanisms and modeling. *Acta Mater.*, 46, 1025–1043.

28. Paton, N. E., Baggerly, R. G. & Williams, J. C. (1976). *Deformation and Solid Solution Strengthening of Titanium-Aluminum Single Crystals*.

29. Williams, J. C., Baggerly, R. G. & Paton, N. E. (2002). Deformation behavior of HCPTi-Al alloy single crystals. *Metall. Mater. Trans. a-Physical Metall. Mater. Sci.*, 33, 837–850.

30. Venkataramani, G., Deka, D. & Ghosh, S. (2006). Crystal Plasticity Based Fe Model for Understanding Microstructural Effects on Creep and Dwell Fatigue in Ti-6242. *J. Eng. Mater. Technol.*, 128, 356–365.

31. Lee, B., Vecchio, K., Ahzi, S. & Schoenfeld, S. (1997). Modeling the mechanical behavior of tantalum. *Metall. Mater. Trans. A.*, 28, 113-122.

32. Asaro, R. J. & Rice, J. R. (1977). Strain localization in ductile single crystals. *J. Mech. Phys. Solids* 25, 309–338.

33. Keshavarz, S. & Ghosh, S. (2015). Hierarchical crystal plasticity FE model for nickel-based superalloys: Sub-grain microstructures to polycrystalline aggregates. *Int. J. Solids Struct.*, 55, 17–31.

34. Arsenlis, A. & Parks, D. (1999). Crystallographic aspects of geometrically-necessary and statistically-stored dislocation density. *Acta Mater.*, 47, 1597–1611.

35. Ogi, H. *et al.* (2004). Titanium's high-temperature elastic constants through the hcp–bcc phase transformation. *Acta Mater.*, 52, 2075–2080.

36. Heckel, T. K., Guerrero-Tovar, A. & Christ, H.-J. (2011). Stress-Dependent Elastic Behaviour of a Titanium Alloy at Elevated Temperatures. *Exp. Mech.*, 52, 323–329.

37. Dohrmann, C. R., Heinstein, M. W., Jung, J., Key, S. W. & Witkowski, W. R. (2000). Node-based uniform strain elements for three-node triangular and four-node tetrahedral meshes. *Int. J. Numer. Methods Eng.*, 47, 1549–1568.

38. Puso, M. A. & Solberg, J. (2006). A stabilized nodally integrated tetrahedral. *Int. J. Numer. Methods Eng.*, 67, 841–867.

39. Cheng, J., Shahba, A. & Ghosh, S. (2015) Stabilized tetrahedral elements for crystal plasticity finite element analysis overcoming volumetric locking. (*submitted for publication*)

40. Neto, E. A. d. S., Pires, F. M. A. & Owen, D. R. J. (2005). F-bar-based linear triangles and tetrahedra for finite strain analysis of nearly incompressible solids. Part I: formulation and benchmarking. *Int. J. Numer. Methods Eng.*, 62, 353–383.

41. Li, H., Mason, D. E., Bieler, T. R., Boehlert, C. J. & Crimp, M. A. (2013). Methodology for estimating the critical resolved shear stress ratios of α -phase Ti using EBSD-based trace analysis. *Acta Mater.*, 61, 7555–7567.

42. Stroh, A. N. (1954). The Formation of Cracks as a Result of Plastic Flow. *Proc. R. Soc. A*

Math. Phys. Eng. Sci., 223, 404–414.

43. Bažant, Z. P. & Pijaudier-Cabot, G. (1988). Nonlocal Continuum Damage, Localization Instability and Convergence. *J. Appl. Mech.*, 55, 287.
44. Sinha, V., Mills, M. J. & Williams, J. C. (2004). Understanding the contributions of normal-fatigue and static loading to the dwell fatigue in a near-alpha titanium alloy. *Metall. Mater. Trans. A*, 35, 3141–3148.
45. Lütjering, G. & Williams, J. C. *Titanium*. (Springer Berlin Heidelberg, 2007). doi:10.1007/978-3-540-73036-1
46. Nie, Y. & Xie, Y. (2007). Ab initio thermodynamics of the hcp metals Mg, Ti, and Zr. *Phys. Rev. B*, 75, 174117.
47. Souvatzis, P., Eriksson, O. & Katsnelson, M. I. (2007). Anomalous Thermal Expansion in α -Titanium. *Phys. Rev. Lett.*, 99, 015901.
48. Nyakana, S. L., Fanning, J. C. & Boyer, R. R. (2005). Quick Reference Guide for β Titanium Alloys in the 00s. *J. Mater. Eng. Perform.*, 14, 799–811.
49. Szccepanski, C. J., Jha, S. K., Larsen, J. M. & Jones, J. W. (2012). The Role of Local Microstructure on Small Fatigue Crack Propagation in an $\alpha + \beta$ Titanium Alloy, Ti-6Al-2Sn-4Zr-6Mo. *Metall. Mater. Trans. A*, 43, 4097–4112.
50. Geathers, J., Torbet, C. J., Jones, J. W. & Daly, S. (2015). Investigating environmental effects on small fatigue crack growth in Ti-6242S using combined ultrasonic fatigue and scanning electron microscopy. *Int. J. Fatigue*, 70, 154–162.
51. Knobbe, H., Köster, P., Christ, H.-J., Fritzen, C.-P. & Riedler, M. (2010). Initiation and propagation of short fatigue cracks in forged Ti6Al4V. *Procedia Eng.*, 2, 931–940.
52. Hoffmann, C., Eylon, D. & McEvily, A. (1982). Influence of Microstructure on Elevated-Temperature Fatigue Resistance of a Titanium Alloy. *Low-Cycle Fatigue and Life Prediction 5–5–18* (ASTM International). doi:10.1520/STP32420S

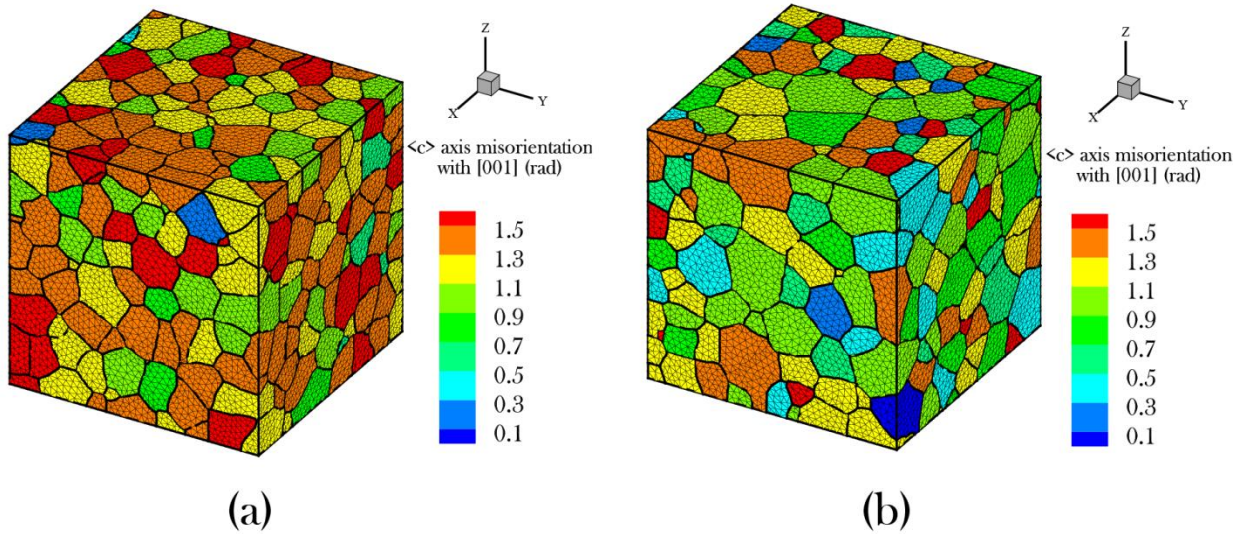


Figure 1. Statistically equivalent 3D microstructures for (a) $680 \times 680 \times 680 \mu\text{m}^3$ Ti-7 polycrystalline volume with 540 grains discretized into 583432 TET4 elements and (b) $29 \times 29 \times 29 \mu\text{m}^3$ Ti-6242 polycrystalline volume with 503 grains discretized into 492733 TET4 elements

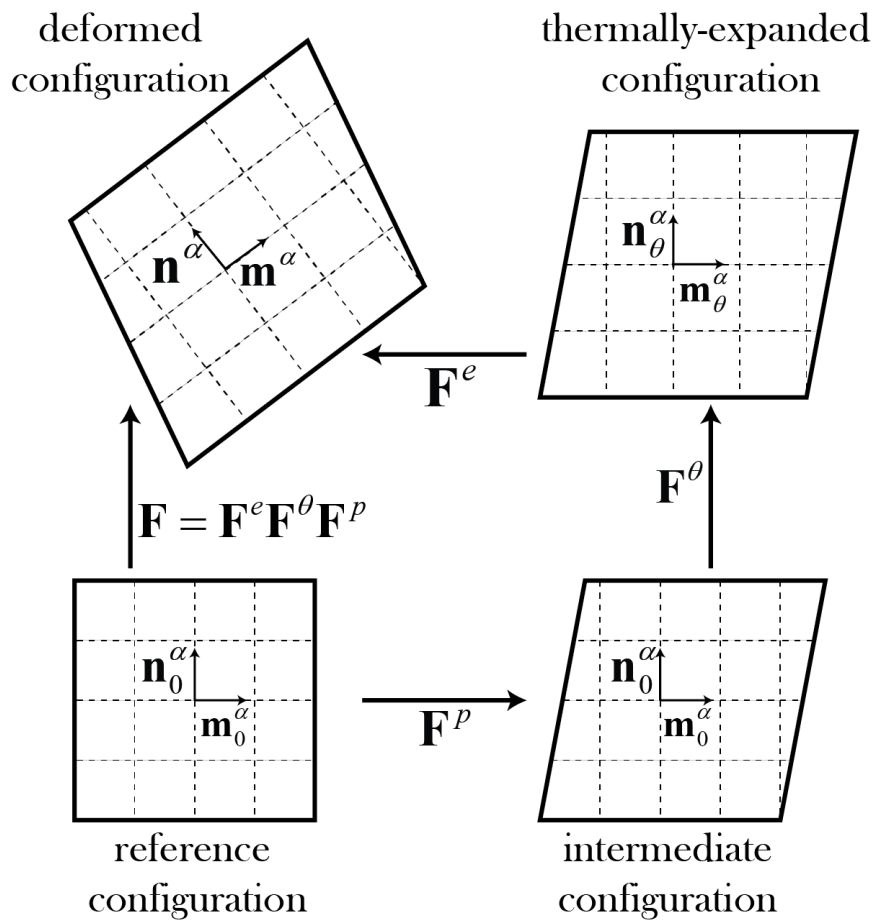


Figure 2. Multiplicative decomposition of total deformation gradient \mathbf{F} into elastic \mathbf{F}^e , thermal \mathbf{F}^θ and inelastic \mathbf{F}^p components

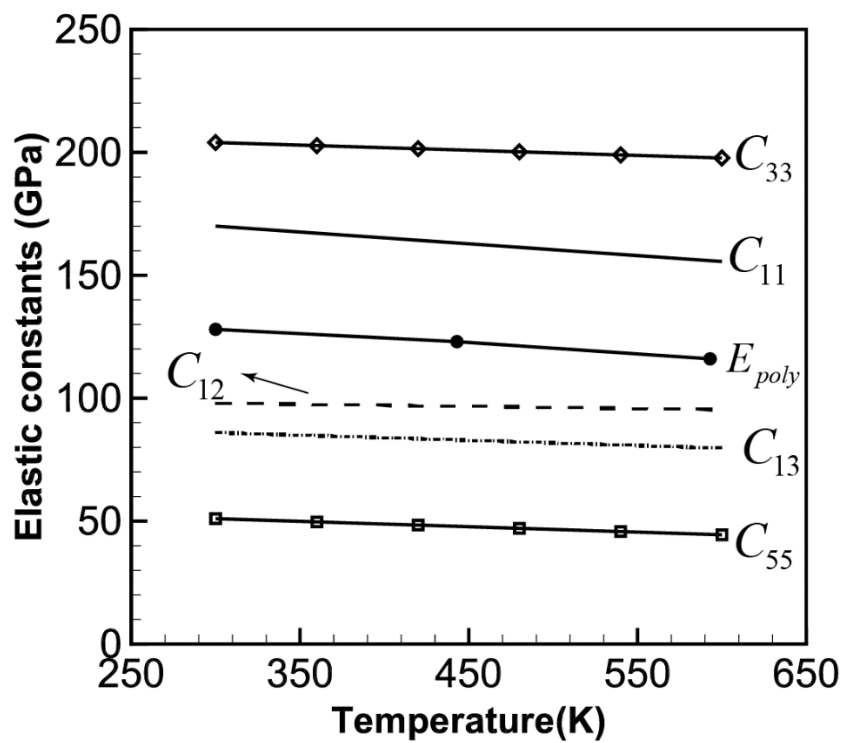


Figure 3. Variations of elastic constants of α Ti, and the simulated Young's modulus of the polycrystalline Ti-6242 with temperature

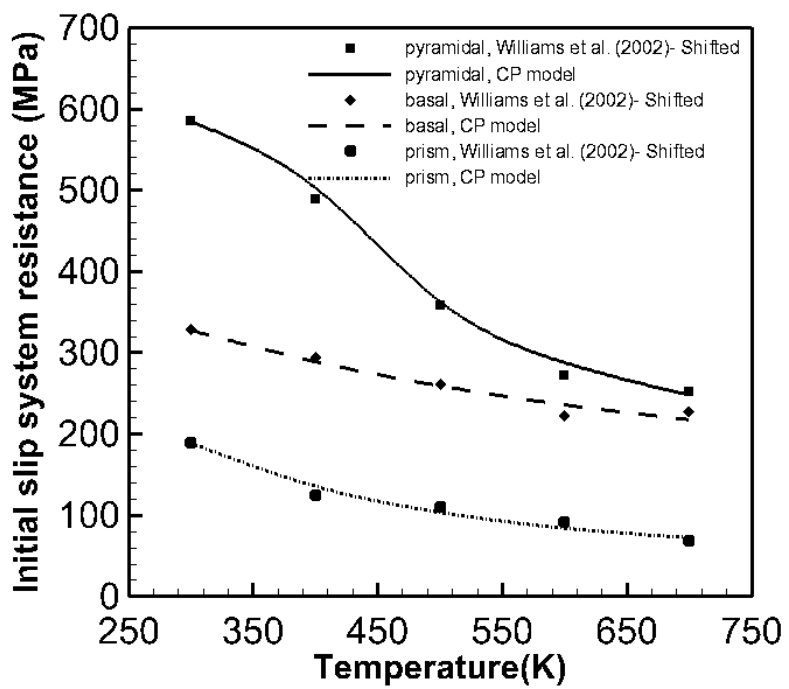


Figure 4. Variation of initial slip system resistance with temperature for α -Titanium.

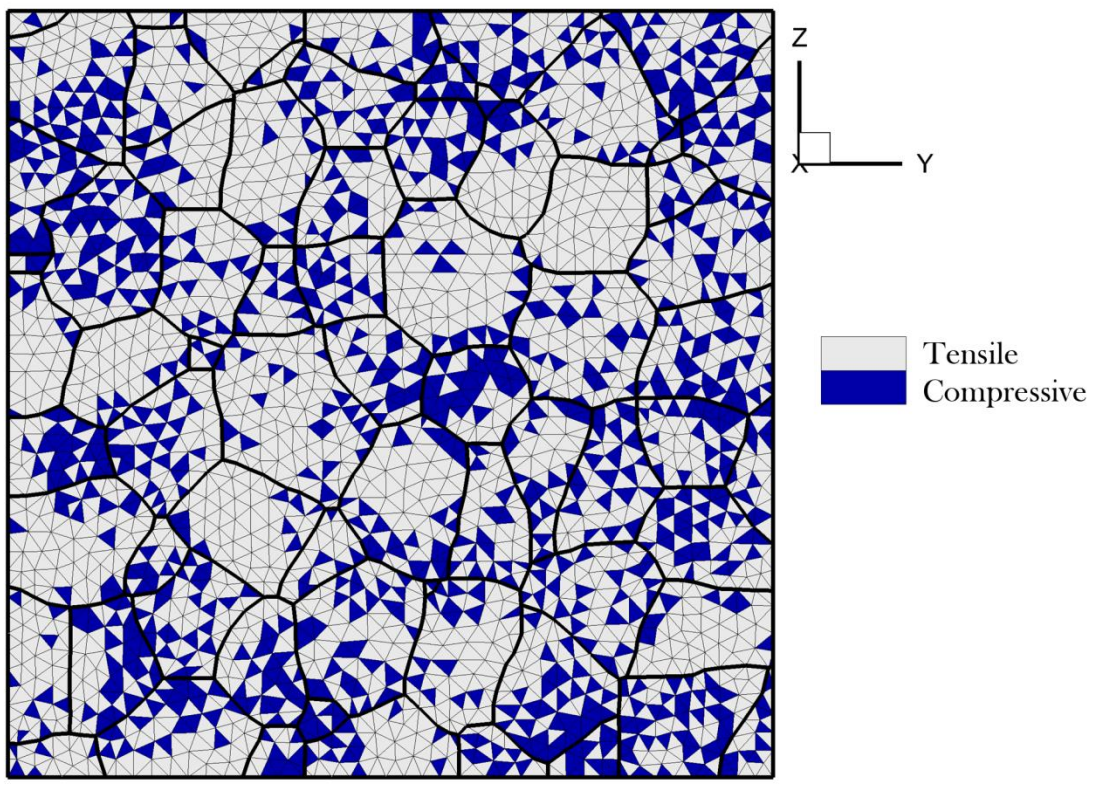


Figure 5. Distribution of hydrostatic stress in the Ti-7 microstructure at 4.5% strain

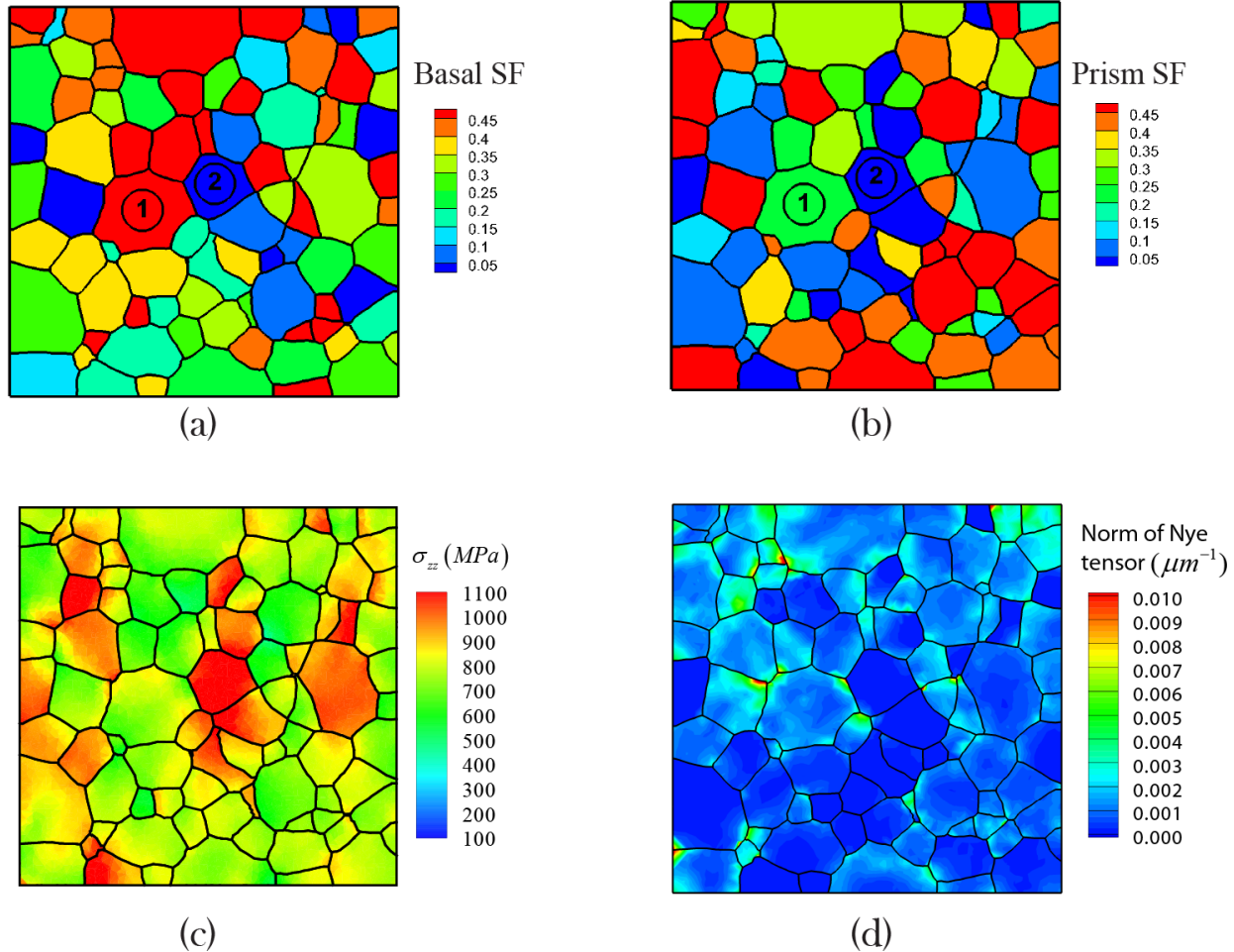


Figure 6. Load shedding on hard grain (2) due to plasticity in adjacent soft grain (1) in polycrystalline Ti-6242 microstructure after 250 dwell cycles. Distribution of (a) basal Schmid factor, (b) prism Schmid factor, (c) σ_{zz} along the loading direction and (d) norm of the Nye tensor, indicating dislocation accumulation within the soft grains and at soft-hard grain boundaries.

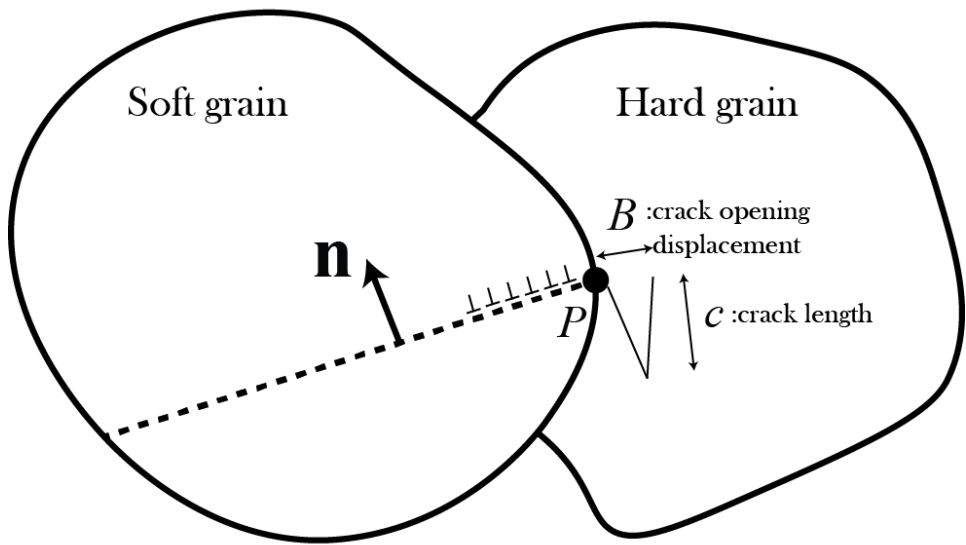


Figure 7. Illustration of wedge-crack opening in the hard grain due to dislocation pile up in the adjacent soft grain

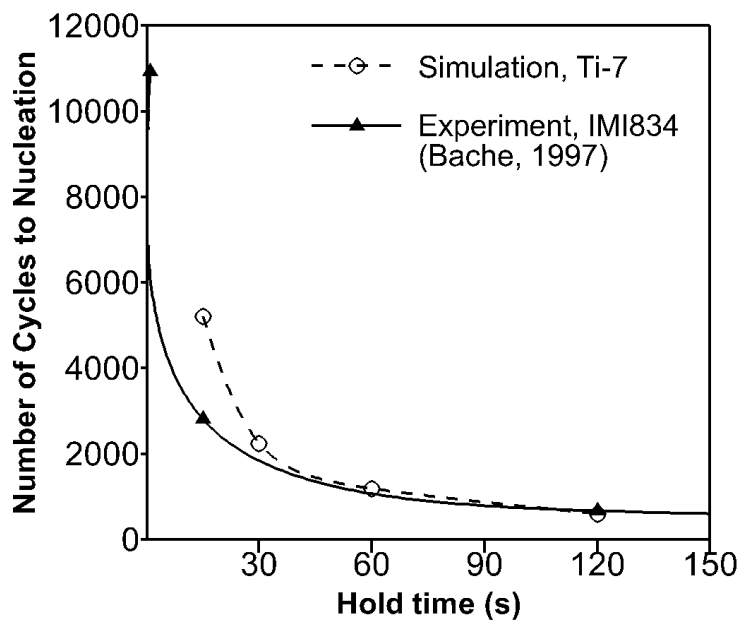


Figure 8. Effect of dwell time on number of cycles to crack nucleation in Ti-7 polycrystalline model, compared with the experimental data for IMI834 reported by Bache (1997).

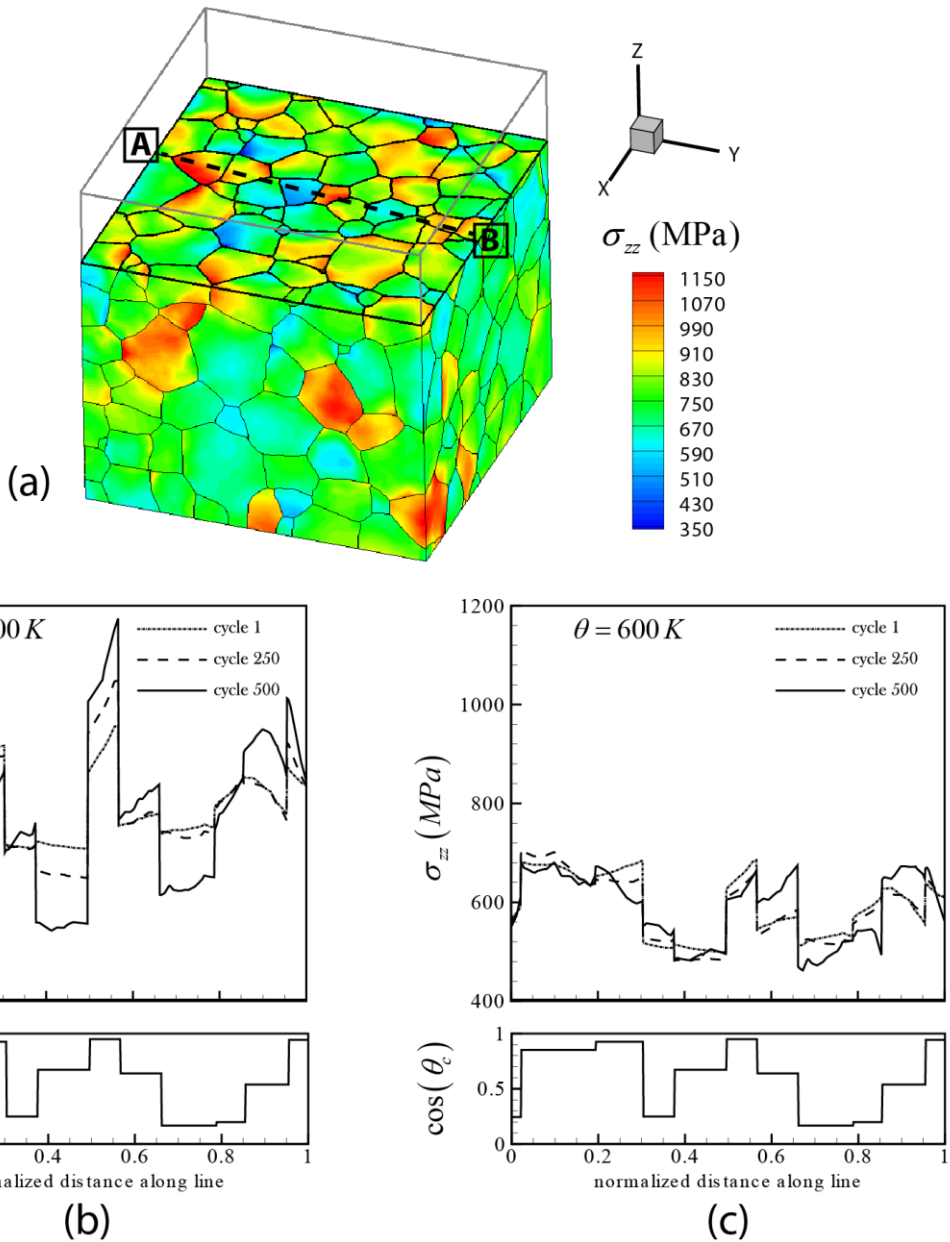


Figure 9. Evolution of local stress σ_{zz} in Ti-6242 polycrystal under dwell fatigue loading at (b) 300 K and (c) 600 K along the line AB shown in (a).

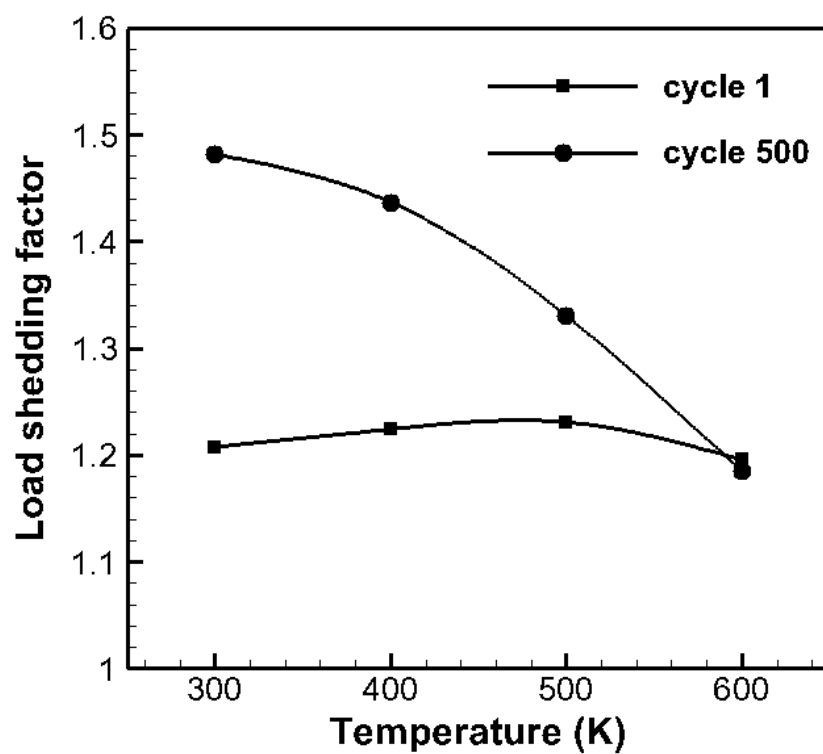


Figure 10. Variation of load shedding concentration factor at different temperatures signifying the diminution of time-dependent load shedding at elevated temperatures in Ti-6242.

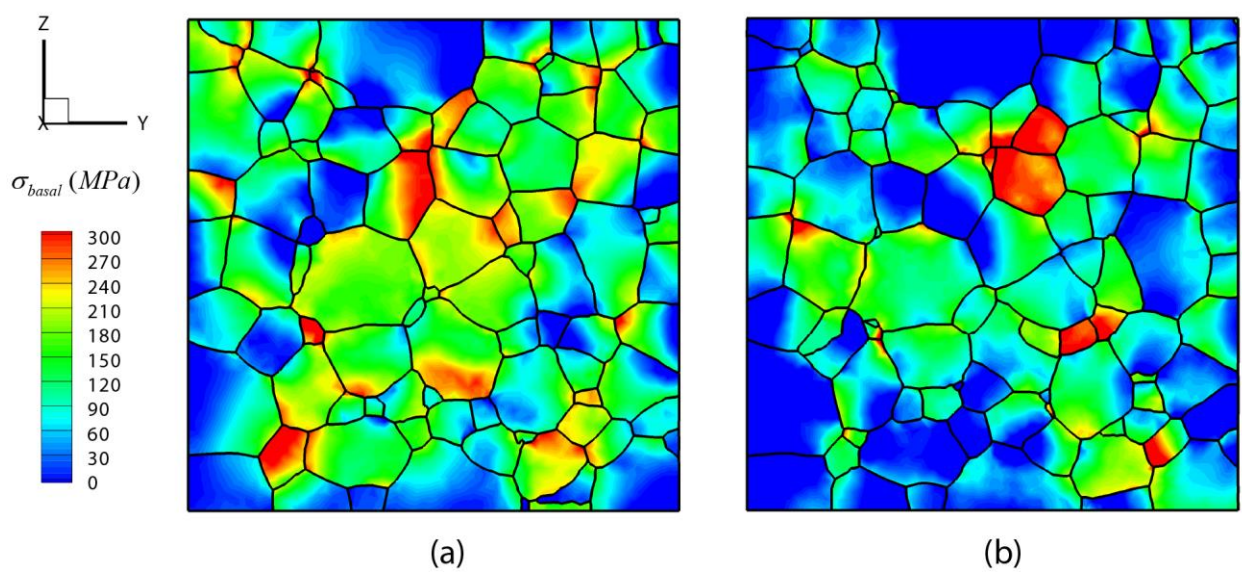
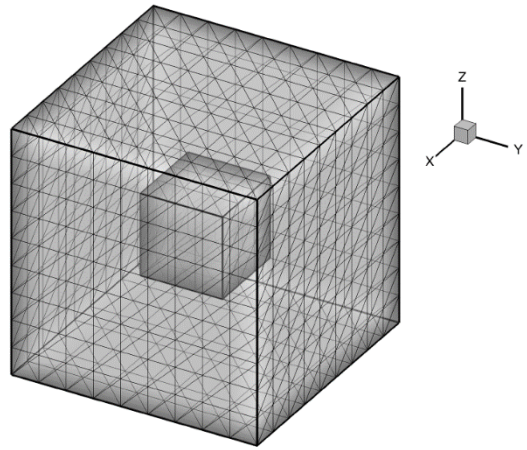
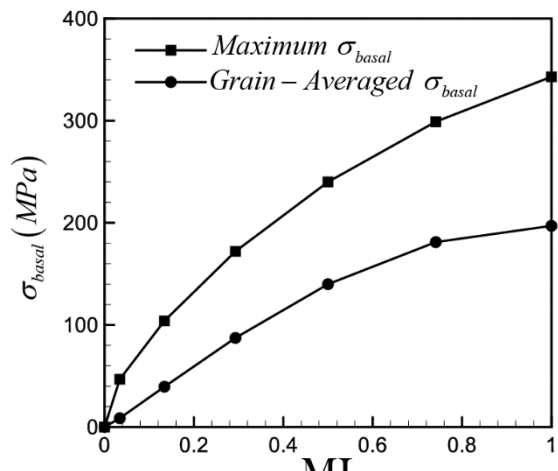


Figure 11. Tensile normal tractions developed on basal planes in (a) Ti-7 and (b) Ti-6242 polycrystals, due to the anisotropic thermal expansion of hcp Ti

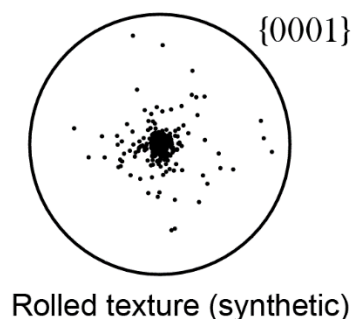
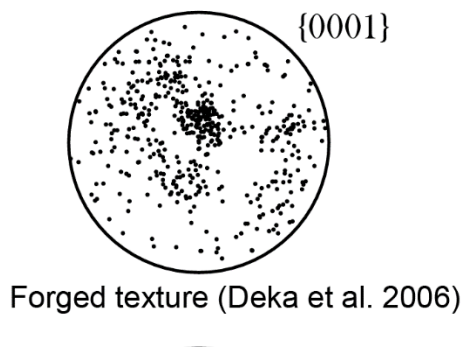


(a)

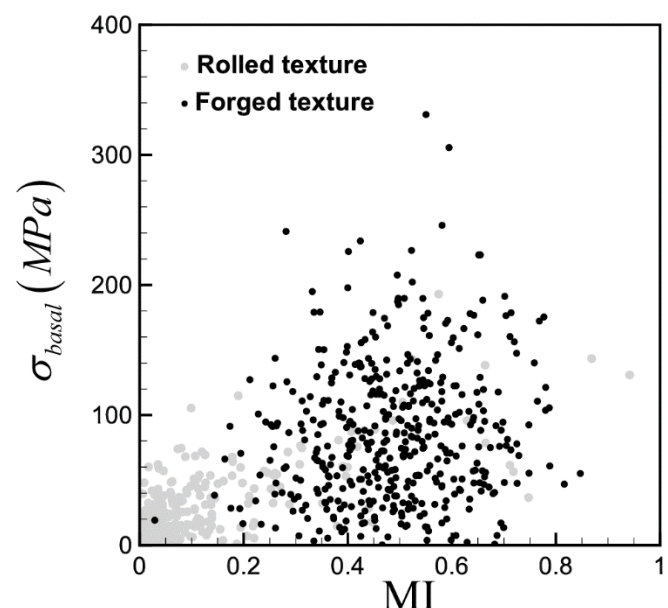


(b)

Figure 12.(a) two-grain model discretized into 4374 TET4 elements, (b) effect of $\langle c \rangle$ -axis misorientation on normal basal stresses induced in the inner grain due to anisotropic thermal expansion



(a)



(b)

Figure 13. (a) $\{0001\}$ pole figures for rolled and forged textures assigned to the Ti-6242 polycrystalline model, (b) distributions of grain-averaged normal basal stresses versus the grain $\langle c \rangle$ -axis misorientation index, for the two textures

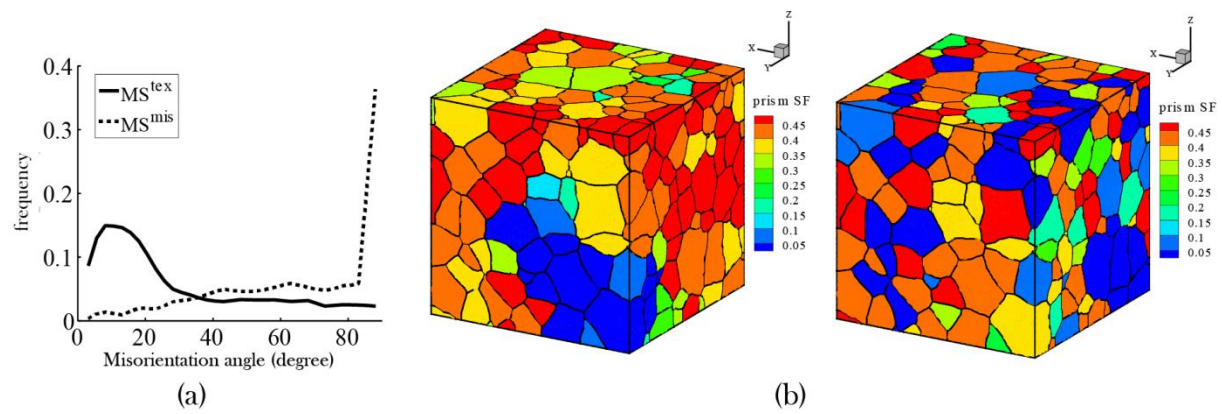


Figure 14. (a) The two limiting cases of misorientation distributions applied to the Ti-6242, MS^{tex} (microtextured) and MS^{mis} (high-misorientation), (b) plots of the prismatic Schmid factors, visualizing the resulting clustering of the grain orientations as microtextured regions in MS^{tex} (left), in comparison to MS^{mis} (right).

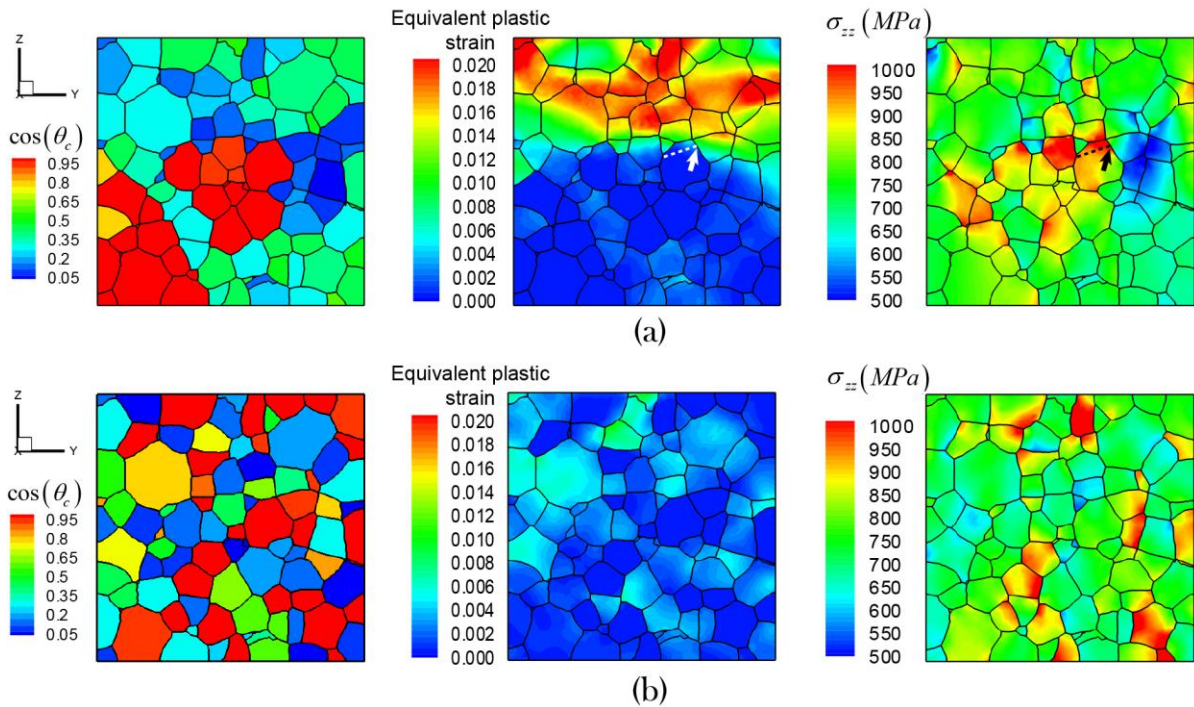


Figure 15. Distribution of $\cos(\theta_c)$, plastic strain and local stress σ_{zz} after 500 dwell cycles for (a) MS^{tex} (microtextured) and (b) MS^{mis} (high-misorientation) models of Ti-6242. Predicted location of crack initiation (arrow) and the trace of the crack plane (dashed line) are shown in (a).

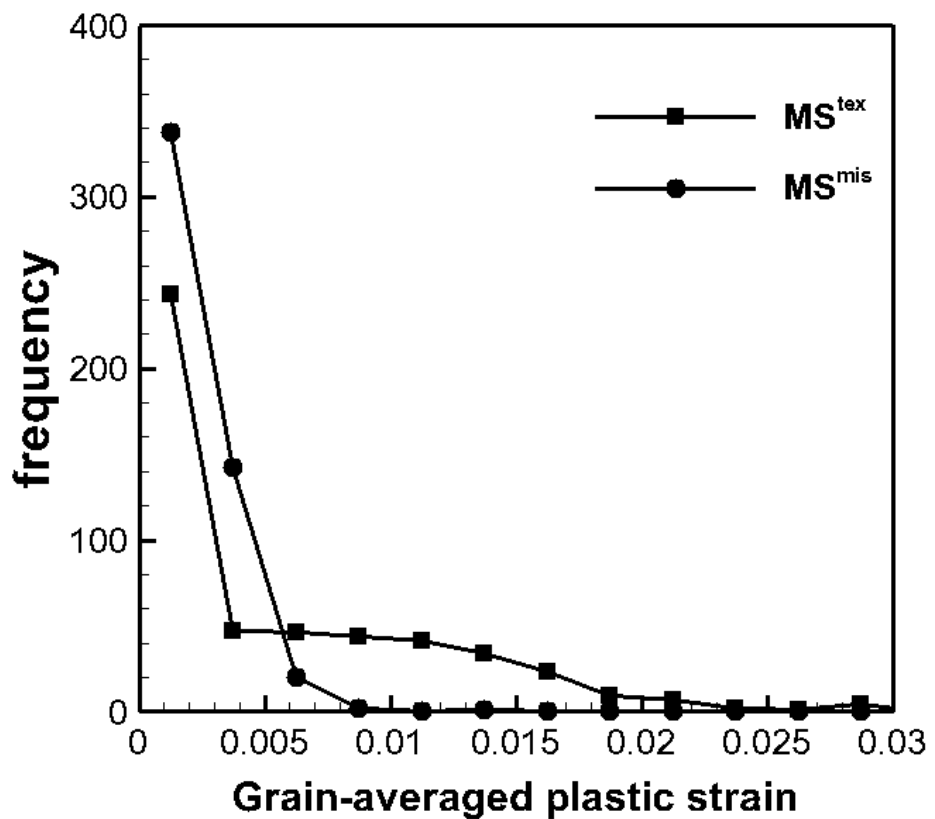
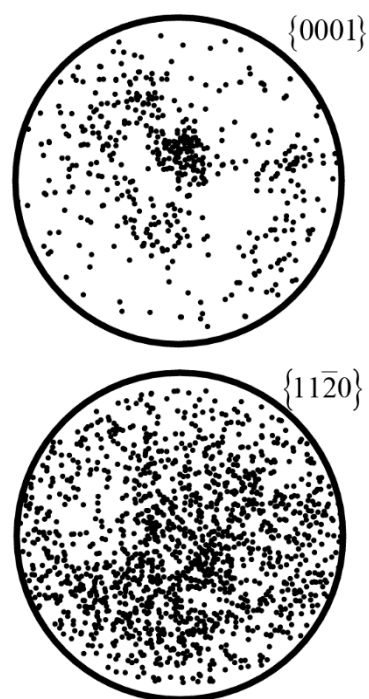
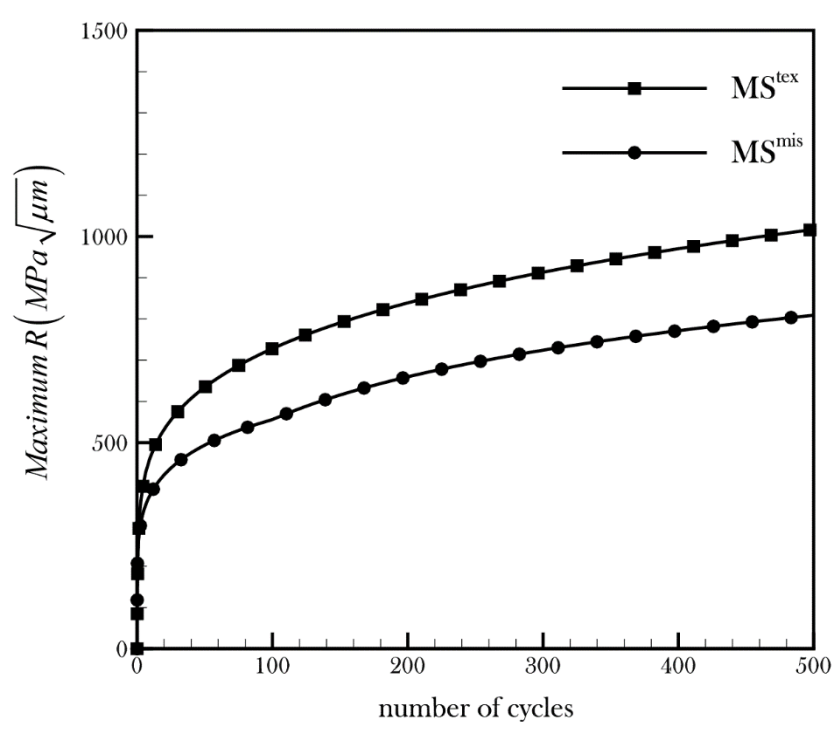


Figure 16. Distribution of grain-averaged plastic strain after 500 dwell cycles for MS^{tex} and MS^{mis} models of Ti-6242, showing the incidence of grains with large plastic strain accumulation, and high variability in plastic strain within MS^{tex} , in contrast to a lower and more uniform plastic strain distribution in MS^{mis} .

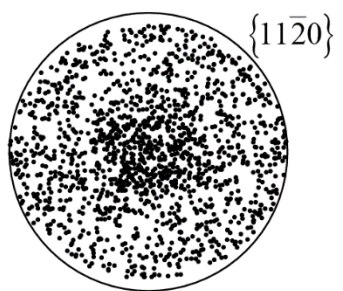
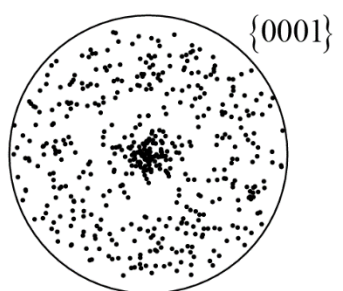


(a)

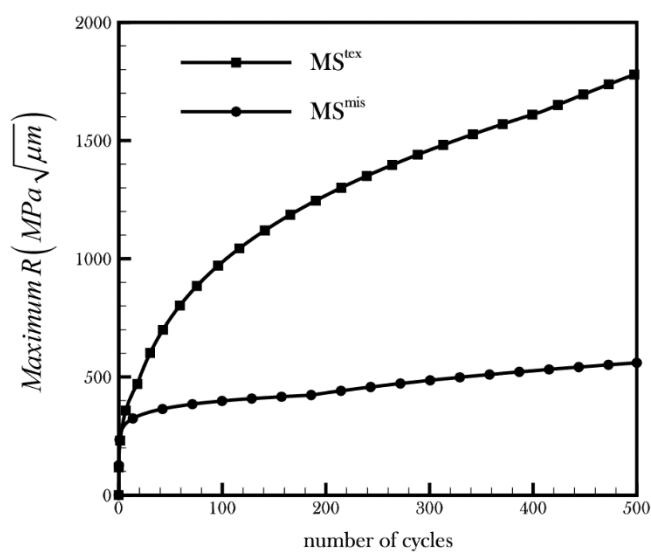


(b)

Figure 17. (a) Pole figures for forged Ti-6242 texture and (b) evolution of maximum R for MS^{tex} and MS^{mis} models



(a)



(b)

Figure 18. (a) Pole figures of the synthetically generated texture for Ti-6242 and (b) evolution of maximum R for MS^{tex} and MS^{mis} models

Table 1. Linear slopes for reduction of elastic constants of α Ti with temperature

Elastic constant	$C_{11} = C_{22}$	C_{12}	$C_{13} = C_{23}$	C_{33}	$C_{55} = C_{66}$
Linear slope (MPa/K)	48	8.9	21	21	21.9

Table 2.Fitting constants for variation of slip system resistances with temperature

Calibrated constants	$\langle a \rangle$ – basal	$\langle a \rangle$ – prism	$\langle a \rangle$ – pyramidal	$\langle c+a \rangle$ – pyramidal (for $\theta > 400K$)
\hat{g}^α (MPa)	176.58	132.43	132.43	353
$\hat{\theta}^\alpha$ (K)	400	200	200	160
θ_{ref}^α (K)	300	300	300	400

Stabilized Tetrahedral Elements for Crystal Plasticity Finite Element Analysis Overcoming Volumetric Locking

Jiahao Cheng ¹ · Ahmad Shahba ¹ ·
Somnath Ghosh ²

Received: date / Accepted: date

Abstract Image-based CPFE modeling involves computer generation of virtual polycrystalline microstructures from experimental data, followed by discretization into finite element meshes. Discretization is commonly accomplished using three-dimensional four-node tetrahedral or TET4 elements, which conform to the complex geometries. It has been commonly observed that TET4 elements suffer from severe volumetric locking when simulating deformation of incompressible or nearly incompressible materials. This paper develops and examines three locking-free stabilized finite element formulations in the context of crystal plasticity finite element analysis. They include a node-based uniform strain (NUS) element, a locally integrated B-bar (LIB) based element and a F-bar patch (FP) based element. All three formulations are based on the partitioning the TET4 element meshes and integrating over patches to obtain favorable incompressibility constraint ratios without adding large degrees of freedom. The results show that NUS formulation introduces unstable spurious energy modes, while the LIB and FP elements stabilize the solutions and are preferred for reliable CPFE analysis. The FP element is found to be computationally efficient over the LIB element.

1 Introduction

Image-based modeling and simulations of polycrystalline microstructures, using crystal plasticity finite element or *CPFE* models, are effective methods for determining microstructure-property relationships. The CPFE models capture details of microstructural features, e.g. crystallographic orientations, misorientations, grain morphology and their distributions and provide a platform for understanding various deformation and failure mechanisms such as the nucleation and propagation

¹ Graduate Research Associate

² M. G. Callas Professor (Corresponding author)

Departments of Civil and Mechanical Engineering, Johns Hopkins University, Baltimore, MD 21218

Tel.: +1-410-516-7833

Fax: +1-410-516-7473

E-mail: sghosh20@jhu.edu

of twins and micro-cracks [1–7]. Image-based CPFE modeling commonly involves computer generation of virtual polycrystalline microstructures from experimental data, followed by discretization into finite element meshes. The polycrystalline microstructures of many metals and alloys are quite complex with sharp and tortuous grain boundaries and multiple grain junctions. Discretization of these domains is best accomplished using three-dimensional four-node tetrahedral or TET4 elements, which conform to the complex geometries [8]. However, it has been commonly observed e.g. in [9–13] that TET4 elements suffer from severe volumetric locking when simulating deformation of incompressible or nearly incompressible materials. A metric that is used to understand element performance for incompressible or nearly incompressible deformations is termed as the *incompressibility constraint ratio*. It is defined as the ratio of number of available degrees of freedom (DOF) to the number of incompressibility constraints in a finite element mesh. Low incompressibility constraint ratio associated with TET4 elements can lead to large spurious hydrostatic stresses in models of plastically deforming metallic materials. This volumetric phenomenon is commonly ignored by most CPFE modelers who have been focused on the development of constitutive laws. This paper aims at developing stable, locking-free TET4 element formulations for efficient and accurate crystal plasticity finite element modeling and simulations.

A variety of methods have been proposed for the stabilization and control of volumetric locking in TET4 elements. A major idea in these methods is to associate nodal points with patches corresponding to an assembly of surrounding sub-elements, and subsequently to integrate the weak form over these patches, thus reducing the incompressibility constraint ratio. An average nodal pressure technique has been proposed for dynamic explicit formulations in [14], where the volumetric strain energy is integrated over the patch for each node. In [10], a node-based uniform strain (NUS) formulation is introduced for four-node tetrahedral elements associated with linear elasticity problems. The volumetric and deviatoric strain energy components are integrated over nodal patches in this formulation. Spurious zero energy modes were identified with this approach in [15], and consequently an additional stabilization term with a modified constitutive law was added to the potential energy functional. This approach was further extended in [16] into a locally integrated weighted strain formulation, where numerical integration is done at local Gauss points instead of nodes. In [11], the fact that instability is linked only to the isochoric strain energy contribution was exploited through a stress splitting operation, to stabilize the formulation in [10]. A generalized node-based, smoothed finite element method (NS-FEM) has been proposed in [17] that adopts an arbitrary polygonal element domain discretization. This method provides an upper-bound solution for the strain energy and is shown to reduce to the formulation in [10] for the special case of linear tetrahedral elements. The strain smoothing operation in NS-FEM is later extended to edge-based smoothed finite element method (ES-FEM) [18, 19] and face-based smoothed finite element method (FS-FEM) [20]. The above methods are however not suitable for anisotropic crystal plasticity finite element formulations, since the stress or the elasto-plastic tangent stiffness tensor cannot be split into isochoric and deviatoric components. An element formulation with a F-bar patch method has been introduced in [12, 13] to overcome volumetric locking in TET4 elements for finite deformation problems. The original F-bar formulation in [21] was developed for four-node quadrilateral

and eight-noded hexahedral elements. This simple and effective model can be used for any constitutive law and is easily implemented in any standard displacement-based finite element code. Other competing strategies in developing locking-free linear tetrahedral elements include stabilizing NUS formulation with additional higher order support function [22], and mixed enhanced elements [9] in which additional augmentation strain fields are used in conjunction with a linearly interpolated pressure field to treat the incompressible constraints. Volume and area bubble functions have been added to mixed tetrahedral elements in [23, 24] to stabilize the displacement and strain fields.

The present paper develops and examines three locking-free stabilized finite element formulations in the context of crystal plasticity finite element or CPFE analysis. They include a node-based uniform strain (NUS) element, a locally integrated B-bar (LIB) based element and a F-bar patch (FP) based element. The locally integrated B-bar element is based on splitting of the gradient operator matrix \mathbf{B} for TET4 elements. It selectively reduces the volumetric strain over a nodal patch and keeps the deviatoric strain unchanged in each TET4 element. The paper compares results with the different methods and provides a guideline for conducting reliable CPFE analysis. The CPFE formulation in an updated Lagrangian framework is briefly reviewed in section 2. In section 3, the three locking-free finite element formulations are described, while their implementation for large deformation CPFE problems are detailed in section 4. Comparison of results, including patch tests, elastic bending problems, bicrystal and polycrystal CPFE simulations, are conducted in section 5. The computational efficiency of these formulations are compared in section 6 and concluding remarks are made in section 7.

2 Finite Deformation Crystal Plasticity FE Formulation

The finite element weak form of equilibrium equations for a body undergoing finite deformation is obtained by taking the product of the governing equations with a weighting function and integrating over the volume in the current or reference configuration. In an incremental formulation and solution process, where a typical time step transcends discrete temporal points t and $t + \Delta t$, the principle of virtual work for a quasi-static process at time $t + \Delta t$ occupying the domain $\Omega^{t+\Delta t} \subset \mathcal{R}^3$ is written as [25] :

$$\begin{aligned} \int_{\Omega^{t+\Delta t}} (\nabla \delta \mathbf{u}^{t+\Delta t}) : \boldsymbol{\sigma} d\Omega^{t+\Delta t} &= \int_{\Omega^{t+\Delta t}} \delta \mathbf{u}^{t+\Delta t} \cdot \mathbf{b} d\Omega^{t+\Delta t} \\ &+ \int_{\Gamma_{\sigma}^{t+\Delta t}} \delta \mathbf{u}^{t+\Delta t} \cdot \bar{\mathbf{t}} d\Gamma_{\sigma}^{t+\Delta t} \quad \forall \delta \mathbf{u}^{t+\Delta t} \in \mathcal{U} \end{aligned} \quad (1)$$

where $\boldsymbol{\sigma}$ is the Cauchy stress tensor, \mathbf{u} is the displacement field and \mathbf{b} is the body force per unit volume. The test function $\delta \mathbf{u} = \delta u_i \mathbf{e}_i$ is defined in the space \mathcal{U} of virtual displacements, i.e.

$$\mathcal{U} = \left\{ \delta u_i^{t+\Delta t} \mathbf{e}_i \in H^1(\Omega), \delta \mathbf{u}^{t+\Delta t} = \mathbf{0} \text{ on } \Gamma_u \right\} \quad (2)$$

where \mathbf{e}_i , $i = 1, 2, 3$ are the orthogonal unit basis vectors. The time dependent boundary conditions are:

$$\boldsymbol{\sigma} \cdot \mathbf{n} = \bar{\mathbf{t}} \quad \text{on} \quad \Gamma_\sigma \quad \text{and} \quad \mathbf{u} = \bar{\mathbf{u}} \quad \text{on} \quad \Gamma_u \quad (3)$$

Here $\bar{\mathbf{t}}$ and $\bar{\mathbf{u}}$ are time-dependent prescribed quantities on the traction boundary Γ_σ and displacement boundary Γ_u respectively, where $\Gamma = \Gamma_\sigma \cup \Gamma_u$, and \mathbf{n} represents the outward unit vector normal to Γ_σ . An updated Lagrangian formulation is developed in this work [25], where the reference configuration for integrating the weak form corresponds to that at the beginning of the time step, i.e. at time t . In this formulation, the weak form in equation (1) reduces to:

$$\int_{\Omega^t} \delta \mathbf{E}_t^{t+\Delta t} : \mathbf{S}_t^{t+\Delta t} d\Omega^t = R^{ext \ t+\Delta t} \quad (4)$$

where

$$\mathbf{u}^{t+\Delta t} = \mathbf{u}^t + \Delta \mathbf{u} \quad \text{Incremental displacement}$$

(5a)

$$\mathbf{E}_t^{t+\Delta t} = \frac{1}{2} \left(\frac{\partial \Delta \mathbf{u}}{\partial \mathbf{x}^t} + \left(\frac{\partial \Delta \mathbf{u}}{\partial \mathbf{x}^t} \right)^T + \left(\frac{\partial \Delta \mathbf{u}}{\partial \mathbf{x}^t} \right)^T \frac{\partial \Delta \mathbf{u}}{\partial \mathbf{x}^t} \right) \quad \text{Green-Lagrange strain tensor}$$

(5b)

$$\mathbf{S}_t^{t+\Delta t} = J_t^{t+\Delta t} \left(\mathbf{F}_t^{t+\Delta t} \right)^{-1} \boldsymbol{\sigma}^{t+\Delta t} \left(\mathbf{F}_t^{t+\Delta t} \right)^{-T} \quad \text{Second Piola-Kirchhoff stress}$$

(5c)

$$R^{ext \ t+\Delta t} = \int_{\Omega^{t+\Delta t}} \delta \mathbf{u}^{t+\Delta t} \mathbf{b} d\Omega^{t+\Delta t} + \int_{\Gamma_\sigma^{t+\Delta t}} \delta \mathbf{u}^{t+\Delta t} \bar{\mathbf{t}} d\Gamma_\sigma^{t+\Delta t} \quad \text{External virtual work}$$

(5d)

\mathbf{F} corresponds to the deformation gradient tensor and J is its determinant or Jacobian. All quantities in equations (5) are at time $t + \Delta t$ and referred to the configuration at time t . Equation (4) may be written in an incremental form as:

$$\int_{\Omega^t} \delta \Delta \mathbf{E} : \Delta \mathbf{S} d\Omega^t + \int_{\Omega^t} \delta \boldsymbol{\eta} : \boldsymbol{\sigma}^t d\Omega^t = R^{ext \ t+\Delta t} - \int_{\Omega^t} \delta \mathbf{e} : \boldsymbol{\sigma}^t d\Omega^t \quad (6)$$

In the above equation, $\Delta \mathbf{S} = \mathbf{S}_t^{t+\Delta t} - \boldsymbol{\sigma}^t$ is the increment of second Piola-Kirchhoff stress, $\Delta \mathbf{E} = \mathbf{E}_t^{t+\Delta t} - \mathbf{E}_t^t$ is the increment of Green-Lagrange strain. Furthermore, \mathbf{e} and $\boldsymbol{\eta}$ are respectively the linear and non-linear parts of $\Delta \mathbf{E}$, expressed as:

$$\mathbf{e} = \frac{1}{2} \left[\left(\frac{\partial \Delta \mathbf{u}}{\partial \mathbf{x}^t} \right)^T + \frac{\partial \Delta \mathbf{u}}{\partial \mathbf{x}^t} \right] \quad \text{and} \quad \boldsymbol{\eta} = \frac{1}{2} \left(\frac{\partial \Delta \mathbf{u}}{\partial \mathbf{x}^t} \right)^T \frac{\partial \Delta \mathbf{u}}{\partial \mathbf{x}^t} \quad (7)$$

The nonlinear equation (6) is solved using an iterative method such as the Newton-Raphson solver. A linearized form of equation (6) is required to set up the tangent matrix. Employing an incremental constitutive law of the form $\Delta \mathbf{S} = \mathbf{C}^t : \mathbf{e}$ and using approximation $\delta \Delta \mathbf{E} = \delta \mathbf{e}$, the linearized equation to be solved becomes

$$\int_{\Omega^t} \delta \mathbf{e} : \mathbf{C}^t : \mathbf{e} d\Omega^t + \int_{\Omega^t} \delta \boldsymbol{\eta} : \boldsymbol{\sigma}^t d\Omega^t = R^{ext \ t+\Delta t} - \int_{\Omega^t} \delta \mathbf{e} : \boldsymbol{\sigma}^t d\Omega^t \quad (8)$$

where \mathbf{C}^t is the history-dependent fourth-order tangent stiffness tensor at time t , which should be obtained for the specific constitutive model.

2.1 Crystal plasticity constitutive model

Polycrystalline microstructures of metals and alloys are modeled using CPFE models that describe micro-mechanisms of crystallographic plastic deformation in individual grains and polycrystalline aggregates. Deformation mechanisms and texture in CPFE models have been used to model creep and deformation response of metals and alloys in [26–29] using a power law description [30], and the thermally activated theory of plastic flow [31]. The author's group has developed crystal plasticity FE models and codes for simulating deformation and failure in a variety of metallic materials. These studies include creep and fatigue simulations for Ti alloys [1–3, 32], dwell fatigue simulations in Ti alloys in [4, 6], cyclic deformation in HSLA steels [33], deformation twin modeling in Mg alloys in [34] and hierarchical models of Ni-based superalloys in [7]. The proposed locking-free element formulations in this paper are not limited to any specific crystal plasticity model and are quite general in their applications to a wide class of elastic-plastic constitutive laws. However a candidate crystal plasticity constitutive model for Mg alloys is chosen for its capability to capture the strong anisotropy in plastic deformation and twin induced material failure [34]. This constitutive model illustrates the significant effect of element locking in predicting material failure.

2.1.1 Kinematic relations and flow rule

The deformation gradient $\mathbf{F}_0^t = \frac{\partial \mathbf{x}^t}{\partial \mathbf{x}^0}$ at time t with respect to the initial reference configuration at $t = 0$, is multiplicatively decomposed into elastic and plastic components as:

$$\mathbf{F}_0^t = \mathbf{F}^e \mathbf{F}^p \quad (9)$$

The component \mathbf{F}^e describes elastic stretching and rigid-body rotation of the crystal lattice, whereas the component \mathbf{F}^p corresponds to the incompressible plastic flow due to dislocation slip on different slip systems. The second Piola-Kirchoff (PK2) stress \mathbf{S} is expressed in terms of elastic Green-Lagrange strain tensor \mathbf{E}^e as:

$$\mathbf{S} = \mathbf{C}^e : \mathbf{E}^e \quad (10)$$

where \mathbf{C}^e is a fourth-order anisotropic elasticity tensor. The evolution of plastic deformation is expressed in terms of plastic velocity gradient \mathbf{L}^p as:

$$\mathbf{L}^p = \dot{\mathbf{F}}^p \mathbf{F}^{p-1} = \sum_{\alpha=1}^{N_{slip}} \dot{\gamma}^\alpha \mathbf{s}_0^\alpha \quad (11)$$

where $\dot{\gamma}^\alpha$ is the slip rate on a slip system α and N_{slip} is the total number of slip systems. The Schmid tensor associated with α -th slip system \mathbf{s}_0^α is expressed in terms of the slip direction \mathbf{m}_0^α and slip plane normal \mathbf{n}_0^α in the reference configuration, i.e. $\mathbf{s}_0^\alpha = \mathbf{m}_0^\alpha \otimes \mathbf{n}_0^\alpha$.

For Mg alloys, 12 active slip systems (of 30 possible systems in *hcp* materials) are distributed among three different families, viz. the $\langle a \rangle$ -basal, $\langle a \rangle$ -prismatic and $\langle c+a \rangle$ pyramidal slip system families as shown in figure 1. A power law model in [34] is used for the slip rate on slip system α , given as:

$$\dot{\gamma}^\alpha = \dot{\gamma}_0^\alpha \left| \frac{\tau^\alpha - s_a^\alpha}{s_*^\alpha} \right|^{\frac{1}{m}} \text{sign}(\tau^\alpha - s_a^\alpha) \quad (12)$$

where $\dot{\gamma}_0^\alpha$ is a reference slip-rate for slip system α and m is the power law exponent representing strain-rate sensitivity. The resolved shear stress on slip system α is $\tau^\alpha = \mathbf{F}^e T \mathbf{F}^e \mathbf{S} : \mathbf{s}_0^\alpha$. Here s_a^α is the athermal resistance arising from the long-range internal stress field between parallel dislocation lines or from grain boundaries, and s_*^α is the thermal shear resistance due to local obstacles such as dislocation jogs and forest dislocations.

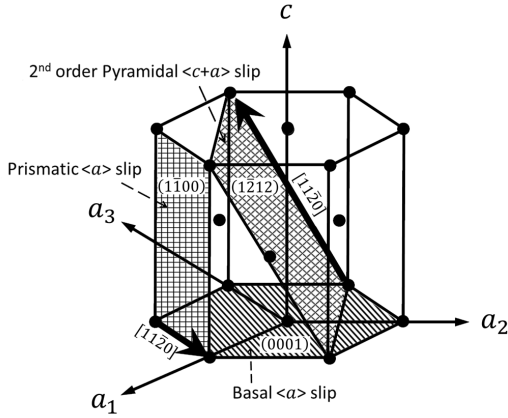


Fig. 1 Schematic showing active slip systems in Mg and Mg alloys

2.1.2 Evolution of slip system resistances

The evolution of athermal (s_a^α) and thermal (s_*^α) shear resistances is controlled by two types of dislocations, viz. statistically stored dislocations (SSDs) and geometrically necessary dislocations (GNDs) [6, 35, 36]. SSDs are responsible for homogeneous plastic deformation and are characterized by vanishing net Burgers vector. On the other hand, GNDs correspond to the storage of polarized dislocation densities, necessary for accommodating crystal lattice curvatures in single crystal bending or near polycrystalline grain boundaries. Accordingly, the total athermal and thermal shear resistances are composed of three components viz. the initial shear resistance, and contributions from the evolution of SSDs and

GNDs respectively. At time t , these are [34]:

$$s_a^\alpha = \hat{s}_{a,0}^\alpha + \int_{t'=0}^{t'=t} \sum_{\beta=1}^{N_{slip}} h^{\alpha\beta} \left| \dot{\gamma}_P^\alpha \sin(\mathbf{n}_0^\alpha, \mathbf{t}_0^\beta) \right| dt' + c_1 G b^\alpha \sqrt{\rho_{GND,P}^\alpha} \quad (13a)$$

$$s_*^\alpha = \hat{s}_{*,0}^\alpha + \int_{t'=0}^{t'=t} \sum_{\beta=1}^{N_{slip}} h^{\alpha\beta} \left| \dot{\gamma}_F^\alpha \cos(\mathbf{n}_0^\alpha, \mathbf{t}_0^\beta) \right| dt' + \frac{Q_{slip}^\alpha}{c_2 c_3 b^{\alpha^2}} \sqrt{\rho_{GND,F}^\alpha} \quad (13b)$$

where $\hat{s}_{*,0}^\alpha$ and $\hat{s}_{a,0}^\alpha$ are grain size-dependent initial thermal and athermal shear resistances, given by Hall-Petch type relation [32, 37, 38]. G is the shear modulus, Q_{slip}^α is the effective activation energy for dislocation slip, and c_1, c_2, c_3 are constants representing the passing stress, jump width, and obstacle width respectively. The hardening of thermal slip resistance on slip system α is caused by the portion of forest SSDs on slip system β whose line direction $\mathbf{t}_0^\beta = \mathbf{m}_0^\beta \otimes \mathbf{n}_0^\beta$ is parallel to the slip plane normal \mathbf{n}_0^α . Therefore, the hardening rate for thermal resistance is projected with $\sin(\mathbf{n}_0^\alpha, \mathbf{t}_0^\beta)$. On the other hand, the hardening of athermal slip resistance is caused by the interaction of the dislocations on slip system α with the portion of SSDs on slip system β whose line direction lies in the slip plane α and consequently perpendicular to \mathbf{n}_0^α . Therefore, the hardening rate for thermal resistance is projected with $\cos(\mathbf{n}_0^\alpha, \mathbf{t}_0^\beta)$ [7]. The hardening rate of slip system α is defined in terms of a hardening matrix $h^{\alpha\beta}$ as:

$$h^{\alpha\beta} = q^{\alpha\beta} h_{ref}^\beta \left| 1 - \frac{s_*^\beta}{s_{sat}^\beta} \right|^r \operatorname{sign} \left(1 - \frac{s_*^\beta}{s_{sat}^\beta} \right) \quad (\text{no sum on } \beta) \quad \text{where } s_{sat}^\beta = \tilde{s}^\beta \left(\frac{\dot{\gamma}^\beta}{\dot{\gamma}_0^\beta} \right)^n \quad (14)$$

The introduction of non-local GND models in CPFE analysis is necessary for accurate representation of stress concentrations near grain boundaries that are responsible for crack and twin nucleation. Accumulation of GNDs occurs with the incompatibility of plastic strain field especially at points of discontinuous plastic flow, such as grain boundaries. Contribution of GNDs to the slip system hardening are from two sources. The dislocation components $\rho_{GND,P}^\alpha$ parallel to slip plane α and the forest dislocation components $\rho_{GND,F}^\alpha$ normal to slip plane α . $\rho_{GND,P}^\alpha$ contributes to the athermal shear resistance s_a^α by providing a long-range stress, and $\rho_{GND,F}^\alpha$ increases the thermal shear resistance s_*^α by hindering the slip of mobile dislocations. These are given in equations (13a) and (13b) respectively. The Nye's dislocation density tensor is used to quantify GND densities on different slip systems. It is expressed in terms of the curl of plastic deformation gradient as [39]:

$$\mathbf{A} = - \left(\nabla_{\mathbf{x}^0} \times \mathbf{F}^{p^T} \right)^T \quad (15)$$

where $\nabla_{\mathbf{x}^0}$ is the gradient operator with respect to the reference configuration at time $t = 0$. Nye dislocation tensor quantifies the closure failure of a circuit in the intermediate configuration due to the presence of GNDs and can be alternatively derived in terms of GNDs densities as [40]:

$$\mathbf{A} = \sum_{\alpha=1}^{N_{slip}} (\rho_{GNDs}^\alpha \mathbf{b}_0^\alpha \otimes \mathbf{m}_0^\alpha + \rho_{GNDet}^\alpha \mathbf{b}_0^\alpha \otimes \mathbf{t}_0^\alpha + \rho_{GNDen}^\alpha \mathbf{b}_0^\alpha \otimes \mathbf{n}_0^\alpha) \quad (16)$$

where \mathbf{b}^α is the Burgers vector for a slip system α in the reference configuration. GNDs on the slip system are decomposed into three components, viz. a screw component ρ_{GNDs}^α with dislocation line parallel to \mathbf{b}_0^α , and two edge components ρ_{GNDen}^α and ρ_{GNDet}^α with dislocation lines parallel to \mathbf{n}_0^α and \mathbf{t}_0^α respectively. There are in general $3 \times N_{slip}$ unknown GND densities, which corresponds to 90 for *HCP* crystals. Of these only 63 are independent for *HCP* crystals, corresponding to 9 ρ_{GNDs}^α s, 24 ρ_{GNDet}^α s and 30 independent ρ_{GNDen}^α s. Equations (15) and (16) constitute an under-determined state of equations that are expressed in a matrix form as:

$$\{\mathbf{A}\} = [\mathbf{A}] \{\rho_{GND}\} \quad (17)$$

$\{\mathbf{A}\}$ is the 9×1 vector representation of the Nye tensor \mathbf{A} , $[\mathbf{A}]$ is a 9×63 matrix containing the basis tensors $\mathbf{b}_0^\alpha \otimes \mathbf{m}_0^\alpha$, $\mathbf{b}_0^\alpha \otimes \mathbf{t}_0^\alpha$ and $\mathbf{b}_0^\alpha \otimes \mathbf{n}_0^\alpha$, and $\{\rho_{GND}\}$ is a 63×1 vector containing the independent GND densities. Following discussions in [40], the geometric constraints in equation (16) allow only certain dislocations to exist on the slip planes. This constraint is taken into account through a Lagrangian multiplier in the functional to be minimized, which is:

$$\mathcal{F}(\{\rho_{GND}\}, \{\lambda\}) = \{\rho_{GND}\}^T \{\rho_{GND}\} + \{\lambda\}^T ([\mathbf{A}] \{\rho_{GND}\} - \{\mathbf{A}\}) \quad (18)$$

where $\{\lambda\}$ is a 9×1 vector of Lagrange multipliers. Equation (18) implies that GNDs correspond to the minimum amount of polarized dislocation densities necessary to recover lattice compatibility. Minimizing equation (18), the GND densities are obtained as:

$$\{\rho_{GND}\} = [\mathbf{A}]^T \left([\mathbf{A}] [\mathbf{A}]^T \right)^{-1} \{\mathbf{A}\} \quad (19)$$

Using dislocation line projection [36], the parallel and forest GND components in equation (13) are obtained as:

$$\begin{aligned} \rho_{GND,P}^\alpha &= \sum_{\beta=1}^{N_{slip}} \chi^{\alpha\beta} \left[\left| \rho_{GNDs}^\beta \sin(\mathbf{n}_0^\alpha, \mathbf{m}_0^\beta) \right| + \left| \rho_{GNDet}^\beta \sin(\mathbf{n}_0^\alpha, \mathbf{t}_0^\beta) \right| \right. \\ &\quad \left. + \left| \rho_{GNDen}^\beta \sin(\mathbf{n}_0^\alpha, \mathbf{n}_0^\beta) \right| \right] \end{aligned} \quad (20a)$$

$$\begin{aligned} \rho_{GND,F}^\alpha &= \sum_{\beta=1}^{N_{slip}} \chi^{\alpha\beta} \left[\left| \rho_{GNDs}^\beta \cos(\mathbf{n}_0^\alpha, \mathbf{m}_0^\beta) \right| + \left| \rho_{GNDet}^\beta \cos(\mathbf{n}_0^\alpha, \mathbf{t}_0^\beta) \right| \right. \\ &\quad \left. + \left| \rho_{GNDen}^\beta \cos(\mathbf{n}_0^\alpha, \mathbf{n}_0^\beta) \right| \right] \end{aligned} \quad (20b)$$

The coefficient $\chi^{\alpha\beta}$ describes the strengthening effect due to the interaction between slip systems α and β , e.g. in the formation of dislocation locks. For *HCP* crystals, $\chi^{\alpha\beta}$ is taken to be 1 in this work.

2.2 TET4 elements in CPFE analysis and associated volumetric locking

For any element in the CPFE model, the displacement increment $\Delta\mathbf{u}$, increment of displacement gradient $\frac{\partial\Delta\mathbf{u}}{\partial\mathbf{x}^t}$ and the linearized strain increment \mathbf{e} in equation (7) are respectively written as:

$$\Delta\mathbf{u} = \mathbf{N}\Delta\mathbf{q}, \quad \frac{\partial\Delta\mathbf{u}}{\partial\mathbf{x}^t} = \frac{\partial\mathbf{N}}{\partial\mathbf{x}^t}\Delta\mathbf{q} = \mathbf{G}\Delta\mathbf{q}, \quad \text{and} \quad \mathbf{e} = \mathbf{B}\Delta\mathbf{q} \quad (21)$$

For the four-node constant strain tetrahedral or TET4 element, the shape function \mathbf{N} is a 3×12 matrix, \mathbf{G} is a 9×12 gradient operator matrix and \mathbf{B} is the 6×12 strain-displacement matrix. Explicit forms of \mathbf{N} , \mathbf{G} and \mathbf{B} for the TET4 element are given in [41]. Stress and strain tensors are represented using the reduced order Voigt vector notation. Substituting equations (21) into equation (8) and integrating using the one-point Gaussian quadrature rule, yields the discrete form of the finite element equations as:

$$\sum_{i=1}^{N_e} \mathbf{B}^{t^T} \mathbf{C}^t \mathbf{B}^t \Omega^{t,i} \Delta\mathbf{q} + \sum_{i=1}^{N_e} \mathbf{G}^{t^T} \tilde{\sigma}^t \mathbf{G}^t \Omega^{t,i} \Delta\mathbf{q} = \mathbf{f}^{extt+\Delta t} - \sum_{i=1}^{N_e} \mathbf{B}^{t^T} \sigma \Omega^{t,i} \quad (22)$$

where $\Omega^{t,i}$ is the volume of element i at time t . The matrix $\tilde{\sigma}^t$ is explicitly written as:

$$\tilde{\sigma}^t = \begin{bmatrix} \sigma^t & \mathbf{0} & \mathbf{0} \\ \mathbf{0} & \sigma^t & \mathbf{0} \\ \mathbf{0} & \mathbf{0} & \sigma^t \end{bmatrix} \quad (23)$$

where σ^t is the 3×3 stress matrix, $\mathbf{0}$ is a 3×3 matrix of zeros and $\mathbf{f}^{extt+\Delta t}$ is the external force vector corresponding to $R^{extt+\Delta t} = \mathbf{f}^{extt+\Delta t} : \delta\Delta\mathbf{q}$. The system of equations to be solved are:

$$\mathbf{K}^t \Delta\mathbf{q} = \mathbf{f}^{extt+\Delta t} - \mathbf{f}^{intt} \quad (24)$$

\mathbf{K}^t and \mathbf{f}^{intt} are the global stiffness matrix and internal force vector respectively. The material tangent stiffness tensor \mathbf{C}^t is needed for the evaluation of \mathbf{K}^t . The formulation of \mathbf{C}^t , which is consistent with the proposed crystal plasticity constitutive model, is given in appendix A.

2.2.1 Volumetric locking in TET4 elements

TET4 elements are known to exhibit volumetric locking for incompressible or nearly incompressible materials. A simple example illustrates the occurrence of volumetric locking emanating from numerical interpolation of strains in the TET4 element. Consider a nearly-incompressible elastic bar of dimensions $4 \times 2 \times 2$ units, with Young's modulus $E = 1 \text{ GPa}$ and Poisson's ratio $\nu = 0.4999$. The bar is discretized into 6 TET4 elements as shown in figure 2. The nodal coordinates and element connectivity list are tabulated in table 1. All the 8 nodes are subjected to prescribed values corresponding to the displacement field

$$u_x = \frac{xy}{2}, \quad u_y = \frac{x^2}{4} - \frac{\nu}{4(1-\nu)} y^2, \quad u_z = 0 \quad (25)$$

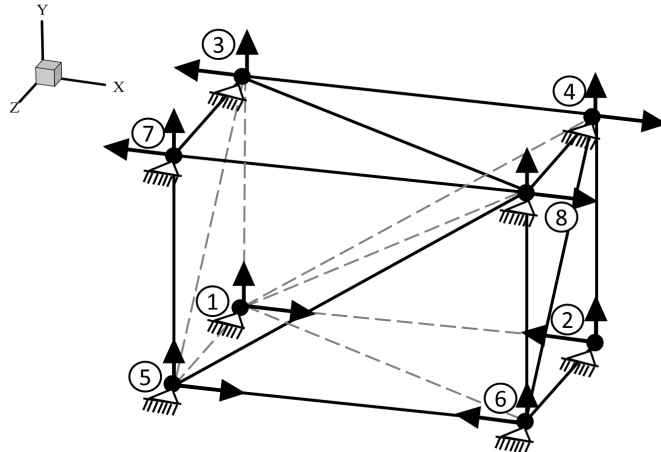


Fig. 2 Mesh of TET4 elements subject to nodal displacements for illustrating volumetric locking.

Node ID	1	2	3	4	5	6	7	8
Coordinates	-2,-1,-1	2,-1,-1	-2, 1,-1	2, 1,-1	-2,-1,1	2,-1,1	-2,1,1	2,1,1
Element ID	1	2	3	4	5	6		
Connectivity	1, 3, 8, 4	1, 3, 5, 8	3, 5, 8, 7	1, 2, 4, 6	1, 6, 8, 5	1, 4, 8, 6		

Table 1 Nodal coordinates and element connectivity for the FE model in figure 2

The normal components of linear strain, corresponding to the prescribed displacement field, is analytically obtained as:

$$e_{xx} = \frac{y}{2}, \quad e_{yy} = -\frac{\nu y}{2(1-\nu)}, \quad e_{zz} = 0 \quad (26)$$

The corresponding volumetric strain is given as $e_{xx} + e_{yy} + e_{zz} = \frac{1-2\nu}{2(1-\nu)}y$. This is clearly dependent on the Poisson's ratio ν and the location y . For the given geometry $y \in [-1, 1]$ and Poisson's ratio $\nu = 0.4999$ the volumetric strain is nearly zero. However, for TET4 elements, the volumetric strain due to the use of the shape functions is clearly non-zero as listed in table 2. The large volumetric strains induce high spurious dilatational energy that results in element locking and high stresses.

Strain Component	Element ①	Element ②	Element ③	Element ④	Element ⑤	Element ⑥
e_{xx}	0.25	0.25	0.25	-0.25	-0.25	-0.25
e_{yy}	0	0	0	0	0	0
Volumetric	0.25	0.25	0.25	-0.25	-0.25	-0.25

Table 2 Strain components for each TET4 element for the problem in figure 2

Crystal plasticity constitutive models exhibit isochoric plastic flow, i.e. $\det \mathbf{F}^p = 1$. Since plastic strains are significantly larger than elastic strains, the use of TET4 element in CPFE simulations may result in volumetric locking under different deformation modes, e.g. bending.

3 Locking-Free Formulations for TET4 Elements

Stabilization of TET4 elements, through node-based uniform strain (NUS) formulation was introduced in [10]. While the NUS method has been successful in avoiding volumetric locking, spurious zero energy modes were reported in [11]. Alternately, the \mathbf{F} -bar patch (FP) formulation [12, 13] has been shown to alleviate volumetric locking without the reintroduction of spurious zero energy modes. As an extension to the NUS formulation, a locally integrated B-bar (LIB) element is developed to stabilize TET4 elements in this paper. The methods are termed in this paper as locking free stabilized or LFS-TET4 elements. These formulations are summarized in the context of CPFE formulation in this section.

3.1 Node-based uniform strain (NUS) element formulation

In the NUS formulation, a patch of sub-elements is assigned to each nodal point in the finite element mesh. Consider $\hat{\Omega}^{s,t}$ to denote such a patch assigned to a node s at time t that is defined as:

$$\hat{\Omega}^{s,t} = \sum_{i=1}^{N^s} \Omega_s^{i,t} = \sum_{i=1}^{N^s} \alpha_s^i \Omega^{i,t} \quad (27)$$

N^s corresponds to the number of TET4 elements attached to the node s , $\Omega_s^{i,t}$ is the volume contribution of the i -th TET4 element to the patch $\hat{\Omega}^s$ and α_s^i is a scalar weighting factor. For 3D meshes, $\alpha_s^i = \frac{1}{4}$. Figure 3a illustrates a 2D patch construction method for a node s , while figure 3b shows the partitioning of a 3D TET4 element to generate its contribution $\Omega_s^{i,t}$ to the patch.

Within each patch, the linear strain increment $\hat{\mathbf{e}}^s$ is taken to be uniform and obtained as the average value from surrounding elements, i.e. :

$$\hat{\mathbf{e}}^s = \sum_{i=1}^{N^s} w^i \mathbf{e}^{i,t} = \sum_{i=1}^{N^s} w^i \mathbf{B}^{i,t} \Delta \mathbf{q}^i = \hat{\mathbf{B}}^{s,t} \Delta \hat{\mathbf{q}}^s \quad (28)$$

where w^i is a relative volume-based weight for element i and $\hat{\mathbf{B}}^{t,s}$ is the gradient matrix associated with the patch s that is obtained by assembling $\mathbf{B}^{i,t}$ from surrounding elements with weight w^i . From equation (27) $w^i = \frac{1}{4} \frac{\Omega^{i,t}}{\hat{\Omega}^{s,t}}$. $\Delta \hat{\mathbf{q}}^s$ is the displacement increment vector associated with the patch s , obtained by assembling \mathbf{q}^i from surrounding elements. Nodal averaging of the gradient of displacement increment $\frac{\partial \Delta \mathbf{u}}{\partial \mathbf{x}^t}$ is obtained in the same way as:

$$\left[\frac{\partial \Delta u_1}{\partial x_1^t} \frac{\partial \Delta u_1}{\partial x_2^t} \frac{\partial \Delta u_1}{\partial x_3^t} \dots \frac{\partial \Delta u_3}{\partial x_1^t} \frac{\partial \Delta u_3}{\partial x_2^t} \frac{\partial \Delta u_3}{\partial x_3^t} \right]_{patch \ s}^T = \sum_{i=1}^{N^s} w^i \mathbf{G}^{i,t} \Delta \mathbf{q}^i = \hat{\mathbf{G}}^{s,t} \Delta \hat{\mathbf{q}}^s \quad (29)$$

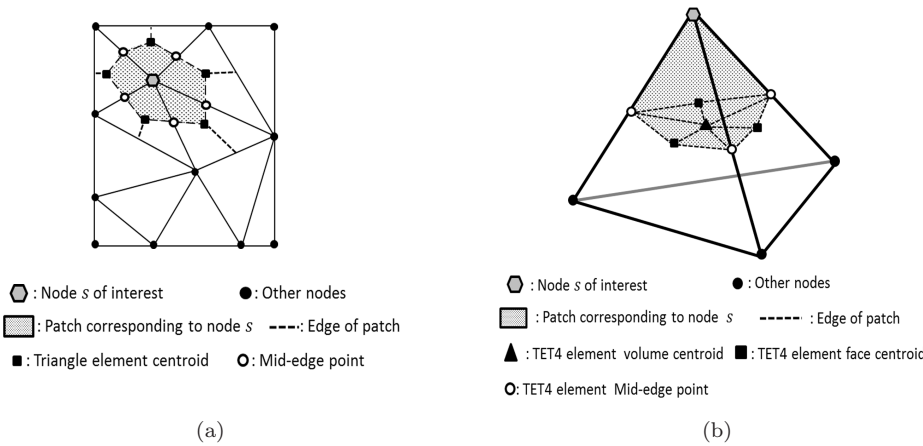


Fig. 3 (a) 2D patch construction for node s ; (b) 3D volume partitioning $\Omega_s^{i,t}$ for node s , in the NUS method .

$\hat{\mathbf{G}}^{s,t}$ is the gradient matrix associated with the patch s created by assembling $\mathbf{G}^{i,t}$ from surrounding elements with weight w^i . From equation (7), (28) and (29) it is seen that the strain increment $\Delta\mathbf{E}$ over the patch is uniform, which makes the cumulative strain uniform as well.

The linearized weak form (8) with constant strain patches is represented for the discrete model as:

$$\sum_{s=1}^{N_{nodes}} \int_{\hat{\Omega}^{s,t}} \mathbf{C}^{s,t} : \hat{\mathbf{e}}^s \delta \hat{\mathbf{e}}^s d\hat{\Omega}^{s,t} + \sum_{s=1}^{N_{nodes}} \int_{\hat{\Omega}^{s,t}} \boldsymbol{\sigma}^{s,t} : \delta \hat{\boldsymbol{\eta}}^s d\hat{\Omega}^{s,t} = R^{ext^{t+\Delta t}} - \sum_{s=1}^{N_{nodes}} \int_{\hat{\Omega}^{s,t}} \boldsymbol{\sigma}^{s,t} : \delta \hat{\mathbf{e}}^s d\hat{\Omega}^{s,t} \quad (30)$$

where $\boldsymbol{\sigma}^{s,t}$ is the Cauchy stress, obtained from the constitutive model, and $\mathbf{C}^{s,t}$ is the crystal plasticity tangent stiffness matrix in node-based patch s . The NUS formulation assumes that $\mathbf{C}^{s,t}$ and $\boldsymbol{\sigma}^{s,t}$ are also uniform and constant over the patch s . Thus the one-point numerical integration may be used for each patch and the crystal plasticity constitutive updates are made for the node of the patch. This removes volumetric locking through a reduction in the number of incompressibility constraints. The incompressibility constraint ratio approaches an optimal value of 3. Substituting equation (28) and (29) into equation (30), the tangent stiffness matrix and internal nodal force vector are derived as:

$$\mathbf{K}^t = \sum_{s=1}^{N_{nodes}} \hat{\mathbf{B}}^{s,t,T} \mathbf{C}^{s,t} \hat{\mathbf{B}}^{s,t} \hat{\Omega}^{s,t} + \sum_{s=1}^{N_{nodes}} \hat{\mathbf{G}}^{s,t,T} \boldsymbol{\sigma}^{s,t} \hat{\mathbf{G}}^{s,t} \hat{\Omega}^{s,t} \quad (31a)$$

$$\mathbf{f}^{int^t} = \sum_{s=1}^{N_{nodes}} \hat{\mathbf{B}}^{s,t,T} \boldsymbol{\sigma}^{s,t} \hat{\Omega}^{s,t} \quad (31b)$$

This node-based uniform strain (NUS) element has however been reported to exhibit spurious zero or low energy modes in [15]. Such spurious energy modes can

cause large distortion of the TET4 element and eventually lead to a negative determinant of the Jacobian matrix.

3.2 Locally integrated B-bar (LIB) element

Several stabilization methods have been developed to overcome the zero-energy modes in the original NUS formulation [11, 15]. These methods are based on splitting the stress or the tangent stiffness matrix \mathbf{C} . Such decomposition is not however possible in CPFE analysis with anisotropic elasto-plastic stiffness matrix \mathbf{C} . To overcome this issue, a locally integrated B-bar (LIB) based element is proposed in this paper. Following procedures in [42], the linear strain increment is decomposed into volumetric and deviatoric parts by splitting the gradient matrix \mathbf{B} in this formulation, i.e.

$$\mathbf{e} = \mathbf{e}^{vol} + \mathbf{e}^{dev} = \mathbf{B}^{vol} \Delta \mathbf{q} + \mathbf{B}^{dev} \Delta \mathbf{q} \quad (32)$$

Only the volumetric part of the linear strain increment \mathbf{e}^{vol} is assumed to be uniform inside the patch for each node to reduce constraints. For node s , the uniform volumetric strain increment $\hat{\mathbf{e}}^{s,vol}$ is obtained as:

$$\hat{\mathbf{e}}^{s,vol} = \sum_{i=1}^{N^s} w^i \mathbf{e}^{i,vol} = \sum_{i=1}^{N^s} w^i \mathbf{B}^{i,vol} \Delta \mathbf{q}^i = \bar{\mathbf{B}}^{s,vol} \Delta \hat{\mathbf{q}}^s \quad (33)$$

$\bar{\mathbf{B}}^{s,vol}$ is the volumetric part of the gradient matrix associated with patch s that is assembled from surrounding element $\mathbf{B}^{i,vol}$'s with weights w^i . The deviatoric part of the strain increment \mathbf{e}^{dev} is constant over each TET4 element. This leads to two separate distributions of the volumetric and deviatoric strain increment over the domain, as illustrated in figure 4.

Each TET4 element is divided into 4 equal sub-domains. Within each sub-domain, the volumetric and deviatoric parts of the strain increment are constant. The strain increment in a sub-domain $\Omega^{i,s}$ is thus represented as:

$$\bar{\mathbf{e}}^{i,s} = \bar{\mathbf{e}}^{s,vol} + \mathbf{e}^{i,dev} = \bar{\mathbf{B}}^{s,vol} \Delta \hat{\mathbf{q}}^s + \mathbf{B}^{i,dev} \Delta \mathbf{q}^i = \bar{\mathbf{B}}^{i,s} \Delta \hat{\mathbf{q}}^s \quad (34)$$

$\bar{\mathbf{B}}^{i,s}$ is the modified gradient matrix associated with sub-domain $\Omega^{i,s}$. Note that $\Delta \mathbf{q}^i$ is contained in $\Delta \hat{\mathbf{q}}^s$ as shown in equation (28). Thus it allows the additive decomposition $\bar{\mathbf{B}}^{i,s} = \bar{\mathbf{B}}^{s,vol} + \mathbf{B}^{i,dev}$. Analogous to \mathbf{B} , the 9×12 gradient matrix \mathbf{G} can be split into volumetric and deviatoric parts i.e. $\mathbf{G} = \mathbf{G}^{vol} + \mathbf{G}^{dev}$. The explicit form of \mathbf{G}^{vol} is :

$$\mathbf{G}^{vol} = [\mathbf{G}_{n1}^{vol}, \mathbf{G}_{n2}^{vol}, \mathbf{G}_{n3}^{vol}, \mathbf{G}_{n4}^{vol}] \quad (35)$$

where $n1, \dots, n4$ are the local node indices in the element. For any $a \in [n1, \dots, n4]$, \mathbf{G}_a^{vol} is explicitly written as:

$$\mathbf{G}_a^{vol} = \begin{bmatrix} G_1 & G_2 & G_3 \\ 0 & 0 & 0 \\ 0 & 0 & 0 \\ 0 & 0 & 0 \\ G_1 & G_2 & G_3 \\ 0 & 0 & 0 \\ 0 & 0 & 0 \\ 0 & 0 & 0 \\ G_1 & G_2 & G_3 \end{bmatrix} \quad (36)$$

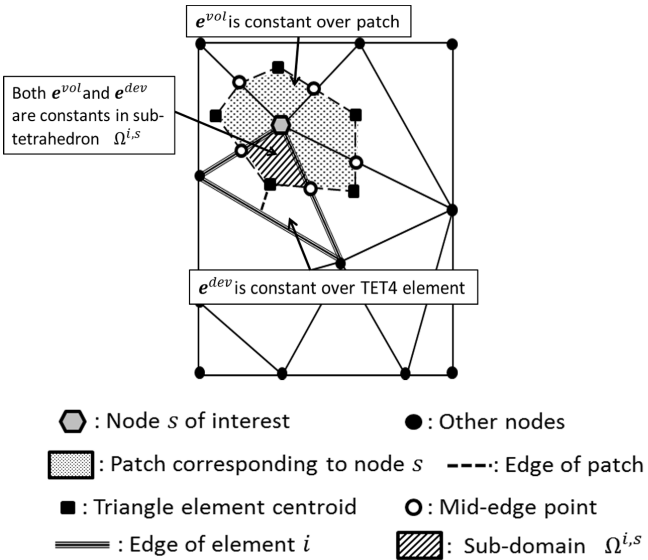


Fig. 4 Strain distributions in the patch, tetrahedron and sub-domain of tetrahedron in the LIB method.

where $G_i = \frac{\partial N_a}{\partial x_i}$ and N_a is the shape function associated with node a . Substituting \mathbf{G}^{vol} and \mathbf{G}^{dev} , the 9×1 displacement gradient vector in the sub-domain $\Omega^{i,s}$ is expressed as:

$$\left[\frac{\partial \Delta u_1}{\partial x_1^t} \frac{\partial \Delta u_1}{\partial x_2^t} \frac{\partial \Delta u_1}{\partial x_3^t} \dots \frac{\partial \Delta u_3}{\partial x_1^t} \frac{\partial \Delta u_3}{\partial x_2^t} \frac{\partial \Delta u_3}{\partial x_3^t} \right]_{\Omega_s^i}^T = \bar{\mathbf{G}}^{s,vol} \Delta \hat{\mathbf{q}}^s + \mathbf{G}^{i,dev} \Delta \mathbf{q}^i = \bar{\mathbf{G}}^{i,s} \Delta \hat{\mathbf{q}}^s \quad (37)$$

Correspondingly, the linearized weak form (8) with constant strain sub-domains reduces to:

$$\sum_{i=1}^{N_{sub-tet}} \int_{\Omega^{i,t}} \mathbf{C}^{i,t} : \bar{\mathbf{e}}^i \delta \bar{\mathbf{e}}^i d\Omega^{i,t} + \sum_{i=1}^{N_{sub-tet}} \int_{\Omega^{i,t}} \boldsymbol{\sigma}^{i,t} : \delta \bar{\boldsymbol{\eta}}^i d\Omega^{i,t} = R^{ext^{t+\Delta t}} - \sum_{i=1}^{N_{sub-tet}} \int_{\Omega^{i,t}} \boldsymbol{\sigma}^{i,t} : \delta \bar{\mathbf{e}}^i d\Omega^{i,t} \quad (38)$$

where $N_{sub-tet}$ ($= 4 \times N_e$) is the total number of sub-domains and $\Omega^{i,t}$ is the sub-domain volume at time t . $\boldsymbol{\sigma}^{i,t}$ and $\mathbf{C}^{i,t}$ are updated using the crystal plasticity constitutive models. Again it is assumed they are uniform and constant over the sub-domain i and one-point numerical integration can be used.

$\mathbf{C}^{i,t+\Delta t}$ and $\boldsymbol{\sigma}^{i,t+\Delta t}$ depend on the deformation gradient \mathbf{F}_0^t , as well as other history-dependent state variables. In the LIB element formulation, the evaluation of $\mathbf{F}_0^{t+\Delta t}$ in each sub-domain must be consistent with the interpolation of strain with $\bar{\mathbf{B}}$. This is achieved using the following relation:

$$\mathbf{F}_0^{t+\Delta t} = \mathbf{F}_t^{t+\Delta t} \mathbf{F}_0^t = \left(\mathbf{I} + \frac{\partial \Delta \mathbf{u}}{\partial \mathbf{x}^t} \right) \frac{\partial \Delta \mathbf{x}^t}{\partial \mathbf{x}^0} = (\mathbf{I} + \bar{\mathbf{G}}^t \Delta \mathbf{q}) \frac{\partial \Delta \mathbf{x}^t}{\partial \mathbf{x}^0} \quad (39)$$

Substituting equations (34) and (37) into (38), the tangent stiffness matrix and internal nodal force vector in the LIB element formulation are expressed as:

$$\mathbf{K}^t = \sum_{i=1}^{N_{sub-tet}} \bar{\mathbf{B}}^{i,t} {}^T \mathbf{C}^{i,t} \bar{\mathbf{B}}^{i,t} \Omega^{i,t} + \sum_{i=1}^{N_{sub-tet}} \bar{\mathbf{G}}^{i,t} {}^T \tilde{\boldsymbol{\sigma}}^{i,t} \bar{\mathbf{G}}^{i,t} \Omega^{i,t} \quad (40a)$$

$$\mathbf{f}^{int,t} = \sum_{i=1}^{N_{sub-tet}} \bar{\mathbf{B}}^{i,t} {}^T \boldsymbol{\sigma}^{i,t} \Omega^{i,t} \quad (40b)$$

The LIB element selectively reduces the volumetric strain components over the node-based patch and keeps the deviatoric strain components unchanged in each tetrahedral element. This stabilization method effectively alleviates volumetric locking without introducing spurious zero-energy modes.

3.3 F-bar patch-based (FP) element

The **F**-bar patch (FP) based stabilization method has been proposed in [12] for relieving volumetric locking in lower order tetrahedral elements. The **F**-bar patch method modifies the deformation gradient for stress tensor calculations such that incompressibility is enforced in the element in a weak sense, rather than a pointwise enforcement.

The Cauchy stress at the end of a time interval $[t, t + \Delta t]$ may be computed in terms of the deformation gradient and state variables α_t at time t as:

$$\boldsymbol{\sigma}^{t+\Delta t} = \boldsymbol{\sigma}(\alpha_t, \mathbf{F}^{t+\Delta t}) \quad (41)$$

The deformation gradient is decomposed into isochoric and volumetric components as:

$$\mathbf{F} = \mathbf{F}_{iso} \mathbf{F}_{vol} \quad \text{where } \mathbf{F}_{iso} = (\det \mathbf{F})^{-\frac{1}{3}} \mathbf{F} \quad \text{and } \mathbf{F}_{vol} = (\det \mathbf{F})^{\frac{1}{3}} \mathbf{I} \quad (42)$$

In the original **F**-bar formulation for four-node quadrilateral and eight-node hexahedral elements in [21], \mathbf{F} is first calculated at all Gauss quadrature points, as well as \mathbf{F}_0 at the element centroid. Subsequently, the stabilized deformation gradient $\bar{\mathbf{F}}$ at the Gauss points are obtained by replacing the volumetric component with its value at the centroid, i.e.

$$\bar{\mathbf{F}} = \mathbf{F}_{iso} (\mathbf{F}_0)_{vol} = \left(\frac{\det \mathbf{F}_0}{\det \mathbf{F}} \right)^{\frac{1}{3}} \mathbf{F} \quad (43)$$

This implies that the determinant of $\bar{\mathbf{F}}$ within the element is equal to the determinant of \mathbf{F}_0 . Thus, incompressibility in the constitutive model is enforced only at the centroid of the element, rather than at all Gauss points. The constitutive model is then solved at Gauss points using $\bar{\mathbf{F}}$, i.e.

$$\boldsymbol{\sigma}^{t+\Delta t} = \boldsymbol{\sigma}(\alpha_t, \bar{\mathbf{F}}^{t+\Delta t}) \quad (44)$$

This methodology has been effective in overcoming volumetric locking for bilinear quadrilateral and trilinear hexahedral elements in [21]. However it is not directly

applicable to linear tetrahedral elements as they have only one Gauss point located at the element centroid. Additionally the deformation gradient is constant in the element and hence, $\bar{\mathbf{F}}$ in equation (43) becomes:

$$\bar{\mathbf{F}} = \mathbf{F}_0 = \mathbf{F} \quad (45)$$

Clearly, this relation will not help in overcoming volumetric locking in TET4 elements in the incompressibility limit. A modified formulation has been proposed in [12] where constitutive incompressibility is enforced over a patch of elements, rather than in each element. This requires that elements in the mesh be assigned to non-overlapping patches as illustrated in figure 5 in 2D. Let \mathcal{P} denote a set of

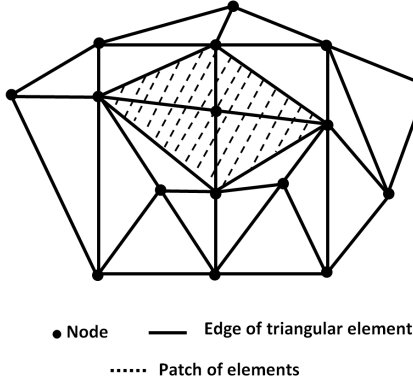


Fig. 5 Patch of elements in the \mathbf{F} -bar-patch method

elements forming a patch. The modified deformation gradient for element $K \in \mathcal{P}$, is defined as

$$\bar{\mathbf{F}}_K = \left[\frac{\Omega_{patch}^{t+\Delta t}}{\Omega_{patch}^0 \det \mathbf{F}_K} \right]^{\frac{1}{3}} \mathbf{F}_K \quad (46)$$

where $\Omega_{patch}^{t+\Delta t}$ and Ω_{patch}^0 are respectively the current and undeformed volumes of the patch \mathcal{P} , calculated as:

$$\Omega_{patch}^0 = \sum_{K \in \mathcal{P}} \Omega^{K,0} \quad , \quad \Omega_{patch}^{t+\Delta t} = \sum_{K \in \mathcal{P}} \Omega^{K,t+\Delta t} \quad (47)$$

It is noteworthy that \mathbf{F} -bar patch method reduces to the conventional tetrahedral element formulation if each element is identified with a patch. Adding more elements to the patch relaxes the incompressibility constraint ratio and helps relieve volumetric locking. However, the presence of too many elements in a patch may result in spurious energy modes. Through numerical experiments, it was inferred in [13] that 8 elements per patch is adequate for 3D problems without spurious mechanisms.

The internal force vector in the \mathbf{F} -bar patch method is evaluated using the modified deformation gradient in equation (46) as:

$$\mathbf{f}^{intK} = \Omega^{K,t} \mathbf{B}^{K,t^T} \boldsymbol{\sigma}^{K,t} \quad (48)$$

The tangent stiffness matrix has a non-conventional structure in the sense that it not only depends on the degrees of freedom of the element, but also on the degrees of freedom of other elements in the patch. The tangent stiffness matrix for element K is derived as:

$$\mathbf{K}^{KK} = \Omega^{K,t} \mathbf{G}^{K,tT} \mathbf{a} \mathbf{G}^{K,t} + \left(\frac{\Omega^{K,t}}{\Omega_{patch}^t} - 1 \right) \Omega^{K,t} \mathbf{G}^{K,tT} \mathfrak{S} \mathbf{G}^{K,t} \quad (49a)$$

$$\mathbf{K}^{KJ} = \frac{\Omega^{K,t}{}^2}{\Omega_{patch}^t} \mathbf{G}^{K,tT} \mathfrak{S} \mathbf{G}^{J,t}, \quad J \in \mathcal{P}; \quad J \neq K \quad (49b)$$

Here \mathbf{K}^{KK} corresponds to stiffness components whose rows and columns are associated with the degrees of freedom of element K , whereas \mathbf{K}^{KJ} corresponds to components whose rows and columns are respectively associated with the degrees of freedom of elements K and J in the patch, *s.t.* $J \neq K$. The fourth-order spatial elasticity tensor \mathbf{a} is evaluated at $\mathbf{F} = \bar{\mathbf{F}}$ [13], as

$$a_{ijkl} = \frac{1}{\det \mathbf{F}} A_{imkn} F_{jm} F_{ln} \quad (50)$$

where \mathbf{A} denotes the elasticity tensor derived from the first Piola-Kirchhoff stress \mathbf{P} as $A_{imkn} = \frac{\partial P_{im}}{\partial F_{kn}}$. \mathfrak{S} in equation (49) corresponds to the fourth-order tensor $\mathfrak{S} = \frac{1}{3} \mathbf{a} : (\mathbf{I} \otimes \mathbf{I}) - \frac{2}{3} (\boldsymbol{\sigma} \otimes \mathbf{I})$.

The FP method is flexible to be used for various material constitutive models. Its implementation in any standard displacement-based FE code is quite straightforward as DOFs are merely nodal displacements and constitutive updates are performed at the element quadrature points. While the calculation of internal force vector is similar to that for TET4 elements, evaluation and assembly of the tangent stiffness matrix in (49) requires more attention.

4 LIB and FP Stabilization Methods in Polycrystalline CPFE Models

This section examines the application of LIB and FP induced LFS-TET4 elements to finite element models of polycrystalline microstructures, incorporating non-local rate-dependent crystal plasticity constitutive models. A special feature of these models is that they must account for discrete polycrystalline grain boundaries in the construction of the FE mesh and associated sub-structures. The constitutive update algorithms for the time increment between t and $t + \Delta t$, use implicit time integration methods [34] to evaluate the Cauchy stress $\hat{\boldsymbol{\sigma}}^{t+\Delta s,t}$, slip rates and all deformation state variables, as well as evaluating the fourth-order tangent moduli tensor $\mathbf{C}^{t+\Delta s,t}$. Important steps in the implementation are discussed next.

4.1 Creating stabilization patches conforming to grain boundaries

For polycrystalline microstructures, the node-based patches needed with the LIB and the FP methods must conform to the grain structures. Consider a node s located on the grain boundary of a 2D model as shown in figure 6. Slip systems are

not continuous across the boundary of grains with crystallographic misorientation, which leads to discontinuities in the plastic strains. With this consideration, the patch assigned to the node s should not cross grain boundaries. It is not logical to construct and smooth over a single patch for a grain boundary node that connects multiple grains. Correspondingly sub-patches that are exclusive to a single grain are created with representation:

$$\hat{\Omega}^{s,t} = \hat{\Omega}_{grain_1}^{s,t} + \hat{\Omega}_{grain_2}^{s,t} \quad (51a)$$

$$\text{where } \hat{\Omega}_{grain_1}^{s,t} = \sum_{K=1}^{N_{grain_1}^s} \frac{1}{4} \Omega^{K,t} \quad \text{and} \quad \hat{\Omega}_{grain_2}^{s,t} = \sum_{J=1}^{N_{grain_2}^s} \frac{1}{4} \Omega^{J,t} \quad (51b)$$

Here $N_{grain_1}^s$ and $N_{grain_2}^s$ correspond to the number of TET4 elements attached to a node s that is common to grains 1 and 2. This procedure can be generalized for nodes at triple and quadruple points. The smoothing process, and evaluation of constitutive variables, tangent stiffness matrix and internal forces, are carried out separately for each sub-patch.

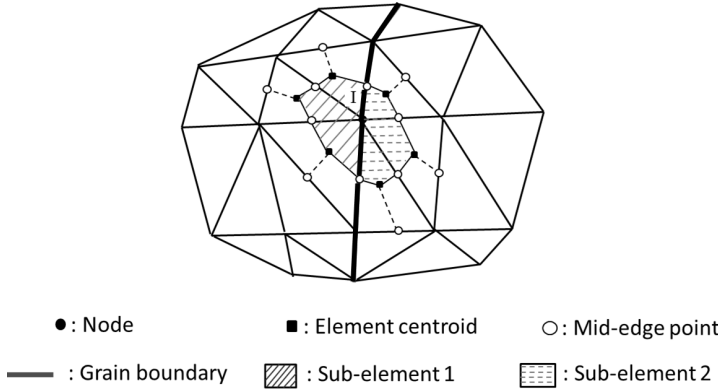


Fig. 6 Constructing sub-patches for nodes on grain boundary in polycrystalline microstructures.

4.2 Evaluating GNDs using a super-convergent patch recovery method

Numerical evaluation of $\{\Lambda\}$ requires computing the derivatives of the plastic deformation gradient. This renders the model to be non-local. Using the linear TET4 shape functions, the Nye tensor is evaluated at any given point inside an element as:

$$\Lambda_{ij} = \varepsilon_{jrs} \frac{\partial \hat{F}_{ir}^p}{\partial x_s^0} = \varepsilon_{jrs} \sum_{\alpha=1}^4 \left(\hat{F}_{ir}^p \right)^\alpha \frac{\partial N^\alpha}{\partial x_s^0} \quad (52)$$

where ε_{jrs} is the permutation tensor component, $(\hat{F}_{ij}^p)^\alpha$ are components of the nodal plastic deformation gradient tensor and N^α are shape functions.

An appropriate interpolation technique should be adopted for calculating the nodal plastic deformation gradient tensor to avoid numerical error in evaluating GND densities resulting in spurious high local stresses. The super-convergent patch recovery (SPR) method in [43] is deemed to be the most appropriate method for this purpose. The SPR method evaluates nodal values inside a super-convergent patch Ω_p by interpolating the variables using a higher order polynomial expansion as:

$$F_{ij}^p(\mathbf{x}) = [\mathbf{P}(\mathbf{x})] \{a\}^{ij} \quad (53)$$

where $F_{ij}^p(\mathbf{x})$ represents a higher order representation of components of plastic deformation gradient at a point \mathbf{x} in the patch. $[\mathbf{P}(\mathbf{x})]$ is the interpolation matrix containing polynomial basis functions as:

$$[\mathbf{P}(\mathbf{x})] = [1, x, y, z, x^2, y^2, z^2, xy, yz, zx, \dots] \quad (54)$$

$\{a\}^{ij}$ is the coefficient vector that is obtained by least squares minimization of the difference between the function in equation (53) and known values of F_{ij}^p at the quadrature points of the elements in the patch. The functional to be minimized with respect to $\{a\}^{ij}$ is

$$f(\{a\}^{ij}) = \sum_{I=1}^{N_P} \left(F_{ij}^p(x, y, z) - [\mathbf{P}(x, y, z)] \{a\}^{ij} \right)_I^2 \quad (55)$$

N_P is the number of elements in the super-convergent patch. The solution to this minimization problem is given in [43] as:

$$\{a\}^{ij} = [\mathbf{X}]^{-1} \{y\}^{ij} \quad (56)$$

where

$$[\mathbf{X}] = \sum_{I=1}^{N_P} [\mathbf{P}(x, y, z)]_I^T [\mathbf{P}(x, y, z)]_I \quad (57a)$$

$$\{y\}^{ij} = \sum_{I=1}^{N_P} [\mathbf{P}(x, y, z)]_I^T F_{ij}^p(x, y, z)_I \quad (57b)$$

Nodal values of F_{ij}^p are evaluated using equation (53). The super-convergent patches can be defined separately for each node by selecting the appropriate surrounding elements. The selection of this patch is important to avoid the ill-conditioning of \mathbf{X} . Typically normalized coordinates are used in the construction of $[\mathbf{P}(x, y, z)]$ [43] as:

$$\bar{x} = -1 + 2 \frac{x - x_{min}}{x_{max} - x_{min}}, \quad \bar{y} = -1 + 2 \frac{y - y_{min}}{y_{max} - y_{min}}, \quad \bar{z} = -1 + 2 \frac{z - z_{min}}{z_{max} - z_{min}} \quad (58)$$

Subscripts *max* and *min* correspond to the maximum and minimum coordinates in the patch. The normalized coordinates lie within the bounds $-1 \leq \bar{x} \leq 1$,

$-1 \leq \bar{y} \leq 1$, and $-1 \leq \bar{z} \leq 1$. A weighted least square method is used in this work that can be used with large patches without discrimination. In this method, a weighting function is used which exponentially decays with the distance of the node from the element centroids in the patch. The functional in (55) is correspondingly modified as:

$$f(\{\mathbf{a}\}^{ij}) = \sum_{I=1}^{N_P} w_I \left(F_{ij}^p(x, y, z) - [\mathbf{P}(x, y, z)] \{\mathbf{a}\}^{ij} \right)_I^2 \quad (59)$$

The exponentially decaying weight is chosen as $w_I = \exp(-d_I/\alpha)$. d_I is the distance from the centroid of I th element in the patch to the node in question and α is the decay length. It is selected such that enough elements lie within this decay length to yield a recovery matrix $[\mathbf{X}]$ with a good condition number.

5 Numerical Examples and Discussions

The performance of the locally integrated B-bar (LIB) and F-bar patch (FP) based TET4 elements in CPFE analysis of polycrystalline materials is studied in this section. A standard patch test is performed in the first example. Subsequently an elastic bending problem and several crystal plasticity examples, including a bicrystal compression test, polycrystalline beam bending and constant strain rate deformation of a polycrystalline aggregate, are solved. The results are compared with those of the standard TET4 element. When possible, the 8-noded hexahedral element with B-bar stabilization method is used to generate reference solutions for comparison. The computational costs for different element formulations are then compared for a crystal plasticity problem. For crystal plasticity problems, two low-symmetry *HCP* metallic alloys, viz. a magnesium alloy *AZ31* and titanium alloy *Ti6Al*, are chosen for numerical simulations. For Mg alloy simulations, the constitutive model presented in section 2.1 is used, while a constitutive model described in [2] is used for Ti alloys.

5.1 Element patch test

The patch test is a necessary condition that should be satisfied for all elements in a finite element ensemble. This test is performed on a $20 \times 20 \times 40$ cube discretized into 48 TET4 elements with 8 nodes on the outer surfaces and 13 nodes inside the cube. The material is assumed to be isotropic, linear elastic. Nodal displacements on the outer surfaces are prescribed using linear functions as:

$$\Delta u_1 = \frac{z+20}{200} - \frac{x-10}{100}, \quad \Delta u_2 = \frac{z+20}{200} - \frac{y-10}{100}, \quad \Delta u_3 = 0 \quad (60)$$

Nodal displacements inside the cube are calculated for NUS, LIB and FP based TET4 elements. A norm of the displacement error is defined as:

$$\overline{err}_{dis} = \frac{\sum_{\alpha=1}^8 \sum_{i=1}^3 (\mathbf{u}_{\alpha}^{exact} - \mathbf{u}_{\alpha}^{FE})^2}{\sum_{\alpha=1}^8 \sum_{i=1}^3 (\mathbf{u}_{\alpha}^{exact})^2}$$

For both LIB and FP elements $\overline{err}_{dis} \leq 2.22 \times 10^{-15}$ and hence they pass the standard patch test. The NUS element, however, does not pass the patch test since the determinant of the Jacobian of some elements becomes negative and the elements undergo non-physical distortion. This corresponds to the presence of spurious modes in NUS element.

5.2 Bending of an elastic beam

In this example, a nearly incompressible elastic beam, subjected to a bending moment, is solved using the LIB, FP and standard TET4 elements. The material is isotropic, linear elastic with Young's modulus $E = 300$ MPa and Poisson ratio $\nu = 0.4999$. Dimensions of the beam are $4m \times 1m \times 1m$, which is discretized into 31758 elements consisting of 6513 nodes. The bending moment boundary condition is manifested through imposing a linearly distributed normal stress σ_{xx} on the $x = 4.0m$ surface. Displacement boundary conditions are applied on the surface $x = 0.0m$ to constrain rigid body motion, as shown in figure 7.

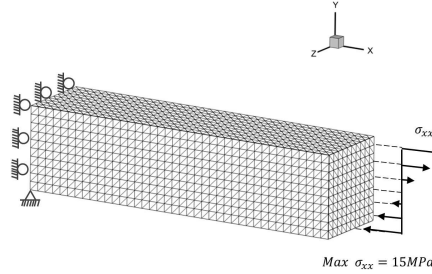


Fig. 7 Mesh and boundary condition for the elastic beam bending problem

TET4 elements exhibits volumetric locking for nearly incompressible materials due to too many incompressibility constraints. To generate a locking-free *reference solution*, the beam is solved using 4961 nodes and 4000 8-noded hexahedral elements with B-bar stabilization [42]. The maximum tip deflections are tabulated in table 3. The results clearly show that the standard TET4 element suffers from severe volumetric locking, resulting in very stiff behavior. The LIB and FP elements, on the other hand, provide satisfactory results in comparison with the reference solution. Convergence of the LIB and FP elements are examined by solving the beam problem with 5 different meshes consisting of 343, 845, 1246, 2929, 6513 nodes respectively. The tip deflections predicted by the LIB and FP elements with a patch size of 4 tetrahedrons (FP4) and FP element with a patch size of 8 tetrahedrons (FP8) are plotted in the figure 8. The reference solution using 8-noded hexahedral element with B-bar stabilization is plotted with the dashed line. The

	8-noded hexahedral element with B-bar stabilization	Standard TET4 element	LIB element	FP element
Beam tip deflection	0.785m	0.271m	0.773m	0.779m

Table 3 Maximum tip deflection of the bending dominated elastic beam at the limits of incompressibility using different element formulations

FP8 element shows the softest response and its solution is closest to the reference solution. This is due to the fact that a larger patch in the FP8 element is able to further reduce the incompressibility constraints. The patch construction for the LIB element formulation does not involve flexible patch size and it is observed that this element solution lies between those of FP4 and FP8 for all the meshes.

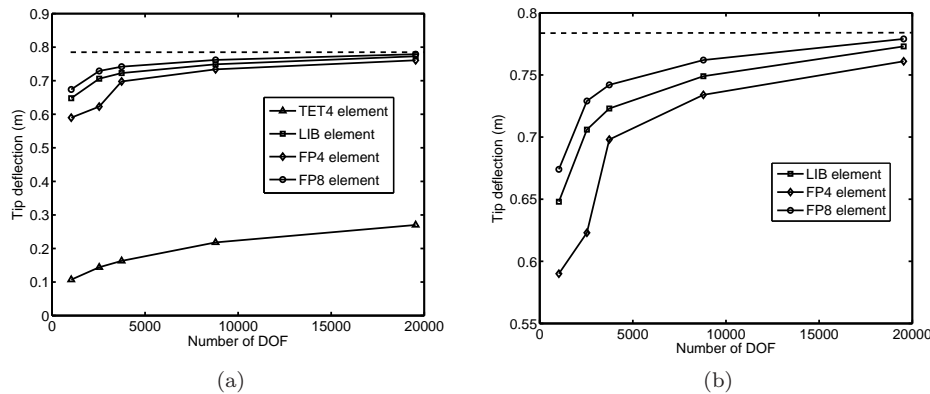


Fig. 8 (a) Convergence of the tip deflection for different element formulations. The dashed line corresponds to the reference solution predicted by 8-noded hexahedral element with B-bar stabilization. (b) zoomed-in view of (a) showing the difference between LIB, FP4 and FP8 elements.

5.3 Bicrystal compression test

A bicrystal uniaxial compression loading test is simulated in this example to understand the effect of volumetric locking in crystal plasticity FE analyses. The loading is applied along Z direction and simulations are conducted using standard TET4, LIB and FP elements. Grain boundaries are important in crystal plasticity analysis as they produce dislocation pile-ups, stress concentration and often trigger failure initiation. A flat simple-tilt grain boundary in the bicrystal is chosen in this example. The grain boundary is characterized by crystal orientations, which have Euler angles $[0^\circ, 0^\circ, 0^\circ]$ and $[0^\circ, 90^\circ, 0^\circ]$ defined in the $Z - X - Z$ convention [44] for crystals 1 and 2 respectively. Both crystals have a dimension of $10\mu\text{m} \times 10\mu\text{m} \times 10\mu\text{m}$, as shown in figure 9a. Displacement boundary conditions are applied on the top surface and minimum displacement boundary conditions

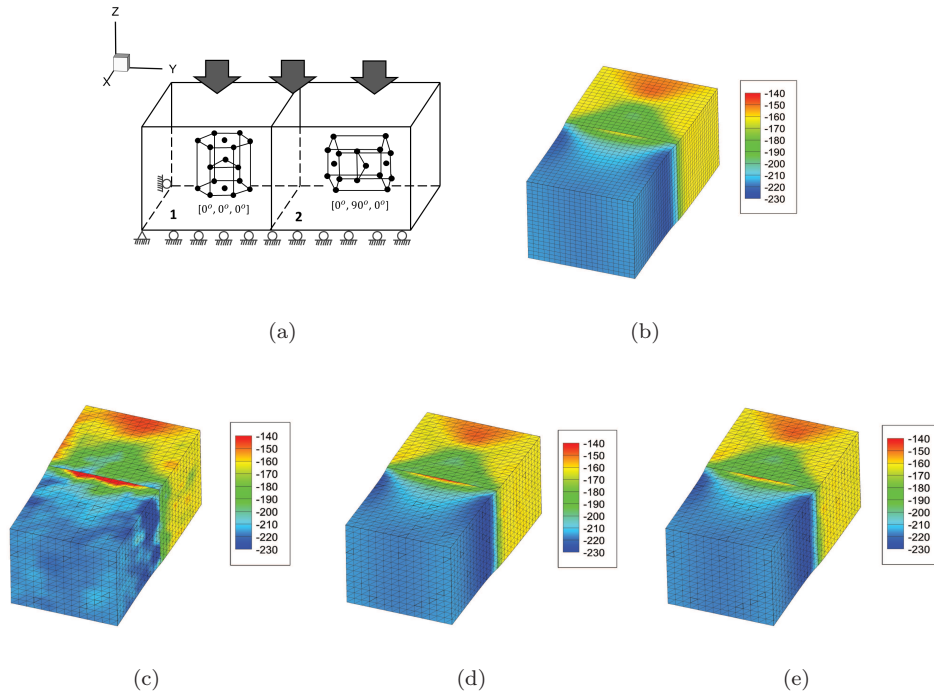


Fig. 9 (a) Illustration of the boundary conditions and the crystallographic orientations for the constant strain rate compression test on a magnesium AZ31 alloy bicrystal; distribution of loading direction stress σ_{zz} in the deformed configuration at 5% strain using simulation results of: (b) 8-noded hexagonal element using B-bar method with a mesh of 18081 nodes, (c) standard TET4 element with a mesh of 11862 nodes, (d) LIB element with a mesh of 11862 nodes, and (e) FP element with a mesh of 11862 nodes.

are imposed on other surfaces to remove the rigid body modes. The material constitutive models are those of the magnesium alloy AZ31 developed in [34].

This example shows that even for uniaxial loading, volumetric locking is observed in crystal plasticity FE analysis. This can be introduced by the lattice structure among grains rather than by external loading. From Schmid factor analysis, plastic deformation is expected to occur primarily on $\langle c+a \rangle$ pyramidal plane in crystal 1 and $\langle a \rangle$ prismatic plane in crystal 2. However dislocation glide may also occur on other slip systems close to the grain boundary as the local stress state deviates from average uniaxial stress state due to the lattice mismatch and plastic strain incompatibilities. Seven different meshes of different density, consisting of 766, 1106, 1583, 2742, 4400, 6421 and 11862 nodes are simulated using the standard TET4, LIB and FP elements. The reference solution, shown in figure 9b, is obtained by solving a mesh of 18081 nodes using the 8-noded hexahedral element with the B-bar stabilization method. The distribution of loading direction stress σ_{zz} using the standard, LIB and FP elements are shown in figures 9c-9e respectively. Very high stress concentration is observed at the grain boundary using standard TET4 element compared to the solution by other stabilized elements.

Additionally, the result of the TET4 element shows a non-smooth distribution of the local stress, which is not seen for solutions with the LIB and FP elements. The error in the stress is evaluated as the L_2 norm of the difference with the reference solution, expressed as:

$$\|e\|_{L_2} = \frac{\left[\int_{\Omega} (\sigma_{ij} - \sigma_{ij}^{ref}) (\sigma_{ij} - \sigma_{ij}^{ref}) d\Omega \right]^{\frac{1}{2}}}{\left(\int_{\Omega} \sigma_{ij} \sigma_{ij} d\Omega \right)^{\frac{1}{2}}} \quad (61)$$

where σ and σ^{ref} are the solution and reference Cauchy stress respectively. The corresponding error plots for different elements with increasing mesh densities are shown in figure 10. The average convergence rate for LIB and FP elements is 0.75. For CPFE analysis, the LIB and FP elements exhibit similar results with much smaller errors compared to the standard TET4 element.

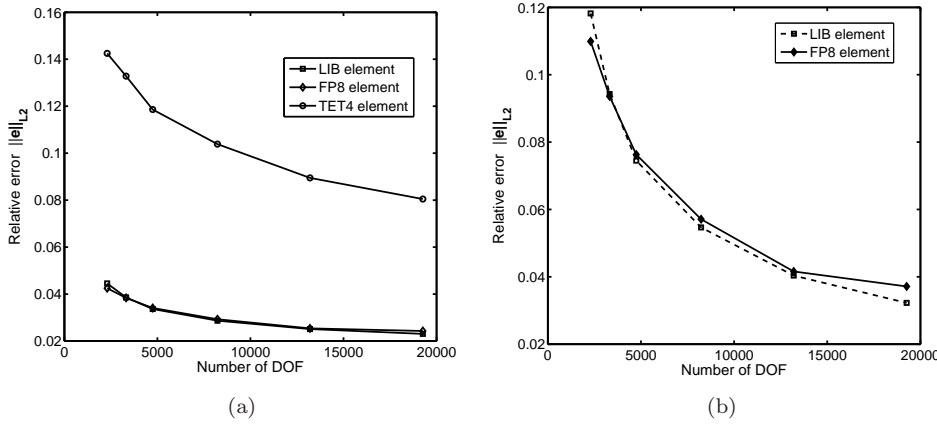


Fig. 10 (a) Error plot of $\|e\|_{L_2}$ with increasing degrees of freedom (DOF). (b) zoomed-in view of (a) to compare the error between FP8 element and LIB element

For further stability analysis, the hydrostatic stress at the grain boundary is plotted in figure 11. Unrealistically large hydrostatic stresses are observed with conventional TET4 elements. With plastic incompressibility, the non-zero volumetric strain at each integration point gives rise to a large strain energy that results in a large hydrostatic stress. LIB and FP elements significantly alleviates this problem and exhibit a saturation of the hydrostatic stress, which is consistent with the results of the stabilized 8-noded hexahedral element. In contrast, all element formulations yield nearly the same values of the von Mises stress, as the deviatoric strain energy is nearly unaffected by volumetric locking for this bicrystal problem. In real polycrystalline microstructures however, the shear stress components are also affected by volumetric locking due to the existence of complex grain boundary patterns.

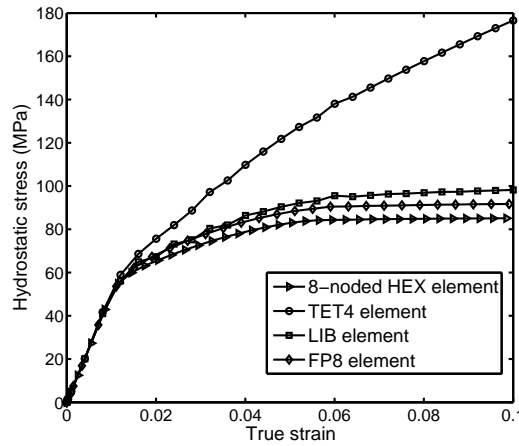


Fig. 11 Evolution of maximum of local hydrostatic stress with strain for different element formulations.

5.4 Bending of a polycrystalline cantilever beam

The effect of volumetric locking on bending of a polycrystalline *Ti6Al* cantilever beam is investigated in this example. The beam is $2000\mu\text{m}$ long with a square cross-section of $300 \times 300\mu\text{m}^2$, as shown in figure 12a. It consists of 327 grains that are cumulatively discretized into 276544 TET4 elements as shown in figure 12a. All 3 translational degrees of freedom are fixed on the left end. A linearly increasing shear traction is imposed in the Y direction on the right end to bend the beam mainly about the Z direction.

Distribution of the effective plastic strain by the different element formulations are plotted in figure 12. At early stages of deformation, the response is primarily elastic and all element formulations predict nearly the same tip deflection with almost no locking. With increasing deformation, the material starts to deform plastically near the fixed end as seen in figure 12b. This leads to formation of a plastic hinge near the clamped end, where the maximum bending moment occurs. As the material undergoes more plasticity near the fixed end further enhances the plastic hinge mechanism and overall rotation is facilitated. Volumetric locking causes less plastic strain with TET4 element than the other two leading to significant under-prediction of the tip deflection.

Figure 13 shows the distribution of hydrostatic stress on the XY face of the beam. A checkerboard type pattern is observed for the analysis done by TET4 elements near the fixed end of the beam where plastic strain is significant. These fluctuations are nearly eliminated in the results from the FP and LIB elements.

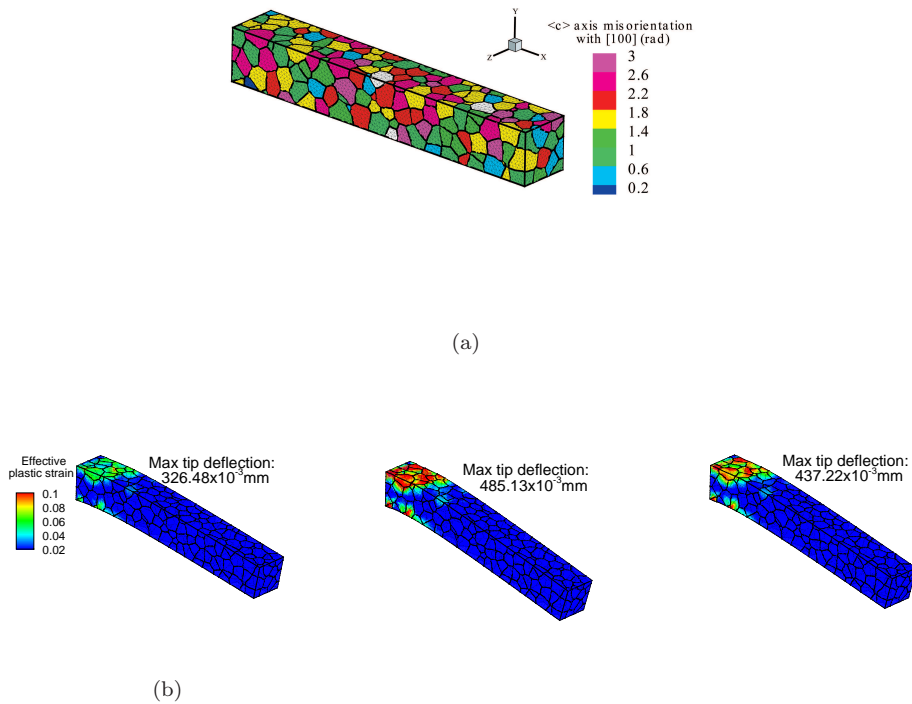


Fig. 12 (a) Schematic of a 327-grain *Ti6Al* polycrystalline beam showing misorientation distribution; (b) distribution of effective plastic strain for different element formulations after 324s

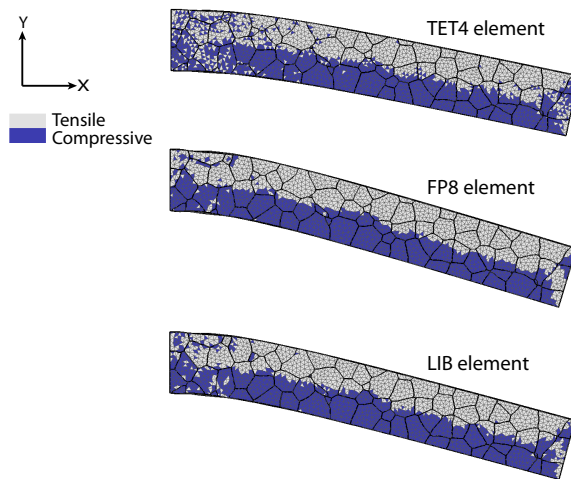


Fig. 13 Distribution of hydrostatic stress on XY face of the beam after 324s using different element formulations.

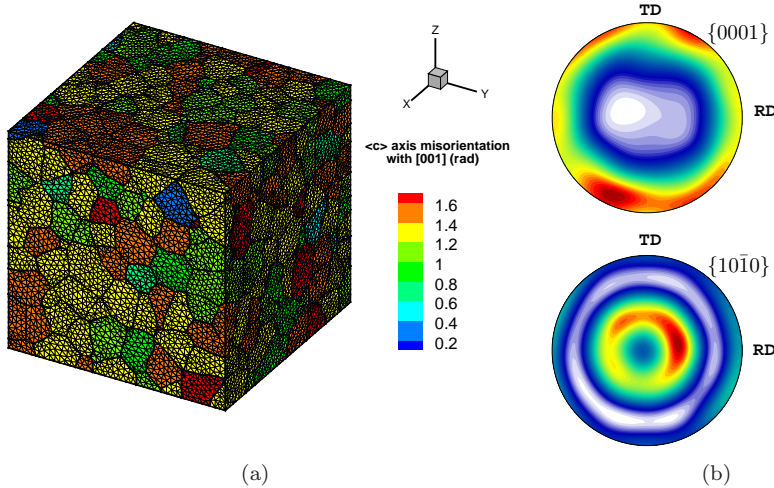


Fig. 14 A 540-grain polycrystalline microstructure of Ti6Al alloy discretized into 583432 TET4 elements.

5.5 Constant strain-rate deformation of a polycrystalline microstructure

CPFE analysis, using different element formulations is performed to investigate the effects of volumetric locking on the response of a polycrystalline microstructure under constant rate of deformation. The $680 \times 680 \times 680 \mu\text{m}^3$ Ti6Al polycrystalline microstructure consists of 540 grains. A constant rate of deformation $\dot{\epsilon} = 9 \times 10^{-5} \text{ s}^{-1}$ is applied in the [001] direction as shown in figure 14 corresponding to the pole figures. Figure 15a shows the results of simulations using different element formulations. In the elastic regime, all formulations predict the same macroscopic response since the material is elastically compressible. With increasing plasticity, response obtained from TET4 element suffers volumetric locking and shows a stiffer response with a higher rate of hardening in comparison with the response predicted by FP8 and LIB elements. The FP8 and LIB elements predict almost the same response. The distribution of hydrostatic stress after 800s, corresponding to nearly 7% strain, in figure 15b clearly shows that TET4 element tends to over-predict hydrostatic stresses. It is observed that the FP8 and LIB elements perform equally well and their results have the same distributions.

5.6 Micro-twin nucleation in polycrystalline magnesium

Micro-twin nucleation in magnesium alloys is of significant interest for a wide range of applications [45–48]. The effect of volumetric locking in CPFE analysis with respect to micro-twin nucleation is illustrated in this example. A detailed CPFE framework has been established in [34] with the capability of capturing microstructural twin nucleation. The model considers non-planar dissociation of a sessile pyramidal $\langle c+a \rangle$ dislocation into a stable twin nucleus, which can propagate under applied in-plane shear stress and leave behind a sessile stair-rod dis-

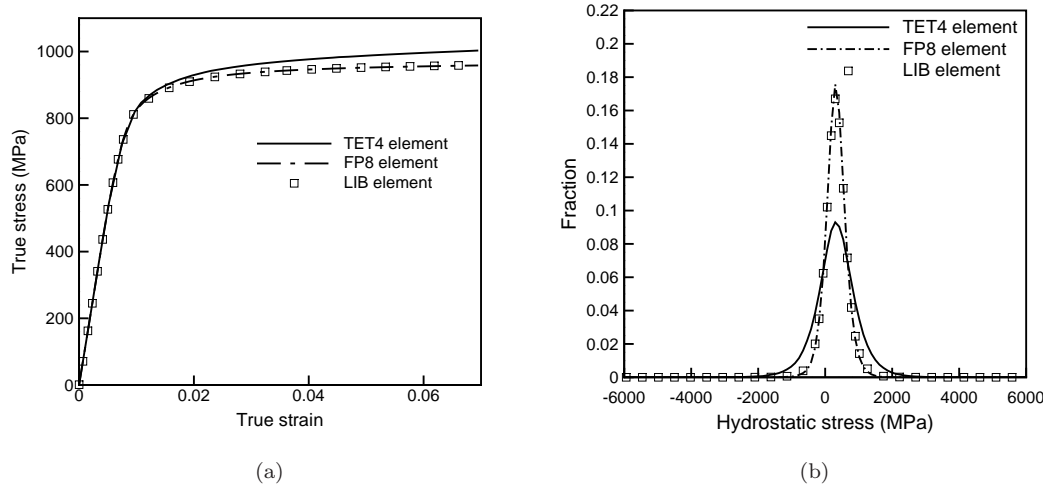


Fig. 15 Comparison of (a) loading-direction true stress-strain response of polycrystalline Ti-6Al alloy under uniaxial tension in the [001] direction, and (b) distribution of hydrostatic stress in the polycrystalline microstructure after 800s, by the different methods.

location to conserve the Burger's vector. Energetic analysis of the dissociation process using 3D elastic theory of dislocations suggests that a stable twin nucleus will form if the following energy-based criteria are satisfied:

$$\begin{aligned} E_{ini} &\geq E_{tw}(d=0) + E_r \quad \text{and} \\ E_{ini} &> E_F(d_s, \tau_{tw}) \quad \forall d_s > 2r_0 \end{aligned} \quad (62)$$

where E_{ini} is the initial energy of the system given by the self-energy of the sessile $\langle c+a \rangle$ dislocation before dissociation. After dissociation occurs, E_{tw} is the self-energy of the twinning dislocation loop, E_r is the self-energy of the stair-rod dislocation, d is the separation distance between the front segment of twinning dislocation loop and the stair-rod dislocation. E_F is the post dislocation energy of the system after dissociation. The first criterion states that the formation of the two partial dislocations are energetically favorable only if the initial energy exceeds the energy of the two partials before any further separation. The second criterion states that the equilibrium separation is energetically favorable and the process is irreversible if the final energy at a saddle point is less than the initial energy, and the saddle point must exceed a threshold separation distance ($d_s > 2r_0$). Critical twin nucleation parameters in equation (62) have been calibrated from experiments in [34].

The CPFE simulation of micro-twin nucleation is conducted on a statistically-equivalent $40\mu\text{m} \times 40\mu\text{m} \times 40\mu\text{m}$ virtual microstructure of the polycrystalline Mg alloy AZ31, as shown in figure 17. The virtual microstructure is constructed using the DREAM.3D software [49] following methods described in [50, 51]. It contains 103 grains with an average grain size of $10\mu\text{m}$, and matches morphological and crystallographic statistics with electron back-scattered diffraction (EBSD)

data obtained from experiments in [52, 53]. The microstructure is discretized into 113425 tetrahedral elements with 21463 nodes. Displacement boundary conditions at a rate of $0.004\mu\text{m}/\text{s}$ are applied on the two surfaces in Y-direction, which tend to bend the microstructure about X-axis on Y-Z plane

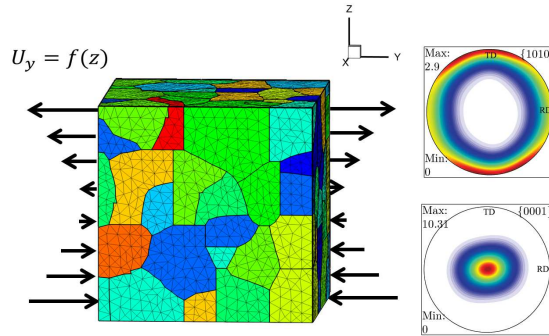


Fig. 16 Schematic of the applied bending boundary condition to polycrystalline Mg alloy AZ31, and the $\{0001\}$ and $\{10\bar{1}0\}$ pole figures showing the texture of the polycrystalline microstructure.

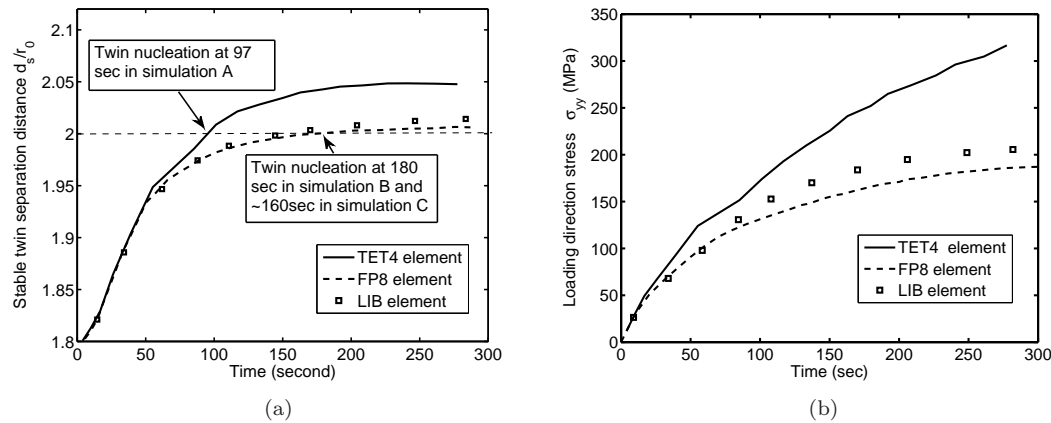


Fig. 17 (a) Stable micro-twin dissociation distance as a function of loading time, and (b) loading direction stress at a material point in the center with loading time.

CPFE simulations using TET4 element (simulation A), F-bar patch element with a patch size of 8 tetrahedrons (FP8) (simulation B) and LIB element (simulation C) reveal the difference when locking is removed. The predicted twin nucleation is plotted in figure 17a. The simulation using TET4 elements shows a

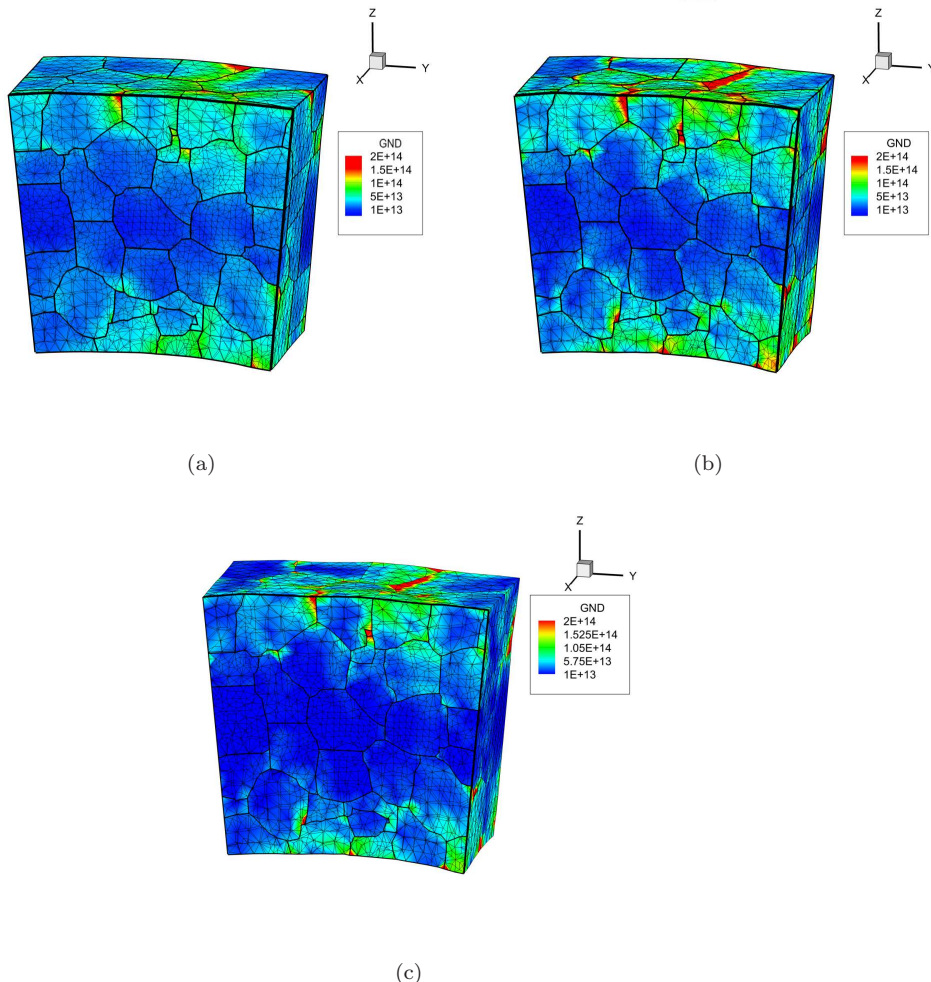


Fig. 18 GND densities distribution at the middle section after 500s using: (a) TET4 elements, (b) FP8 elements, and (c) LIB elements.

much earlier twin nucleation time (97 seconds) than that using the LIB element (160 seconds) and FP8 element (180 seconds). This difference is due to the difference in stress states predicted by the two element formulations. For the same level of displacement on the two surfaces, the conventional TET4 element shows a much stiffer response with much higher stresses. This is shown in figure 17b where the loading direction stresses at the material point from which twin nucleates are plotted. The non-physical stresses leads to a unrealistic external work in the TET4 elements to separate twin partials from stair-rod dislocations and result in an early twin nucleation prediction. Thus it inaccurately predicts material failure in polycrystalline microstructures. This is clearly remedied with the locking-free elements. It is noticed that the FP8 element shows a slightly higher level of locking removal than LIB element elements, due to a better constraint ratio. Comparison

of the GND densities in figure 18 reveals that the simulation using LIB elements and FP8 elements shows highest GND concentrations close to grain boundaries. Volumetric locking in TET4 elements predicts a stiffer response to bending and constrained lattice distortion, which results in lower GND density.

6 Computational Efficiency with Different Element Formulations

Methods of alleviating volumetric locking in either the LIB or FP elements result in more computational costs in comparison with the conventional TET4 element. The CPU time spent for LU factorization of the tangent stiffness matrix and element-level calculations, including computation of residual force and tangent stiffness matrix, are compared for efficiency of the three formulations. Only one processor is used in all the simulations to rule out the effects of improper parallel computing algorithms, if any, on the reported CPU times. LU factorization is carried out using the SuperLU package [54].

A small *Ti6Al* microstructure with 14 grains that is discretized into 2141 elements is considered for the efficiency study. The CPU times expended for LU factorization and element-level calculations for one iteration in the Newton-Raphson solution scheme are compared in table 4. The CPU time spent on LU factorization for locking-free elements is more than that for TET4 elements. This is due to the fact that more degrees of freedom are connected to one another in FP and LIB formulations. This makes the bandwidth of the tangent stiffness matrix larger and more vector operations are needed for LU factorization. The factorization for FP elements takes less time than LIB elements since the bandwidth of the former tangent stiffness matrix is generally smaller. In regard to element-level calculations, the FP elements take slightly longer time than TET4 elements. This is mostly due to calculating the modified deformation gradient in the patch, calculating and assembling the cross-stiffness matrix K^{KJ} in equation (49). The LIB elements take significantly longer time to perform element-level calculations since each element is divided into 4 sub-tetrahedrons where the constitutive law is solved. The number of constitutive updates and assembly processes increases the CPU times for the LIB element. From this study, it is deemed that FP elements are preferred over LIB elements in CPFE simulations from an efficiency point of view.

Element Formulation	Time spent for LU factorization (s)	Time spent for element-level calculations (s)
TET4	0.098	0.832
FP	0.145	1.175
LIB	0.186	27.072

Table 4 Comparison of CPU time for different element formulations.

7 Summary and Conclusions

This paper examines three methods to overcome volumetric locking in 3D constant strain tetrahedral (TET4) elements and augments them for crystal plasticity finite element or CPFE analysis of polycrystalline metals and alloys. The three methods include node-based uniform strain (NUS) element, the locally integrated B-bar (LIB) element and the F-bar patch (FP) based element that incorporate stabilization patches for selectively integrating parts of the constitutive relations. The LIB element splits the gradient operator matrix into isochoric and volumetric components and then reduces the incompressibility constraint by smoothing the volumetric component within the patch. The FP element changes the deformation gradient tensor at each integration point to volume-averaged value within each patch. Both the LIB and FP elements provide stabilized solution without introducing spurious low-energy modes as with the NUS element. These elements also do not require isotropy in the material tangent stiffness tensor and can be applied to any constitutive law. Both of these elements pass the element patch test.

Various finite deformation CPFE simulations are conducted to investigate the performance of LIB and FP elements in eliminating volumetric locking. Bending simulations of a nearly incompressible elastic bar show that both the LIB and FP elements provide satisfactory results and converge to the reference solution. The FP element is capable of providing slightly better result than the LIB element for an optimal patch size. CPFE simulations of polycrystalline magnesium and titanium alloys under various loading modes reveal that these elements are able to relieve volumetric locking present with linear TET4 elements. The effects of locking are dominant near grain boundaries and cause locally high hydrostatic stresses and low plastic strains. The LIB and FB elements stabilize the displacement, local stresses and plastic strains, and GND distributions in CPFE analyses. Linear convergence rates are seen in bicrystal compression tests. In modeling micro-twin induced material failure in polycrystalline microstructures of AZ31 alloy, significantly premature micro-twin nucleation time is predicted by linear TET4 elements. This can be overcome by using the LIB or FP elements in CPFE analyses. Finally, when computational efficiency is considered the FP element outperforms the LIB element with a considerably lower simulation time. The fact that LIB element performs constitutive updates once for each sub-tetrahedrons, increases the number of Gauss points and slows down the simulations. From both accuracy and efficiency consideration, the FP element is deemed more suitable for stabilized CPFE analysis.

8 ACKNOWLEDGMENTS

This work has been supported by the National Science Foundation, Mechanics and Structure of Materials Program through grant No. CMMI-1100818 (Program Manager: Dr. T. Siegmund), by the Army Research Office through grant No. W911NF-12-1-0376 (Program Manager: Dr. A. Rubinstein) and by the Air Force Office of Scientific through a grant FA9550-13-1-0062, (Program Manager: Dr. David Stargel). Computing support by the Homewood High Performance Compute Cluster (HHPC) is gratefully acknowledged.

References

1. D. Deka, D. S. Joseph, S. Ghosh, and M. J. Mills. Crystal plasticity modeling of deformation and creep in polycrystalline Ti-6242. *Metall. Trans. A.*, 37A(5):1371–1388, 2006.
2. V. Hasija, S. Ghosh, M. J. Mills, and D. S. Joseph. Modeling deformation and creep in Ti-6Al alloys with experimental validation. *Acta Mater.*, 51:4533–4549, 2003.
3. G. Venkataramani, K. Kirane, and S. Ghosh. Microstructural parameters affecting creep induced load shedding in Ti-6242 by a size dependent crystal plasticity FE model. *Int. Jour. Plas.*, 24:428–454, 2008.
4. M. Anahid, M. K. Samal, and S. Ghosh. Dwell fatigue crack nucleation model based on crystal plasticity finite element simulations of polycrystalline Titanium alloys. *Jour. Mech. Phys. Solids*, 59(10):2157–2176, 2011.
5. S. Ghosh and M. Anahid. Homogenized constitutive and fatigue nucleation models from crystal plasticity fe simulations of ti alloys, part 1: Macroscopic anisotropic yield function. *Int. Jour. Plast.*, 47:182–201, 2013.
6. S. Ghosh and P. Chakraborty. Microstructure and load sensitive fatigue crack nucleation in ti-6242 using accelerated crystal plasticity fem simulations. *Int. Jour. Fatigue*, 48:231 – 246, 2013.
7. S. Keshavarz and S. Ghosh. Multi-scale crystal plasticity fem approach to modeling nickel based superalloys. *Acta Mater.*, 61:6549–6561, 2013.
8. Simmetrix. <http://www.simmetrix.com/>, 2014.
9. K. Matou and A.M. Maniatty. Finite element formulation for modelling large deformations in elasto-viscoplastic polycrystals. *Int. J. Numer. Meth. Eng.*, 60:2313 – 2333, 2004.
10. CR. Dohrmann, MW. Heinstein, J. Jung, SW. Key, and WR. Witkowski. Node-based uniform strain elements for three-node triangular and four-node tetrahedral meshes. *Int. J. Numer. Meth. Eng.*, 47:1549 – 1568, 2000.
11. M.W. Gee, C.R. Dohrmann, S.W. Key, and W.A. Wall. A uniform nodal strain tetrahedron with isochoric stabilization. *Int. J. Numer. Meth. Eng.*, 78:429 – 443, 2009.
12. E.A. de Souza Neto, F.M. Andrade Pires, and D.R.J. Owen. F-bar-based linear triangles and tetrahedra for finite strain analysis of nearly incompressible solids. part i: formulation and benchmarking. *Int. J. Numer. Meth. Eng.*, 62:353 – 383, 2005.
13. E.A. de Souza Neto, D. Peric, and D.R.J. Owen. *Computational methods for plasticity: theory and applications*. John Wiley and Sons Ltd., 2008.
14. J. Bonet, H. Marriott, and O. Hassan. Stability and comparison of different linear tetrahedral formulations for nearly incompressible explicit dynamic applications. *Int. J. Numer. Meth. Eng.*, 50:119 – 133, 2001.
15. M. A. Puso and J. Solberg. A stabilized nodally integrated tetrahedral. *Int. J. Numer. Meth. Eng.*, 67:841 – 867, 2006.
16. G. Laschet, I. Caylak, S. Benke, and R. Mahnken. Locally integrated node-based formulations for four-node tetrahedral meshes. Private communication.
17. G.R. Liu, T. Nguyen-Thoi, H. Nguyen-Xuan, and K.Y. Lam. A node-based smoothed finite element method (ns-fem) for upper bound solutions to solid mechanics problems. *Comput. struc.*, 87:14–26, 2009.

18. H. Nguyen-Xuan and G.R. Liu. An edge-based smoothed finite element method softened with a bubble function (bes-fem) for solid mechanics. *Comput. struc.*, 128:14–30, 2013.
19. G.R. Liu, T. Nguyen-Thoi, and Lam K.Y. An edge-based smoothed finite element method (es-fem) for static, free and forced vibration analyses of solids. *J Sound Vib*, 320:1100–1130, 2009.
20. T. Nguyen-Thoi, G.R. Liu, Lam K.Y., and Zhang G.Y. A face-based smoothed finite element method (fs-fem) for 3d linear and non-linear solid mechanics problems using 4-node tetrahedral elements. *Int. J. Numer. Meth. Eng.*, 78:324–353, 2009.
21. E.A. de Souza Neto, D. Peric, M. Dutko, and D.R.J. Owen. Design of simple low order finite elements for large strain analysis of nearly incompressible solids. *Int. J. Solids Struct.*, 33:3277 – 3296, 1996.
22. Wolff S. and Bucher C. A finite element method based on c0 continuous assumed gradients. *Int. J. Numer. Meth. Eng.*, 86:876–914, 2011.
23. R. Mahnken and I. Caylak. Stabilization of bi-mixed finite elements for tetrahedral with enhanced interpolation using volume and area bubble functions. *Int. J. Numer. Meth. Eng.*, 75:377–413, 2008.
24. R. Mahnken, I. Caylak, and G. Laschet. Two mixed finite element formulations with area bubble functions for tetrahedral elements. *Comput. Meth. in Appl. Mech. And Eng.*, 197:1147–1165, 2008.
25. K.J. Bathe. *Finite element procedures*. Prentice-Hall, Inc, 1996.
26. A. Staroselsky and L. Anand. A constitutive model for hcp materials deforming by slip and twinning: application to magnesium alloy az31b. *Int. J. Plast.*, 19:843–1864, 2003.
27. E. Busso, F. Meissonier, and N. ODowd. Gradient-dependent deformation of two-phase single crystals. *Jour. Mech. Phys. Solid.*, 48(11):2333–2361, 2000.
28. C. Zambaldi, F. Roters, D. Raabe, and U. Glatzel. Modeling and experiments on the indentation deformation and recrystallization of a single-crystal nickel-base superalloy. *Mater. Sci. Engng. A*, 454455:433440, 2007.
29. F. Roters, P. Eisenlohr, L. Hantcherli, D.D. Tjahjantoa, T.R. Bieler, and D. Raabe. Overview of constitutive laws, kinematics, homogenization and multiscale methods in crystal plasticity finite-element modeling: Theory, experiments, applications. *Acta Mater.*, 58(4):1152–1211, 2010.
30. R.J. Asaro and A. Needleman. Texture development and strain hardening in rate dependent polycrystals. *Acta Mater.*, 33(6):923–953, 1985.
31. U.F. Kocks, A.S. Argon, and M.F. Ashby. Thermodynamics and kinetics of slip. *Progress in materials science*, 19:141–145, 1975.
32. G. Venkataramani, S. Ghosh, and M. J. Mills. A size dependent crystal plasticity finite element model for creep and load-shedding in polycrystalline Titanium alloys. *Acta Mater.*, 55:3971–3986, 2007.
33. S. Sinha and S. Ghosh. Modeling cyclic ratcheting based fatigue life of hsla steels using crystal plasticity fem simulations and experiments. *Int. Jour. Fatig.*, 28:1690–1704, 2006.
34. J. Cheng and S. Ghosh. A crystal plasticity fe model for deformation with twin nucleation in magnesium alloys. *Int. J. Plast.*, 67(0):148 – 170, 2015.
35. M. F. Ashby. Deformation of plastically non-homogeneous maaterials. *Philos. Mag.*, 21:399–424, 1970.

36. A. Ma, F. Roters, and D. Raabe. A dislocation density based constitutive model for crystal plasticity fem including geometrically necessary dislocations. *Acta Mater.*, 54:2169–2179, 2006.
37. G. Cao, L. Fu, J. Lin, Y. Zhang, and C. Chen. The relationships of microstructure and properties of a fully lamellar tial alloy. *Intermetallics*, 8:647–653, 2000.
38. JCM. Li and YT. Chou. The role of dislocations in the flow stress grain size relationships. *Metall. Mater. Trans.*, 52:97–120, 2001.
39. JF. Nye. Some geometrical relations in dislocated crystals. *Acta Metall.*, 1(2):153–162, 1953.
40. A. Arsenlis and D. M. Parks. Crystallographic aspects of geometrically-necessary and statistically-stored dislocation density. *Acta Mater.*, 47:1597–1611, 1998.
41. MA Crisfield. *nonlinear finite element analysis of solids and structures, Volume 1: Essentials*. John Wiley and Sons, Inc, 1997.
42. T.J.R. Hughes. *The finite element method: linear Static and dynamic finite element analysis*. Prentice-Hall, Inc, 1987.
43. O. C. Zienkiewicz and J. Z. Zhu. The superconvergent patch recovery (spr) and adaptive finite element refinement. *Comput.Method Appl M*, 101:207 – 224, 1992.
44. Morawiec A. *Orientations and rotations: computations in crystallographic textures*. Springer Science Business Media, 2004.
45. C.J. Bettles and M.A. Gibson. Material rate dependence and localized deformation in crystalline solids. *Jour. Miner. Met. Mater. Soc.*, 57(5):46–49, 2005.
46. K.U. Kainer. *Magnesium alloys and their applications*. Wiley-VCH, Weinheim, 2003.
47. L.R. Barnett. Twinning and the ductility of magnesium alloys: Part i: Tension twins. *Mater. Sci. Engng.*, A464:1–7, 2007.
48. Q. Yu, J. Zhang, and Y. Jiang. Fatigue damage development in pure polycrystalline magnesium under cyclic tensioncompression loading. *Materials Science and Engineering: A*, 528(2526):7816 – 7826, 2011.
49. M. A. Groeber and M. A. Jackson. Dream.3d: A digital representation environment for the analysis of microstructure in 3d. *Integrating Materials and Manufacturing Innovation*, 3:5, 2014.
50. M. Groeber, S. Ghosh, M. D. Uchic, and D. M. Dimiduk. A framework for automated analysis and simulation of 3d polycrystalline microstructures.: Part 1: Statistical characterization. *Acta Mater.*, 56(6):1257–1273, 2008.
51. M. Groeber, S. Ghosh, M. D. Uchic, and D. M. Dimiduk. A framework for automated analysis and simulation of 3d polycrystalline microstructures. part 2: Synthetic structure generation. *Acta Mater.*, 56(6):1274–1287, 2008.
52. R. Mishra and K. Inal. Microstructure data. Unpublished work, 2013.
53. A. S. Khan, A. Pandey, T. Gnaupel-Herold, and R. K. Mishra. Mechanical response and texture evolution of az31 alloy at large strains for different strain rates and temperatures. *Int. J. Plast.*, 27:688–706, 2011.
54. Xiaoye S. Li. An overview of superlu: Algorithms, implementation, and user interface. *Trans. Math. Soft.*, 31(3):302–325, 2005.
55. FT. Meissonnier, EP. Busso, and NP. O'Dowd. Finite element implementation of a generalised non-local rate-dependent crystallographic formulation for

finite strains. *Int. J. Plast.*, 17:601 – 640, 2001.

A Evaluation of the tangent stiffness matrix

In this appendix, the tangent stiffness tensor \mathbf{C}^t in equation (8) is derived from the crystal plasticity constitutive model. \mathbf{C}^t at time t is expressed as:

$$\mathbf{C}^t = \frac{1}{\det \mathbf{F}_0^t} (\mathbf{F}_0^t \otimes \mathbf{F}_0^t) : \mathbf{C}^0 : (\mathbf{F}_0^t \otimes \mathbf{F}_0^t) \quad (63)$$

where \mathbf{C}^0 has been derived in [55] as:

$$\begin{aligned} \mathbf{C}^0 &= \frac{\partial \mathbf{S}_0^t}{\partial \mathbf{E}_0^t} = (\det \mathbf{F}^p) (\mathbf{F}^p \underline{\otimes} \mathbf{F}^p)^{-1} \\ &: \left\{ \frac{\partial \mathbf{S}^*}{\partial \mathbf{E}} + \left[\mathbf{S}^* \otimes \mathbf{F}^{p-T} - (\det \mathbf{F}^p)^{-1} \left[\mathbf{I} \underline{\otimes} (\mathbf{S} \mathbf{F}^{pT})^T + (\mathbf{F}^p \mathbf{S}) \bar{\otimes} \mathbf{I} \right] \right] : \frac{\partial \mathbf{F}^p}{\partial \mathbf{E}} \right\} \quad (64) \end{aligned}$$

with

$$\mathbf{S}^* = (\det \mathbf{F}^p)^{-1} \mathbf{F}^p \mathbf{S} \mathbf{F}^{pT} \quad (65a)$$

$$\frac{\partial \mathbf{S}^*}{\partial \mathbf{E}} = \left[\mathbf{I} \underline{\otimes} \mathbf{I} + \sum_{\alpha}^{N_{slip}} \left(C^{\alpha} \otimes \frac{\partial \Delta \gamma^{\alpha}}{\partial \mathbf{S}^*} \right) \right]^{-1} \left[\mathbf{A}^{\alpha} - \sum_{\alpha}^{N_{slip}} \Delta \gamma^{\alpha} \mathbf{B}^{\alpha} \right] \quad (65b)$$

$$\mathbf{A} = \mathbf{C}^e : \left(\mathbf{F}^{p-1} \underline{\otimes} \mathbf{F}^{p-1} \right) \quad (65c)$$

$$\mathbf{B}^{\alpha} = \mathbf{C}^e : \left[\mathbf{F}^{p-T} \underline{\otimes} \left(\mathbf{F}^{p-1} \mathbf{s}_0^{\alpha} \right)^T + \left(\mathbf{F}^{p-1} \mathbf{s}_0^{\alpha} \right)^T \underline{\otimes} \mathbf{F}^{p-T} \right] \quad (65d)$$

$$\frac{\partial \mathbf{F}^p}{\partial \mathbf{E}} = \sum_{\alpha}^{N_{slip}} (\mathbf{s}_0^{\alpha} \mathbf{F}^p) \otimes \left(\frac{\partial \Delta \gamma^{\alpha}}{\partial \mathbf{S}^*} \frac{\partial \mathbf{S}^*}{\partial \mathbf{E}} \right) \quad (65e)$$

The lower and upper tensor product operators $\underline{\otimes}$ and $\bar{\otimes}$ are defined as $(A \underline{\otimes} B)_{ijkl} = A_{ik} B_{jl}$ and $(A \bar{\otimes} B)_{ijkl} = A_{il} B_{jk}$. \mathbf{C}^t is a function of path-dependent state variables, i.e. $\mathbf{C}^t = \mathbf{C}^t(\mathbf{F}^t, \mathbf{F}^{pT}, \dot{\gamma}^t, \dots)$. The time-integration algorithm developed in [34] is implemented here to incrementally update state variables. The fourth order tensor \mathbf{C}^t is written as a 6×6 matrix, using the property of major symmetry, for implementation to finite element weak form.

A dislocation density-based multi-rate crystal plasticity finite element model for *hcp* metals

Ahmad Shahba^a, Xiaohui Tu^a, Emily L. Huskins^b, Brian E. Schuster^c,
Somnath Ghosh^{a,*}

^a*Department of Civil Engineering, Johns Hopkins University, Baltimore, MD 21218*

^b*Mechanical Engineering Department, US Naval Academy, Annapolis, MD 21402*

^c*US Army Research Laboratory, RDRL-WM, Aberdeen Proving Ground, MD 21005*

Abstract

Dislocation motion in metals is governed by the thermally-activated and drag-dominated processes under low and high rates of deformation, respectively. This work develops a unified dislocation density-based crystal plasticity (CP) constitutive model for *hcp* metals by combining the thermally-activated and drag-dominated stages of dislocation slip. The model is suitable for modeling deformation under a wide range of strain rates. The effects of temperature on both elasticity and plasticity are considered and carefully calibrated using experimental results. The proposed constitutive model is incorporated into a stabilized locking-free large deformation finite element (FE) framework. Competency of the methodology is demonstrated for two types of Ti-7Al alloy polycrystals. For simulations, the CPFE model uses the image-based virtual polycrystalline microstructures generated from 2D surface data. Room temperature compression tests at quasi-static ($10^{-3}s^{-1}$) and dynamic strain rates ($1000-4000s^{-1}$) are used to calibrate and validate the constitutive model. Rate-dependency of the flow stress is investigated at both single and polycrystalline levels. An elastic overshoot followed by a stress relaxation is observed at very high strain rates in single crystals. In the polycrystalline level, the model is observed to effectively capture the increase in the rate sensitivity at high strain rates. Under adiabatic conditions, the decrease in the hardening rate due to the promotion of slip-driven plasticity is observed to be significant. The effect of degradation of elastic constants on the macroscopic behavior seems to become noticeable only at the later stages of deformation. A careful study on adiabatic heating revealed that unexpectedly the grains undergoing severe plastic deformation do not necessarily endure higher temperatures. In other words, temperature increase in severely plastically deformed grains could be lower than the temperature increase in grains which have undergone a small amount plastic strain.

Keywords: *hcp* metals, crystal plasticity, dislocation glide, thermal

*Corresponding author, Tel.: +1-410-516-7833, Fax: +1-410-516-7473
Email address: sghosh20@jhu.edu (Somnath Ghosh)

1. Introduction

Titanium alloys are widely used in manufacturing components for automotive and aerospace industries due to their high strength to weight ratio, high fracture toughness and good corrosion resistance at elevated temperatures. Extensive use of these alloys in critical industrial and military applications, such as compressor blades of jet engines and armor of ground combat vehicles [1], has motivated researchers to understand, measure and tailor the mechanical properties of these alloys over a wide range of strain rates and temperatures. Of special interest has been the mechanical response of these alloys under high rates of deformation [2–6] and failure under cyclic/dwell fatigue [7–9]. Over the years, these experimental observations have provided modelers with enlightening insight to develop new constitutive models and methodologies to explain many of the observations from a computational mechanics point of view and hopefully help designers design components with a better understanding of the failure modes and expected lifetime of the components.

One of the most powerful methods developed in the past two decades for modeling material behavior is crystal plasticity finite element method (CPFE). Its advantages inhere within its capability to describe the mechanical anisotropy and material heterogeneity via micro-mechanism-based constitutive laws, which could be informed from multiple length-scales ranging from sub-grain level to the polycrystalline level [10]. The accuracy of CPFE models and their capability in prediction of material response in polycrystalline level are dependent on majorly three factors, including creation of a virtual realistic polycrystalline aggregate model, utilization of a robust element formulation for finite element calculations and description of material response with a proper constitutive law.

Accuracy of CPFE models have significantly improved over the past few years due to the advances in image-based modeling and reconstructing statistically equivalent polycrystalline aggregates using the collected 2D or 3D data [11–13]. This is a crucial step toward understanding the macroscopic behavior of the material in terms of its morphological and crystallographic properties. Development of meshing codes and software products [14] which can discretize the complex polycrystalline microstructures into simple finite elements has been also instrumental in paving the way towards realistic CPFE simulations.

In order to carry out a finite element analysis, it is required that the elements conform to the geometry of the computational domain. This requirement has an implication for CPFE analysis of polycrystalline aggregates. Linear constant strain tetrahedral elements are used to discretize the polycrystalline aggregates due to the complex morphology of grains and the magnificent capability of these elements to conform to tortuous geometries. However, these elements suffer from severe volumetric locking when simulating the deformation of (nearly-) incompressible materials. Various methods have been proposed to relieve volumetric locking in tetrahedral elements, for instance node-based uniform strain

45 formulation [15, 16], F-bar-patch method [17] and mixed enhanced formulation [18]. Since plasticity is inherently isochoric, volumetric locking of tetrahedral elements is highly relevant to the CPFE simulation; however, its detrimental effect on the solution has been generally overlooked by the materials modeling community. The adverse effects of volumetric locking on predicting the response of microstructures in 2D [19] and 3D [20] have been shown recently. In this work, the model proposed in Cheng et al [20] is used to relieve volumetric locking in 50 CPFE simulations.

55 Describing the material response with a proper constitutive law plays a key role in the success of the CPFE models to represent the behavior of the material. The most critical part of a CP constitutive law is the flow rule which interrelates the local material state (e.g. dislocation density) and local stress state with the kinematics (e.g. slip rates). Suitability of a constitutive law for a certain application inheres in how rigorously the flow rule can capture the governing deformation mechanism(s). Selection of the proper type of flow rule is largely 60 problem-dependent since flow rules are developed on the premise of certain assumptions and pose some limitations with respect to their use. The most commonly used expressions for the flow rule are the phenomenological power-law model [21], Arrhenius-type activation energy-based model [22] and linear model [22].

- 65 • The **power-law model** is a simple and yet effective flow rule for modeling materials deforming under low strain rates. This flow rule could be also used for modeling moderately high strain deformations, provided that the effects of temperature increase on the plastic flow are taken into account.
- 70 • Arrhenius-type **activation energy-based model** [23, 24] is applicable as long as the dislocation glide is governed by the thermally-activated processes, e.g. deformations under low up to moderately high strain rates ($10^4 \sim 10^5 s^{-1}$). Since this flow rule has explicit dependence on the temperature, it can be effectively used for simulating phenomena which are highly temperature-dependent such as dwell fatigue in Ti alloys [25, 26].
- 75 • The **linear flow rule** is suitable for modeling metals deforming under strain rates exceeding $10^5 s^{-1}$ where the dislocation motion is administered by the drag-dominated processes.

80 Deriving a rate-dependent physics-based flow rule whose application is not limited to a certain range of strain rates is desired. Using such a flow rule is encouraged in simulation of polycrystalline aggregates where the local stress and strain rates might be lower or higher than the applied macroscopic stress or strain rate. For instance, in Ti alloys under applied creep load σ_{app} , stress redistribution happens locally in the microstructure due to the grain-level load shedding from the *soft* grains to the adjacent *hard* grains [27]. This is known as *load-shedding* mechanism which induces stresses higher than σ_{app} in the *hard* grains while the stress in the adjacent *soft* grain could be lower than σ_{app} . 85 Similarly, a polycrystalline microstructure which is macroscopically deforming

under a very high strain rate (in the range of applicability of linear flow rule) could locally undergo a lower rate of deformation (in the range of applicability of activation energy-based flow rule). A new unified flow rule is sought which could be used for both low and high rates of deformation. This unified flow rule should 90 automatically adjusts its functional form based on the local deformation rate , local stress state and internal state variables. Such a flow rule can be obtained based on some physical considerations via combining the thermally-activated and drag-dominated stages of dislocation motion.

Valuable works have been done towards deriving a unified flow rule by formulating new formulations for average velocity of dislocations. Frost and Ashby 95 [28] were the first to propose a dislocation velocity formulation based on combining the thermal activation and drag mechanisms. Dislocation inertial models were later developed to model plasticity in superconductors [29, 30]. Hiratani and Nadgorny [31] developed a unified model to study dislocation motion in 100 2D through an array of obstacles in a prototype *fcc* metal. A similar unified model was implemented in a discrete dislocation dynamics code to model dislocation behavior in *fcc* metals under creep conditions [32]. Unified flow rules were developed in the context of macroscale J2 plasticity for modeling deformation behavior of *bcc* vanadium and tantalum [33, 34]. Recently, Austin and McDowell 105 [35] developed a unified flow rule to model visco-plastic deformation of *fcc* aluminum alloys under shock loading using a dislocation density-based crystal plasticity framework. Most of the works on the development of a unified flow rule have been in the realm of analytical models or modeling motion of discrete 110 dislocations in a 2D array of obstacles. There are very few works that have investigated the capability of these unified flow rules in modeling deformation of polycrystalline aggregates within the framework of CPFE analysis. In this paper, we build upon the existing formulations in the literature and extend the idea of unified flow rules to the CPFE simulation of *hcp* metals, Ti alloys in particular.

115 In this paper, the mechanical response of an α Ti alloy with two different microstructures (due to different methods of material processing) is investigated under low and high rates of deformation. Section 2 discusses the materials and explains the procedure of reconstructing statistically equivalent microstructures from collected 2D data. This section concludes with a FE mesh convergence 120 study. Section 3 provides the details of the quasi-static and dynamic tests. Section 4 discusses the constitutive model in details. Stabilization of the linear tetrahedral elements will be briefly explained in Section 5. Section 6 discusses the procedure of calibration and validation of the constitutive models. Numerical results are provided which highlight the rate-dependency of flow stress and 125 importance of temperature in the context of isothermal and adiabatic simulations. The paper concludes with some concluding remarks in Section 7.

2. Materials, reconstruction of statistically-equivalent microstructure and mesh convergence study

To predict mechanical response of crystalline metals, it is important to represent relevant morphological and crystallographic features of the microstructure, such as grain size distribution, orientation distribution and misorientation distribution, in the 3D reconstructed virtual microstructures. There are different methods to generate 3D virtual microstructures based on experimental measurements. Electron back-scattered diffraction (EBSD) data collected from focused ion beam (FIB)-based serial sectioning of polycrystalline samples could be utilized to obtain 3D statistics and generate realistic microstructures [36, 37]. Alternatively if data for serial sectioning of the microstructure is not available, it is possible to reconstruct virtual microstructures based on the 3D statistical distributions estimated from the 2D measurements.

In this section, the material used in this study is briefly introduced and reconstruction of 3D virtual microstructures from 2D measurements is then explained in details. A mesh convergence study is then conducted for the CPFE simulations of statistically-equivalent microstructures.

2.1. Material description

The material studied in this paper is Ti-7.02Al-0.11O-0.015Fe (wt%) alloy with a predominant *hcp* microstructure [38]. The composition of this alloy is very close to the α phase of many commercially important titanium alloys [9]. Mechanical testing is done on two variants of this alloy in this study, referred to as the AR (as-rolled) and RA (rolled-annealed) samples. The AR sample corresponds to the one which has been only rolled whereas the RA sample corresponds to a sample manufactured by first rolling and subsequently annealing it to improve its ductility and increase the grain size, followed by a cooling process. Scanning electron microscopy (SEM) based electron back-scattered diffraction (EBSD) is done under supervision of Dr. Adam Pilchak in the Air Force Research Laboratory (AFRL) to quantify the texture of large-area EBSD scans. The surface EBSD scans for the AR and RA samples are respectively $5425 \times 2190 \mu\text{m}^2$ and $5175 \times 2135 \mu\text{m}^2$, collected at $5 \mu\text{m}$ step size. Figure 1 shows a part of surface EBSD scans collected for both samples after being processed to remove *noise* from the data. Average diameter for equivalent projected circle in 2D is calculated to be $34.12 \mu\text{m}$ and $83.4 \mu\text{m}$ for the AR and RA samples, respectively.

2.2. Reconstruction of virtual microstructures

2D surface EBSD images for both samples are characterized and crystallographic distributions, viz. orientation and misorientation distributions, and morphological distribution, i.e. distribution of equivalent projected circle diameters (*ECD*), are obtained. 2D crystallographic distributions could be directly used for generating 3D crystallographic statistics; however, it is necessary to employ stereology [39] to estimate 3D morphological distributions from 2D

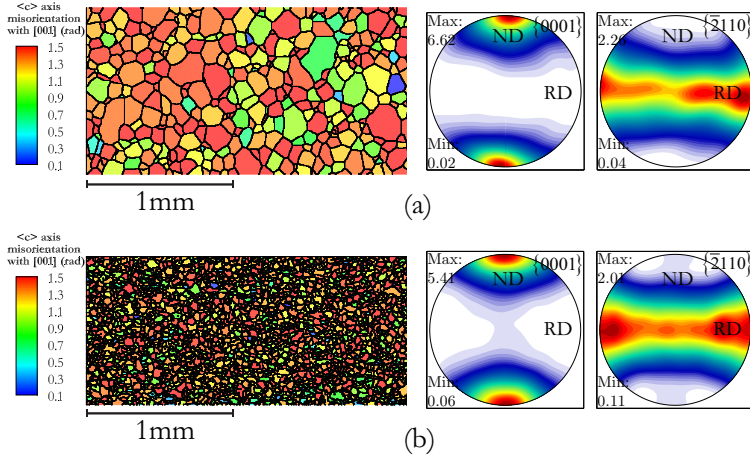


Figure 1: processed EBSD scans and pole figures for the (a) RA and (b) AR samples

measurements. Using the principles of stereology, the average equivalent sphere diameter (\overline{ESD}) could be expressed in terms of \overline{ECD} as

$$\overline{ESD} = \frac{4}{\pi} \overline{ECD} \quad (1)$$

It has been observed that a log-normal distribution function can adequately represent the grain size distribution in Ti alloys [40]. Method of maximum-likelihood is used to estimate the average and standard deviation parameters for the grain size distribution function. Eventually both morphological and crystallographic distributions are fed into DREAM.3D software [13] to create 3D statistically-equivalent virtual microstructures using the methods described in [11, 12].

Following the aforementioned steps, several statistically-equivalent microstructures, with different numbers of grains, are reconstructed for each sample. Figure 2 shows the convergence of orientation, misorientation, and grain size distributions as the number of grains increases in the RA microstructure. Comparing the statistical distributions of virtual microstructures with the ones from 2D EBSD data, it is observed that the distributions for the 529-grain RA microstructure generally show a good agreement; hence, it will be used for the CPFE simulations. Following the same strategy, a convergence study on the distributions is conducted for the AR sample and a 515-grain microstructure is deemed suitable and used for the CPFE simulations. The reconstructed AR and RA microstructures are depicted in Figure 3.

2.3. Mesh convergence study

It is necessary to conduct a mesh convergence study with respect to both macroscopic and microscopic quantities in CPFE simulations. Simmetrix® software [14] is used to discretize the computational domain into linear constant

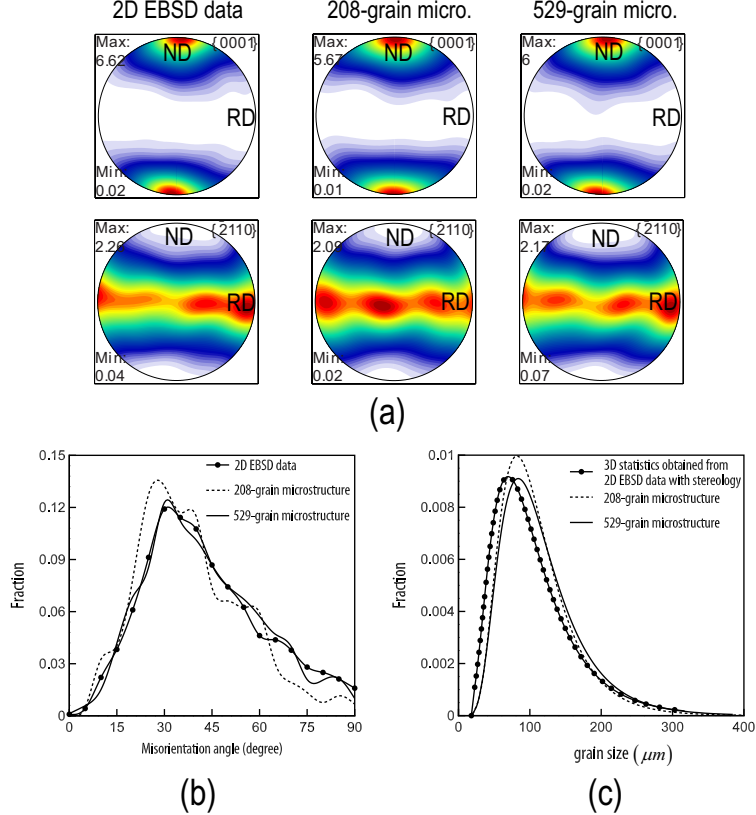


Figure 2: Convergence of different distributions with increasing number of grains for the RA microstructure, (a) orientation distribution, (b) misorientation distribution and (c) grain size distribution

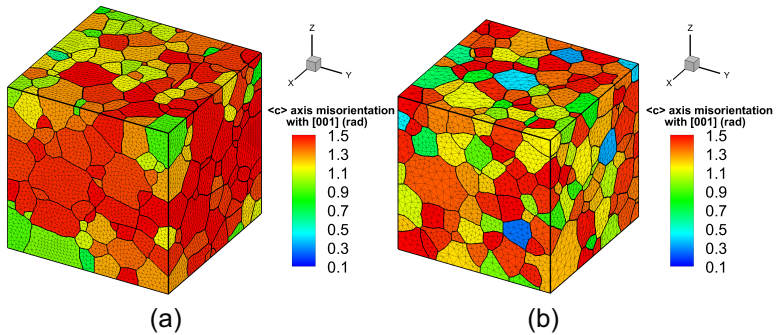


Figure 3: Statistically-equivalent microstructures for (a) $960 \times 960 \times 960 \mu\text{m}^3$ RA polycrystalline volume with 529 grains discretized into 536090 linear tetrahedral elements and (b) $300 \times 300 \times 300 \mu\text{m}^3$ AR polycrystalline volume with 515 grains discretized into 517023 linear tetrahedral elements

strain tetrahedral (TET4) elements. Deformation of the microstructure under constant rate of deformation $\dot{\epsilon} = 1.1 \times 10^3 s^{-1}$ along [100] is modeled using CPFE simulation. Figure 4 shows the results for two mesh densities with 536090 and 754916 elements in terms of macroscopic volumetric-averaged stress-strain response and von Mises stress along an X-directed line passing through the centroid of the RA microstructure. It is inferred from the mesh convergence study that the 536090-element mesh provides sufficient resolution for the CPFE simulations. Similar mesh convergence study is conducted for the AR microstructure where a 517023-element mesh is observed to provide satisfactory convergent results.

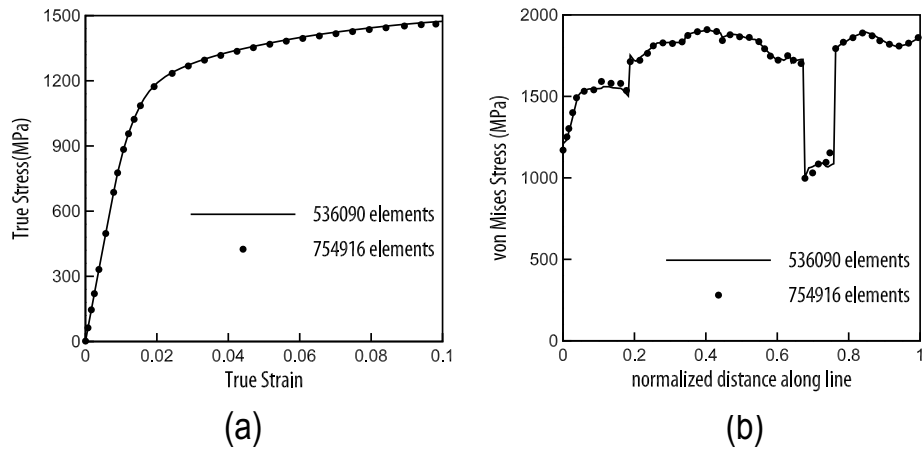


Figure 4: mesh convergence study for the RA microstructure with respect to (a) volumetric-averaged loading direction stress-strain response and (b) von Mises stress at 2% strain along an X-directed line passing through the centroid

3. Mechanical testing of polycrystalline samples

The mechanical response of the material was evaluated through room temperature compression tests at quasi-static ($10^{-3} s^{-1}$) and dynamic strain rates (1000 - $4000 s^{-1}$). Tests were conducted along the three orthogonal directions (normal, rolled, and transverse) for both the as-rolled and rolled-annealed materials. To minimize the frictional effects in all tests, the ends of the specimens were polished and lubricated.

Quasi-static (QS) tests were conducted on a screw-driven Instron load frame under displacement control conditions. The specimens were rectangular with dimensions $3.5 \times 3.5 \times 7 mm$ (aspect ratio of 2). A compression subpress fixture ensured proper axial alignment during loading. Displacement was measured using a stereoscopic digital image correlation (DIC) system consisting of two

215 2.3 MP cameras. The choice of a two-camera system was made to eliminate the
effect of out of plane motion on the strain measurements. DIC speckle pattern
was applied to the surface of the specimen using a fine airbrush. VicSnap and
Vic3D were used to acquire the images and perform the correlation (subset 29,
step 10). Uniaxial strain was calculated using a digital extensometer. None
220 of the specimens failed during testing. Unloading was initiated either after
sufficient data was obtained or the specimen began to deform in a non-uniform
manner upon which the data became invalid. The response of the material along
rolling and transverse directions was observed to be very similar. Compared to
the response along the rolling and transverse directions, over 26% increase is
225 observed in the 0.2% yield strength along the normal direction. Strain hardening
is observed for all orientations and is slightly higher along the normal direction.
The hardening does not change significantly at dynamic strain rates.

230 Dynamic strain rate tests were conducted on a compression Kolsky (Split-
Hopkinson) bar. The specimens were rectangular with dimensions $3.5 \times 3.5 \times 2.5\text{mm}$ (aspect ratio of 0.7). The Kolsky bar consists of two $3/8\text{in}$ (9.5mm)
235 maraging steel bars, referred to as the input and output bars, with the specimen
sandwiched between them. A gas gun accelerates a projectile, which strikes the
input bar, creating a compressive stress pulse that travels down the input bar
and loads the specimen. The foil strain gages located on the input and output
bars record the reflected and transmitted stress pulses, respectively. These data
240 are used to calculate the stress and strain rate history of the specimen once it
has reached stress equilibrium. The strain rate history is integrated over time
to obtain the strain history, which is correlated with the stress history to form
stress-strain curves. A complete description of the Kolsky bar experimental
technique is provided by Chen and Song [41].

4. Crystal plasticity constitutive model

245 Microstructure of commercial titanium alloys is composed of either a hexagonal
close packed (*hcp*) α or body-centered cubic (*bcc*) β phase or a combination
of these two phases. The microstructure phase is highly dependent on the al-
loying elements and the material processing [42]. In this paper, we focus on
250 modeling deformation mechanisms in α Ti alloys. Dislocation activity is con-
sidered to be the main deformation mechanism for plasticity in these alloys.
Dislocation slip was observed to be distributed inhomogeneously into planar ar-
rays due to short range ordering of Ti and Al atoms [43]. Plastic deformation is
255 accommodated by dislocation slip on 30 possible slip systems, categorized into
five different families of slip system as shown in Figure 5. The $\langle a \rangle$ - basal and
prism slip families have the lowest critical resolved shear stress (CRSS), making
them the most active slip families in α Ti alloys. The $\langle c+a \rangle$ - pyramidal slip
systems [44].

260 Twinning is another deformation mechanism, contributing to plasticity in
hcp metals. Deformation twinning is observed in Ti alloys deforming either un-
der high rates or at low temperatures. Deformation twinning has been observed

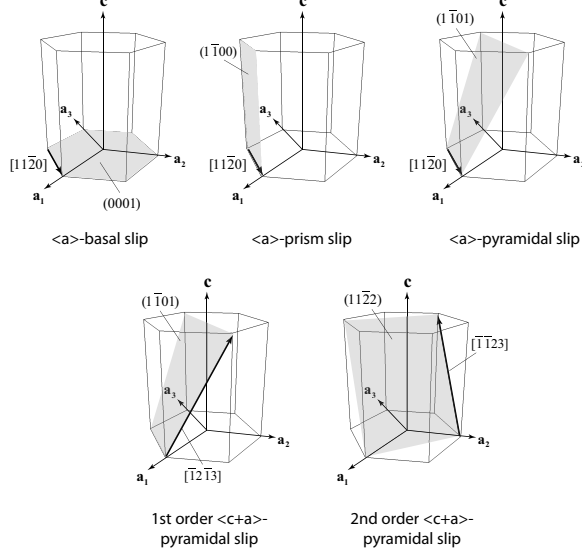


Figure 5: Schematic of non-orthogonal base vectors $\{\mathbf{a}_1, \mathbf{a}_2, \mathbf{a}_3, \mathbf{c}\}$ and slip system families in *hcp* metals

in unalloyed Ti at all temperatures below $500^\circ C$ [2]. However, alloying Ti with Al inhibits twinning such that titanium alloyed with $\% 6$ Al does not twin even at temperatures as low as $100K$ [45, 46]. Due to the high level of Al content in the alloy of interest, deformation twinning is not considered in the constitutive model.

In this section, the constitutive model is first described and the flow rule is explained in details. Evolution laws for dislocation densities and adiabatic heating are then introduced. This section concludes with the time integration scheme used for updating the CP constitutive law.

4.1. The constitutive model

Crystal plasticity FE models describe deformation of polycrystalline aggregates in terms of micro-mechanisms and crystallographic orientations at individual material points. The CP constitutive model presented here is developed for finite deformation of crystalline metals under general non-isothermal conditions. As illustrated in Figure 6, the total deformation gradient \mathbf{F} could be multiplicatively decomposed into elastic \mathbf{F}^e , thermal \mathbf{F}^θ and plastic \mathbf{F}^p components as

$$\mathbf{F} = \mathbf{F}^e \mathbf{F}^\theta \mathbf{F}^p \quad (2)$$

\mathbf{F}^e accounts for the elastic stretch and rigid body rotations. \mathbf{F}^θ represents the deformation of the crystal lattice due to thermal loading and evolves as [47]

$$\dot{\mathbf{F}}^\theta = \dot{T} \boldsymbol{\alpha} \mathbf{F}^\theta \quad (3)$$

where T is the temperature and the overdot represents differentiation with respect to time. α is a diagonal tensor containing thermal expansion coefficients along the principal crystallographic directions expressed with respect to the principal crystallographic coordinate system. *Ab initio* calculations [48, 49] and experimental observations [50] have shown the anisotropic thermal expansion of α titanium over a wide range of temperatures. The thermal expansion coefficients along $\langle a \rangle$ (in the basal plane) and $\langle c \rangle$ (normal to the basal plane) are respectively taken as $1.8 \times 10^{-5} K^{-1}$ and $1.1 \times 10^{-5} K^{-1}$ [49].

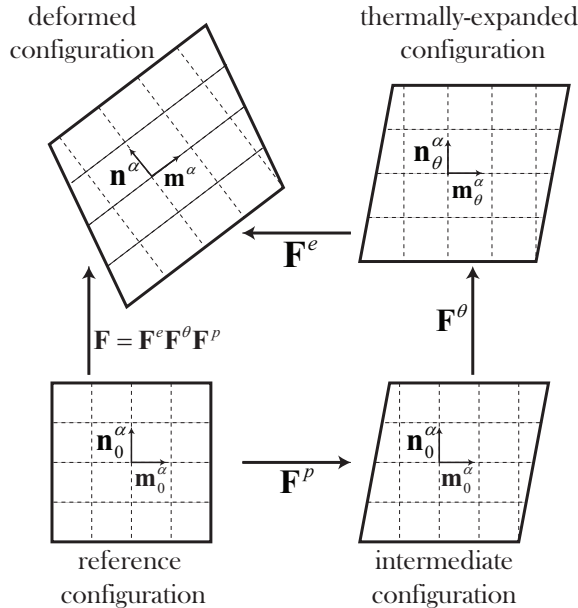


Figure 6: Multiplicative decomposition of the total deformation gradient \mathbf{F} into elastic \mathbf{F}^e , thermal \mathbf{F}^θ and plastic \mathbf{F}^p components

\mathbf{F}^p corresponds to the isochoric plastic deformation due to dislocation slip, i.e. $\det \mathbf{F}^p = 1$. The \mathbf{F}^p mapping neither distorts nor rotates the crystal lattice. Using the kinematics of dislocation glide, the plastic velocity gradient tensor \mathbf{L}^p in the intermediate configuration is obtained as [51]

$$\mathbf{L}^p = \dot{\mathbf{F}}^p \mathbf{F}^{p-1} = \sum_{\alpha=1}^{n_{\text{slip}}} \dot{\gamma}^\alpha \mathbf{m}_0^\alpha \otimes \mathbf{n}_0^\alpha \quad (4)$$

where $\dot{\gamma}^\alpha$ is the slip rate on slip system α . The summation is done over all slip systems n_{slip} in the crystal, $n_{\text{slip}} = 30$ for the *hcp* crystalline structure. \mathbf{m}_0^α and \mathbf{n}_0^α denote respectively the slip direction and slip plane normal for slip system α in the reference configuration.

The constitutive law is written in the thermally-expanded configuration as

$$\mathbf{S} = \det(\mathbf{F}^e) \mathbf{F}^{e-1} \boldsymbol{\sigma} \mathbf{F}^{e-T} = \mathbb{C} : \mathbf{E}^e \quad (5)$$

²⁹⁵ \mathbb{C} corresponds to the fourth order anisotropic elasticity tensor. \mathbf{S} denotes the second Piola-Kirchhoff stress in the thermally-expanded configuration which is work conjugate to the elastic Green-Lagrange strain $\mathbf{E}^e = \frac{1}{2} (\mathbf{F}^{eT} \mathbf{F}^e - \mathbf{I})$. $\boldsymbol{\sigma}$ is the Cauchy stress. The time integration scheme used for the constitutive updates will be explained later in Section 4.5.

³⁰⁰ *4.2. The Flow rule*

³⁰⁵ Slip-driven plasticity is interpreted in terms of dislocation glide on specific plane and quantified in terms of slip rates on individual slip systems. In the CP framework, this is achieved by adopting a proper flow rule which expresses the slip rates in terms of the stress state and relevant internal state variables. In the following, first the phenomenological power-law flow rule is briefly introduced. Then the new physics-based flow rule would be derived and explained in details. Both of these flow rules will be used to model deformation of Ti alloys under various conditions in Section 6 where their limitations and capabilities will be highlighted.

³¹⁰ *4.2.1. Phenomenological power-law flow rule*

³¹⁵ Phenomenological power-law flow rule, referred to as PL flow rule hereafter, is a simple and yet effective flow rule which has been used for modeling plastic deformation in metals with different crystalline structures. In this section, the PL flow rule developed in [27, 52–54] for modeling deformation of Ti alloys under low strain rates, creep and dwell fatigue conditions is briefly introduced. The rate-dependent PL flow rule reads as

$$\dot{\gamma}^\alpha = \dot{\gamma}_0^\alpha \left(\frac{|\tau^\alpha| - s_{\text{GND,P}}^\alpha}{s^\alpha} \right)^{\frac{1}{m}} \text{sign}(\tau^\alpha) \quad (6)$$

Here m and $\dot{\gamma}_0^\alpha$ are respectively the material rate sensitivity parameter and reference plastic shearing rate. τ^α is the resolved shear stress on slip system α calculated as

$$\tau^\alpha = \det(\mathbf{F}^\theta) \mathbf{C}^e \mathbf{S} : (\mathbf{F}^\theta \mathbf{m}_0^\alpha \otimes \mathbf{n}_0^\alpha \mathbf{F}^{\theta-1}) \quad (7)$$

³²⁰ $s_{\text{GND,P}}^\alpha$ denotes the long-range stresses due to the geometrically necessary dislocations (GNDs). $\mathbf{C}^e = \mathbf{F}^{eT} \mathbf{F}^e$ is the right elastic Cauchy-Green deformation tensor. s^α stands for the resistance to dislocation glide on slip system α due to the interaction with other dislocations through self and latent hardening mechanisms. $s_{\text{GND,P}}^\alpha$ and s^α are formulated as

$$s_{\text{GND,P}}^\alpha = c_1 \mu^\alpha b^\alpha \sqrt{\rho_{\text{GND,P}}^\alpha} \quad (8a)$$

$$s^\alpha = s_0^\alpha + \int_{t'=0}^{t'=t} \sum_{\beta=1}^{n_{\text{slip}}} h^{\alpha\beta} |\dot{\gamma}^\beta| dt' + \frac{Q^\alpha}{c_2 c_3 b^\alpha} \sqrt{\rho_{\text{GND,F}}^\alpha} \quad (8b)$$

325

where μ^α and b^α are respectively the shear modulus and magnitude of Burgers vector for slip system α . c_1 is the fitting constant for the long-range impeding stresses arising due to GNDs. c_2 and c_3 are respectively the jump and obstacle width constants [55]. c_1 , c_2 and c_3 are calibrated for *hcp* crystals as 0.1, 0.2 and 1.0, respectively [56]. Q^α is the activation energy to overcome forest GND dislocation population, approximated as $Q^\alpha = 10\mu^\alpha b^\alpha$ for *hcp* crystals [56]. $h^{\alpha\beta}$ is the hardening matrix which accounts for the self and latent hardening of slip systems. $h^{\alpha\beta}$ is calculated as

$$h^{\alpha\beta} = \chi^{\alpha\beta} h_{ref}^\beta \left| 1 - \frac{s^\beta}{s_{sat}^\beta} \right|^r \text{ sign} \left(1 - \frac{s^\beta}{s_{sat}^\beta} \right) \quad \text{where} \quad s_{sat}^\beta = \tilde{s}^\beta \left(\frac{\dot{\gamma}^\beta}{\dot{\gamma}_0^\beta} \right)^n \quad (9)$$

r , n and h_{ref}^β are fitting constants. \tilde{s}^β denotes the saturation stress on slip system β . $\chi^{\alpha\beta}$ is the interaction factor, defining the strengthening effect of slip system β on slip system α . $\chi^{\alpha\beta}$ is taken as 1 in this work. s_0^α corresponds to the grain-size dependent initial slip system resistance which follows a Hall-Petch type relationship as [53]

$$s_0^\alpha = s_{0*}^\alpha + \frac{K^\alpha}{\sqrt{D_g}} \quad (10)$$

where s_{0*}^α and D_g are the inherent initial slip system resistance and equivalent grain diameter, respectively. $K^\alpha = \sqrt{\frac{(2-\nu)\pi\tau^*Gb^\alpha}{2(1-\nu)}}$ is the Hall-Petch coefficient. Here ν , G and τ^* are respectively the Poisson's ratio, shear modulus of material and barrier strength for the grain boundary taken as $\tau^* = 0.01G$ [53].

$\rho_{GND,P}^\alpha$ in Eq. 8a is the parallel GND density, defined as total GND density projected onto the slip plane α . $\rho_{GND,F}^\alpha$ in Eq. 8b corresponds to the forest GND density, defined as total GND density projected along the normal to slip plane α . The Parallel and forest GND dislocation densities for slip system α could be calculated as

$$\rho_{GND,P}^\alpha = \sum_{\beta=1}^{n_{slip}} \chi^{\alpha\beta} \left[\left| \rho_{GNDs}^\beta \sin \left(\mathbf{n}_0^\alpha, \mathbf{m}_0^\beta \right) \right| + \left| \rho_{GNDet}^\beta \sin \left(\mathbf{n}_0^\alpha, \mathbf{t}_0^\beta \right) \right| + \left| \rho_{GNDen}^\beta \sin \left(\mathbf{n}_0^\alpha, \mathbf{n}_0^\beta \right) \right| \right] \quad (11a)$$

$$\rho_{GND,F}^\alpha = \sum_{\beta=1}^{n_{slip}} \chi^{\alpha\beta} \left[\left| \rho_{GNDs}^\beta \cos \left(\mathbf{n}_0^\alpha, \mathbf{m}_0^\beta \right) \right| + \left| \rho_{GNDet}^\beta \cos \left(\mathbf{n}_0^\alpha, \mathbf{t}_0^\beta \right) \right| + \left| \rho_{GNDen}^\beta \cos \left(\mathbf{n}_0^\alpha, \mathbf{n}_0^\beta \right) \right| \right] \quad (11b)$$

ρ_{GNDs}^β , ρ_{GNDen}^β and ρ_{GNDet}^β are the vectorial components of GND density on slip system β with Burgers vector along \mathbf{m}_0^β and line tangent vector parallel

to \mathbf{m}_0^β , \mathbf{n}_0^β and $\mathbf{t}_0^\beta = \mathbf{m}_0^\beta \times \mathbf{n}_0^\beta$ [55]. Augmenting the slip resistances in Eqs. 8 with GND-related resistances renders the model non-local as calculation of GNDs involves some non-local calculations on \mathbf{F}^p mapping. The procedure for calculation of GNDs will be elaborated in details in Section 4.3.2.

355 *4.2.2. Unified flow rule*

Dislocation motion in the glide plane is controlled by both thermal activation and drag mechanisms. The strength of these mechanisms changes with the stress level and rate of deformation such that the thermally-activated processes are the main rate controlling mechanism up to strain rates of $10^4 \sim 10^5 \text{ s}^{-1}$ 360 while the drag processes take over the dislocation glide at strain rates beyond 10^5 s^{-1} . Motivated by this fact, generally flow rules have been developed either in a thermal activation framework or a drag-dominated one. Unifying the two 365 classes of flow rules and formulating one physics-based unified flow rule, whose application is not limited to a specific range of strain rates, is desired. Using such a flow rule is encouraged as it ensures the mechanism of local dislocation-induced plasticity in consistent with the local stresses and strain rates. It becomes 370 important in simulation of polycrystalline aggregates where the local stress and strain rates might be lower or higher than the applied macroscopic stress or strain rate. The unified flow rule is obtained by combining thermal activation and drag-dominated (CTD) processes. This type of flow rule is referred to an CTD flow rule hereafter.

In this paper, we use Orowan equation which expresses the slip rate on slip system α in terms of dislocation density ρ^α and average dislocation velocity v^α as

$$\dot{\gamma}^\alpha = \rho^\alpha b^\alpha v^\alpha \text{sign}(\tau^\alpha) \quad (12)$$

375 Experimental observations [38, 46] have shown that dislocations of screw character are responsible for plastic deformation in Ti alloys. Screw dislocations move over the Peierls hills in the glide plane through the well-known double-kink mechanism. This mechanism involves thermally-activated nucleation of kink pairs. Considering some simplifying assumptions such as nucleation of one 380 kink pair per dislocation line, dislocation motion by this mechanism could be thought to take place in two stages. In the first stage, the dislocation lies in a Peierls valley and waits for some time, referred to as the *waiting time* t_w^α , until a successful local thermal activation takes place and a pair of kinks with a separation distance of l_{kink}^α nucleates and moves to the next Peierls valley [57]. 385 Figure 7 illustrates nucleation of a pair of kinks. The second stage is a drag-dominated stage where the kinks move apart and bring the whole dislocation line to the next Peierls valley [22]. The time spent in this stage is called the *running time* t_r^α . The average dislocation velocity could be formulated as [32]

$$v^\alpha = \frac{\lambda^\alpha}{t_w^\alpha + t_r^\alpha} \quad (13)$$

390 where λ^α is the spacing between two consecutive Peierls valleys, approximated as b^α here.

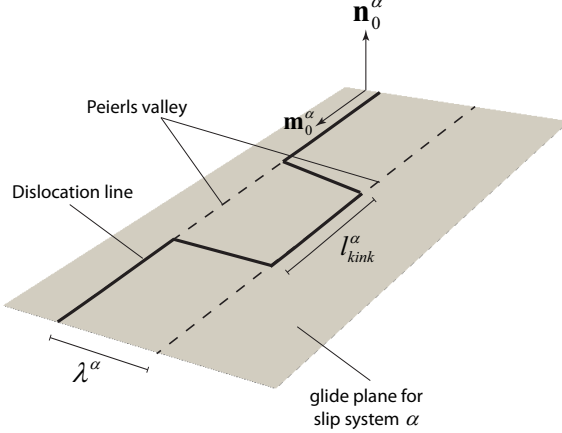


Figure 7: Illustration of screw dislocation motion over Peierls hills in the glide plane via a double-kink mechanism

Waiting time corresponds to the thermally-activated nucleation of a kink pair. Hence, an Arrhenius-type relationship can be invoked to formulate t_w^α in terms of temperature as [58]

$$t_w^\alpha = \left[2 \frac{\nu_D b^\alpha}{l_{kink}^\alpha} \frac{l^\alpha}{l_{kink}^\alpha} \exp\left(-\frac{Q_{slip}^\alpha}{K_B T}\right) \sinh\left(\frac{|\tau^\alpha| - \tau_{ath}^\alpha}{\tau_{th}^\alpha}\right) \right]^{-1} \quad (14)$$

in which l^α is the average length of a straight dislocation line which is inversely proportional to the square root of the forest dislocation population ρ_F^α ; that is, $l^\alpha = c_l^\alpha / \sqrt{\rho_F^\alpha}$ where c_l^α is a fitting constant [59]. K_B is the Boltzmann constant and ν_D is the Debye frequency ($9.13 \times 10^{13} s^{-1}$ for titanium). Q_{slip}^α is the effective activation energy for dislocation slip. The term $\frac{\nu_D b^\alpha}{l_{kink}^\alpha}$ corresponds to the attempt frequency for nucleation of a kink pair and the term $\frac{l^\alpha}{l_{kink}^\alpha}$ is the number of competing sites for the nucleation on the dislocation line. τ_{ath}^α and τ_{th}^α are respectively the athermal and thermal resistances to dislocation motion on slip system α , given by [55]

$$\tau_{ath}^\alpha = c_{ath}^\alpha \mu^\alpha b^\alpha \sqrt{\rho_P^\alpha} + s_0^\alpha \quad (15a)$$

$$\tau_{th}^\alpha = \frac{K_B T}{c_{act}^\alpha l_{kink}^\alpha b^{\alpha 2}} \quad (15b)$$

c_{ath} and c_{act} are fitting parameters. The term $c_{act}^\alpha l_{kink}^\alpha b^{\alpha 2}$ corresponds to the activation volume. As described earlier in Eq. 10, s_0^α is the grain size-dependent initial resistance which contributes to the athermal resistance [60]. Similar to Eq. 11, the total parallel and forest dislocation populations on slip system α

could be calculated as

$$\rho_P^\alpha = \sum_{\beta=1}^{n_{slip}} \chi^{\alpha\beta} \left[\left| \rho_{GNDs}^\beta \sin(\mathbf{n}_0^\alpha, \mathbf{m}_0^\beta) \right| + \left| \rho_{GNDet}^\beta \sin(\mathbf{n}_0^\alpha, \mathbf{t}_0^\beta) \right| + \left| \rho_{GNDen}^\beta \sin(\mathbf{n}_0^\alpha, \mathbf{n}_0^\beta) \right| + \left| \rho^\beta \sin(\mathbf{n}_0^\alpha, \mathbf{m}_0^\beta) \right| \right] \quad (16a)$$

$$\rho_F^\alpha = \sum_{\beta=1}^{n_{slip}} \chi^{\alpha\beta} \left[\left| \rho_{GNDs}^\beta \cos(\mathbf{n}_0^\alpha, \mathbf{m}_0^\beta) \right| + \left| \rho_{GNDet}^\beta \cos(\mathbf{n}_0^\alpha, \mathbf{t}_0^\beta) \right| + \left| \rho_{GNDen}^\beta \cos(\mathbf{n}_0^\alpha, \mathbf{n}_0^\beta) \right| + \left| \rho^\beta \cos(\mathbf{n}_0^\alpha, \mathbf{m}_0^\beta) \right| \right] \quad (16b)$$

In the last term on RHS of Eqs. 16a and 16b, the angle between \mathbf{n}_0^α and \mathbf{m}_0^β is used to project ρ^β onto the slip system α . \mathbf{m}_0^β is used here since the tangent line is parallel to the Burgers vector for the screw dislocations.

Running time corresponds to the stage where dislocation motion is governed by the retarding drag forces due to the phonon-dislocation interactions. Running time can be written in terms of viscous drag velocity v_d^α as [31, 32]

$$t_r^\alpha = \frac{\lambda^\alpha}{v_d^\alpha} \quad (17)$$

Depending on the temperature, several types of phonon-dislocation interaction are possible such as flutter, scattering, radiation mechanisms and etc [22, 31]. These interactions yield a temperature-dependent drag coefficient B_0 of the form [22]

$$B_0 = \frac{c_d K_B T}{v_s b^{\alpha 2}} \quad (18)$$

Here v_s is the shear wave speed. c_d is the drag constant, taken as 45 in this paper. Solving the equation of motion for a unit length of dislocation line and recognizing that the effective dislocation line mass density is negligible compared to the drag coefficient B_0 , viscous drag velocity is obtained as [61]

$$v_d^\alpha = \frac{(|\tau^\alpha| - \tau_{ath}^\alpha) b^\alpha}{B_0} \quad (19)$$

In order to ensure that the dislocation drag velocity does not exceed the shear wave speed, relativistic effects should be implemented, i.e. the drag coefficient needs to be modified as [35]

$$B = \frac{B_0}{1 - \left(\frac{v_d^\alpha}{v_s} \right)^2} \quad (20)$$

This modification basically implies that as the dislocation drag velocity v_d^α approaches the shear wave speed, the drag coefficient B grows very large and

consequently very large resolved shear stresses would be required. Replacing B_0 in Eq. 19 with B and solving for v_d^α , the modified dislocation drag velocity is obtained as [35]

$$v_d^\alpha = v_s \left[\sqrt{1 + \left(\frac{B_0 v_s}{2(|\tau^\alpha| - \tau_{ath}^\alpha) b^\alpha} \right)^2} - \frac{B_0 v_s}{2(|\tau^\alpha| - \tau_{ath}^\alpha) b^\alpha} \right] \quad (21)$$

Substituting Eqs. 17 and 14 into Eq. 13, the expression for the unified average dislocation velocity, informed by both thermally-activated and drag-dominated processes, is obtained as

$$v^\alpha = \frac{v_d^\alpha}{\frac{v_d^\alpha}{\lambda^\alpha} \left[2 \frac{\nu_D b^\alpha}{l_{kink}^\alpha} \frac{l^\alpha}{l_{kink}^\alpha} \exp \left(-\frac{Q_{slip}^\alpha}{K_B T} \right) \sinh \left(\frac{|\tau^\alpha| - \tau_{ath}^\alpha}{\tau_{th}^\alpha} \right) \right]^{-1} + 1} \quad (22)$$

The unified average dislocation velocity profile is plotted in Figure 8 and compared with the velocity profile for a purely thermally-activated and purely drag-dominated dislocation motion. In this plot, only the resolved shear stress is varied to obtain a schematic of the average dislocation velocity for a given dislocation density and temperature. It is observed that at low stresses the unified velocity profile is following the average velocity of a purely thermally-activated motion. As stress increases, the rate of successful thermal activations boosts up and t_w^α decreases exponentially, therefore diminishing the rate controlling effect of thermally-activated processes. At higher stress levels, the unified average velocity follows the average velocity of a purely drag-dominated dislocation motion. Note the transition of the unified velocity from a thermally-activated regime to a mixed regime at about an average velocity of 90m/s. This transition point is close to that of the screw dislocations in tantalum [33]. The multi-scale strength model developed by Barton et al. [33] suggested that the average velocity of screw dislocations departs from a thermally-activated regime at roughly 100m/s.

Having derived the average dislocation velocity, one can evaluate the slip rate on different slip systems using Eq. 12, provided that the dislocation density is known. Section 4.3 discusses the evolution of dislocation density on different slip systems during the course of plastic deformation.

4.3. Evolution of dislocation densities

Dislocation population could be divided into two distinct classes, namely statistically stored dislocations (SSDs) and geometrically necessary dislocations (GNDs). SSDs are characterized by a vanishing net Burgers vector. They evolve during deformation through numerous mechanisms such as multiplication, thermal and athermal annihilation and etc [55]. GNDs, on the other hand, correspond to the storage of polarized dislocation densities and are characterized by a non-zero net Burgers vector [62]. GNDs account for the crystal lattice curvatures which become prominent in single crystal bending and near the polycrystalline grain boundaries.

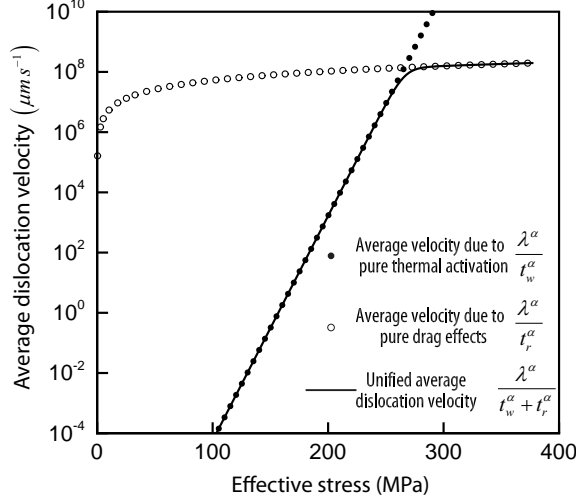


Figure 8: Comparison of the unified average dislocation velocity profile with purely thermally-activated and purely drag-dominated average velocities

The overall slip resistance is assumed to be due to both the SSDs and GNDs. The SSD density, unlike the GND density, is not an internal state variable for the PL flow rule. Therefore, as shown in Eqs. 8, the effect of GND densities on the slip system resistances is explicitly taken into account, whereas the contribution of SSDs to the evolution of slip system resistances are considered in a phenomenological form via Eq. 9. In contrast with the PL flow rule, the CTD flow rule considers both the SSD and GND densities as internal state variables. This enables us to explicitly formulate and explain the slip system hardening in terms of both SSD and GND densities, as shown in Eqs. 15. In the following, the evolution of SSDs (applicable only to the CTD flow rule) and GNDs (applicable to both PL and CTD flow rules) are explained in details.

4.3.1. Evolution of statistically stored dislocations

A dislocation density-based CP framework gives the modelers the opportunity to track material hardening more tangibly in terms of the interaction and entanglement of dislocations on different slip systems. Dislocation population is controlled by a competition between dislocation multiplication and annihilation mechanisms. Multiplication corresponds to the introduction of new dislocations from a pre-existing population of dislocations. The multiplication rate is proportional to the square root of dislocation density [63] and could be written as

$$\dot{\rho}_{mult}^{\alpha} = c_{multi}^{\alpha} \sqrt{\rho^{\alpha}} |\dot{\gamma}^{\alpha}| \quad (23)$$

where c_{multi}^{α} is a fitting constant. Two dislocations of opposite sign can annihilate each other athermally if they come within a critical distance. The rate of

othermal annihilation could be formulated as [59]

$$\dot{\rho}_{anni}^\alpha = c_{annih}^\alpha \rho^\alpha |\dot{\gamma}^\alpha| \quad (24)$$

c_{annih}^α is a fitting constant. The rate of dislocation evolution could then be written as

$$\dot{\rho}^\alpha = \dot{\rho}_{mult}^\alpha - \dot{\rho}_{anni}^\alpha \quad (25)$$

This equation is basically a simplified Kocks-Mecking type relationship [64].
490 Note that multiplication and athermal annihilation are only two of the many possible mechanisms that could contribute to the evolution of dislocation population. Considering other dislocation evolution mechanisms is absolutely possible; however, it is at the expense of adding to the complexity of the model and introducing more fitting constants.

495 *4.3.2. Calculation of geometrically necessary dislocations*

Presence of GNDs in the microstructure are attributed to the incompatibility in the plastic strain field. Due to plastic anisotropy of *hcp* crystal, plastic response is highly dependent on the crystallographic orientation of grains. This strong orientation-dependent plastic response leads to the accumulation 500 of GNDs majorly near the grain boundaries where high gradients in plastic strain take place due to the distinct crystallographic orientation across the grain boundary.

From a continuum mechanics viewpoint, the Nye dislocation tensor Λ which measures the incompatibility in the intermediate configuration could be derived 505 in terms of \mathbf{F}^p mapping as

$$\Lambda = -(\nabla_X \times \mathbf{F}^p)^T \quad (26)$$

where ∇_X is the gradient operator with respect to the reference coordinates. The Nye dislocation tensor could be equivalently expressed in terms of GNDs from a dislocation mechanics viewpoint as [65]

$$\Lambda = \sum_{\alpha=1}^{n_{slip}} b^\alpha (\rho_{GNDs}^\alpha \mathbf{m}_0^\alpha \otimes \mathbf{m}_0^\alpha + \rho_{GNDet}^\alpha \mathbf{m}_0^\alpha \otimes \mathbf{t}_0^\alpha + \rho_{GNDen}^\alpha \mathbf{m}_0^\alpha \otimes \mathbf{n}_0^\alpha) \quad (27)$$

There are in general $3 \times n_{slip}$ unknown GND densities; 90 for *hcp* crystals.
510 However, one could observe that there are only 9 independent ρ_{GNDs}^α , 24 independent ρ_{GNDet}^α and 30 independent ρ_{GNDen}^α . Hence, the number of unknown GND densities reduces to 63 for *hcp* crystals. Equating Eqs. 26 and 27, yields

$$\hat{\Lambda} = \mathbf{A} \rho_{GND} \quad (28)$$

in which $\hat{\Lambda}$ is the 9×1 vectorial form of Λ , \mathbf{A} is a 9×36 matrix containing the basis vectors $\mathbf{m}_0^\alpha \otimes \mathbf{m}_0^\alpha$, $\mathbf{m}_0^\alpha \otimes \mathbf{t}_0^\alpha$ and $\mathbf{m}_0^\alpha \otimes \mathbf{n}_0^\alpha$ and ρ_{GND} is the 63×1 column vector of unknown independent GND components. It is clear that Eq.
515

28 is an under-determined system of linear equation and may not have a unique solution. Based on geometric considerations, Arsenlis and Parks [62] set up a functional of the form

$$\mathcal{F}(\rho_{\text{GND}}, \boldsymbol{\lambda}) = \rho_{\text{GND}}^T \rho_{\text{GND}} + \boldsymbol{\lambda}^T (\mathbf{A} \rho_{\text{GND}} - \hat{\boldsymbol{\Lambda}}) \quad (29)$$

whose minimization yields the GND densities. Here $\boldsymbol{\lambda}$ is the vector of Lagrange multipliers. Minimizing the functional \mathcal{F} , the GND densities are obtained as

$$\rho_{\text{GND}} = \mathbf{A}^T (\mathbf{A} \mathbf{A}^T)^{-1} \hat{\boldsymbol{\Lambda}} \quad (30)$$

Incorporating GNDs in the CP framework renders the model size-dependent and non-local since the Nye dislocation tensor is derived in terms of the gradient of \mathbf{F}^p field in Eq. 26. In this work, the constitutive updates are performed at the integration points of the elements. Therefore, all the internal state variables and kinematic quantities such as \mathbf{F}^p are known only at the the integration points of the elements. In order to calculate the gradient of \mathbf{F}^p field over an element, one could interpolate \mathbf{F}^p field using the shape functions N_i as $\mathbf{F}^p(\mathbf{X}) = \sum_{i=1}^{n_{\text{node}}} N_i(\mathbf{X}) \mathbf{F}_{\text{nodal}_i}^p$ where n_{node} is number of nodal points per element and $\mathbf{F}_{\text{nodal}_i}^p$ is the value of \mathbf{F}^p at the nodal points. It is clear that the nodal values of \mathbf{F}^p should be determined from the known values of \mathbf{F}^p at the integration points. The super-convergent patch recovery method (SPR) developed by Zienkiewicz and Zhu [66] is deemed to be an appropriate method for this purpose. A detailed discussion on the derivation of nodal value of \mathbf{F}^p using SPR technique is given in Cheng and Ghosh [56].

4.4. Adiabatic heating

Plastic deformation generates heat in the material. The energy dissipated due to the plasticity converts into thermo-plastic heating, thermo-elastic heating and defect energy [67]. At low strain rates, the generated heat conducts out of the microstructure; however, if the deformation process is rapid, there is not enough time to conduct heat away and temperature increases locally in an adiabatic fashion. Even deformations at moderate strain rates could be treated as essentially adiabatic [3]. Temperature increase due to adiabatic heating is very important since it promotes plasticity by boosting up the rate of thermal activation.

The rate of temperature increase due to adiabatic heating could be formulated as

$$\dot{T} = \frac{\beta_t}{\rho \hat{c}} \dot{W}_p \quad (31)$$

in which ρ is the material mass density, 4428kg/m^3 for typical Ti alloys. \hat{c} is the specific heat capacity which changes with temperature as $\hat{c} = 559.77 - 0.1473T + 0.00042949T^2 \text{JKg}^{-1}\text{K}^{-1}$ for $278 < T < 1144 \text{K}$ [68]. $\dot{W}_p = \boldsymbol{\sigma} : \mathbf{d}^p$ is the plastic power per unit deformed volume. \mathbf{d}^p is the symmetric part of the plastic velocity gradient in the current configuration $\mathbf{l}^p = \mathbf{F}^e \mathbf{F}^{\theta} \dot{\mathbf{F}}^p \mathbf{F}^{p-1} \mathbf{F}^{\theta-1} \mathbf{F}^{e-1}$. β_t

corresponds to the fraction of plastic work which converts into heat. Ignoring the thermo-elastic heating, $1 - \beta_t$ denotes the fraction of plastic work which is stored in the material in the form of defects, referred to as the stored energy of cold work. Most of the plastic work has been observed to convert into heat for metals. In this work, β_t is taken as 1.

4.5. Time integration algorithm for crystal plasticity constitutive model

Several time integration algorithms have been proposed in the literature for updating CP constitutive models. An excellent summary of various time integration schemes is provided by Ling et al [69]. In this work, a set of six nonlinear algebraic equations, corresponding to each component of the second Piola-Kirchhoff stress, is derived. Then, a semi-implicit algorithm is used to solve the set of equations. In an increment from t to $t + \Delta t$, the following quantities are known/prescribed:

- known values of kinematic quantities, viz. $\mathbf{F}(t)$, $\mathbf{F}^\theta(t)$, $\mathbf{F}^p(t)$
- known values of internal state variables (ISV), viz. $T(t)$, $\dot{W}_p(t)$, $s^\alpha(t)$ (only for PL flow rule) and $\rho^\alpha(t)$ (only for CTD flow rule)
- prescribed $\mathbf{F}(t + \Delta t)$

For the constitutive updates in the time interval $(t, t + \Delta t]$, the GND densities are calculated using $\mathbf{F}^p(t)$. Furthermore, it is necessary to update temperature and thermal deformation gradient for simulation of high rate deformations. For adiabatic simulations, thermal deformation gradient at $t + \Delta t$ is obtained as $\mathbf{F}^\theta(t + \Delta t) = \exp\left(\boldsymbol{\alpha} \frac{\beta_t \dot{W}_p(t) \Delta t}{\rho \hat{c}}\right) \mathbf{F}^\theta(t)$ and temperature is found explicitly using the information at time t as $T(t + \Delta t) = T(t) + \frac{\beta_t \dot{W}_p(t) \Delta t}{\rho \hat{c}}$.

Integrating Eq. 4 with respect to time, \mathbf{F}^p at time $t + \Delta t$ is obtained as

$$\mathbf{F}^p(t + \Delta t) = \left(\mathbf{I} + \sum_{\alpha=1}^{n_{slip}} \Delta \gamma^\alpha \mathbf{m}_0^\alpha \otimes \mathbf{n}_0^\alpha \right) \mathbf{F}^p(t) \quad (32)$$

where $\Delta \gamma^\alpha = \dot{\gamma}^\alpha \Delta t$. Using Eqs. 32 and 2, the elastic deformation gradient is derived as

$$\mathbf{F}^e(t + \Delta t) = \mathbf{F}(t + \Delta t) \mathbf{F}^{p^{-1}}(t) \left(\mathbf{I} - \sum_{\alpha=1}^{n_{slip}} \Delta \gamma^\alpha \mathbf{m}_0^\alpha \otimes \mathbf{n}_0^\alpha \right) \mathbf{F}^{\theta^{-1}}(t + \Delta t) \quad (33)$$

Substituting $\mathbf{F}^e(t + \Delta t)$ into Eq. 5, a set of nonlinear equations in terms of the updated second Piola-Kirchhoff stress is obtained as

$$\mathbf{S}(t + \Delta t) = \mathbf{S}^{tr} - \sum_{\alpha=1}^{n_{slip}} \Delta \gamma^\alpha (\mathbf{S}(t + \Delta t), \text{ISV}) \mathbf{B}^\alpha \quad (34)$$

580 where

$$\tilde{\mathbf{A}} = \mathbf{F}^{p^{-T}}(t) \mathbf{F}^T(t + \Delta t) \mathbf{F}(t + \Delta t) \mathbf{F}^{p^{-1}}(t) \quad (35a)$$

$$\mathbf{S}^{tr} = \mathbb{C} : \left[\frac{1}{2} \left(\mathbf{F}^{\theta^{-T}}(t + \Delta t) \tilde{\mathbf{A}} \mathbf{F}^{\theta^{-1}}(t + \Delta t) - \mathbf{I} \right) \right] \quad (35b)$$

$$\mathbf{B}^\alpha = \frac{1}{2} \mathbb{C} : \left[\mathbf{F}^{\theta^{-T}}(t + \Delta t) \left(\tilde{\mathbf{A}} (\mathbf{m}_0^\alpha \otimes \mathbf{n}_0^\alpha) + (\mathbf{n}_0^\alpha \otimes \mathbf{m}_0^\alpha) \tilde{\mathbf{A}} \right) \mathbf{F}^{\theta^{-1}}(t + \Delta t) \right] \quad (35c)$$

Newton-Raphson iterative solver is used to solve the nonlinear equation 34 in two stages. In the first stage, Eq. 34 is solved for $\mathbf{S}(t + \Delta t)$ while the slip system resistance-related quantities, i.e. $s^\alpha(t + \Delta t)$ for PL flow rule or $\rho^\alpha(t + \Delta t)$ for CTD flow rule, are held fixed. The i -th iteration of the Newton-Raphson algorithm reads as

$$\mathbf{S}^{i+1}(t + \Delta t) = \mathbf{S}^i(t + \Delta t) - \mathbb{J}^{-1} : \mathbf{R}^i \quad (36)$$

where the residual \mathbf{R} and Jacobian \mathbb{J} are computed

$$\mathbf{R}^i = \mathbf{S}^i(t + \Delta t) - \mathbf{S}^{tr} + \sum_{\alpha=1}^{n_{slip}} \Delta \gamma^\alpha \mathbf{B}^\alpha \quad (37a)$$

$$\mathbb{J} = \frac{\partial \mathbf{R}}{\partial \mathbf{S}^i} = \mathbb{I}_{sym} + \sum_{\alpha=1}^{n_{slip}} \mathbf{B}^\alpha \otimes \frac{\partial \Delta \gamma^\alpha}{\partial \mathbf{S}^i} \quad (37b)$$

590 where \mathbb{I}_{sym} is the symmetric fourth order identity tensor. Once $\mathbf{S}(t + \Delta t)$ is determined, the slip system resistance-related quantities are evolved in the second stage. Next the first stage is repeated again with the evolved resistances and so on. The sequence of computational operation needed for CP constitutive update in given in Table 1.

5. Stabilization of linear tetrahedral elements for CPFE modeling

595 Modeling material response and predictions of localized phenomenon such as fatigue crack nucleation [70, 71] and twinning [56] in the framework of CP are highly dependent on the ability of the model (both material constitutive model and numerical method) to accurately calculate the local state of the material, viz. local stress state and kinematic variables. This calls for the development of appropriate constitutive models and robust numerical schemes. In this section, 600 we focus on improving the conventional finite element for the CP modeling of microstructures.

Linear constant strain tetrahedral elements (TET4) are preferred for CPFE simulations due to their inherent simplicity, high efficiency and their excellent capability to conform to the complex geometry of polycrystalline aggregates

Step A	Purpose: determining second Piola-Kirchhoff stress and slip rates
I	<i>Initialization of relevant quantities for Newton-Raphson algorithm:</i> $\mathbf{S}^0(t + \Delta t) = \mathbf{S}(t)$ $s^\alpha(t + \Delta t) = s^\alpha(t)$ (for PL flow rule) $\rho^\alpha(t + \Delta t) = \rho^\alpha(t)$ (for CTD flow rule)
II	<i>for the i-th iteration in the Newton-Raphson algorithm:</i> (a) Calculate the resolved shear stress using Eq. 7 (b) Evaluate the slip rate using Eq. 6 for PL flow rule or Eq. 12 for CTD flow rule (c) Update the second Piola-Kirchhoff stress using Eq. 36 (d) Check for convergence: if no, return to step (a); if yes, proceed to step III
III	<i>calculate the resolved shear stress and slip rate based on the converged second Piola-Kirchhoff stress</i>
Step B	Purpose: updating slip system resistances
IV	<i>Compute hardening-related quantities:</i> Calculate the hardening matrix using Eq. 9 for PL flow rule Evolve dislocation densities using Eq. 25 for CTD flow rule
V	<i>Update slip system resistances:</i> Use Eq.8b for PL flow rule Use Eq.15a for CTD flow rule
VI	<i>Check for convergence of slip system resistances: if no, return to step II; if yes, proceed to step VII</i>
VII	<i>Evaluate elastic deformation gradient using Eq. 2 and Cauchy stress using Eq. 5</i>

Table 1: Sequence of computational operations for constitutive update procedure

605 with tortuous grains. However, these elements have been observed to suffer from volumetric locking for modeling (nearly-) incompressible materials. Volumetric locking of TET4 elements can adversely affect the accuracy of CPFE simulations in both local and global levels due to the presence of isochoric plastic deformation. The locking-induced instability is manifested in the simulation results in the form of over-predicted stress levels, checker-board pattern of pressure field and under-predicted displacement field.

610 In this paper, the methodology proposed in a recent paper by the authors [20] is used to relieve volumetric locking for efficient and accurate CPFE simulations. In this model, the **F**-bar-patch method [17] is implemented into the CPFE framework. The basic idea behind **F**-bar-patch method is to modify deformation gradient for constitutive calculations such that the incompressibility is enforced over a patch of elements, rather than on individual elements. In order to apply **F**-bar-patch method for CPFE simulations, it is required to divide the entire mesh into non-overlapping patches of elements. Consider a set of elements forming a patch \mathcal{P} . The modified deformation gradient for element $K \in \mathcal{P}$ at time t is calculated as

$$\bar{\mathbf{F}}_K = \left[\frac{\Omega_{\mathcal{P}}^t}{\Omega_{\mathcal{P}}^0 \det \mathbf{F}_K} \right]^{\frac{1}{3}} \mathbf{F}_K \quad (38)$$

615 where $\Omega_{\mathcal{P}}^{t+\Delta t}$ and $\Omega_{\mathcal{P}}^0$ are respectively the volume of the patch in the current and undeformed configurations. The modified deformation gradient $\bar{\mathbf{F}}_K$ is then passed on to the material routine for constitutive calculations.

620 **F**-bar-patch method could be used for any type of material constitutive law. It does not require addition of new degrees of freedom to the system, and the constitutive updates are performed at the quadrature points of the element. Implementation of **F**-bar-patch method into any standard displacement-based FE code is straightforward.

630 6. Numerical results

635 In this section, the PL and CTD flow rules are first calibrated and validated using the results of quasi-static and dynamic experiments. The models are then used to investigate the effect of deformation rate on the flow stress. The section concludes with an investigation on the effect of temperature on the material behavior in the context of isothermal and adiabatic conditions.

6.1. Calibration and validation of constitutive models with experiments

640 Calibration and validation of material constitutive models against experiments are critical to meaningful simulation of deformation processes of metals. The material parameters are calibrated using quasi-static and dynamic experiments. For the sake of brevity, the experiments are referred to in an XX-YY-ZZ format. XX corresponds to the type of microstructure, either AR or RA microstructure. YY corresponds to the rate of deformation, either quasi-static (QS) or dynamic (DY). ZZ refers to the loading direction which could be either

645 normal (ND), rolling (RD) or transverse (TD) direction. It is worthy to mention
 650 that ND, RD and TD correspond respectively to the global [100], [010] and [001] directions in our simulations. There are in total eight experiments where four of them are used for the calibration of parameters and the other four are used for the validation of the models. Table 2 reports the types of experiments used in this study along with their role in either calibration or validation of the models. A high-fidelity calibration is expected since various experiments with different rates and loading directions are employed.

microstructure	strain rate (s^{-1})	loading direction	experiment title	role
RA	1.0×10^{-3}	ND	RA-QS-ND	calibration
	$1.1 \times 10^{+3}$	ND	RA-DY-ND	calibration
	2.0×10^{-3}	RD	RA-QS-RD	calibration
	$2.6 \times 10^{+3}$	RD	RA-DY-RD	calibration
	1.0×10^{-3}	TD	RA-QS-TD	validation
	$2.7 \times 10^{+3}$	TD	RA-DY-TD	validation
AR	$1.1 \times 10^{+3}$	ND	AR-DY-ND	validation
	$2.6 \times 10^{+3}$	RD	AR-DY-RD	validation

Table 2: details of experiments used for calibration and validation purposes

645 The material parameters to be calibrated are generally the anisotropic elastic
 650 constants and slip system-dependent crystal plasticity parameters. α titanium with an *hcp* lattice-parameter ratio $c/a = 1.59$ shows a transversely isotropic elastic response. Consider a material coordinate system defined by the orthonormal basis $(\mathbf{e}_1^c, \mathbf{e}_2^c, \mathbf{e}_3^c)$ where 1, 2 and 3 directions correspond respectively to $[\bar{1}2\bar{1}0]$, $[\bar{1}010]$ and $[0001]$ directions of the *hcp* crystal lattice. The anisotropic elasticity tensor in this coordinate system could be expressed in Voigt notation as

$$[C_{IJ}^e] = \begin{bmatrix} C_{11} & C_{12} & C_{13} & 0 & 0 & 0 \\ C_{21} & C_{22} & C_{23} & 0 & 0 & 0 \\ C_{31} & C_{32} & C_{33} & 0 & 0 & 0 \\ & & & C_{44} & 0 & 0 \\ & & & & C_{55} & 0 \\ & & & & & C_{66} \end{bmatrix} \quad (39)$$

660 Due to the transverse isotropic property, there are only 5 independent elastic constants, viz. $C_{11} = C_{22}$, $C_{12} = C_{23}$, $C_{33} = C_{66}$ and $C_{44} = (C_{11} - C_{12})/2$. The elastic constants are measured via resonant ultrasound spectroscopy experiments on Ti-7 single crystal samples at room temperature [72] and tabulated in Table 3. Experimental measurements for elastic constants of α Ti show that they decrease almost linearly with increasing the temperature, but with different slopes. The experimental results of Ogi et al. [73] are used to obtain the linear slopes for different elastic constants. Figure 9 depicts the

variation of different principal elastic constants with temperature. The linear slopes corresponding to the reduction of elastic constants with temperature are given in Table 3.

	C_{11}	C_{12}	C_{13}	C_{33}	C_{55}
$[C_{IJ}]$ (GPa)	164.7	82.5	61.8	175.2	48.5
Linear slope (MPa/K)	48	8.9	21	21	21.9

Table 3: anisotropic elastic constants obtained from resonant ultrasound spectroscopy measurements at room temperature and linear slopes for reduction of elastic constants with temperature

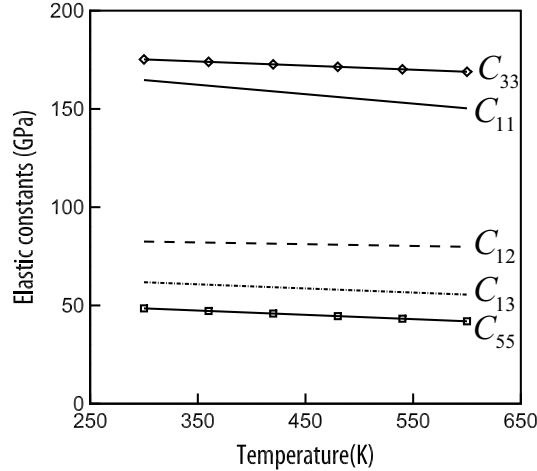


Figure 9: Variation of principal elastic constants with temperature

PL model has been previously calibrated for Ti-6Al alloy [27] with a chemical composition relatively close to that of Ti-7Al alloy. Hence, we start with the calibration of the PL model since the bounds of fitting parameters are fairly known. Performing a sensitivity analysis, it is realized that $\dot{\gamma}_0^\alpha$, s_{0*}^α and m are the parameters controlling the onset of plasticity, i.e. yield point, and h_{ref}^α , \tilde{s}^α , r^α and n^α are the ones controlling the hardening rate. It is also observed that m is the main rate-controlling parameter. The general idea is to use quasi-static tests done at room temperature to calibrate parameters controlling the onset of plasticity and hardening-related parameters. Dynamic tests are then utilized to calibrate the rate-controlling parameter. This process is clearly iterative as the rate-controlling parameter m has an impact on the yield stress, as well.

Using the four calibration tests mentioned earlier in Table 2, the PL model is calibrated and stress-strain plots comparing simulation results with experiments are shown in Figure 10. The calibrated parameters for the PL model are given

685 in Table 4. It is observed that the response to ND loading is stiffer than the RD one. This is due to the rolling process done on the material which aligns the $\langle c \rangle$ - axis of grains along ND; therefore, loading along ND direction will favor activation of $\langle c + a \rangle$ - pyramidal slip systems whose critical resolved shear stress is $2 \sim 3$ times larger than the $\langle a \rangle$ - basal or prismatic slip systems [44].

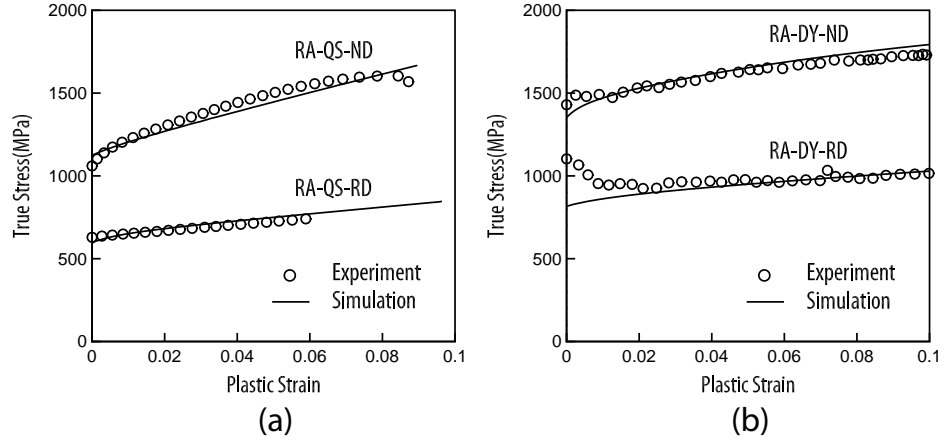


Figure 10: Calibration of the PL model using (a) quasi-static and (b) dynamic experiments

parameters	unit	$\langle a \rangle$ - basal	$\langle a \rangle$ - prismatic	$\langle a \rangle$ - pyramidal	$\langle c + a \rangle$ - pyramidal
s_{0*}^α	MPa	230	205	500	610
$\dot{\gamma}_0^\alpha$	s^{-1}	0.003	0.003	0.003	0.003
h_{ref}^α	MPa	250	250	1200	2000
m	-	0.019	0.019	0.019	0.019
r^α	-	0.02	0.02	0.02	0.02
n^α	-	0.3	0.3	0.3	0.3
\tilde{s}^α	MPa	1600	1600	1600	1800

Table 4: Calibrated parameters of the PL model for different slip systems

690 It is necessary to take into account the effect of temperature increase on plasticity in high strain rate simulations due to adiabatic heating. As temperature increases, the rate of successful thermal activation attempts is boosted up and consequently plastic flow is enhanced. In other words, the resistance to plastic flow reduces as temperature rises. This is automatically captured in the CTD model where temperature is explicitly considered. In the PL model, 695 this is phenomenologically accounted for by scaling the slip system resistances with temperature as $s_*^\alpha = s_{ref*}^\alpha (T/T_{ref})^p$ where s_{ref*}^α is the slip system resistance at reference temperature T_{ref} and p is a fitting parameter [67]. In this

work, T_{ref} is set to room temperature and s_{ref*}^α will consequently correspond to s_{0*}^α . The p exponent is set to -1 using the experimental results of Williams et al. [46] on α Ti alloys in which they measured the variation of yield stress and critical resolved shear stresses for different slip systems in a wide range of temperatures. The results reported in [46] are shifted such that yield stress at room temperature matches the one using the calibrated parameters in Table 4. Figure 11 shows the variation of 0.2% yield stress with temperature for single crystal samples oriented for activation of $\langle a \rangle$ -basal and $\langle c+a \rangle$ - pyramidal slip systems. For the sake of clarity of the plot, the results for $\langle a \rangle$ - prism slip is not shown since it is very close to the response of $\langle a \rangle$ - basal slip system.

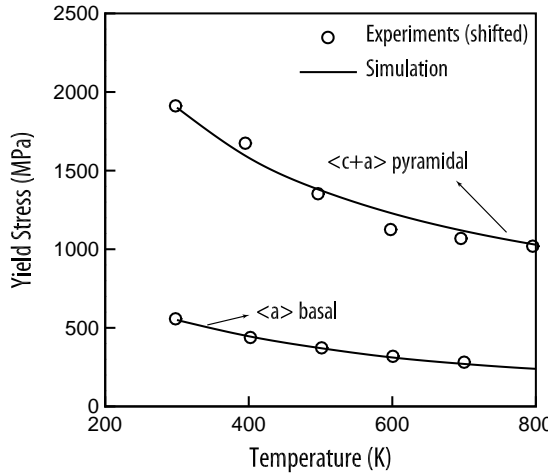


Figure 11: Variation of yield stress with temperature for single crystals oriented for activation of different slip systems

In order to validate the PL model and check the fidelity of calibrated parameters, the four validation tests are simulated and compared with experiments in Figure 12 where a good agreement is observed. It is worth noting that the model predicts the deformation of AR microstructure very well although the parameters were calibrated using the RA tests. This indicates that the grain size-dependence mechanisms in the model, i.e. GND hardening and Hall-Petch effect, are properly developed since the major difference between the AR and RA microstructures is the average grain size.

Similar to the calibration of the PL model, it is possible to calibrate the CTD model following the same steps. However since CPFE simulation of single crystals takes considerably less time compared to that of the polycrystalline microstructures, it is desirable to calibrate parameters using single crystal tests. Unfortunately single crystal experimental tests are not available for this alloy; nevertheless this is possible to reproduce such tests using the validated PL model. A single crystal model shown in Figure 13 is set up where the crystal is

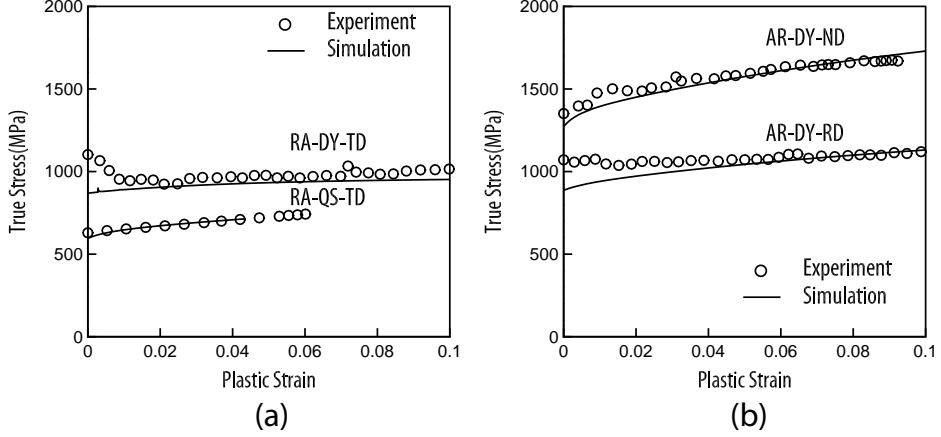


Figure 12: Validation of PL model using quasi-static and dynamic experiments on (a) RA and (b) AR microstructures

725 oriented differently to favor activation of different slip systems. PL constitutive model is first used to simulate deformation of this model under different strain rates ranging from 10^{-3} to $10^{+3} s^{-1}$. The stress-strain plots are then used to calibrate parameters in the CTD model. The stress-strain plots comparing the two constitutive models are shown in Figure 14. Experimental observations [74, 75] suggest that the effective activation energy is generally temperature-
730 dependent. In this study, effective activation energy is expressed in terms of temperature as $Q_{\text{slip}}^{\alpha}(T) = Q_{\text{ref}}^{\alpha} + c_Q^{\alpha} (T/T_{\text{ref}} - 1)^{p_Q^{\alpha}}$ and is being calibrated using Williams et al. [46] data. The complete list of calibrated parameters for the CTD model is given in Table 5.

735 CPFE simulations are carried out using the calibrated CTD model and the simulation results are compared with the experiments in Figure 15 for validation purposes. A good agreement is observed between the simulation results and experiments for all the eight tests, indicating the competency of the proposed constitutive model for modeling deformation processes under both low and high rates of deformation.

740 *6.2. Rate dependence of flow stress*

745 CPFE simulation of single crystals under uniaxial deformation is informative and provides insight into deformation processes in complex polycrystalline aggregates. Deformation of single crystal models illustrated earlier in Figure 13 is revisited in this section to understand how underlying dislocation glide mechanisms change under a wide range of strain rates. Figure 16 shows the dependence of flow stress at 8% true strain predicted by the PL and CTD models for different strain rates ranging from 10^{-4} to $10^{+7} s^{-1}$. It is observed that the two models are generally in good agreement in terms of flow stress before they

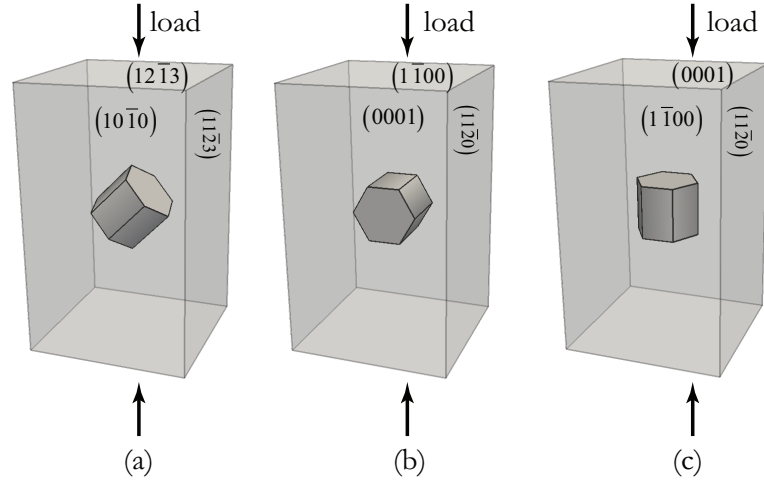


Figure 13: Single crystal model oriented for activation of (a) $\langle a \rangle$ - basal, (b) $\langle a \rangle$ - prismatic and (c) $\langle c+a \rangle$ - pyramidal slip systems

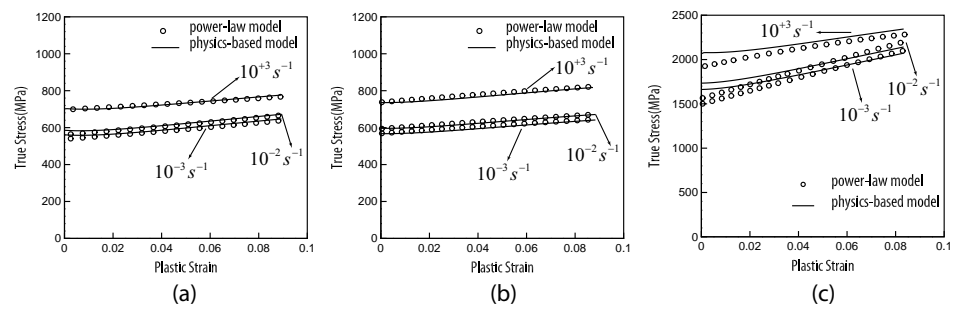


Figure 14: Calibration of CTD model using the validated PL model for (a) $\langle a \rangle$ - basal (b) $\langle a \rangle$ - prismatic and (c) $\langle c+a \rangle$ - pyramidal slip systems

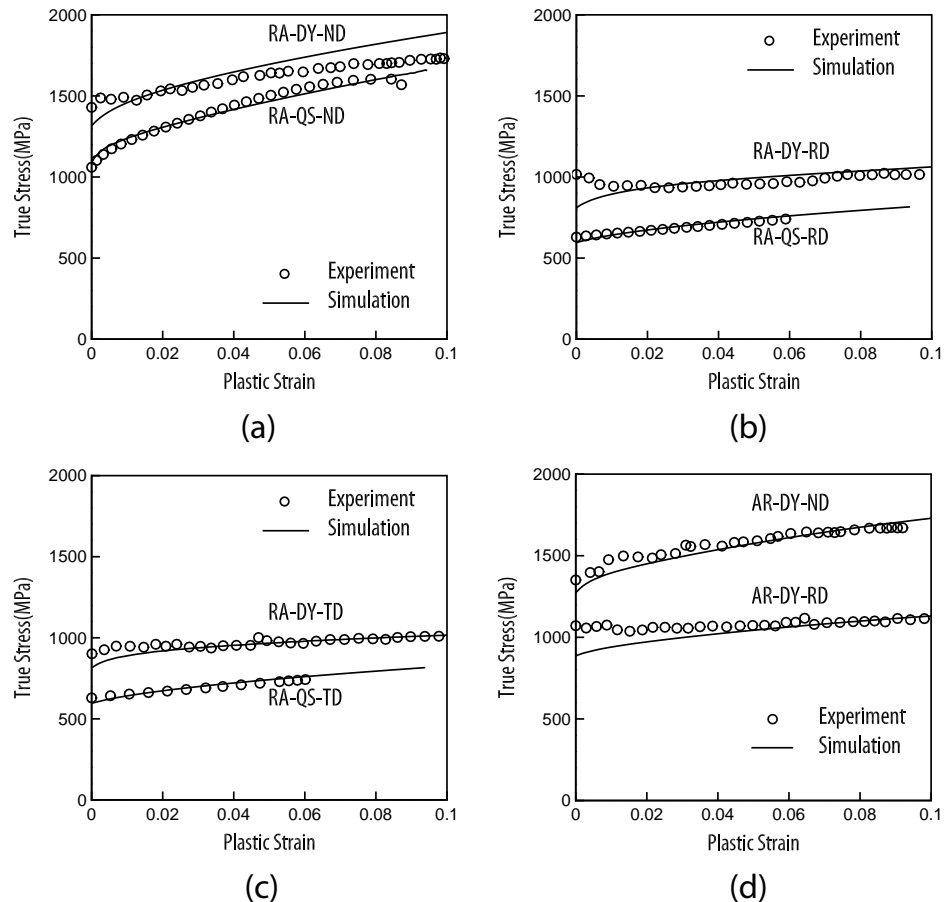


Figure 15: Validation of CTD constitutive model using quasi-static and dynamic experiments on (a-c) RA and (d) AR microstructures

parameters	unit	$\langle a \rangle$ - basal	$\langle a \rangle$ - prismatic	$\langle a \rangle$ - pyramidal	$\langle c + a \rangle$ - pyramidal
Q_{ref}^α	J	2.1×10^{-19}	2.2×10^{-19}	3.0×10^{-19}	2.6×10^{-19}
l_{kink}^α	b^α	20	20	20	20
s_{0*}^α	MPa	5.0	5.0	5.0	5.0
c_{ath}^α	-	0.8	0.62	0.7	0.5
c_{act}^α	-	0.7	0.7	0.1	0.04
c_l^α	-	8.0	8.0	8.0	8.0
c_{multi}^α	μm^{-1}	150	230	500	500
c_{annih}^α	-	10	10	10	10
c_Q^α	J	2.3×10^{-20}	3.7×10^{-20}	1.8×10^{-20}	0.9×10^{-20}
p_Q^α	-	1.6	1.6	1.6	1.6

Table 5: Calibrated parameters of CTD model for different slip systems

start to deviate for strain rates higher than $10^5 s^{-1}$. The CTD model predicts that the flow stress increases linearly with the logarithm of strain rate up to a critical strain rate, here $10^5 s^{-1}$. Beyond this critical strain rate, the flow stress still varies linearly with the logarithm of strain rate, but with a higher slope. Similar observations were made for single crystal model favorable for prism slip which is not shown in Figure 16 for the sake of clarity of the plot. This trend is observed to be the case for different orientations. This change in rate sensitivity is not unusual and has been observed to be the case for many metals [76]. The results in Figure 16 suggest that the PL model can decently model deformation up to strain rates as high as $10^5 s^{-1}$.

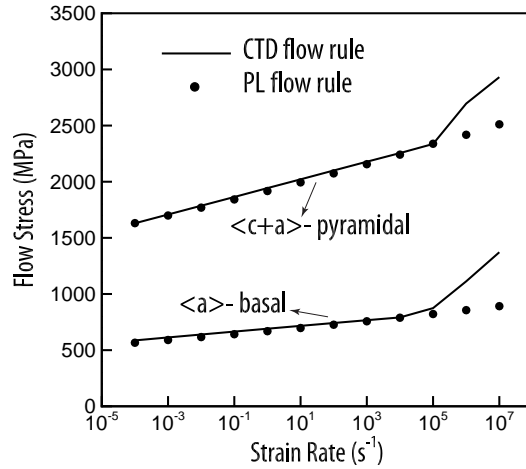


Figure 16: rate dependence of flow stress of single crystal model at 8% strain

Studying the response of the single crystal model oriented favorably for $\langle a \rangle$ -
 760 basal slip under high rate of deformation reveals some salient features of the
 CTD model. Figure 17 depicts the loading direction stress-strain response for
 the single crystal model oriented favorably for $\langle a \rangle$ - basal slip at different strain
 rates. An elastic overshoot occurs in the stress response at strain rates beyond
 $10^6 s^{-1}$, and it becomes more pronounced as the applied strain rate increases.
 765 Elastic overshoot has been also reported in the simulations of copper [61] and
 vanadium [33] under high rates of deformation.

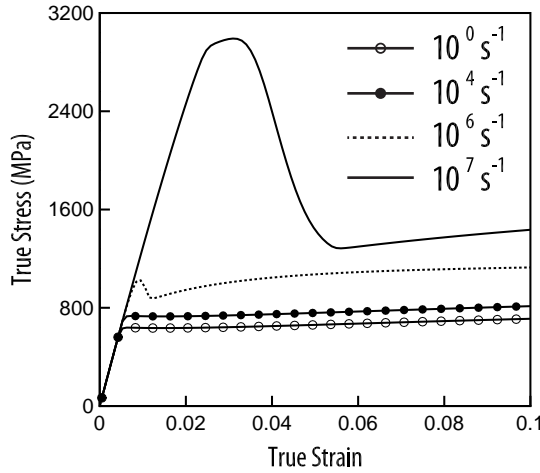


Figure 17: the loading direction stress-strain response for the single crystal model oriented favorably for $\langle a \rangle$ - basal slip

The initial peak in the stress can be explained in terms of dislocation activity on individual slip systems. Schmid factor analysis can provide some insight regarding the activity of slip systems. The Schmid factor analysis given in Table
 770 6 indicates that $[2\bar{1}10]$ basal slip system has the highest Schmid factor, leading to a prevailing single-slip mode. The Schmid factor is not provided in Table 6 for $\langle a \rangle$ - pyramidal and $\langle c+a \rangle$ - pyramidal slip system families due to their inactivity in this particular loading case. In order to measure the importance of the effects of thermally-activated and drag-dominated processes on dislocation
 775 glide, a quantity, referred to as *drag proportion*, is introduced and defined as the ratio of the time spent on the drag-dominated stage over the total travel time, i.e. $f_d = t_r / (t_w + t_r)$. f_d is only defined for active slip systems and falls in the range $(0, 1]$, where $f_d \rightarrow 0$ corresponds to predominantly thermally-activated dislocation glide and $f_d = 1$ denotes purely drag-dominated glide.
 780 Figure 18 shows the evolution of temperature, plastic shearing rate and drag proportion on the basal and prism slip system families at the strain rate of $10^7 s^{-1}$. All slip systems in the basal and prism families become active at some point during deformation except for P2; therefore, it is not included in the plots

in Figure 18. The course of deformation could be generally divided into multiple stages, enumerated in Figure 18. Stage I corresponds to a purely elastic regime where the resolved shear stress on all slip systems is smaller than the long-range stress, viz. passing stress. In stage II, dislocation slip starts to occur on B2; however, the initial dislocation density is not sufficient to accommodate the applied strain rate with plastic deformation. Therefore, the material needs to deform elastically until a sufficient amount of dislocations becomes available. This translates into an increase in the stress level and consequently provides enough resolved shear stress to activate the other basal and prism slip systems with lower Schmid factors, as shown in Figure 18b. Figure 18d shows the transition of dislocation glide from a thermally-activated mechanism into a drag-dominated one in this stage. In stage III, there is collectively sufficient dislocation content to accommodate the applied strain rate with plastic shearing rate, and therefore the macroscopic stress-strain response deviates clearly from a predominant elastic response. During this stage, dislocation glide remains in the drag-dominated regime, and plastic shearing rate on active slip systems, specifically on B2, increases, causing the self and latent hardening to become more pronounced. Figure 18c shows the evolution of temperature in this stage due to the significant amount of plastic work. During stage IV, dislocation glide on B2 remains in the drag-dominated regime, and sufficient dislocation density accumulates on B2 to accommodate further plastic deformation. Hence a drop in the stress level is observed in this stage. As the stress decreases, the plastic contribution of slip systems with lower Schmid factor, namely B1, B3, P1 and P3, progressively reduces until these slip systems eventually become inactive at the end of this stage. In Stage V, B2 is the sole active slip system, and self hardening through the evolution of the parallel dislocation population is the main source of strain hardening observed in Figure 18a. During this step, the thermally-activated processes become more significant, and the mechanism governing dislocation glide transitions from a drag-dominated mode to a mixed mode.

The high stresses induced by the elastic overshoot at very high strain rates could be relieved in real materials by either nucleating new dislocations (in addition to the dislocation multiplication considered in this paper) [35] or deformation twinning [2, 77]. Considering the contribution of homogeneous and heterogeneous dislocation nucleation to the evolution of dislocation population could be of benefit in simulation of polycrystals subject to very high strain rate and shock loading [78, 79].

The model presented in this paper considers dislocation slip as the major deformation mechanism based on the experimental results in [45, 46] where twinning was not reported for Ti alloys with high Al concentration. Nevertheless, augmenting the model with deformation twinning mechanism could be advantageous for simulating deformation of (un-)alloyed titanium at very low temperatures or high strain rates.

Experiments on polycrystalline Ti samples have shown an increasing rate sensitivity with logarithm of strain rate [2]. Based on the rate sensitivity study conducted on the single crystal models, it is expected that the CTD model

slip system family	Miller-Bravais index	label	Schmid factor
basal	(0001) $[1\bar{2}10]$	B1	-0.25
	(0001) $[\bar{2}110]$	B2	0.50
	(0001) $[11\bar{2}0]$	B3	-0.25
prism	(10\bar{1}0) $[\bar{1}2\bar{1}0]$	P1	0.22
	(01\bar{1}0) $[\bar{2}110]$	P2	0.00
	(\bar{1}100) $[\bar{1}\bar{1}20]$	P3	-0.22

Table 6: List of Schmid factors for basal and prism slip families for the single crystal model oriented favorably for $\langle a \rangle$ - basal slip

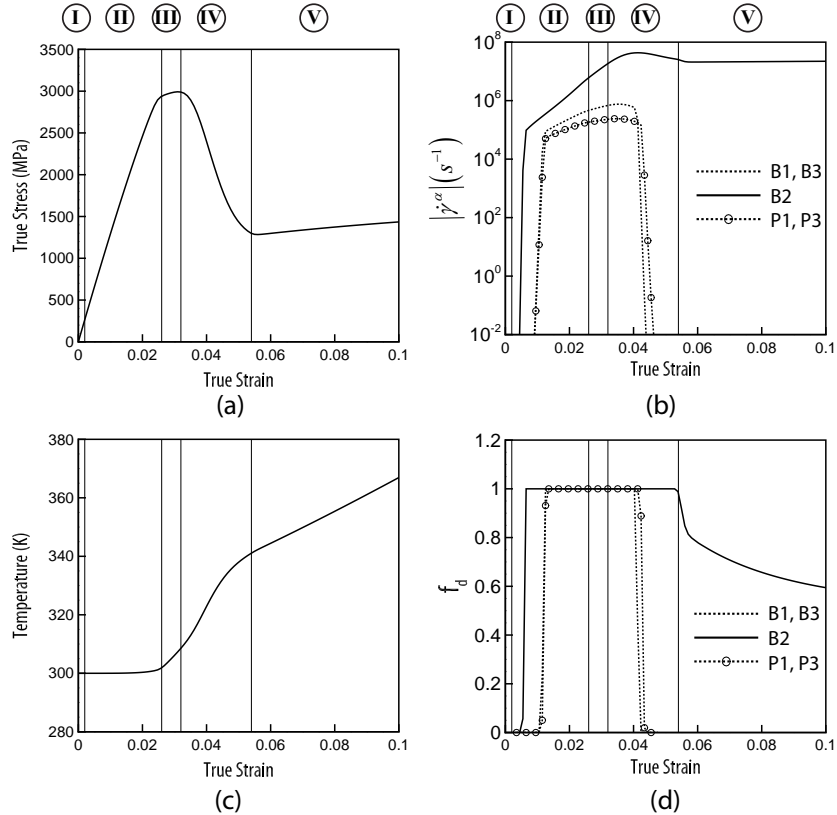


Figure 18: CPFE simulation of the single crystal model oriented favorably for $\langle a \rangle$ - basal slip at strain rate of $10^7 s^{-1}$, (a) the loading direction stress-strain response, evolution of (b) plastic shearing rate, (c) temperature and (d) drag proportion. (the Roman numerals denote

830 could show the change in the rate sensitivity of polycrystalline microstructures, as well. Compression of the RA sample along ND is simulated under different rates of deformation. Flow stress at 6% strain is extracted and compared with the available experimental results on rate sensitivity of some Ti polycrystals in Figure 19. It is observed that the PL model exhibits a constant rate sensitivity 835 across different strain rates whereas the CTD model shows a change in the rate sensitivity for strain rates higher than $10^5 s^{-1}$. This is in good agreement with the experimental results of Casem [80] where an enhanced hardening effect is observed beyond strain rates of $10^4 s^{-1}$.

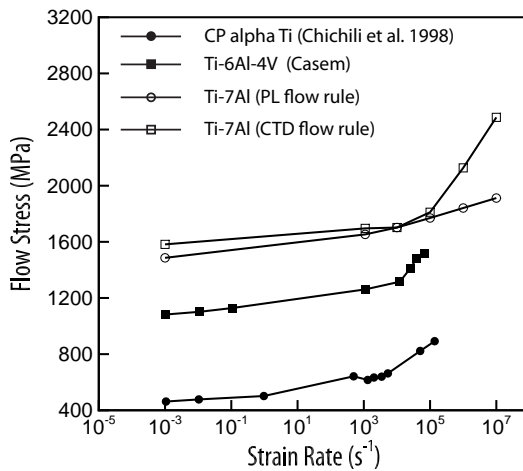


Figure 19: rate dependence of flow stress in Ti polycrystals at 6% strain

6.3. Temperature-dependence of flow stress

840 Ti alloys are used in military and aerospace components which experience different thermal environments during service. Changes in temperature influence both the elastic and plastic responses of the material. As temperature increases, the elastic constants reduce which indirectly affect the slip-driven plasticity by reducing the shear modulus-dependent strength of slip systems 845 [81], represented by the athermal stress in this paper. Increasing temperature would also directly promote plasticity by boosting up the rate of successful thermal activation attempts. In this section, the effects of temperature on deformation is studied in the context of deformations under isothermal conditions. In the remainder of this paper, all simulations are done using the CTD model.

850 Compression of the AR microstructure along ND and RD at strain rate of $10^{-3} s^{-1}$ is simulated under isothermal conditions, but at different initial temperatures. The loading direction stress-strain responses are plotted in Figure 20a. As the temperature increases, it is seen that the yield stress decreases significantly while the elastic stiffness reduces negligibly. Figure 20b shows the

855 variation of the yield stress with temperature within a temperature range of
 856 300K to 700K. It is observed that the yield stress decreases almost linearly
 857 with temperature within the specified temperature range, consistent with the
 858 experimental results of Khan et al. [4] on another Ti alloy, Ti-6Al-4V. It is
 859 worthy to note that the yield stress corresponding to the AR-ND simulations
 860 decreases more rapidly with temperature in comparison with the one for the AR-
 861 RD simulations. This is owing to the crystallographic orientation of the grains
 862 and dissimilar variation of critical resolved shear stress (CRSS) on different slip
 863 systems with temperature. The crystallographic orientations of the grains in
 864 the AR sample are such that the $\langle a \rangle$ - basal and prism slip systems are the
 865 favorable modes of slip when the sample is loaded along RD, whereas $\langle c+a \rangle$ -
 866 pyramidal slip is the favorable one for the case of loading along ND. As shown
 867 earlier in Figure 11, the CRSS for the $\langle c+a \rangle$ - pyramidal slip system reduces
 868 at a higher rate with respect to temperature, compared to the one for the $\langle a \rangle$ -
 869 basal and prism slip systems. This explains why the yield stress corresponding
 870 to the AR-ND simulations decreases more rapidly with temperature in Figure
 20b.

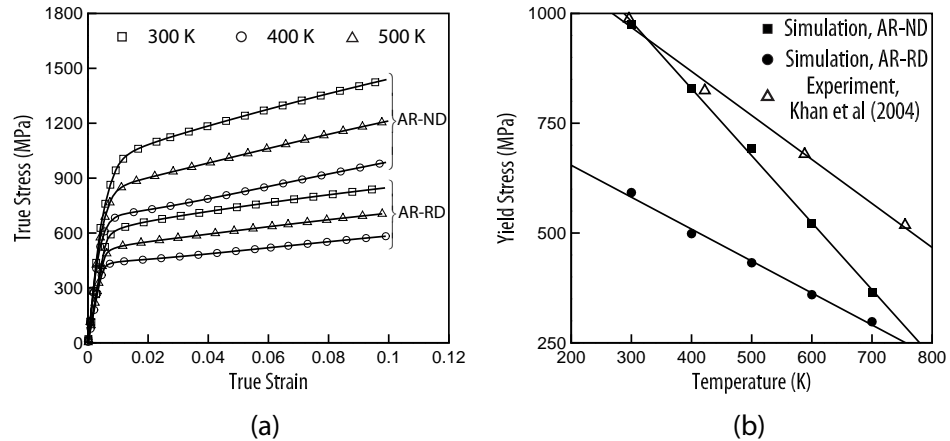


Figure 20: CPFE simulation of the AR microstructure at different initial temperatures subject to strain rate of $10^{-3}s^{-1}$, (a) the loading direction stress-strain response, (b) variation of yield stress with temperature

6.4. Adiabatic heating

875 The effects of temperature on the high-rate deformation of metals could be
 876 investigated in the context of adiabatic thermal conditions. In order to perceive
 877 the effects of adiabatic heating on the elasticity and plasticity, compression of
 878 the AR microstructure along ND is simulated at strain rate of 10^4s^{-1} . Different
 879 cases are considered in the simulations. Case I corresponds to a simulation in

which adiabatic heating is ignored, i.e. isothermal condition is assumed. Case II refers to a simulation where adiabatic heating is taken into account; however, the reduction of elastic constants with temperature is neglected. Case III denotes a simulation in which both adiabatic heating and reduction of elastic constants with temperature are considered. The macroscopic stress-strain response for the three different cases are given in Figure 21. Comparing the macroscopic stress-strain curves, it is observed that the pre-yield part of the stress-strain response is barely affected by the adiabatic heating since the amount of plastic work is limited and the local temperature slightly increases in this stage of deformation. With the evolution of temperature during the course of deformation, the effect of adiabatic heating becomes more evident at higher strains where a lower strain hardening is obtained for case III, compared to case I where the temperature evolution was suppressed. Moreover, based on the the macroscopic response for cases II and III in Figure 21, it is inferred that the effect of reduction of elastic constants with temperature becomes noticeable only at strains beyond 0.15. In other words, considering elastic softening is of secondary importance if the failure processes of the material due to nucleation and evolution of microstructural defects start at early stages of deformation. This is consistent with the results in [82] where the effect of temperature evolution on the failure of Ti alloys were investigated.

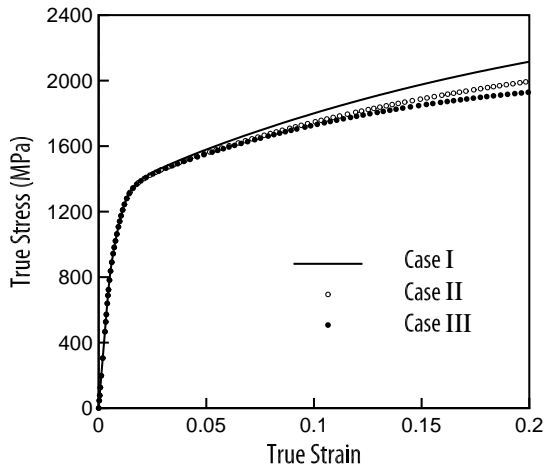


Figure 21: the loading direction stress-strain response for compression of the AR microstructure along ND at strain rate of $10^4 s^{-1}$

Failure of Ti alloys under high rates of deformation is attributed to formation of adiabatic shear bands (ASBs) which could in turn be related to the emergence of hot spots due to adiabatic heating. In order to inspect the temperature evolution at the grain level for case III, the granular temperature increase, denoted by $\Delta\bar{T}_g$, is calculated for each grain, and its distribution over the entire

microstructure at four different stages of deformation is plotted in Figure 22a. The granular temperature increase for an arbitrary grain, say g , is evaluated as
905
$$\Delta\bar{T}_g = \sum_{i=1}^{N_e^{(g)}} \Omega_i \Delta\bar{T}_i / \sum_{i=1}^{N_e^{(g)}} \Omega_i$$
 where $N_e^{(g)}$ is the number of elements in grain g and Ω_i and $\Delta\bar{T}_i$ are respectively the volume and temperature increase in the i -th element in grain g . Evolution of $\Delta\bar{T}_g$ distribution clearly indicates that not only the average temperature in individual grains, but also the standard deviation increases during the course of deformation. Similar trend is observed
910 for the distribution of the granular effective plastic strain, shown in Figure 22b. The increase in the heterogeneity of plastic strain field implies that the microplasticity distribution transitions from a nearly uniform state in the early stages of deformation to a non-uniform one in the later stages. The tendency of the deformation towards non-uniform distribution of the plastic strain indicates the
915 development of severely plastically-deformed grains. If the grains happen to be located adjacent to each other, a large region of localized deformation is created, as shown in Figure 23. In this region, both plastic deformation and temperature are high. Formation of these regions may facilitate nucleation of the adiabatic shear bands and therefore expedite activation of the failure processes.

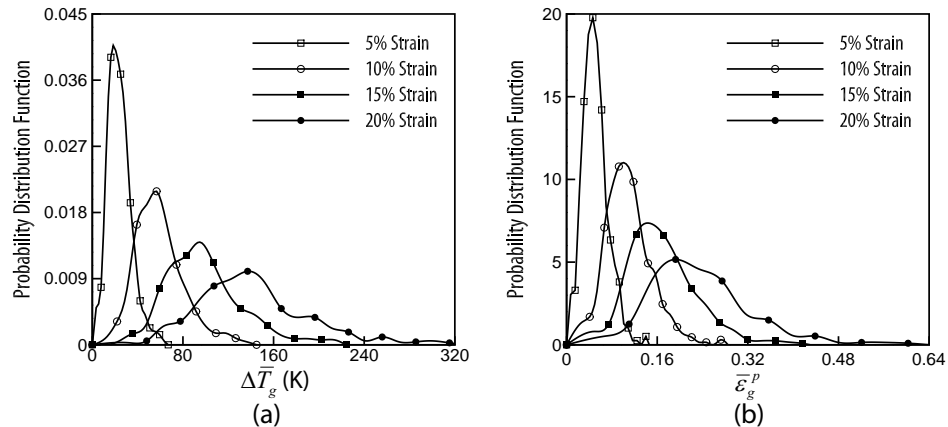


Figure 22: CPFE simulation of the AR microstructure along ND at strain rate of 10^4 s^{-1} , evolution of probability distribution function of (a) $\Delta\bar{T}_g$ and (b) $\bar{\epsilon}_g^p$ at different stages of deformation

920 Since the adiabatic heating is inter-related with the plastic deformation, one might think that the distributions shown in Figure 22 are consistent with each other; that is, as plasticity gets localized in certain grains, the temperature also adiabatically increases in those grains and causes the increase in the standard deviation in Figure 22a. However, further inspection of the microstructure
925 revealed some unexpected behavior in the contours of plastic strain and temperature. It was observed that the regions with high value of plastic strain does

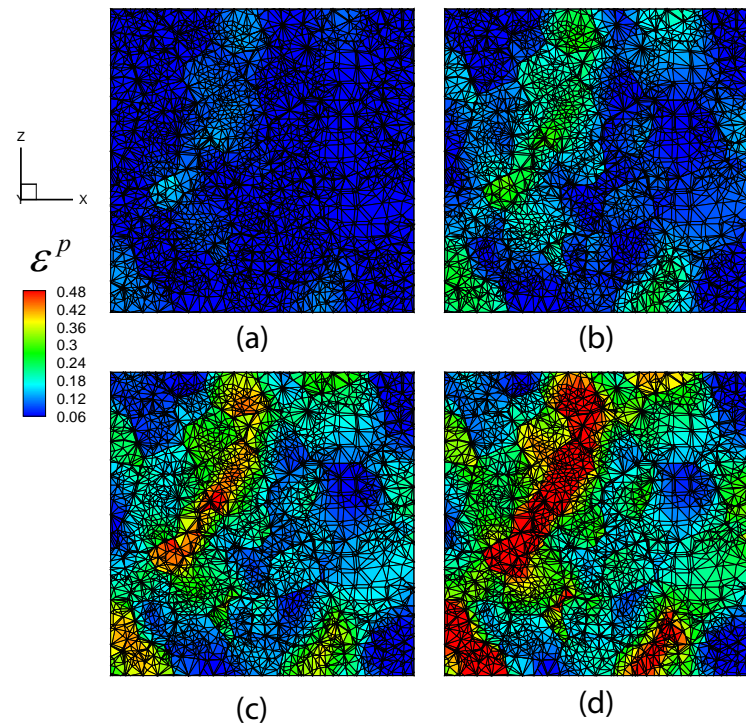


Figure 23: Development of a region of plastic localization in the AR microstructure under compression along ND at strain rate of $10^4 s^{-1}$. The contours are drawn in the undeformed configuration.

not necessarily correspond to the hot spots in the contour plot of temperature field and vice versa. For example, the contour plot of effective plastic strain in Figure 24a shows that grain *A* is highly plastically deformed, however the contour plot of temperature field in Figure 24b does not suggest an elevated temperature in this grain. On the other hand, grains *B*, *C* and *D* are experiencing an elevated thermal field although they are undergoing moderate plastic deformation. In order to realize the reason behind this unexpected behavior, the formulation of plastic power density is recalled, $W_p = \boldsymbol{\sigma} : \mathbf{d}^p$. The rate of plastic work is dependent on the stress level and the rate of plastic deformation in a multiplicative form. Hence, a high value of plastic strain by itself does not constitute a high value of plastic work and consequently adiabatic heating. Temperature may increase more at a material point with high level of stress but low plastic strain, compared to another material point with higher plastic strain and lower stress. In light of this point, the temperature trends in grains *A*, *B*, *C* and *D* sound more reasonable by considering the contour plot of von Mises stress, as a measure of stress tensor, shown in Figure 24c.

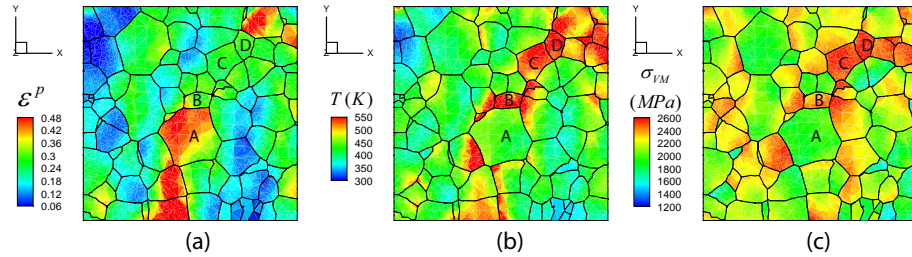


Figure 24: CPFE simulation of the AR microstructure along ND at strain rate of $10^4 s^{-1}$, contour plots of (a) effective plastic strain, (b) temperature and (c) von Mises stress at 20% strain

The observation that the grains with severe plastic deformation do not necessarily endure high rates of adiabatic heating is not a coincidence. A bi-crystal model consisting of a *hard* and *soft* grain is generated, as shown in Figure 25a. The orientations of the *soft* and *hard* grains are identical to the ones shown in Figures 13a and 13c, respectively. Figure 25b shows the macroscopic loading direction stress-strain response of the bi-crystal model under compression along [001] at strain rate of $10^4 s^{-1}$. Three stages of deformation are selected as indicated in Figure 25b. The evolution of relevant micro-mechanical variables are investigated at these stages along an X-directed line passing through the centroid of the bi-crystal model. At stage I, the plastic flow has already started in the soft grain whereas the hard grain has barely deformed plastically. Thus, as shown in Figure 26a, the temperature in the soft grain is higher than the one in the hard grain, but slightly. In the next stages of deformation, it is observed that the temperature in the hard grain becomes much higher in comparison

with the soft grain. It is instructive to remember that it is the soft grain which undergoes a higher level of plastic strain during the entire deformation. Here again the rate of adiabatic heating is governed by the stress state. The temperature difference between the two grains grows larger in the course of deformation 960 as shown in Figures 26b and 26c.

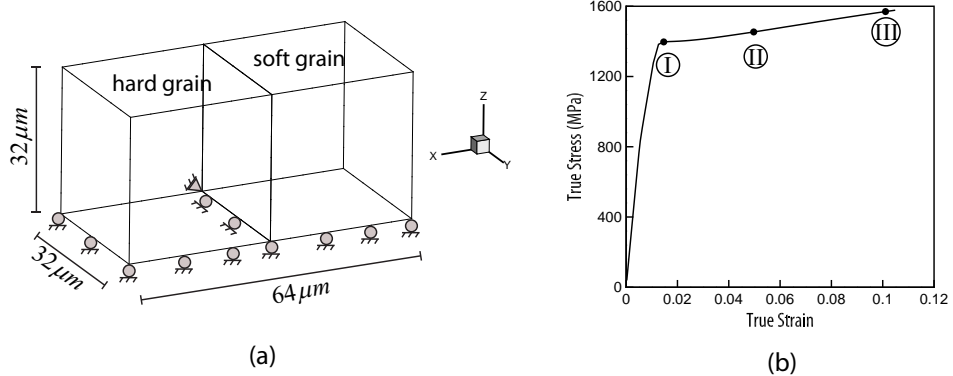


Figure 25: (a) bi-crystal model consisting of 5103 linear tetrahedral elements, (b) macroscopic loading direction stress-strain response for compression at strain rate of $10^4 s^{-1}$ along [001]

This bi-crystal problem is a simple but yet enlightening problem. The importance of the results in Figure 26 goes beyond the determination of the *hot* grain and impacts the predictions of models for formation of adiabatic shear 965 bands under high rates of deformation. Given the formation and propagation of ASBs are beyond the scope of the paper, we content with a brief introduction to different criteria for formation of ASBs and simply state their implication on nucleation site of ASBs in the bi-crystal problem. Different criteria have been proposed in the literature for estimating the formation of adiabatic shear 970 bands. These criteria are based on selecting a specific thermo-mechanical quantity, such as plastic shear strain [83], temperature [84] and stored energy of cold work [82, 85]. These criteria predict formation of ASBs in the material once the specified thermo-mechanical quantity exceeds a critical value. In light of the results shown in Figure 26, these criteria do not predict the same grain as 975 the nucleation site for ASBs in the bi-crystal problem. Using the critical plastic shear strain criterion, ASBs nucleate in the soft grain since it undergoes higher levels of plasticity, whereas both the critical temperature and critical stored energy of cold work criteria suggest that the nucleation site for ASBs is the hard grain due to the higher level of plastic work. If the experimental apparatus allows for the experimentation on a bi-crystal sample, the observations in terms of 980 nucleating site for ASBs could provide some insight and be used to test validity of the nucleation models.

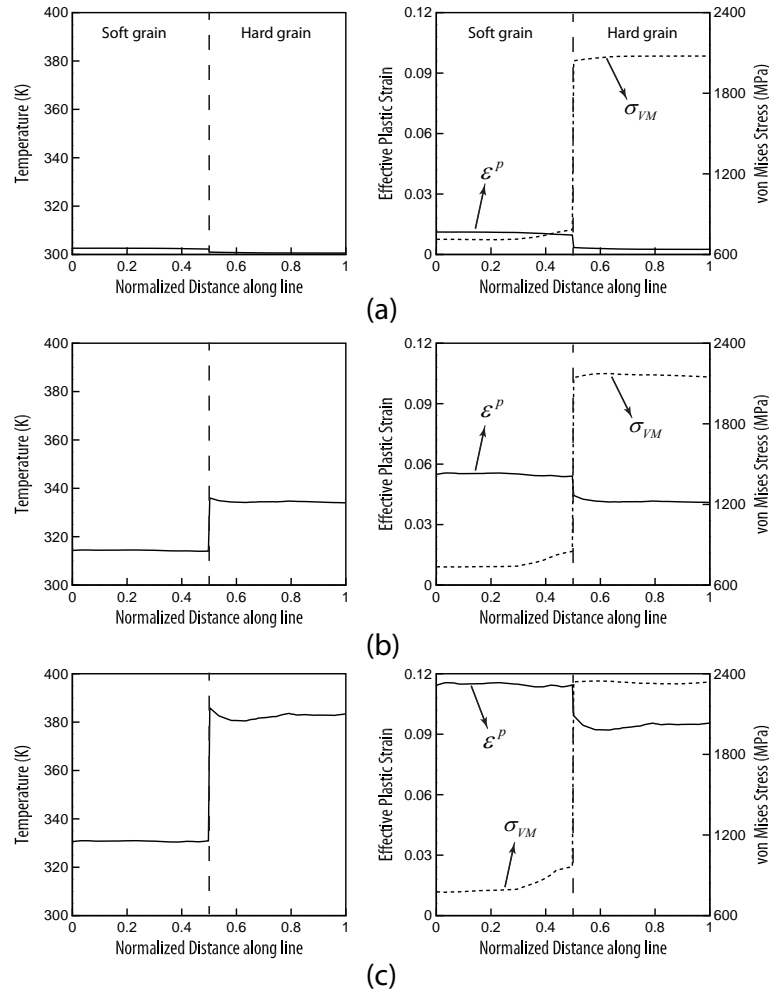


Figure 26: Profile of temperature, effective plastic strain and von Mises stress along a line at (a) 1.5% strain (stage I), (a) 5% strain (stage II) and (a) 10% strain (stage III)

7. Concluding remarks

A crystal plasticity constitutive model is proposed which could be used for a wide range of strain rates. Flow rule in the proposed constitutive model is the Orowan equation which expresses the slip rate on a given slip system in terms of the dislocation density and average dislocation velocity. Capability of the model in simulating deformations across decades of strain rate inheres in formulating the average dislocation velocity in terms of both the thermally-activated and drag-dominated stages of screw dislocation motion in the glide plane. The proposed constitutive model is explicitly temperature dependent which makes it suitable for modeling high strain rate deformations where temperature increase adiabatically due to the conversion of plastic work into heat. Effects of temperature on elasticity and plasticity are carefully calibrated using the experimental results.

Simulation results demonstrate the competency of the model in predicting material response in quasi-static and dynamic rates. The model can effectively capture the increase in the rate sensitivity of flow stress at higher rates of deformation due to the transition in the rate controlling mechanism of dislocation motion. The model predicts an elastic overshoot in the single crystal level under very high strain rates due to the insufficient dislocation content to accommodate the applied strain rate. Consistent with experiments, isothermal quasi-static simulations show that the 0.2% yield stress decreases almost linearly with temperature in the temperature range of interest. The rate of decrease is observed to be higher along ND since the CRSS for $\langle c+a \rangle$ - drops faster with temperature compared to the one for the $\langle a \rangle$ - type slip systems. Adiabatic simulations show that the effect of temperature on enhancing plasticity is more pronounced than its effect on degradation of the elastic constants. Analysis of high strain rate simulations showed the tendency of the microstructure towards localizing plastic deformation as the material straining progresses. Unexpectedly careful analysis of adiabatic heating revealed that the grains with severe plastic deformation do not necessarily endure high temperatures as a result of conversion of plastic work into heat.

The work presented in this paper focused on modeling the deformation under different strain rates. This is the first step towards modeling failure in Ti alloys. The next step of the research is to develop proper physics-based criterion for nucleation of adiabatic shear bands, a precursor to the material failure. The propensity of the material for twinning and its relationship with the local temperature increase need to be investigated as well.

ACKNOWLEDGMENTS

This work has been supported by the Army Research Office through grant No. W911NF-12-1-0376 (Program Manager: Dr. A. Rubinstein). The authors would like to thank Dr. Adam Pilchak for providing the Ti-7Al samples. Computing support by the Homewood High Performance Compute Cluster (HHPC)

¹⁰²⁵ and the Maryland Advanced Research Computing Center (MARCC) is gratefully acknowledged.

References

[1] J. Montgomery, M. Wells, B. Roopchand, J. Ogilvy, Low-cost titanium armors for combat vehicles, *JOM* 49 (1997).

[2] D. Chichili, K. Ramesh, K. Hemker, The high-strain-rate response of alpha-titanium: experiments, deformation mechanisms and modeling, *Acta Mater* 46 (1998) 1025 – 1043.

[3] G. Ravichandran, A. J. Rosakis, J. Hodowany, P. Rosakis, On the conversion of plastic work into heat during high-strain-rate deformation, in: *Shock Compression of Condensed Matter*, volume 620 of *American Institute of Physics Conference Series*, 2002, pp. 557–562. doi:10.1063/1.1483600.

[4] A. S. Khan, Y. S. Suh, R. Kazmi, Quasi-static and dynamic loading responses and constitutive modeling of titanium alloys, *Int J Plasticity* 20 (2004) 2233 – 2248.

[5] A. S. Khan, R. Kazmi, B. Farrokh, Multiaxial and non-proportional loading responses, anisotropy and modeling of Ti6Al4V titanium alloy over wide ranges of strain rates and temperatures, *Int J Plasticity* 23 (2007) 931 – 950.

[6] A. S. Khan, S. Yu, Deformation induced anisotropic responses of Ti6Al4V alloy. part i: Experiments, *Int J Plasticity* 38 (2012) 1 – 13.

[7] M. Bache, A review of dwell sensitive fatigue in titanium alloys: the role of microstructure, texture and operating conditions, *Int J Fatigue* 25 (2003) 1079 – 1087.

[8] V. Sinha, M. Mills, J. Williams, Determination of crystallographic orientation of dwell-fatigue fracture facets in Ti-6242 alloy, *J Mater Sci* 42 (2007) 8334–8341.

[9] A. L. Pilchak, Fatigue crack growth rates in alpha titanium: Faceted vs. striation growth, *Scripta Mater* 68 (2013) 277 – 280.

[10] S. Keshavarz, S. Ghosh, Hierarchical crystal plasticity {FE} model for nickel-based superalloys: Sub-grain microstructures to polycrystalline aggregates, *Int J Solids Struct* 55 (2015) 17 – 31.

[11] M. Groeber, S. Ghosh, M. Uchic, D. Dimiduk, A framework for automated analysis and simulation of 3D polycrystalline microstructures: Part 1: statistical characterization, *Acta Mater* 56 (2008) 1257–1273.

[12] M. Groeber, S. Ghosh, M. Uchic, D. Dimiduk, A framework for automated analysis and simulation of 3D polycrystalline microstructures. part 2: Synthetic structure generation, *Acta Mater* 56 (2008) 12741287.

1065 [13] M. Groeber, M. Jackson, DREAM.3D: A digital representation environment for the analysis of microstructure in 3D, *Integr Mater Manuf Innov* 3 (2014).

1070 [14] Simulation Modeling Suite, Simmetrix Inc., <http://www.simmetrix.com>, 2015.

1075 [15] C. Dohrmann, M. W. Heinstein, J. Jung, S. W. Key, W. R. Witkowski, Node-based uniform strain elements for three-node triangular and four-node tetrahedral meshes, *Int J Numer Meth Eng* 47 (2000) 1549–1568.

1080 [16] M. A. Puso, J. Solberg, A stabilized nodally integrated tetrahedral, *Int. J. Numer. Meth. Eng.* 67 (2006) 841 – 867.

1085 [17] E. A. de Souza Neto, F. M. A. Pires, D. R. J. Owen, F-bar-based linear triangles and tetrahedra for finite strain analysis of nearly incompressible solids. part I: formulation and benchmarking, *Int J Numer Meth Eng* 62 (2005) 353–383.

[18] K. Matou, A. Maniatty, Finite element formulation for modelling large deformations in elasto-viscoplastic polycrystals, *Int. J. Numer. Meth. Eng.* 60 (2004) 2313 – 2333.

1090 [19] W. Zeng, J. Larsen, G. Liu, Smoothing technique based crystal plasticity finite element modeling of crystalline materials, *Int J Plasticity* 65 (2015) 250 – 268.

[20] J. Cheng, A. Shahba, S. Ghosh, Stabilized tetrahedral elements for crystal plasticity finite element analysis overcoming volumetric locking, *Comput Mech* (2016) in press.

1095 [21] D. Peirce, R. Asaro, A. Needleman, An analysis of nonuniform and localized deformation in ductile single crystals, *Acta Metal* 30 (1982) 1087 – 1119.

[22] U. Kocks, A. Argon, M. Ashby, Thermodynamics and kinetics of slip, *Prog Mater Sci* 19 (1975).

1100 [23] S. Keshavarz, S. Ghosh, Multi-scale crystal plasticity finite element model approach to modeling nickel-based superalloys, *Acta Mater* 61 (2013) 6549 – 6561.

[24] F. Dunne, D. Rugg, A. Walker, Lengthscale-dependent, elastically anisotropic, physically-based hcp crystal plasticity: Application to cold-dwell fatigue in Ti alloys, *Int J Plasticity* 23 (2007) 1061 – 1083.

1105 [25] Z. Zhang, M. A. Cuddihy, F. P. E. Dunne, On rate-dependent polycrystal deformation: the temperature sensitivity of cold dwell fatigue, *Proc Royal Soc London A* 471 (2015).

1100 [26] D. Ozturk, A. Shahba, S. Ghosh, Crystal plasticity FE study of the effect of thermo-mechanical loading on fatigue crack nucleation in titanium alloys, *Fatigue Fract Eng Mater Struct* (2016) in press.

1105 [27] V. Hasija, S. Ghosh, M. J. Mills, D. S. Joseph, Deformation and creep modeling in polycrystalline Ti6Al alloys, *Acta Mater* 51 (2003) 4533–4549.

1110 [28] H. J. Frost, M. F. Ashby, Motion of a dislocation acted on by a viscous drag through an array of discrete obstacles, *J Appl Physics* 42 (1971) 5273–5279.

1115 [29] A. I. Landau, The effect of dislocation inertia on the thermally activated low-temperature plasticity of materials. i. theory, *Physica Status Solidi A* 61 (1980) 555–563.

1120 [30] R. D. Isaac, A. V. Granato, Rate theory of dislocation motion: Thermal activation and inertial effects, *Phys Rev B* 37 (1988) 9278–9285.

1125 [31] M. Hiratani, E. Nadgorny, Combined model of dislocation motion with thermally activated and drag-dependent stages, *Acta Mater* 49 (2001) 4337 – 4346.

1130 [32] M. Hiratani, H. Zbib, M. Khaleel, Modeling of thermally activated dislocation glide and plastic flow through local obstacles, *Int J Plasticity* 19 (2003) 1271 – 1296.

1135 [33] N. Barton, J. Bernier, R. Becker, A. Arsenlis, R. Cavallo, J. Marian, M. Rhee, H. Park, B. Remington, R. Olson, A multiscale strength model for extreme loading conditions, *J Appl Physics* 109 (2011).

1140 [34] R. Becker, A. Arsenlis, J. Marian, M. Rhee, M. Tang, L. Yang, Continuum level formulation and implementation of a multi-scale model for vanadium, Technical Report, Lawrence Livermore National Laboratory, 2009.

1145 [35] R. Austin, D. McDowell, A dislocation-based constitutive model for viscoplastic deformation of fcc metals at very high strain rates, *Int J Plasticity* 27 (2011) 1 – 24.

1150 [36] Y. Bhandari, S. Sarkar, M. Groeber, M. Uchic, D. Dimiduk, S. Ghosh, 3D polycrystalline microstructure reconstruction from FIB generated serial sections for FE analysis, *Comput Mater Sci* 41 (2007) 222 – 235.

1155 [37] S. Ghosh, Y. Bhandari, M. Groeber, CAD-based reconstruction of 3D polycrystalline alloy microstructures from FIB generated serial sections, *Computer-Aided Design* 40 (2008) 293 – 310.

1160 [38] M. Brandes, Creep, fatigue, and deformation of alpha and alpha-beta titanium alloys at ambient temperature, Ph.D. thesis, Materials science and engineering, Ohio State University, USA, 2008.

1165 [39] J. Russ, R. Dehoff, Practical streology, 2nd edition, Plenum press, 1999.

[40] J. Thomas, M. Groeber, S. Ghosh, Image-based crystal plasticity FE framework for microstructure dependent properties of Ti6Al4V alloys, *Mater Sci Eng A* 553 (2012) 164–175.

[41] W. Chen, B. Song, Split Hopkinson (Kolsky) Bar: Design, Testing and Applications, Springer Science+Business Media, LLC, Boston, MA, 2011.

[42] H. Conrad, M. Doner, B. de Meester, Titanium science and technology, Plenum press, 1973.

[43] T. Neeraj, M. Mills, Short-range order (sro) and its effect on the primary creep behavior of a Ti6wt. % Al alloy, *Mater Sci Eng A* 319321 (2001) 415 – 419.

[44] H. Li, D. Mason, T. Bieler, C. Boehlert, M. Crimp, Methodology for estimating the critical resolved shear stress ratios of α -phase ti using ebsd-based trace analysis, *Acta Mater* 61 (2013) 7555 – 7567.

[45] N. Paton, R. Baggerly, J. Williams, Deformation and Solid Solution Strengthening of Titanium-Aluminum Single Crystals, Technical Report, Rockwell Int. Report, 1976.

[46] J. Williams, R. Baggerly, N. Paton, Deformation behavior of HCP Ti-Al alloy single crystals, *Metall Mater Trans A* 33 (2002) 837850.

[47] B.-J. Lee, K. Vecchio, S. Ahzi, S. Schoenfeld, Modeling the mechanical behavior of tantalum, *Metal Mater Trans A* 28 (1997) 113–122.

[48] Y. Nie, Y. Xie, *Ab initio* thermodynamics of the hcp metals Mg, Ti, and Zr, *Phys Rev B* 75 (2007) 174117.

[49] P. Souvatzis, O. Eriksson, M. I. Katsnelson, Anomalous thermal expansion in α -titanium, *Phys Rev Lett* 99 (2007) 015901.

[50] V. Nizhankovskii, M. Katsnelson, G. Peschanskikh, A. Trefilov, Anisotropy of the thermal-expansion of titanium due to proximity to an electronic topological transition, *JETP lett* 59 (1994) 733–737.

[51] R. Asaro, J. Rice, Strain localization in ductile single crystals, *J Mech Physics Solids* 25 (1977) 309 – 338.

[52] D. Deka, D. S. Joseph, S. Ghosh, M. J. Mills, Crystal plasticity modeling of deformation and creep in polycrystalline Ti-6242, *Metall Trans A* 37A(5) (2006) 1371–1388.

[53] G. Venkataramani, S. Ghosh, M. J. Mills, A size dependent crystal plasticity finite element model for creep and load-shedding in polycrystalline Titanium alloys, *Acta Mater* 55 (2007) 3971–3986.

[54] G. Venkataramani, K. Kirane, S. Ghosh, Microstructural parameters affecting creep induced load shedding in Ti-6242 by a size dependent crystal plasticity FE model, *Int J Plasticity* 24 (2008) 428–454.

[55] A. Ma, F. Roters, D. Raabe, A dislocation density based constitutive model for crystal plasticity {FEM} including geometrically necessary dislocations, *Acta Mater* 54 (2006) 2169 – 2179.

[56] J. Cheng, S. Ghosh, A crystal plasticity {FE} model for deformation with twin nucleation in magnesium alloys, *Int J Plasticity* 67 (2015) 148 – 170.

[57] P. Guyot, J. Dorn, a critical review of the Peierls mechanism, *Canadian J Physics* 45 (1967) 983–1016.

[58] M. Tang, L. Kubin, G. Canova, Dislocation mobility and the mechanical response of b.c.c. single crystals: A mesoscopic approach, *Acta Mater* 46 (1998) 3221 – 3235.

[59] A. Alankar, P. Eisenlohr, D. Raabe, A dislocation density-based crystal plasticity constitutive model for prismatic slip in α -titanium, *Acta Mater* 59 (2011) 7003 – 7009.

[60] S. Nemat-Nasser, W. Guo, J. Cheng, Mechanical properties and deformation mechanisms of a commercially pure titanium, *Acta Mater* 47 (1999) 3705 – 3720.

[61] B. Hansen, I. Beyerlein, C. Bronkhorst, E. Cerreta, D. Dennis-Koller, A dislocation-based multi-rate single crystal plasticity model, *Int J Plasticity* 44 (2013) 129 – 146.

[62] A. Arsenlis, D. M. Parks, Crystallographic aspects of geometrically-necessary and statistically-stored dislocation density, *Acta Mater* 47 (1998) 1597–1611.

[63] U. Essmann, H. Mughrabi, Annihilation of dislocations during tensile and cyclic deformation and limits of dislocation densities, *Phil Mag A* 40 (1979) 731–756.

[64] H. Mecking, U. Kocks, Kinetics of flow and strain-hardening, *Acta Metal* 29 (1981) 1865 – 1875.

[65] H. Dai, Geometrically-necessary dislocation density in continuum plasticity theory, FEM implementation and applications, Ph.D. thesis, Department of Mechanical Engineering, Massachusetts Institute of Technology, USA, 1997.

[66] O. Zienkiewicz, J. Zhu, The superconvergent patch recovery (SPR) and adaptive finite element refinement, *Comput Meth Appl Mech Eng* 101 (1992) 207 – 224.

[67] J. Clayton, Dynamic plasticity and fracture in high density polycrystals: constitutive modeling and numerical simulation, *J Mech Phys Solids* 53 (2005) 261301.

[68] Metallic Materials and Elements for Aerospace Vehicle Structures, U.S. Department of Defense, 1998.

[69] X. Ling, M. F. Horstemeyer, G. P. Potirniche, On the numerical implementation of 3d rate-dependent single crystal plasticity formulations, *Int J Numer Meth Eng* 63 (2005) 548–568.

[70] M. Anahid, M. K. Samal, S. Ghosh, Dwell fatigue crack nucleation model based on crystal plasticity finite element simulations of polycrystalline titanium alloys, *J Mech Physics Solids* 59 (2011) 2157 – 2176.

[71] M. Anahid, S. Ghosh, Homogenized constitutive and fatigue nucleation models from crystal plasticity {FE} simulations of Ti alloys, part 2: Macroscopic probabilistic crack nucleation model, *Int J Plasticity* 48 (2013) 111 – 124.

[72] P. Shade, Private communication.

[73] H. Ogi, S. Kai, H. Ledbetter, R. Tarumi, M. Hirao, K. Takashima, Titanums high-temperature elastic constants through the hcpbcc phase transformation, *Acta Mater* 52 (2004) 2075–2080.

[74] A. Akhtar, E. Teghtsoonian, prismatic slip in α -titanium single crystals, *Metall Mater Trans A* 6 (1975) 2201–2208.

[75] T. Tanaka, H. Conrad, Deformation kinetics for $10\bar{1}011\bar{2}0$ slip in titanium single crystals below $0.4t_m$, *Acta Metal* 20 (1972) 1019 – 1029.

[76] P. Follansbee, G. Regazzoni, U. Kocks, Mechanical Properties at High Rates of Strain, *Proceedings of the Third Conference on the Mechanical Properties of Materials at High Rates of Strain Held in Oxford, 9-12 April 1984, Conference series, Inst. of Physics, 1984.*

[77] P. Follansbee, G. Gray, An analysis of the low temperature, low and high strain-rate deformation of Ti-6Al-4V, *Metall Trans A* 20 (1989) 863 – 874.

[78] M. Meyers, F. Gregori, B. Kad, M. Schneider, D. Kalantar, B. Remington, G. Ravichandran, T. Boehly, J. Wark, Laser-induced shock compression of monocrystalline copper: characterization and analysis, *Acta Mater* 51 (2003) 1211 – 1228.

[79] L. Capolungo, D. Spearot, M. Cherkaoui, D. McDowell, J. Qu, K. Jacob, Dislocation nucleation from bicrystal interfaces and grain boundary ledges: Relationship to nanocrystalline deformation, *J Mech Phys Solids* 55 (2007) 2300 – 2327.

1245 [80] D. Casem, Private communication.

[81] M. Ashby, The deformation of plastically non-homogeneous materials, Phil Magazine 21 (1970) 399–424.

[82] S. Osovski, D. Rittel, A. Venkert, The respective influence of microstructural and thermal softening on adiabatic shear localization, Mech Mater 1250 56 (2013) 11 – 22.

[83] R. Culver, Thermal instability strain in dynamic plastic deformation, Metallurgical efects at high strain rates, Plenum press, 1973.

[84] S. N. Medyanik, W. K. Liu, S. Li, On criteria for dynamic adiabatic shear band propagation, J Mech Phys Solids 55 (2007) 1439 – 1461.

1255 [85] D. Rittel, Z. G. Wang, M. Merzer, Adiabatic shear failure and dynamic stored energy of cold work, Phys Rev Lett 96 (2006) 075502.